A study on the validity of the Lattice Boltzmann Method as a way to simulate high Reynolds number flows past porous obstacles.

Navin M. Sangtani Lakhwani

Supervisors: **Dr. F. Nicolleau**[1] **& Prof. W. Brevis**[2]

A thesis submitted in partial fulfilment of the requirements for the degree of
Doctor of Philosophy.

The University of Sheffield.
Department of Mechanical Engineering.
December 2018

---

[1] Department of Mechanical Engineering, The University of Sheffield

[2] Department of Hydraulics and Environmental Engineering & Mining Engineering, Pontifical Catholic University of Chile.

Abstract

With ever growing levels of urbanisation across the globe, a good understanding of canopy flows is paramount to reduce pollution in major cities and prevent unwanted aerodynamic loading on structures. The multi-scale nature of not only urban construction but that of natural environments requires a more complex modelling system be employed. Fractal geometries have only recently been investigated in turbulent flows, their multi-scale properties make them the logical choice for modelling and simulating flows involving such complex geometries. Additionally, in recent years the usage of Lattice Boltzmann Methods (LBM) vs Computational Fluid Dynamics (CFD) has increased, since LBM offers better computational efficiency and speed over CFD. However, the shortcomings of LBM still need to be benchmarked since macroscopic quantities of the flow are extracted using a probabilistic model of the flow at microscopic scales. A plan to investigate turbulent flows over a fractal and non-fractal obstacles has been presented by implementing a LBM numerical analysis over a range of Reynolds numbers (100-49410). The suitability of LBM's multiple dynamics models including: Bhatnagar Gross Krook (BGK), Multiple Relaxation Time (MRT) and Regularised Lattice Boltzmann (RLB) have been studied for high reynolds number cases. Results from LBM cases were compared to available experimental data and published literature, although, results of fractal cases were not mesh independent compelling agreement between all three tested obstacles show a significant validation of LBM as tool to investigate high Reynolds number flows.

Acknowledgements

The University of Sheffield has seen me through my entire journey in higher education from my undergraduate till now as I prepare to present my thesis. Therefore, I would like to sincerely thank the department of Mechanical Engineering at the University of Sheffield for granting me this opportunity.

Although the presentation of this thesis is done so for the purposes of attaining a PhD, an individual degree, it would not have been possible for myself to have reached this stage without the help, support and guidance of my supervisors Dr. Franck Nicolleau and Prof. Wernher Brevis, both of whom, are the reason for even deciding to pursue my PhD. I would like to sincerely thank Dr. Nicolleau for introducing me to the fascinating subject that is turbulence and fractals, his profound knowledge of the subject matter and his commitment to my success have made it a pleasure to have known and learnt from him. Prof. Brevis, I consider a true mentor, he has on multiple occasions been the one to make me refocus on my strengths when I felt most critical about myself and my work. Both of them I consider my greatest assets during this journey, and I sincerely thank for all the time they have invested in me.

Secondly, I would like to acknowledge Dr. Amirul Khan of the University of Leeds, for allowing me to use his LBM software and for providing the introductory knowledge that I needed to start working with LBM. For his consistent help with all matters relating to the use of the HPC facilities at the University of Sheffield I would like to thank Dr. Desmond Ryan of the University of Sheffield.

Thirdly, I would like to thank, Dr. Yi Li and Dr. Thomas Michelitsch who agreed to evaluate and examine this thesis. It was an honour to sit across you and defend my work, which I hope you enjoyed reading.

To my family and friends, who have seen me through the highs and lows, whose unwavering support and outright belief in my success I would like to say: I did it! Thank you!

Finally to all those who contributed to my education any way shape or form, know that the work presented here is definite proof of all your hard work to get me to this point.

Publications

The following is a list of the publications submitted based on the research laid out in this thesis:

Sangtani Lakhwani et al. (2018):
Sangtani Lakhwani, N. M., Nicolleau, F. C. G. A. & Brevis, W. (2018), ‘Lattice boltzman method simulation of high reynolds number flows pass porous obstacles’, International Journal of Applied Mechanics **00**(submitted), 00.

Contents

List of Figures

List of Tables

Nomenclature

Abbreviations

BGK	Bhatnagar Gross Krook
CE	Chapman Enskog
CFD	Computational Fluid Dynamics
DNS	Direct Numerical Simultion
FCHC	Face Centered Hyper Cube
FHP	Frisch Hardy Pomeau
GPU	Graphical Processing Unit
HPP	Hardy Pomeau Pazzis
LBE	Lattce Boltzmann Equation
LBGK	Lattice Bhatnagar Gross Krook
LBM	Lattice Boltzmann Method
LES	Large Eddy Simulation
LGA	Lattice Gas Automata
MD	Molecular Dynamics
MRT	Multiple Relaxation Time
ODE	Ordinary Differential Equation
PDE	Partial Differential Equation
RANS	Reynolds Averaged Navier Stokes
RLB	Regularised Lattice Boltzmann
SRT	Single Relaxation Time
TRT	Two Relaxation Time

Mathematical Operators

	Unless explicitly specified, bold characters signify vector quantities
$\overline{*}$	Time averaged
δ_{ij}	Kronecker delta
$\cdot$	Dot product
∇	Gradient
$\nabla\cdot$	Divergence operator

Symbols

A	Cross sectional area
C_D	Drag coefficient
C_s	Smagorinsky constant
c	Lattice speed
c_s	Lattice speed of sound
D	Obstacle Diameter
D_F	Fractal dimension
e	Internal energy
F_D	Drag force
f	Distribution function
f^{eq}	Equilibrium distribution function
f^{neq}	Non-equilibrium distribution function
KE	Kinetic energy
Kn	Knudsen Number
K_{ij}	Collision Matrix
k	Boltzmann constant
L	Characteristic length
m	Mass
N	Number of particles
P	Pressure
p	Phase space momentum
q	Phase space position
R	Ideal gas constant
Re	Reynolds Number

S	Entropy
St	Strouhal number
T	Temperature
t	Time
U	Average/bulk streamwise velocity
U_c	Characteristic convective velocity
U_s	Maximum velocity deficit
U_∞	Free stream velocity
V	Volume
w_i	Numerical weight of the distribution function
X	Maximum streamwise spatial coordinate
x	Streamwise spatial coordinate
Y	Maximum cross stream spatial coordinate
y	Cross stream spatial coordinate
Z	Maximum vertical spatial coordinate
z	Vertical spatial coordinate

δ_t	timestep
ϵ	Small parameter
ζ	Frequency
μ	Dyniamic viscosity
ν	Kinematic viscosity
ξ	Particle velocity
$\boldsymbol{\pi}$	Flux tensor
ρ	Density
τ	Relaxation factor
ϕ	Porosity
ψ	Collisional invariant
Ω	Collision operator

Chapter 1

Introduction

A canopy flow is one such that the fluid passes above and through a single or number of obstacles attached at the bottom boundary. A clear example of this is an atmospheric flow, where the atmosphere passes through buildings and or vegetation. These flows are difficult to simulate under laboratory conditions due to the number of scales that are involved. Interest in investigating these flow conditions aims to understand the aerodynamic effects that both natural, such as vegetation, and man-made, urban developments, have. These investigations can reveal insights on how modern urban planning can be tailored to improve aerodynamic conditions within and surrounding urban environments, which can help in reducing pollution and improve air quality.

As the fluid flows through and above the canopy certain aerodynamics effects occur, momentum is transported vertically by turbulent diffusion and individual elements of the canopy will generate wakes. In the case of vegetation other effects need to be considered like the swaying of the elements by the airflow, however, this effect will not be considered as the scope of this investigation will be limited to a fixed rigid canopy.

1.1 Aims and Objectives

In the field of civil aerodynamics there is a growing concern for the environmental impact modern city planning can have, especially since more and more high rise buildings are constructed. Additionally, it is still not fully understood how the geography of a city can affect the natural ventilation rates, i.e. how much of the air going through the city is exchanged with air above the city, which in turn are directly responsible for the pollution levels.

A recent report by the European Environment Agency (2016), on urban sprawl (i.e. “the physical pattern of low-density expansion of large urban areas”) indicates that increasingly more cities have areas of low density population, and expansion into these areas are not planned in advance allowing for undeveloped areas to form. However, the spreading of populations are responsible for a lower concentration of pollutants than in densely populated areas. Hence, by understanding the relations between the geometries of cities and ventilation rates, it should be possible to minimise the health impacts of pollution in cities.

On the other hand in densely populated areas high rise buildings are becoming more popular, this is increasingly concerning as these structures can have fatal impact on pedestrian safety in high wind conditions.

As such it is imperative to understand fully both how air is transported through a city and how momentum exchanges occur.

Since a city is a collection of multiple structures of differing scales a fractal object (see section 1.3) can be an apt descriptor for such a geometry. Therefore, the purpose of this investigation is to simulate the flow past a fractal canopy, Figure 1.1, using the Lattice Boltzmann Method (LBM) (see chapter 2) and identify whether this is a viable alternative to established numerical methods. The choice for a LBM approach instead of a traditional Computational Fluid Dynamics (CFD) solver is that LBM is computationally cheaper due to the fact that LBM codes are easily parallelised, which gives the possibility of acceleration via Graphical Processing Units (GPU). Additionally, until recently the large domain required to solve a city scale problem could only be realistically achieved with Reynolds Averaged Navier Stokes (RANS) simulations, since Direct Numerical Simulations (DNS) solutions would require ridiculous computing resources. LBM permits Large Eddy Simulations (LES) closure models to be implemented allowing for the unsteady structures to be investigated something not possible with a RANS approach.

An experimental investigation using the same fractal beds proposed has already been conducted in a water flume, the data set should be used to validate and confirm final results obtained from LBM analysis. Additionally, data from simpler cases, such that of flow past an obstacle are also available and will serve as starting point for LBM benchmarking.

Finally, the reason for conducting a numerical analysis, is quite simply the fact that full domain data can be obtained at a fraction of the cost compared to an experimental approach. Therefore, an experimental approach is better suited to investigate extremely small and precise areas to fully understand more fundamental aspects of the flow.

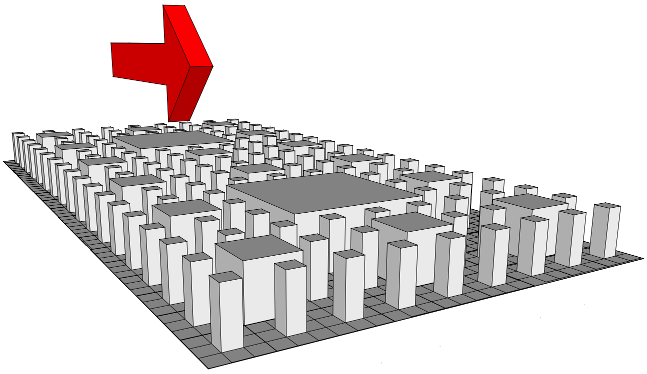

Figure 1.1: Isometric view of the Sierpinski fractal canopy, flow direction is indicated by the arrow above the obstacle.

The aims of this project are:

- Develop the criteria for conducting a numerical analysis of a canopy flow using LBM.
- Validate the numerical results of base cases with available experimental data.
- If possible compare the momentum transfer, as it pertains to the ventilation rates, in the vertical direction between the canopy and the top layer for canopies of different geometries but equal porosity and how this relates to the different drag coefficients of each geometry.

1.2 Turbulence

Of all the flows occurring in nature, turbulent flows are the most common in the universe. They occur across all range of scales, from the smallest flows inside living organisms to the largest motions of galactic gas clouds. The prevalence of this phenomenon signifies that the understanding of these motions can be critical in any field of engineering, and due to its widespread occurrence poses a significant challenge to describe it, Richard Feynman when speaking about the subject said (Feynman et al. 2013, p. 3-9):

> there is a physical problem that is common to many fields, that is very old, and that has not been solved. [...] Nobody in physics has really been able to analyse it mathematically satisfactorily in spite of its importance to the sister sciences. It is the analysis of circulating or turbulent fluids.

Furthermore, a key characteristic of turbulent flows is that they are random in space and time. That is, when an experiment is repeated under the same conditions it will not yield the exact same result. Therefore, a deterministic approach is not possible to obtain a valid result, and statistical approach is required.

In order for a flow to be considered turbulent it must meet the following criteria as well:

Wide Range of Scales: Turbulent flows involve a wide range eddies that span both temporal and spatial scales. The integral length scale, being the largest, is defined by the characteristic length of the geometries wherein the flow is contained, these are responsible for the majority of the system's energy. The smallest scales, Kolmogorov, are those where the dissipation occurs and tend to be similar for different turbulent flows, therefore, they are representative of the intrinsic nature of the turbulent flow.

Dissipation: In order to maintain turbulence an energy input is required as the kinetic energy is converted to internal energy by viscous shear stresses. The energy is introduced at the largest scales, which is then dissipated into heat at the smallest scales. This process naturally makes turbulent flows irreversible.

Rotationality: A turbulent flow is composed of many eddies, i.e. there is a non-zero vorticity. They are generated via the vortex stretching mechanism, which is the cornerstone of the energy cascade, wherein energy from the largest scales is transferred to smaller scales .

Diffusion: The diffusivity of turbulence accelerates mixing of mixtures and increased rates of heat, mass and momentum transfer.

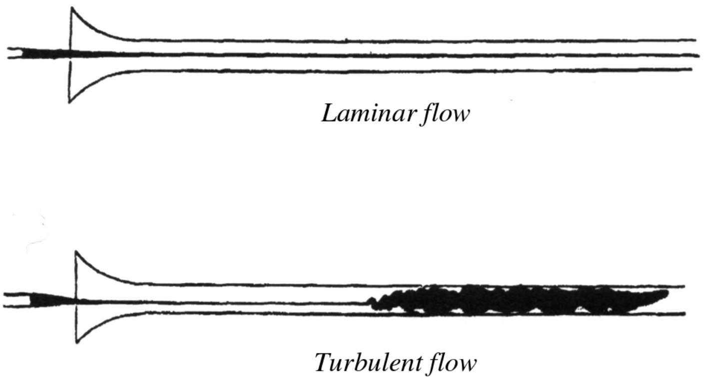

Figure 1.2: Reynolds sketches on the transition from laminar to turbulent flow

1.2.1 Turbulence transition

The transition into a turbulent flow was first observed and described by Reynolds (1883), in which the now famous experiment determined a relation between the inertial and viscous forces of a fluid. The Reynolds number, Re, is defined as

$$Re = \frac{\rho U L}{\mu} \tag{1.1}$$

where, ρ, U, L and μ are the density, characteristic velocity, length scale and dynamic viscosity respectively. The Reynolds number has come to be known is a measurement criterion used to determine if a flow is turbulent. Whenever the Reynolds number is sufficiently small, the viscous forces prevail and the flow is said to be laminar.

In Reynolds' original experiment, Figure 1.2, a dye was injected into a flow. If the flow is laminar, the dye will remain as a well defined line (or laminae), which indicates that there is no mixing in directions perpendicular to the bulk flow. Once the inertial forces become greater the dye streak cannot be followed and the flow ceases to be a laminar. Since the transition from laminar to turbulent flow is not known exactly, it can only be said that turbulence occurs at high Reynolds numbers.

1.3 Fractals

A fractal is a mathematical object, constructed such that a self repeating pattern appears in ever diminishing scales. Fractals were first introduced by Mandelbrot (1983), those occurring in nature, e.g. romanesco broccoli, snowflakes and lightning bolts, all show self repeating patterns in smaller scales, but unlike those in mathematics there is no repetition till infinity, instead the self similar pattern will stop at a scale after which they will become smooth. In a turbulent flow, the repeating pattern can be seen as a the eddies repeating in all scales of the energy cascade.

1.3.1 Fractal Dimension

Due to the self repeating nature of fractal objects, their geometry does not fall into the classical Euclidean definitions (1: line, 2: surface, 3: volume). For example, the wake after an obstacle in a turbulent flow is not a single three dimensional object neither a fully two dimensional surface. Instead a more apt description would be a three dimensional space filled with rotating vortices of varying length scales and intensities, where small structures are contained inside larger ones. Therefore, most fractals will lie somewhere in between these definitions and the Hausdorff dimension is used instead. A popular way to visualise this definition of dimension is to use the box counting method, which involves covering the object in boxes of a determined length, and then a fractal dimension can be calculated using the following equation:

$$D_F = -\frac{\ln(N(r))}{\ln(r)} \tag{1.2}$$

where $N(r)$ is the number of boxes of length r required to cover the object. An important point to make is that for non fractal objects the Hausdorff dimension for said objects will be the same as the Euclidean dimension. A detailed approach to how the Hausdorff dimension is derived using the box counting method can be seen in Appendix A

The eventual goal of this investigation is to observe the effects of a fractal canopy with a Sierpinski carpet design, Figure 1.3, with $D_F = 1.89$. As a comparison the effects of a regular canopy with the same porosity and a randomly arranged Sierpinski carpet should also be investigated, as they are of equal porosity but differing geometries. An isometric view of a fractal canopy can be seen

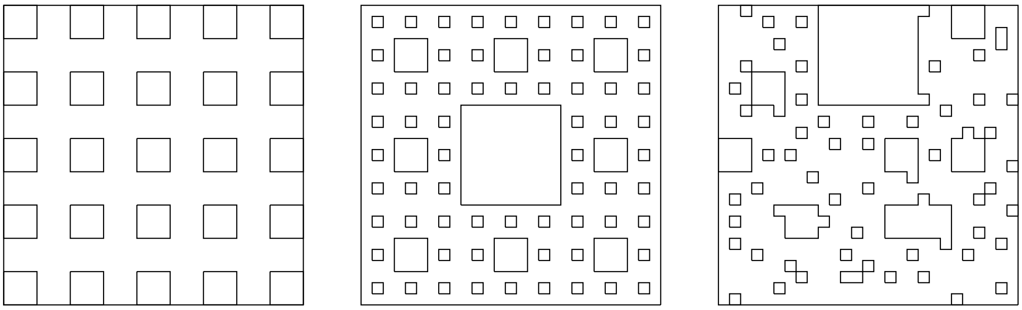

(a) Regular **(b)** Sierpinski **(c)** Random

Figure 1.3: Top view of porous clusters with different obstacle arrangements.

in Figure 1.1.

1.4 Wakes

When a solid object is placed in the path of a fluid, it forces an interaction between the two media resulting in the formation of a wake behind said object. If the interaction between the solid object and the incoming flow is strong enough, it can result in severe structural damage to the object. Therefore, it is vitally important for engineers to study and understand the causes and behaviour of solid and fluid interactions to mitigate future problems but also enhance designs for better efficiency.

Wake dynamics have been investigated for all kinds of objects in both two and three dimensions hereby referred to as plates and obstacles respectively (For the purposes of this investigation research will be focused on wakes produced by obstacles and not plates.). By convention the wake is divided in two sections:

Near wake region. This encompasses the portion of the wake spanning from the base of the object to approximately two diameters downstream.

Far wake region. This encompasses everything after the near wake region.

Furthermore, wakes from obstacles can be categorised as such:

Plane wake. These consist of obstacles constructed by extruding a profile perpendicularly, such as in the case of cylinders. Since the object is quasi two dimensional the flow is statistically stationary along the extruded axis

Axisymmetric wake. This is created by a fully three dimensional object such as a disk or sphere.

1.4.1 Solid Obstacles

The archetypal case of a solid obstacle is a single cylinder. In this case, a circular or square cylinder is placed perpendicular to the flow direction, it's length usually spanning from one end of the domain to the other representing a case of infinite aspect ratio. Similarly in the case of finite aspect ratio numerous research can be found on slow past a sphere. Both of these two classical experiments stem from the work conducted by von Karman (1911) where he describes the process by which the vortex street which bares his name is formed. The free shear layer formed at the shoulder points of the obstacle rolls up behind the obstacle in an alternating manner, this results in the formation of a vortex street as vortices of opposite signs are shed by the object. The vortices cause the obstacle to experience a pressure force orthogonal to the flow direction. Since the vortices alternate in time so does the force, this causes the obstacle to oscillate transversely to the flow. This, wake induced load, can be catastrophic in one of two methods; due to the cyclical nature of the load, the obstacle may fail due to fatigue but more concerning is if the frequency of the shed vortices matches the resonant frequency of the obstacle it will cause the obstacle to resonate and fail. To characterise the oscillation in the flow the Strouhal number is used, it is defined as:

$$St = \frac{\zeta D}{U_\infty} \tag{1.3}$$

where ζ is the frequency of vortex shedding, D is the characteristic length (or obstacle diameter) and U_∞ is the flow velocity.

As explained by Williamson (1996) the three dimensional wake of a single cylinder has been modelled using the Ginzburg-Laundau equations, and the instability which causes the formation of a vortex street has been describes as a hopf bifurcation.

Using a collection of data from a number of sources Williamson (1996) showed that with increasing Reynolds number, a number of different regimes could be observed:

- Laminar Steady Re < 49
- Laminar vortex shedding 49 < Re < 140-194
- 3D Wake-transition Regime 190 < Re < 260
- Increasing Disorder in the Fine-Scale Three Dimensionalities

- Shear-Layer Transition Regime 1,000 $<$ Re $<$ 200,000
- Asymmetric Reattachment Regime
- Symmetric Reattachment Regime
- Boundary-Layer Transition Regime

1.4.2 Self Similar Wake Theory

As described by Pope (2000) the concept of self similarity in a turbulent flow is one that if a given quantity, $Q(x, y)$, which can have characteristic scales as functions of one of the independent variables, i.e. $Q_0(x)$ and $l(x)$. Then a set of scaled variables can be defined as follows:

$$\begin{aligned} \eta &\equiv \frac{y}{l(x)} \\ Q^*(\eta, x) &\equiv \frac{Q(x, y)}{Q_0(x)} \end{aligned}$$

Then if the scaled variable is shown to be independent of x then it is said that $Q(x, y)$ is self similar, and as such the expression $Q^*(\eta, x) = \hat{Q}(\eta)$ is true. In addition the following must also be taken into consideration:

- The scales $Q_0(x)$ and $l(x)$ usually have a power law dependency
- In certain circumstances general expressions for the scaled variables are required. i.e.
  $$Q^*(\eta, x) \equiv \frac{Q(x, y) - Q_\infty(x)}{Q_0(x)}$$
- The self similar behaviour will not be observed over the entirety of x instead it will be valid for a range.
- If the quantity, $Q(x, y)$ is governed by a partial differential equation then the variables $Q_0(x)$, $l(x)$ and $\hat{Q}(\eta)$ are governed by ordinary differential equations.

The theory behind self-similar wakes has been explored extensively by other researchers such as Tennekes & Lumley (1972), Pope (2000) and George (1989). Below is the derivation that shows the self similarity of a plane wake as illustrated by Tennekes & Lumley (1972).

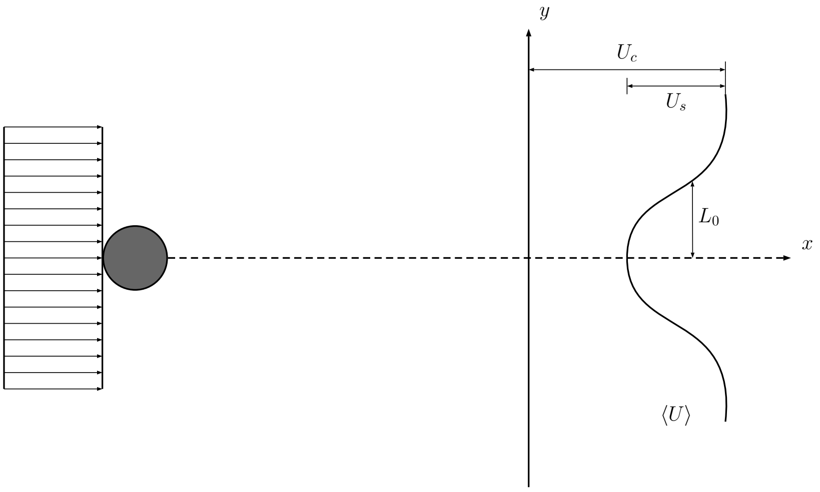

Figure 1.4: Sketch of a plane wake past a cylinder. Showing the flow width δ, characteristic convective velocity U_c and the characteristic velocity difference U_s

In the case of a plane wake the characteristic convective velocity, U_c is the same as the free stream velocity U_∞. We can also expect that the velocity distribution in a plane wake to follow the form;

$$\frac{U_\infty - U}{U_s} = f\left(\frac{y}{L_0}, \frac{L_0}{L}, \frac{L_0 U_s}{\nu}, \frac{U_s}{U_\infty}\right) \tag{1.4}$$

where U_∞ is the free stream velocity, U_s is the maximum velocity deficit, L_0 is the wake half width, L is the streamwise distance from the bluff body and y is the coordinate of the wake width.

As the flow travels further downstream it is expected that the wake region will spread, because of this we can say that $\frac{L_0}{L} \to 0$, $\frac{U_s}{U_\infty} \to 0$, $\frac{L_0 U_s}{\nu} \to \infty$, and as such this reduces Eq 1.4 to:

$$\frac{U_\infty - U}{U_s} = f\left(\frac{y}{L_0}\right) \tag{1.5}$$

We must also take note that L_0 can change downstream and as such $L_0 = L(x)$. Additionally, we know that in a wake the turbulence intensity is of the order U_s, therefore, the Reynolds stress is expected to have the form:

$$-\overline{uv} = {U_s}^2 g(\frac{y}{L_0}) \tag{1.6}$$

where g is the self similar profile function for the Reynolds stress. Now equations

Eq 1.6 and Eq 1.5 are the two scaled variables, Reynolds stress and the velocity deficit respectively. Hence, if they can be expressed in terms of the local length and velocity scales it will signify an invariance with respect to x. Now to prove this, we will start with the streamwise equation of motion:

$$U\frac{\partial U}{\partial x} + V\frac{\partial U}{\partial y} + \frac{\partial(\overline{u^2} - \overline{v^2})}{\partial x} + \frac{\partial}{\partial y}(\overline{uv}) = \nu\left(\frac{\partial^2 U}{\partial x^2} + \frac{\partial^2 V}{\partial y^2}\right) \tag{1.7}$$

The above equation can now be reduced by eliminating the following terms:

- $V\frac{\partial U}{\partial y}$ in the far wake $V \sim 0$ so it is negligible.
- $\frac{\partial(\overline{u^2} - \overline{v^2})}{\partial x}$ assuming that the flow is isotropic at small scales renders this term negligible.
- $\nu\left(\frac{\partial^2 U}{\partial x^2} + \frac{\partial^2 V}{\partial y^2}\right)$ In the far wake region the Reynolds number is expected to be large enough to render the viscous effects negligible as well.

Hence, now the equation of motion can be expressed as:

$$U_\infty\frac{\partial U}{\partial x} + \frac{\partial(\overline{uv})}{\partial y} = 0 \tag{1.8}$$

Substituting Eq 1.5 and Eq 1.6 into Eq 1.8, and by defining $\eta = y/L_0$ we obtain, (Note that the prime here denotes a differential with respect to η.)

$$U_\infty\left(-\frac{\partial U_s}{\partial x}f + \frac{U_s}{L_0}\frac{\partial L_0}{\partial x}\eta f'\right) = -\frac{{U_0}^2}{L_0}g' \tag{1.9}$$

$$-\frac{U_\infty L_0}{{U_s}^2}\frac{\partial U_s}{\partial x}f + \frac{U_\infty}{U_s}\frac{\partial L_0}{\partial x}\eta f' = g' \tag{1.10}$$

For there to be a valid self similarity situation, the coefficients of f and $\eta f'$ must be constants, so:

$$\frac{L_0}{{U_s}^2}\frac{\partial U_s}{\partial x} = constant \text{ and } \frac{1}{U_s}\frac{\partial L_0}{\partial x} = constant \tag{1.11}$$

We can, therefore, state that the general solution for both Eq 1.11 is of the form:

$$L_0 \sim x^n \text{ and } U_s \sim x^{n-1}$$

However this still leaves an indeterminate solution and another relation can be found by using the momentum integral.

$$\int_{-\infty}^{\infty} U(U_\infty - U)dy = -M/\rho \tag{1.12}$$

Substituting Eq 1.5 into the above yields:

$$U_\infty U_s L_0 \int_{-\infty}^{\infty} f(\eta)d\eta - {U_0}^2 L_0 \int_{-\infty}^{\infty} f^2(\eta)d\eta = -M/\rho \tag{1.13}$$

The second term is of the order of U_s/U_∞ in comparison with the first term, since we have established previously that U_∞/U_s approaches zero in the far wake, the second term can be neglected. Additionally substituting $M = -\rho\theta {U_\infty}^2$, where θ is the momentum thickness we get

$$U_s L_0 \int_{-\infty}^{\infty} f(\eta)d\eta = U_\infty \theta \tag{1.14}$$

We can see from the above equation that $U_s L_0$ must also be independent of x, therefore using the general solutions obtained above we can say: $L_0 \sim x^n$ and $U_s = x^{n-1}$ then $2n - 1 = 0$ so that $n = 1/2$

$$U_s = Ax^{-1/2} \text{ and } L_0 = Bx^{1/2} \tag{1.15}$$

Substituting the solutions obtained above into the equation motion, Eq 1.10 we are left with:

$$0.5U_\infty(B/A)(f + \eta f') = g' \tag{1.16}$$

defining an eddy viscosity as $-\bar{u}v \equiv \nu_T(\partial U/\partial y)$ we can now use Eq 1.5 and Eq 1.6 to state:

$$\nu_T = -U_s L_0 g/f' \tag{1.17}$$

assuming that ν_T is constant, and using the expression for turbulent Reynolds number $R_T = U_s L_0/\nu_T$

$$\nu_T/U_s L_0 \equiv 1/R_T = -g/f' \tag{1.18}$$

By substituting Eq 1.16 into the above we get:

$$0.5U_\infty(B/A)(f+\eta f') = f''/R_T \tag{1.19}$$

$$\alpha(f+\eta f') = f'' \tag{1.20}$$

Finally the solution to Eq 1.20 is:

$$f = exp(0.5\alpha\eta^2) \tag{1.21}$$

According to Pope (2000) and Tennekes & Lumley (1972) for the solution presented in Eq 1.21 when plotted alongside experimental data such as that presented by Wygnanski et al. (1986), there is very little deviation from the theoretical solution, especially near the centreline. Towards the edges of the velocity profile the predicted profile overestimates the actual value recoded in experiments. The deviation as explained by Tennekes & Lumley (1972) in the centre of the wake the assumption made earlier of a constant ν_T is appropriate. However, towards the edges of the profile this assumption is not exactly true, due to intermittency, but for most applications the deviation is small enough to be acceptable.

1.4.3 Porous obstacles

In most natural environments, obstacles will not be entirely solid, and as such the fluid will be able to pass through the obstacle's gaps or pores. A porous obstacle is composed of multiple elements that can be interconnected forming one single body, like in the case of a tree, or the they can be separated forming a cluster of bodies bonded by a perimeter, as is the case for a forest or a city. The porosity, ϕ, of an obstacle is usually defined as the ratio of the empty volume to its total volume.

$$\phi = \frac{V_{Empty}}{V_{Total}} \tag{1.22}$$

The most basic porous obstacle is the case of two cylinders placed close to each other in the flow. This was studied by Williamson (1985) where the wakes of two side by side cylinders produced a synchronised shedding of vortices either in phase or anti-phase. For the case of anti-phase shedding their observations showed that the vortex streets remained parallel to each other and do not interact with each other, conversely, when the vortex street is in phase it is more unstable, giving it a tendency for vortices to merge forming a binary vortex street where each a vortex pair would be composed of vortices of the same sign from either cylinder. Furthering the observations of Williamson, Zdravkovich (1987) observed that separation between the two cylinders was also responsible in modifying the behaviour of the wake, he observed that at their closest only a single vortex street would form and as expected when the cylinders were furthest apart the vortex street from each cylinder would be in phase. When the gap ratio (ratio of the gap to the diameter of the cylinder) lied between 2-2.2 the wakes from each cylinder would differ in size with a bias towards one of the cylinders which could change at irregular time intervals. Observations on different arrangements of cylinders were also carried out, by placing the cylinders in line three new regimes were described. In the closet case the free shear layer does not reattach itself to the second cylinder and a vortex street is formed behind the second. At gap ratios of 1.8-3.4 the free shear layer is able to reattach to the second cylinder and then form a vortex street. Continuing to higher gap ratios a vortex street is able to form behind the first cylinder causing the vortex street of the second to be of a binary kind.

Nepf (1999) studied the effect of vegetation on flow. They postulated a model for the drag, turbulence and diffusion of the flow in an emergent vegetation scenario. Using as a basis previous models that used isolated cylinders to model the drag of vegetation, they included the porosity as contributing factor to the drag produced. Therefore, assuming that their scenario consisted of a group of said cylinders. They stated that in low density distributions, less than 10%, the cumulative effects of multiple wake interactions could be neglected, allowing for the assignment of a local drag coefficient to each element in the group using previously made observations on cylinder pairs. Hence, the total drag from the group could be estimated by summing the individual drags of each element. They were also able to derive an expression for turbulence intensity and diffusion within the vegetation patch. Additionally, they set-up an experimental investigation, using a combination of acoustic and laser doppler techniques, to prove the validity of their model. They were able to conclude that their model is correct in identifying the relationship between turbulent intensity, $\sqrt{k}/U$, and the vegetative drag.

Nicolle & Eames (2011) looked into both the local and global effects of a even circular group of cylinders on an incoming flow. Their numerical simulations allowed them to recognise the appearance of three distinct flow regimes based on the porosity of the obstacle. The basic principle follows that the maximum vorticity in the wake decays faster for highly porous obstacles. i.e. the large separations between the elements does not allow for any wake interactions which causes these wakes to be quickly advected downstream by the flow. Obstacles which have elements more tightly grouped showed a tendency to behave as a group and individual element characteristics are lost as the flow interacts with the nearby elements. In the intermediate case, a steady wake region is formed immediately after the group which is sustained by the flow passing through the obstacle, eventually downstream the diffusion of the free shear layers cause an instability which in turn creates a vortex street.

1.5 Fractal Canopy Flows

Due to the multiple scales involved it becomes very difficult to model canopies, as such previous models presented have used overly simplified geometries (Raupach & Shaw 1982, Seginer et al. 1976), such as cylinders, to describe the canopies. This is not representative of either vegetation or urban canopies since a wide range of length scales are associated with each case. In this case, it becomes more reasonable to use fractal objects to describe such canopies since the complexities can be simply described.

One of the earliest investigations into canopy flows include that of Wilson et al. (1982) who conducted a series of experiments measuring the airflow past a cornfield, based upon the experiments of Shaw et al. (1974) who first indicated that the momentum flux was proportional to the square of the velocity. Due to the fact that the investigation was conducted in the open air and the limitations of the use of anemometers data could only be collected on relatively windy days, 'cup' wind speeds in the range of 1.36-3.10 m s^{-1} It was shown that under these conditions the drag of the vegetation was responsible for the vertical momentum flux. The drag, F_D, being characterised as,

$$F_D = \rho C_D A s^2 \tag{1.23}$$

where C_D is the drag coefficient, A is the vegetative area per volume and s is the cup wind speed ($s = \sqrt{u^2 + v^2}$). It was also postulated, that a variable drag coefficient with height would be more accurate, however, the use of a constant drag gives a sufficiently good approximation. As such, a mean C_D 0.17 was found for the canopy. Building on the work by both Wilson et al. (1982) and

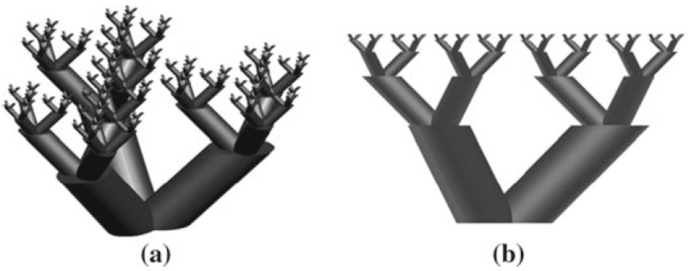

Figure 1.5: Fractal tree object used by Bai et al. (2012), (a) Perspective view and (b) Frontal view

Shaw et al. (1974), Yue et al. (2007*b*) conducted a numerical analysis using Large Eddy simulation (LES) on a corn canopy model and compared their results with those of Wilson and Shaw. Their model differed from previously used models, which involved a homogeneous distribution (field scale) of objects to a more apt representation using the plant features (plant scale). Their results showed that the older field scale approach yielded comparable results for basic statistics such as mean flow, but in higher order statistics such as rms velocity the plant scale approach is better suited. So it can be inferred from Yue's analysis that the canopies cannot be represented using a singular length scale, therefore, a fractal representation of the canopy would be better suited.

Bai et al. (2012) conducted an investigation on a "fractal tree", Figure 1.5, to observe the structure of the wake behind the structure. Their observations of the transverse flow structures indicated that the eddy viscosity varied with the length scale of the obstacle preceding it, i.e in the bottom region where only the large structures are present the eddy viscosity was the largest, and got progressively smaller higher up in the wake. In the study the interest was focused on the transversal plane which is perpendicular to the direction in which the fractal scale changes. Although, the research presented was for a single object to represent a sparse canopy, some similarity is to be expected for the proposed fractal beds and should serve as a starting point for analysis, although in this research the variations of eddy viscosity should be observed in the vertical plane in the forms of sweeps and ejections.

Additional research into fractal turbulence has been conducted by other groups. However, the focus has been towards grid generated turbulence wherein features such as high turbulence intensities caused by the interactions of the wakes at varying lengths downstream of a fractal grid were reported. (Seoud & Vassilicos

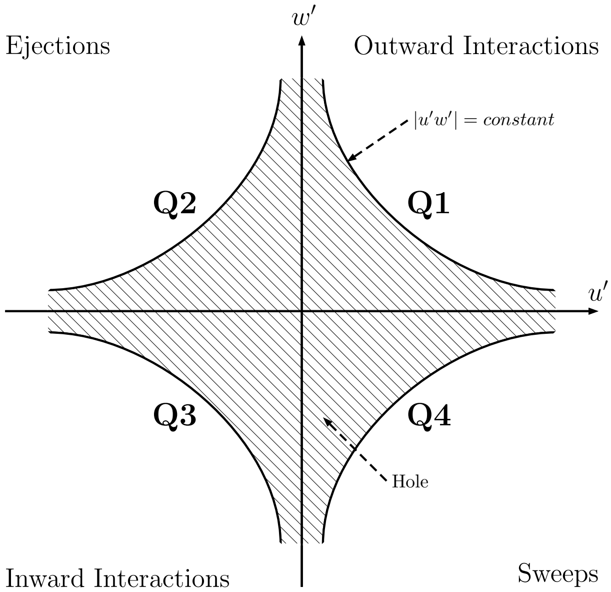

Figure 1.6: Schematic of quadrant events and 'hole' region

2007, Mazellier & Vassilicos 2010, Stresing et al. 2010, Laizet & Vassilicos 2012)

Lu & Willmarth (1973) first introduced the notion of a quadrant analysis, by decomposing the shear stress into four quadrant events, as shown in Figure 1.6. The second and fourth quadrants indicate the events known as ejection and sweeps which are responsible for the downward momentum flux in the system, whilst the remaining two quadrants indicate the upward transfer of momentum. Additionally the 'hole' acts as a filter to eliminate small fluctuating components of the velocity signal, such as to only consider significant events. Quadrant analysis has been applied to canopy flows in both experimental, by Shaw et al. (1983), and simulations, by Yue et al. (2007*a*) both indicated that the largest fraction of events corresponded to sweeps followed by ejections and both the outward and inward interactions events have the shortest time frame.

1.6 Summary

A brief introduction to the subject of turbulence has been given along with a description of fractal objects and how they relate to natural, every-day structures. Canopy flows have been introduced along with certain flow structures common to these types of flows. In the next chapter an introduction of a novel technique known as the Lattice Boltzmann Method (LBM) will be given. An overview into the formulation and mechanics of LBM will be presented including derivations of fundamental equations.

Chapter 2

The Lattice Boltzmann Method

A fluid like any state of matter is composed of a number of atoms and molecules (hereafter referred to as particles), but unlike solid matter when a shear force is applied it offers no resistance and continually deforms. Additionally the motion of fluids is heavily influenced by the time and length scales involved. At the microscopic levels each particle's motion appears random and therefore the fluid becomes inhomogeneous. On the other hand, at the macroscopic level, localised fluctuations of the particle velocities are averaged out and the whole fluid behaves as a single continuous body. The Lattice Boltzmann Method (LBM) introduces an intermediary meso-scale between the macro- and micro-scale. By considering particle collections, the statistical mechanics of a system can be described as a distribution function, $f(\boldsymbol{x}, \boldsymbol{\xi}, t)$, which indicates the probability of encountering a particle in the system at position $\boldsymbol{x}$, with velocity $\boldsymbol{\xi}$, at time t.

This approach allows LBM to be used in both macro- and micro-scale scenarios with reasonable computing resources. LBM is also simple to apply on domains with complex geometries, and the code is readily adaptable to Graphical Processing Units (GPU) processing, but it requires more memory than a continuum method solver. Furthermore with LBM, problems in both macro- and micro-scale can be resolved with reasonable accuracy.

In order to simulate the flow of a fluid, mathematical models have been developed for each scale. Macroscopic scales use a continuum approach, microscopic descriptions are based on molecular dynamics (MD) and mesoscopic scales use models rooted in kinetic theory. In the next few sections a brief overview of the macroscopic and microscopic methods will be introduced. For a further in depth explanations on how each method works and implemented the reader is directed to the extensive literature such as Rapaport & Rapaport (2004), Versteeg & Malalasekera (2007), Anderson & Wendt (1995).

2.1 Macroscopic Scales - Continuum Method

Any model of a fluid, be it in macro-, meso- or micro-scale, intends to solve a number of transport equations for mass, momentum and energy. By applying general conservation principles to said quantities a set of continuity equations may be derived.

The continuum method, which is what most computational fluid dynamics (CFD) methods use, approaches the problem by considering the system to be one continuous entity wherein the motion of individual particles do not affect the overall motion of the fluid. In this approach, the transport equations are obtained by applying the conservation principles to a control volume. This results in a number of ordinary (ODE) and partial differential equations (PDE).

These equations for mass, momentum, and energy conservation as defined by Batchelor (2000) are as follows:

$$\text{Mass:} \qquad \frac{\partial \rho}{\partial t} + \nabla \cdot (\rho \boldsymbol{u}) = 0 \tag{2.1}$$

$$\text{Momentum:} \qquad \frac{\partial (\rho \boldsymbol{u})}{\partial t} + \nabla \cdot (\rho \boldsymbol{u}\boldsymbol{u}) = -\nabla p + \nabla \cdot \tau \tag{2.2}$$

$$\text{Energy:} \qquad \frac{\partial (\rho e)}{\partial t} + \nabla \cdot (\rho \boldsymbol{u} e) = -\nabla \cdot \boldsymbol{q} - p\nabla \cdot \boldsymbol{u} + \tau : \nabla \boldsymbol{u} \tag{2.3}$$

where ρ is the density, t is the time, $\boldsymbol{u}$ is the flow velocity field, p is the pressure, τ is the deviatoric stress tensor, and $\boldsymbol{q}$ is the energy flux.

Eq 2.2 is known as the Navier-Stokes equations, named after the two physicists who formulated them. These equations are to date unsolved, as such, they are one of the seven Millennium Prize Problems to which the Clay Institute offers a one million dollar award to whomever can solve any of the seven problems. They describe the motions of a fluid by applying Newton's second law to the motion of a fluid.

The major drawback of this system is that it does not produce a closed set of equations as p, $\mathbf{q}$, and τ still remain unknown. To resolve this each variable must be independently modelled, in the case of pressure an equation of state must be used. For the deviatoric stress in the case of an incompressible fluid it can be modelled as:

$$\tau = 2\mu \boldsymbol{S} \tag{2.4}$$

where μ is the dynamic viscosity , and the strain rate tensor $\boldsymbol{S} = 0.5(\nabla \boldsymbol{u} + (\nabla \boldsymbol{u})^T)$. Hence the incompressible Navier-Stokes becomes,

$$\frac{\partial \boldsymbol{u}}{\partial t} + (\boldsymbol{u} \cdot \nabla)\boldsymbol{u} = -\frac{1}{\rho}\nabla p + \nu \nabla^2 \boldsymbol{u} \tag{2.5}$$

where ν is the kinematic viscosity, and finally the heat flux can be modelled using the Fourier's Law,

$$\boldsymbol{q} = -\kappa \nabla \boldsymbol{T} \tag{2.6}$$

where κ is the thermal conductivity and $\nabla \boldsymbol{T}$ is the temperature gradient.

Since the focus of this investigation will be in isothermal flows, Eq 2.3 can be ignored in its entirety. Although this now represents a complete model for the fluid, due to many reasons such as non-linearity of the Navier-Stokes equations, complex boundary conditions, geometry etc, they still can't be solved analytically. Therefore, Finite Elements (FE), Finite Volume (FV) and Finite Difference (FD) methods convert the ODEs and PDEs into a system of algebraic equations which are solved iteratively until a convergence is achieved.

2.2 Microscopic Scales - Molecular Dynamics

From a microscopic point of view any fluid is composed of a number of particles randomly moving in space conserving mass, momentum and energy. For a gas, under ideal conditions, the following hold true;

- The number of molecules is very large, but their separation is also very large compared to their molecular size.
- Molecules move randomly with a distribution in speeds that does not change.
- Molecules undergo elastic collisions with other molecules and boundaries but they do not exert any aditional forces on each other.
- Molecules obey Newton's second law.

So Newton's Second law applied to each particle is as follows:

$$\boldsymbol{F}_i = m\frac{d^2\boldsymbol{x_i}}{dt^2} \tag{2.7}$$

where m is the mass of the particle i and $\boldsymbol{x}_i$ is the position vector of that particle. The total force, $\boldsymbol{F}_i$ can be further decomposed into the sum of intermolecular forces and the external forces.

$$\boldsymbol{F}_i = \sum_{j=1, j\neq i}^{N} \boldsymbol{f}_{ij} + G_i \tag{2.8}$$

To determine the force exerted by the particles on the walls of a system, we consider a box of length, L, and the average force, $\overline{F}$, exerted by a particle on the wall is the rate of change momentum.

$$\overline{F}\Delta t = 2m\xi_x \tag{2.9}$$

Taking the time interval to be the time for a particle to collide with a wall and return back, $\Delta t = 2L/\xi_x$, the average force for N particles is

$$\overline{F} = \frac{mN\overline{\xi_x^2}}{L} \tag{2.10}$$

Taking into account that the displacement in all directions is similar, i.e. $\overline{\xi^2} = \overline{\xi_x^2} + \overline{\xi_y^2} + \overline{\xi_z^2} = 3\overline{\xi_x^2}$, the pressure in the container is

$$P = \frac{\overline{F}}{A} \tag{2.11}$$

$$= \frac{2N}{3V}\overline{\left[\frac{1}{2}m\xi^2\right]} \tag{2.12}$$

where V is the volume of the container. Additionally, it is known that for an ideal gas the following is true

$$PV = nRT \tag{2.13}$$

where n is the number of moles of the gas and R is the ideal gas constant. Equating Eq 2.12 and Eq 2.13 yields

$$\overline{KE} = \frac{3}{2}kT \tag{2.14}$$

where k is the Boltzmann constant defined as the ratio of the ideal gas constant and Avogadro's number equal to $1.38 \times 10^{-23}\,\mathrm{J\,K^{-1}}$

Eq 2.14 demonstrates the concept of kinetic temperature, which shows that the temperature, which is a macroscopic quantity, is proportional to the average molecular kinetic energy of the particles. Therefore, an increase in molecular velocities would increase the average kinetic energy raising the temperature and also increase the the frequency of particles colliding with the boundaries of the system measured as an increase in pressure.

A key disadvantage of the MD method is that it is very resource intensive, as it models every particle in the medium. Large size problems are considered in the order of $10^{-2}m$, hence, this approach is infeasible for any kind of engineering scenario.

2.3 Mesoscopic Scales - Kinetic Theory

When making observations in mesoscopic scales its necessary to consider particle clusters, to do so a probability distribution function (pdf) is used. In an N-body fluid, the pdf $f_N(\boldsymbol{q}, \boldsymbol{p}, t)$, is a statistical description of the system which represents the number of particles at any given time positioned between $\boldsymbol{q} + d\boldsymbol{q}$ with momentum $\boldsymbol{p} + d\boldsymbol{p}$ in the phase space. That is, a $6N$ dimensional space where the Cartesian coordinates are the $3N$ components of position, $\boldsymbol{q}_N$, and momentum, $\boldsymbol{p}_N$.

2.3.1 Boltzmann Distribution

It has been established that from a microscopic point of view a fluid is composed of many particles moving randomly. For a system, the microstate is, at a given time, the collection of positions and momenta for all particles in the system, which correspond to a given macrostate. The macrostate refers to the macroscopic properties such as pressure, temperature, volume and density. Boltzmann was the first to show that system's entropy, S, and the possible number of microstates of the system, Ω, follows the following,

$$S = klog(\Omega), \tag{2.15}$$

i.e. an increase in entropy is a change resulting from increasing the number of microscopic arrangements. He was also able to demonstrate that the number of microstates for a given energy are far greater when the system was in thermal equilibrium than any other. He later established that for any system at thermal equilibrium the probability of being in a particular state at energy, E is

$$f(E) = Ae^{\frac{-E}{kT}}, \tag{2.16}$$

where A is a normalisation constant. A more comprehensive derivation can be seen in Appendix B.

This is known as the Boltzmann distribution. In the following section it will be shown that Maxwell was able to show that an ideal gas has a specific distribution at equilibrium but it was Boltzmann's contribution that showed how the equilibrium is reached.

2.3.2 Maxwell-Boltzmann Distribution

When considering any kind of engineering fluid flow scenario, the number of particles that would need to be considered for a microscopic analysis is preposterous and would be impossible to solve using modern computing resources. Maxwell (1860) proposed that its unnecessary to know the velocity and position of every molecule at each instant in time. Since momentum is conserved for a gas in thermal equilibrium the distribution is not one of time but instead of velocity. By imagining the distribution of the particles in a three-dimensional velocity space, where the coordinates represent the component value of the particle's velocity, all the particles that lie within a spherical surface from the origin will have the same speed. Therefore the distribution of particles between a range of speeds was shown to be

$$f(\xi) = 4\pi\xi^2 \left(\frac{m}{2\pi kT}\right)^{3/2} e^{\frac{-m\xi^2}{2kT}}. \tag{2.17}$$

The above equation is derived from the Boltzmann distribution as shown in Appendix B. It should be noted that the function increases parabolically from zero to a maximum and then decreases exponentially. Then as the temperature increases the maxima is shifted towards the right, as can be seen in Figure 2.1.

2.3.3 The Boltzmann Equation

The issue when trying to solve for a system of N particles arises from the Liouville equation (Liouville 1838) wherein the the pdf for a single particle depends on the

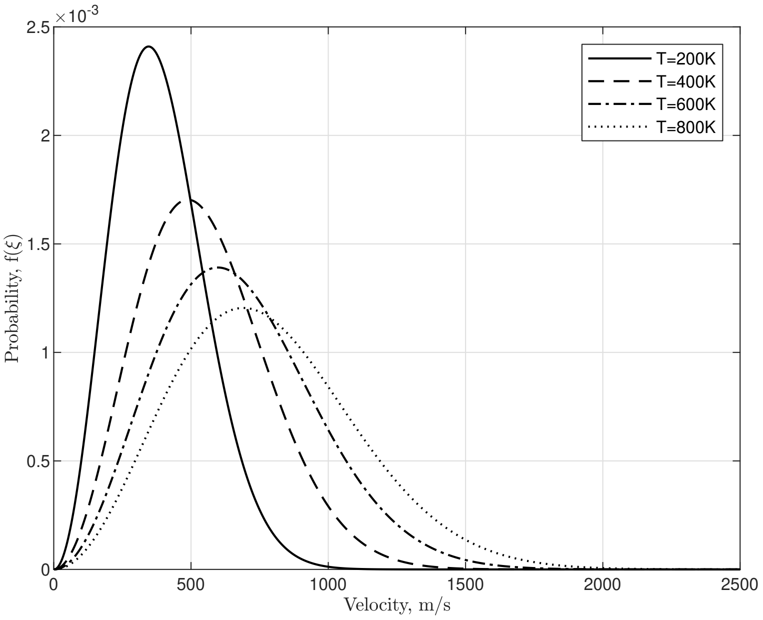

Figure 2.1: Maxwell-Boltzmann probability distribution for nitrogen gas N_2, as a function of molecular velocity, ξ adapted from Eq 2.17 using molecular mass of nitrogen, $m = 4.65 \times 10^{-26}$ kg

pdf for two particles and so on and so on.

$$F_s(\boldsymbol{q}_1, \boldsymbol{p}_1, ..., \boldsymbol{q}_s, \boldsymbol{p}_s) = \int \boldsymbol{f}_N(\boldsymbol{q}_1, \boldsymbol{p}_1, ..., \boldsymbol{q}_N, \boldsymbol{p}_N) d\boldsymbol{q}_{s+1}, d\boldsymbol{p}_{s+1}, ..., d\boldsymbol{q}_N, d\boldsymbol{p}_N \quad (2.18)$$

This results in a function of N variables, and considering that a simple fluid is considered to be of the order 10^{23}, arriving at a solution is impossible by today's standards. Therefore, to simplify the problem only the pdf of a single particle is considered, such that the velocity distribution function can now be defined as

$$f(\boldsymbol{x}, \boldsymbol{\xi}, t) = mNF_1(\boldsymbol{q}_1, \boldsymbol{p}_1, t) \quad (2.19)$$

where the particle position $\boldsymbol{x} = \boldsymbol{q}_1$ and velocity $\boldsymbol{\xi} = \boldsymbol{p}_1/m$ show a change in notation to the physical space.

The assumption made by Boltzmann to only consider the one particle pdf is apt because the averaged statistics of the system can be obtained via the moments of of the velocity distribution function.

$$\rho = \int f d\boldsymbol{\xi} \quad (2.20)$$

$$\rho \boldsymbol{u} = \int \boldsymbol{\xi} f d\boldsymbol{\xi} \tag{2.21}$$

$$\rho e(\boldsymbol{x}, t) = \int \frac{|(\boldsymbol{\xi} - \boldsymbol{u})|^2}{2} f d\boldsymbol{\xi} \tag{2.22}$$

Now the particles in the system do collide with each other which is represented as the rate of change between the initial and final distributions in a given time period. Given the following assumptions, Boltzmann (1872) was able to define Eq 2.23 known as the Boltzmann Transport Equation.

- Particles interact via binary collisions. Figure 2.2
- Collisions are localised in space and time - they occur at a determined position and time.
- Collisions are elastic - momentum and kinetic energy are preserved.
- Collisions are microreversible - this means that microscopic dynamics are time reversible, i.e. the probability that the pre-collision velocities are changed to the post-collision velocities is the same as post-collision velocities being changed to the pre-collision velocities
- Boltzmann chaos is true - signifying that the velocities of the two particles are uncorrelated.

$$\frac{\partial f}{\partial t} + \frac{\partial f}{\partial \boldsymbol{x}} \boldsymbol{\xi} + \frac{F_E}{m} \frac{\partial f}{\partial \boldsymbol{\xi}} = \Omega(f, f) \tag{2.23}$$

The external force, F_E, can be neglected for the scope of this investigation. The left hand side of Eq 2.23 represents the streaming motion of particles and the right hand side the collisions defined by the collision integral as

$$\Omega_{12}(\xi) = \int_{\mathbb{R}^N} \int_{\mathbb{S}^{N-1}} B(|\xi - \xi_*|, cos\theta)[f(\xi')f(\xi'_*) - f(\xi)f(\xi_*)] d\sigma d\xi_* \tag{2.24}$$

where ξ and ξ_* represent the velocity of each particle before the collision and the prime denotes the velocity after the collision. Furthermore, the term $B(|\xi - \xi_*|, cos\theta)$ is called the Boltzmann collision kernel which depends only on the relative velocities and the deviation angle, θ (Mouhot & Strain 2007, Villani 2002)

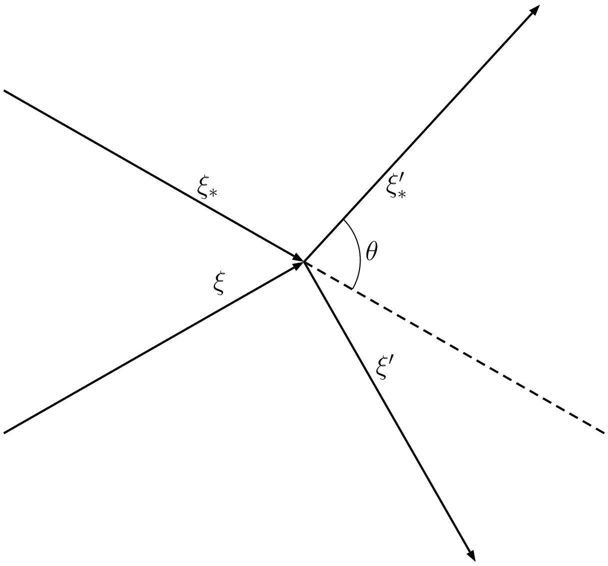

Figure 2.2: A Binary Collision

As per Cercignani (1988) the conservation properties of the Boltzmann Equation are demonstrated through the collisional invariants, $\psi_i(\boldsymbol{\xi})$ such that

$$\int \psi_i(\boldsymbol{\xi})\Omega_{12}(\xi)d\boldsymbol{\xi} = 0 \tag{2.25}$$

which take the form; 1,$\boldsymbol{\xi}$, and $|\boldsymbol{\xi} - \boldsymbol{u}|^2/2$. Additionally, as per the Boltzmann H-Theorem it was also proven that the system at its equilibrium state the distribution is Maxwellian see Wolf-Gladrow (2004) for further details on how this is proven.

2.3.3.1 The Bhatnagar Gross Krook (BGK) Approximation

Due to the complicated nature of the collision operator the first step to produce an effective computational model for the Boltzmann transport equation relies on the simplification of this integral, the most popular one being the approximation introduced by Bhatnagar, Gross & Krook (1954). They suggested that over time the system would tend to a local equilibrium and as such the integral form of the collision operator can be expressed in the form

$$\Omega_{BGK} = \frac{f^{eq} - f}{\tau} \tag{2.26}$$

where τ is referred as the relaxation factor. The relaxation factor here acts very much like the viscosity in the fluid where a lower value of τ means a faster decay towards the local equilibrium, which is indicative of high Reynolds number flows. In section 2.5 we will demonstrate that there is indeed a relationship between the relaxation factor and the viscosity by means of the Chapman-Enskog (CE) expansion.

2.4 Lattice Boltzmann Equation

2.4.1 Lattice Gas Automata (LGA)

LBM evolved from more simple models called Lattice Gas Automata (LGA) these methods treated the fluid as set of of simulated particles on a regular lattice with certain symmetry properties. The reasoning being that the macroscopic dynamics of the system could be represented as a statistical collective of the micro-dynamics of the fluid particles. Therefore, as long as the physical laws are not violated then simple micro fluid models can replace the complex continuum fluid models already known.

The first LGA model proposed by Hardy, Pomeau and de Pazzis, known as the HPP model (Hardy et al. 1973*a*,*b*) consisted in a two dimensional square lattice wherein a particle is allowed to move to any of the four neighbouring nodes. Additionally the collision rule is such that when two particles with opposite velocities move to the same node they will be deflected perpendicularly to their direction of travel. In the case that a particle meets a boundary it may rebound from said boundary and in all other cases the particles will continue unaffected, this can be seen in Figure 2.3.

Mathematically this is expressed as

$$\underbrace{n_i(\boldsymbol{x}+\boldsymbol{c}_i\delta_t, t+\delta_t)}_{Streaming} = \underbrace{n_i(\boldsymbol{x}, t) + \Omega_i(n(\boldsymbol{x}, \boldsymbol{t}))}_{Collisions} \tag{2.27}$$

where n_i is the number of particles moving with velocity $\boldsymbol{c}_i$ at node $\boldsymbol{x}$ at time t, and δ_t is the timestep. It can take either the value 1 or 0 depending whether there is a particle present or not at the node. The discrete velocity of the particles is the product of the lattice speed, $c = \delta_x/\delta_t$, and the unit vector indicating the direction in which the particle is moving. Consequently the subsequent flow variables can be obtained using the ensemble average of the boolean number $f_i = \langle n_i \rangle$

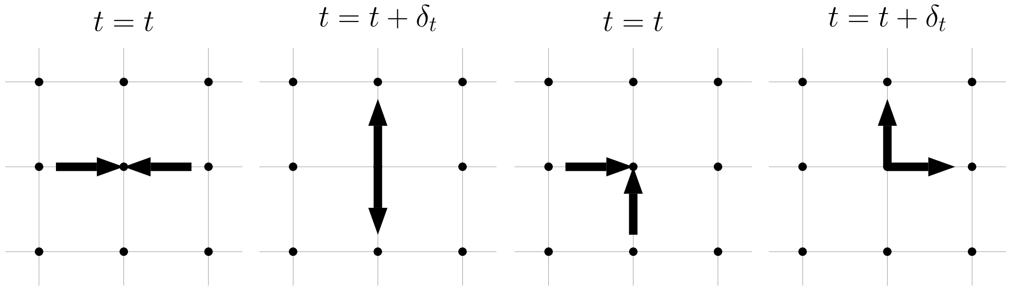

(a) 2 particles head on

(b) 2 particles perpendicular

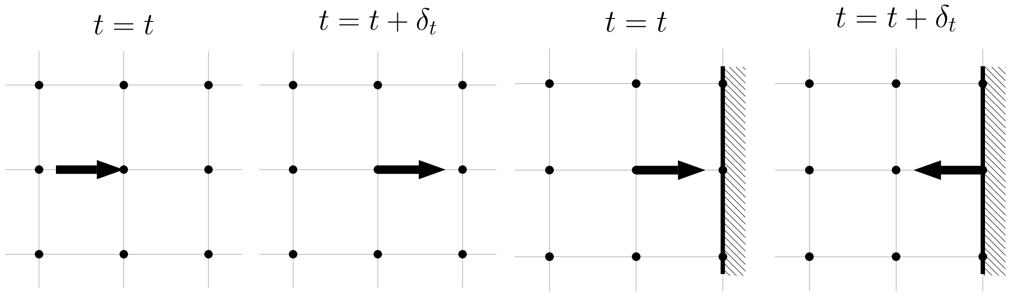

(c) 1 particle alone

(d) 1 particle and a solid boundary

Figure 2.3: Collision rules for the HPP model

$$\begin{aligned}\rho &= \sum_i m f_i \\ \rho \boldsymbol{u} &= \sum_i m \boldsymbol{c}_i f_i \\ \rho e = \rho R T &= \sum_i \frac{m}{2} (\boldsymbol{c}_i - \boldsymbol{u}_i)^2 f_i\end{aligned} \tag{2.28}$$

Although HPP was shown to satisfy the basic conservation laws, it fails to satisfy the continuum equations because of lack of symmetry in the lattice. Specifically, the lack of a robust rotational symmetry meaning that angular momentum is not preserved, which results in anisotropy in the results. Additionally, this model produces spurious invariants which make it unphysical. For example, whilst linear momentum is conserved the HPP model goes one step further and also conserves momentum along each row and each column of the lattice. There is also the ‘chequerboard’ invariant, wherein any particle that would be in a ‘white cell’ of the lattice would always be in a ‘black cell’ in the next timestep. This results in the system being divided into two subsystems which is not representative of an actual fluid flow.

The symmetry requirements was first explored by Frisch, Haslacher, and Pomeau in 1986 who presented a new LGA model now called FHP after the authors (Frisch et al. 1986). The obvious difference between FHP and HPP is that FHP uses a triangular lattice, where each node is surrounded by 6 neighbouring nodes. In this case the discrete velocities are $\boldsymbol{c}_i = c(cos\theta_i, sin\theta_i)$ where $\theta_i = (i-1)\pi/3$ and $i = 1 - 6$ and similarly to the HPP model, the state is described by six Boolean values, n_i. In this model five different types of collisions are allowed as shown in Figure 2.4

It was also later shown by Frisch et al. (1987) that the equilibrium distribution function takes the form of a Fermi-Dirac distribution and allowing for the physical constraints of mass and momentum, it can be written as,

$$f_i^{eq} = \frac{\rho}{6}\left[1 + \frac{\boldsymbol{c}_i \cdot \boldsymbol{u}}{c_s^2} + G(\rho)\frac{\boldsymbol{Q}_i : \boldsymbol{uu}}{2c_s^4}\right] \tag{2.29}$$

where c_s is the speed of sound, specifically for the FHP model $c_s^2 = c^2/2$, $G(\rho) = (6-2\rho)/(6-\rho)$ and $\boldsymbol{Q}_i = \boldsymbol{c}_i\boldsymbol{c}_i - c_s^2$. Given these inferences it was shown that the FHP model was superior to the HPP model because it would satisfy the hydrodynamic equations. However, when rescaling the model it results in the pressure being dependent on the velocity which is unphysical when dealing with flows of high Mach numbers. If the case remains in the incompressible range the model is acceptable.

It is clear that both the HPP and FHP models are only suitable for a 2D flow. Therefore, if one expects to use LGA for anything other than simple fluid models a 3D lattice had to be devised. The lattice arrangement proposed by d'Humières et al. (1986) was a face centered hyper-cube (FCHC) with 24 discrete velocities. This results in a collision rule which is necessarily large in the order of 2^{24}! But, as it was explained by d'Humières this is not necessarily a detriment as it allows for more collisions to be simulated and, therefore, the model can be used at higher Reynolds numbers. Additionally, in comparison to other 3D lattices proposed the 4D hyper-cubic lattice option is naturally isotropic making it a more robust option. The theoretical formulation for the collision operator was proposed by Frisch et al. (1987) and Wolfram (1986).

The fundamental basis of LGA is quite simple, the model requires only Boolean operations to solve the equations. This simplicity and the fact that update process for each node relies only on local information mean that LGA is

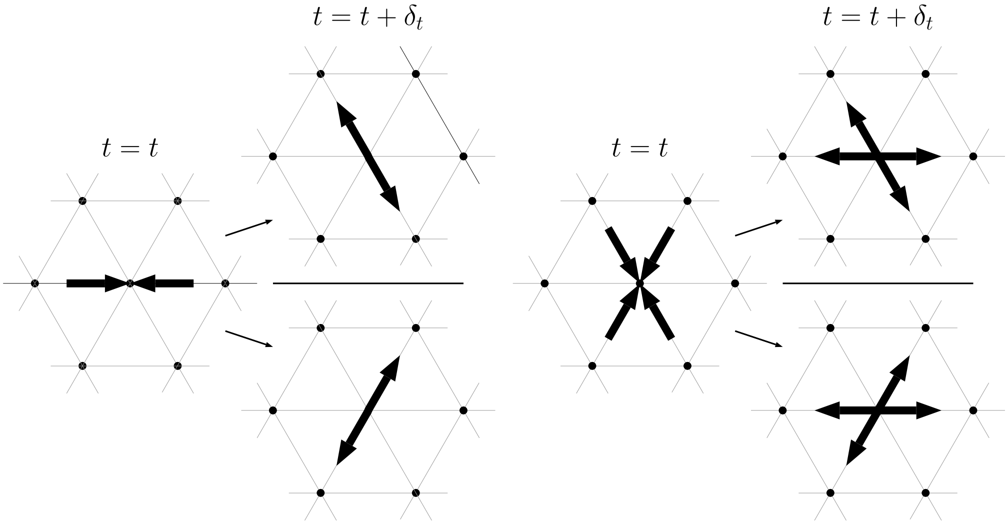

(a) 2 particles head on

(b) 4 particles symmetric head on

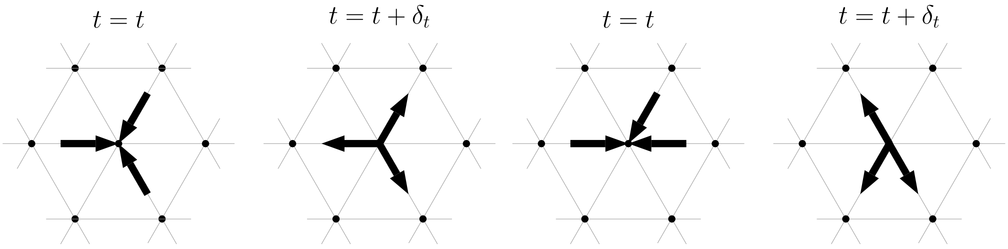

(c) 3 particles symmetric head on

(d) 2 particles head on with a spectator

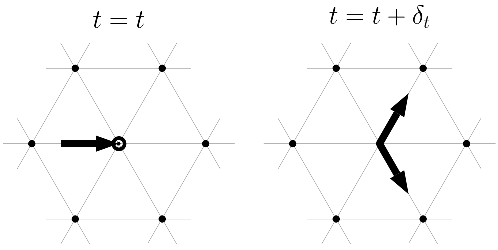

(e) 1 particle with another at rest

Figure 2.4: Collision rules for the FHP model. Where the model has two outcomes for a given set of incoming velocities, either has an equal probability of occurring

heavily and easily parallelised for faster simulation time. However, the advantages of LGA do not come without its disadvantages. The reliance on Boolean operations gives rise to statistical noise in the model, it violates the Gallilean invariance and the dependence of pressure on velocity were all motivators for the development of LBM as an alternative to LGA.

2.4.2 LGA to LBE

A proposal by McNamara & Zanetti (1988) showed that by replacing the Boolean operator n_i with the more realistic velocity distribution function f_i the statistical noise of the LGA could be removed. As such the new model is expressed as,

$$f_i(\boldsymbol{x} + \boldsymbol{c}_i\delta_t, t + \delta_t) - f_i(\boldsymbol{x}, t) = \Omega_i(f(\boldsymbol{x}, \boldsymbol{t})) \tag{2.30}$$

where $\Omega_i(f)$ is the collision operator. As a way to simplify the computation of the collision operator Higuera & Jiménez (1989) proposed a linearisation of the distribution function, such that it is composed of an equilibrium and a non-equilibrium component,

$$f_i = f_i^{eq} + f_i^{neq}, \tag{2.31}$$

where the equilibrium distribution function takes the form of a Fermi-Dirac equation as shown previously. This leads to the formulation of the collision operator as:

$$\Omega_i(f) = K_{ij}(f_j - f_j^{eq}) \tag{2.32}$$

where the collision matrix $K_{ij} = \partial\Omega_i/\partial f_i$. Further simplifications to the collision matrix were brought forwards by a number of groups (Chen et al. 1991, Koelman 1991, Qian et al. 1992), this resulted in the definition of the collision matrix to be,

$$\boldsymbol{K} = -\tau^{-1}\boldsymbol{I} \tag{2.33}$$

$$\therefore \Omega_i(f) = -\frac{1}{\tau}\left[f_i - f_i^{eq}\right] \tag{2.34}$$

2.4.3 Continuous Boltzmann Equation to LBE

A more direct way to derive the LBE is to do so from the continuous Boltzmann Equation instead of through LGA. Starting at the isothermal continuous

Boltzmann equation with the BGK approximation,

$$\frac{\partial f(\boldsymbol{x},\boldsymbol{\xi},t)}{\partial t} + \boldsymbol{\xi} \cdot \nabla f(\boldsymbol{x},\boldsymbol{\xi},t) = -\frac{1}{\tau_c}\left[f(\boldsymbol{x},\boldsymbol{\xi},t) - f^{eq}(\boldsymbol{x},\boldsymbol{\xi},t)\right] \tag{2.35}$$

In order to discretise $\boldsymbol{\xi}$ into a set of discrete velocities $\boldsymbol{c}_i$, we expand the equilibrium distribution function, which is Maxwelian, into a Taylor series,

$$f^{eq} = \frac{\rho}{(2\pi RT)^{D/2}} exp\left(-\frac{\boldsymbol{\xi}^2}{2RT}\right)\left[1 + \frac{\boldsymbol{\xi}\cdot\boldsymbol{u}}{RT} + \frac{(\boldsymbol{\xi}\cdot\boldsymbol{u})^2}{2(RT)^2} - \frac{u^2}{2RT}\right] \tag{2.36}$$

Hence the discrete velocities must be set such that the following numerical quadrature holds exactly,

$$\int \boldsymbol{\xi}^k f^{eq} d\boldsymbol{\xi} = \sum_i w_i \boldsymbol{c}_i^k f^{eq}(\boldsymbol{c}_i), \quad 0 \le k \le 3 \tag{2.37}$$

where w_i and $\boldsymbol{c}_i$ are the weights and points of the numerical quadrature respectively. This leads to the formulation of the discrete distribution function as,

$$f_i(\boldsymbol{x},t) = w_i f(\boldsymbol{x},\boldsymbol{c}_i,t) \tag{2.38}$$

$$\therefore \frac{\partial f_i}{\partial t} + \boldsymbol{c}_i \cdot \nabla f_i = -\frac{1}{\tau_c}\left[f_i - f_i^{eq}\right] \tag{2.39}$$

finally integrating the above equation over t to $t + \delta_t$ will yield the lattice BGK (LBGK) model,

$$f_i(\boldsymbol{x} + \boldsymbol{c}_i\delta_t, t + \delta_t) - f_i(\boldsymbol{x},t) = -\frac{1}{\tau}[f_i(\boldsymbol{x},t) - f_i^{eq}(\boldsymbol{x},t)] \tag{2.40}$$

The macroscopic quantities, density and velocity of the fluid can therefore be obtained from the discrete distribution functions as follows,

$$\begin{aligned} \rho &= \sum_i f_i \\ \rho\boldsymbol{u} &= \sum_i \boldsymbol{c}_i f_i \end{aligned} \tag{2.41}$$

It then follows that by the construction of a series of lattice tensors of the form,

$$L_{\alpha_1\alpha_2\ldots\alpha_n} = \sum_i \boldsymbol{c}_{i\alpha_1}\boldsymbol{c}_{i\alpha_2}\ldots\boldsymbol{c}_{i\alpha_n} \tag{2.42}$$

the discrete equilibrium distribution function, $f_i^{(eq)}$, has the following velocity moments:

$$\begin{aligned}\sum_i f_i^{eq} &= \rho \\ \sum_i \boldsymbol{c_i} f_i^{eq} &= \rho \boldsymbol{u} \\ \sum_i \boldsymbol{c_i}\boldsymbol{c_i} f_i^{eq} &= \rho \boldsymbol{u}\boldsymbol{u} + p\boldsymbol{I} \\ \sum_i c_{i\alpha} c_{i\beta} c_{i\gamma} f_i^{eq} &= c_s^2 \rho [\boldsymbol{u}\boldsymbol{\delta}]_{\alpha\beta\gamma} \\ &= c_s^2 \rho (u_\alpha \delta_{\beta\gamma} + u_\beta \delta_{\alpha\gamma} + u_\gamma \delta_{\alpha\beta})\end{aligned} \tag{2.43}$$

2.5 Chapman-Enskog Expansion. From Boltzmann to Navier Stokes

Up until now the Boltzmann equation and Maxwell distribution functions are all representations of microscopic systems, whilst fluid flows are continuous systems. Hence, a method to retrieve the macroscopic properties of the system from its microscopic behaviour is needed. There are other methods that can link the continuous description of a fluid flow (i.e. Navier Stokes equations) with the Boltzmann Equation such as Grad's method (Grad 1949) which discretises the Navier-Stokes to achieve the Boltzmann Equation. However, for the purposes of this thesis, only the Chapman-Enskog procedure will be detailed as this is the most widely utilised and implemented method.

The Chapman-Enskog procedure entails the multi-scale expansion of the distribution function's spatial and temporal variables with respect to the Knudsen number. The Knudsen number, Kn, is a non-dimensional quantity represented as the ratio between the molecular mean free path, l_{mfp}, and the characteristic length scale, L, of the system.

$$Kn = \frac{l_{mfp}}{L} \tag{2.44}$$

The significance of the Knudsen number is that it determines whether the system should be considered an continuum, $Kn << 1$, where the flow is heavily influenced by intermolecular interactions rather than the interactions between molecules and solid boundaries.

First the following multi-scale expansions are introduced:

$$\begin{aligned} f_i &= f_i^0 + \epsilon f_i^1 + \epsilon^2 f_i^2 \\ \partial_t &= \epsilon \partial_{t_0} + \epsilon^2 \partial_{t_1} \\ \partial_\alpha &= \epsilon \partial_{0_\alpha} \end{aligned} \tag{2.45}$$

where ∂_t, ∂_α and ϵ are short notations for $\partial/\partial t$, $\partial/\partial x_\alpha$ and Kn respectively. Additionally the superscript 0 is used to denote the local equilibrium and the others indicate a departure from the local equilibrium in increasing order. Now the second order Taylor expansion of Eq 2.40 is as follows,

$$D_i f_i + \frac{\delta_t}{2} D_i^2 f_i = \frac{1}{\tau \delta_t}(f_i^{eq} - f_i) + O(\delta_t^2) \tag{2.46}$$

where $D_i = \partial_t + c_{i\alpha}\partial_\alpha$. Substituting the multiscale expansions Eq 2.45 into the taylor expansion Eq 2.46 and collecting all the terms in the same order yields,

$$\epsilon^0 : \qquad f_i^0 = f_i^{eq} \tag{2.47}$$

$$\epsilon^1 : \qquad D_i^0 f_i^0 = -\frac{1}{\tau \delta_t} f_i^1 \tag{2.48}$$

$$\epsilon^2 : \qquad \partial_{t_1} f_i^0 + \left(1 + \frac{1}{2\tau}\right) D_i^0 f_i^1 = -\frac{1}{\tau \delta_t} f_i^2 \tag{2.49}$$

where $D_i^0 = \partial_{t_0} + \boldsymbol{c}_i \cdot \nabla_0$. Given that Eq 2.43 and Eq 2.41 are true then using Eq 2.47 the following can be stated, for $k > 0$,

$$\begin{aligned} \sum_i f_i^k &= 0 \\ \sum_i \boldsymbol{c}_i f_i^k &= \boldsymbol{0} \end{aligned} \tag{2.50}$$

The conservation equations for mass and momentum can be obtained by pre-multiplying Eq 2.48 by 1 and $\boldsymbol{c}_i$ and taking the summation over i.
Mass Conservation:

$$\begin{aligned} 1\left[D_i^0 f_i^0\right] &= 1\left[-\frac{1}{\tau \delta_t} f_i^1\right] \\ (\partial_{t_0} + \boldsymbol{c}_i \cdot \nabla_0) f_i^{eq} &= -\frac{1}{\tau \delta_t} f_i^1 \end{aligned}$$

$$\tag{2.51}$$

Using Eq 2.43 and Eq 2.50 the mass conservation is shown to be,

$$\partial_{t_0}\rho + \nabla_0 \cdot \rho \boldsymbol{u} = 0 \tag{2.52}$$

Momentum Conservation:

$$\begin{aligned} \boldsymbol{c}_i\left[D_i^0 f_i^0\right] &= \boldsymbol{c}_i\left[-\frac{1}{\tau\delta_t} f_i^1\right] \\ (\partial_{t_0} + \boldsymbol{c}_i \cdot \nabla_0) f_i^{eq} \boldsymbol{c}_i &= -\frac{\boldsymbol{c}_i}{\tau\delta_t} f_i^1 \end{aligned}$$

Again substituting the results of Eq 2.43 and Eq 2.50 the momentum conservation is shown as,

$$\partial_{t_0}(\rho \boldsymbol{u}) + \nabla_0 \cdot \boldsymbol{\pi}^0 = 0 \tag{2.53}$$

where the zeroth order flux tensor, $\pi^0_{\alpha\beta} = \sum_i c_{i\alpha} c_{i\beta} f_i^0 = \rho u_\alpha u_\beta + p\delta_{\alpha\beta}$ and $p = c_s^2 \rho$. Similarly the conservation equations in at the order ϵ^2 are as follows. Mass conservation:

$$\begin{aligned} 1\left[\delta_{t_1} f_i^0 + \left(1 + \frac{1}{2\tau}\right) D_i^0 f_i^1\right] &= 1\left[-\frac{1}{\tau\delta_t} f_i^2\right] \\ \delta_{t_1} f_i^{eq} + \left(1 + \frac{1}{2\tau}\right)(\partial_{t_0} + \boldsymbol{c}_i \cdot \nabla_0) f_i^1 &= -\frac{1}{\tau\delta_t} f_i^2 \\ \therefore \partial_{t_1}\rho &= 0 \end{aligned} \tag{2.54}$$

Momentum Conservation:

$$\begin{aligned} \boldsymbol{c}_i\left[\partial_{t_1} f_i^0 + \left(1 + \frac{1}{2\tau}\right) D_i^0 f_i^1\right] &= \boldsymbol{c}_i\left[-\frac{1}{\tau\delta_t} f_i^2\right] \\ \partial_{t_1} f_i^{eq} \boldsymbol{c}_i + \left(1 + \frac{1}{2\tau}\right)(\partial_{t_0} + \boldsymbol{c}_i \cdot \nabla_0) f_i^1 \boldsymbol{c}_i &= -\frac{\boldsymbol{c}_i}{\tau\delta_t} f_i^2 \\ \therefore \partial_{t_1}(\rho \boldsymbol{u}) + \left(1 - \frac{1}{2\tau}\right) \nabla_0 \cdot \boldsymbol{\pi}^1 &= 0 \end{aligned} \tag{2.55}$$

where $\pi^1_{\alpha\beta} = \sum_i c_{i\alpha} c_{i\beta} f_i^1$. To evaluate this term pre-multiply Eq 2.48 by $c_{i\alpha} c_{i\beta}$ and sum over i

$$c_{i\alpha} c_{i\beta}\left[-\frac{1}{\tau\delta_t} f_i^1\right] = c_{i\alpha} c_{i\beta}\left[f_i^0(\partial_{t_0} + \boldsymbol{c}_i \cdot \nabla_0)\right]$$

$$\begin{aligned}
-\frac{1}{\tau\delta_t}\sum_i c_{i\alpha}c_{i\beta}f_i^1 &= \partial_{t_0}\sum_i c_{i\alpha}c_{i\beta}f_i^0 + \partial_{0_\gamma}\sum_i c_{i\alpha}c_{i\beta}c_{i\gamma}f_i^0 \\
&= \partial_{t_0}\underbrace{\sum_i c_{i\alpha}c_{i\beta}f_i^{eq}}_{\boldsymbol{\pi}^0} + \partial_{0_\gamma}\underbrace{\sum_i c_{i\alpha}c_{i\beta}c_{i\gamma}f_i^{eq}}_{Eq\ 2.43} \\
&= \partial_{t_0}\left(\rho u_\alpha u_\beta + c_s^2\rho\delta_{\alpha\beta}\right) + \partial_{0_\gamma}\left(c_s^2\rho(u_\alpha\delta_{\beta\gamma} + u_\beta\delta_{\alpha\gamma} + u_\gamma\delta_{\alpha\beta})\right) \\
&= \partial_{t_0}(\rho u_\alpha u_\beta) + \partial_{t_0}(c_s^2\rho)\delta_{\alpha\beta} + \partial_{0_\gamma}(c_s^2\rho u_\alpha\delta_{\beta\gamma}) \\
&\quad + \partial_{0_\gamma}(c_s^2\rho u_\beta\delta_{\alpha\gamma}) + \partial_{0_\gamma}(c_s^2\rho u_\gamma\delta_{\alpha\beta})
\end{aligned}$$

Expand the first, third and fourth terms via product rule:

$$\begin{aligned}
&= u_\beta\left[\partial_{t_0}(\rho u_\alpha)\right] + u_\alpha\left[\rho\partial_{t_0}(u_\beta)\right] + \partial_{t_0}(c_s^2\rho)\delta_{\alpha\beta} \\
&\quad + u_\alpha\left[\partial_{0_\gamma}(c_s^2\rho)\delta_{\beta\gamma}\right] + c_s^2\rho\left[\partial_{0_\gamma}(u_\alpha\delta_{\beta\gamma})\right] \\
&\quad + u_\beta\left[\partial_{0_\gamma}(c_s^2\rho)\delta_{\alpha\gamma}\right] + c_s^2\rho\left[\partial_{0_\gamma}(u_\beta\delta_{\alpha\gamma})\right] + \partial_{0_\gamma}c_s^2\rho u_\gamma\delta_{\alpha\beta} \\
&= c_s^2\left[\partial_{t_0}\rho + \partial_{0_\gamma}(\rho u_\gamma)\right] + u_\beta\left[\partial_{t_0}(\rho u_\alpha + \partial_{0_\alpha}(c_s^2\rho))\right] \\
&\quad + u_\alpha\left[\partial_{t_0}(\rho u_\beta + \partial_{0_\beta}(c_s^2\rho))\right] + c_s^2\rho\left[\partial_{0_\alpha}u_\beta + \partial_{0_\beta}u_\alpha\right]
\end{aligned}$$

Using the first order conservation equations, Eq 2.52 and Eq 2.53, the above equation reduces down to:

$$\begin{aligned}
&= c_s^2\rho(\partial_{0_\alpha}u_\beta + \partial_{0_\beta}u_\alpha) - \partial_{0_\gamma}(\rho u_\alpha u_\beta u_\gamma) \\
&= c_s^2\rho(\partial_{0_\alpha}u_\beta + \partial_{0_\beta}u_\alpha) + O(M^3)
\end{aligned}$$

where M is the Mach number. For incompressible flows the Mach number is relatively low, therefore, the second term may be neglected and the first order flux tensor becomes,

$$\pi_{\alpha\beta}^1 = -\tau\delta_t p(\partial_{0_\alpha}u_\beta + \partial_{0_\beta}u_\alpha)$$

Now that the first and second order conservation equations have been defined, combining them together will yield the conservation equations for a continuum. Mass conservation:

ϵ^1 : $$\partial_{t_0}\rho + \nabla_0\cdot\rho\boldsymbol{u} = 0$$

ϵ^2 : $$\partial_{t_1}\rho = 0$$

$$\begin{aligned}\partial_{t_0}\rho + \nabla_0 \cdot \rho\boldsymbol{u} + \partial_{t_1}\rho &= 0\\ \partial_t\rho + \nabla \cdot \rho\boldsymbol{u} &= 0\end{aligned}$$

Momentum Conservation:

$$\begin{aligned}\epsilon^1 : \qquad & \partial_{t_0}(\rho\boldsymbol{u}) + \nabla_0 \cdot \boldsymbol{\pi}^0 = 0\\ \epsilon^2 : \qquad & \partial_{t_1}(\rho\boldsymbol{u}) + \left(1 - \frac{1}{2\tau}\right)\nabla_0 \cdot \boldsymbol{\pi}^1 = 0\end{aligned}$$

$$\begin{aligned}\partial_{t_0}(\rho\boldsymbol{u}) + \partial_{t_1}(\rho\boldsymbol{u}) + \nabla_0 \cdot \boldsymbol{\pi}^0 &= -\left(1 - \frac{1}{2\tau}\right)\nabla_0 \cdot \boldsymbol{\pi}^1\\ \partial_t(\rho\boldsymbol{u}) + \nabla \cdot (\rho\boldsymbol{u}\boldsymbol{u} + p\boldsymbol{I}) &= -\left(1 - \frac{1}{2\tau}\right)\nabla \cdot \left[-\tau p\delta_t(\nabla\boldsymbol{u} + \nabla\boldsymbol{u}^T)\right]\\ \partial_t(\rho\boldsymbol{u}) + \nabla \cdot (\rho\boldsymbol{u}\boldsymbol{u}) + \nabla p &= -\nabla \cdot \left[\left(-\tau p\delta_t + \frac{p\delta_t}{2}\right)(\nabla\boldsymbol{u} + \nabla\boldsymbol{u}^T)\right]\\ \partial_t(\rho\boldsymbol{u}) + \nabla \cdot (\rho\boldsymbol{u}\boldsymbol{u}) &= -\nabla p + \nabla \cdot \left[\left(c_s^2\rho\tau\delta_t - \frac{c_s^2\rho\delta_t}{2}\right)(\nabla\boldsymbol{u} + \nabla\boldsymbol{u}^T)\right]\\ \partial_t(\rho\boldsymbol{u}) + \nabla \cdot (\rho\boldsymbol{u}\boldsymbol{u}) &= -\nabla p + \nabla \cdot \left[c_s^2\rho\delta_t\left(\tau - \frac{1}{2}\right)(\nabla\boldsymbol{u} + \nabla\boldsymbol{u}^T)\right]\\ \partial_t(\rho\boldsymbol{u}) + \nabla \cdot (\rho\boldsymbol{u}\boldsymbol{u}) &= -\nabla p + \nabla \cdot \left[\rho\nu\left(\nabla\boldsymbol{u} + \nabla\boldsymbol{u}^T\right)\right]\end{aligned}$$

it can be seen that from this expansion, that a definition for the kinematic viscosity, ν, in the lattice space is:

$$\nu = c_s^2\left(\tau - \frac{1}{2}\right)\delta_t \tag{2.56}$$

This definition becomes very significant when balancing the resource requirements needed for computations, as will be explained in chapter 4

In order to retrieve the familiar incompressible Navier-Stokes equations, it is assumed that the density variations are negligible such that the conservation equations take the form,

$$\nabla \cdot \boldsymbol{u} = 0 \tag{2.57}$$

$$\partial_t\boldsymbol{u} + \boldsymbol{u} \cdot \nabla\boldsymbol{u} = -\frac{1}{\rho}\nabla p + \nu\nabla^2\boldsymbol{u} \tag{2.58}$$

2.6 Dynamics Models

The core of the LBM is to solve the Lattice Boltzmann Equation, Eq 2.40, as such a dynamics model must be implemented to appropriately resolve the collision operator, Eq 2.24. As detailed in the prior section the Chapman-Enskog expansion makes the assumption that the Mach number is low enough to neglect the $O(M^3)$ term, this is only feasible if the flow is incompressible. Therefore, most dynamics models implemented in LBM are so called quasi-compressible since they can be used for compressible flows, but usually a flow with very low Mach number is used to dampen out compressibility effects of the model. Of the different types of dynamics models used the following three are of interest:

- Single Relaxation Time (SRT)
- Multiple Relaxation Time (MRT)
- Regularised Lattice Boltzmann (RLB)

2.6.1 Single Relaxation Time (SRT)

This method is simply the BGK approximation as explained earlier. It is simple enough from here to infer that in order to adapt the BGK model to a particular case the appropriate f^{eq} must be chosen. In its general form the equilibrium distribution function takes the form,

$$f_i^{eq} = \Phi \mathrm{w}_i \left[A + B\boldsymbol{c}_i \cdot \boldsymbol{u} + C(\boldsymbol{c}_i \cdot \boldsymbol{u})^2 + Du^2 \right] \tag{2.59}$$

where u is the macroscopic flow velocity, w_i is a weighting factor, Φ is a scalar parameter (e.g density) and constants A, B, C, and D vary depending on the type of lattice used to discretise the domain.

Due to the fact that only a single equilibrium function is used to describe the entire dynamics of the flow, it can result in numerical instabilities when trying to simulate cases of high Reynolds numbers. This is because as Reynolds numbers increase the value of the relaxation factor gets increasingly closer to 0.5 which result in diverging solutions when simulated.

2.6.2 Multiple Relaxation Time (MRT)

As it has been previously stated, SRT methods lack stability because all the collisions are relaxed by a single criteria, therefore, as the flow increases in complexity the model oversimplifies the process and looses accuracy. So a more reasonable approach is to have multiple relaxation factors for each of the different modes in the flow, such that the collision operator is replaced with a collision matrix whose eigenvalues are the relaxation factors. A generalised form of the LBE had already been formulated by d'Humières (1992), which included a collision matrix, but it wasn't until Lallemand & Luo (2000) that it was fully implemented as an alternative to the BGK scheme. Since then there have been a number of different schemes that use more than one relaxation factor and as such any method that interprets relaxation parameters as the eigenvalues of the collision matrix and tuned via a linear stability analysis fall under the class of MRT scheme. The process starts with the generalised form of the LBE as presented by d'Humières,

$$f_i(\boldsymbol{x} + \boldsymbol{c}_i\delta_t, t + \delta_t) - f_i(\boldsymbol{x}, t) = -\sum_j \Lambda_{ij}\left[f_j - f_j^{eq}\right], \quad i = 0 \sim b - 1 \tag{2.60}$$

where Λ_{ij} is the collision matrix and b is the number of discrete velocities. Subsequently as d'Humières (2002) formulated, the model needs to be transformed from the velocity space to the moment space. This splits the collisions into their respective modes which can be classified as conserved ("hydrodynamic") or non-conserved ("kinetic") and as such the relaxation parameters of the kinetic moments can be tuned to increase the stability of the model.

$$\boldsymbol{m} = \boldsymbol{M}\boldsymbol{f} \tag{2.61}$$

where $\boldsymbol{M}$ is an invertible matrix composed of i vectors each of which has b polynomials of the discrete velocities and $\boldsymbol{f}$ is the set of i distribution functions. So the LBE in moment space is,

$$\boldsymbol{m}(\boldsymbol{x} + \boldsymbol{c}_i\delta_t, t + \delta_t) - \boldsymbol{m}(\boldsymbol{x}, t) = -\boldsymbol{S}(\boldsymbol{m} - \boldsymbol{m}^{eq}) \tag{2.62}$$

where the diagonal matrix $\boldsymbol{S} = \boldsymbol{M}\boldsymbol{\Lambda}\boldsymbol{M}^{-1}$ and the moment space equilibria $\boldsymbol{m}^{eq} = \boldsymbol{M}\boldsymbol{f}^{eq}$. Since only the collision step is dependent on the moment space computation a typical timestep calculation for an MRT scheme would follow the following steps,

- Transform the the distribution functions to the moment space
- Compute the collisions in the moment space
- Transform the post collision moment space distributions back to the velocity space
- Compute the streaming step in the velocity space

So the LBE-MRT can be generalised as:

$$\boldsymbol{f}(\boldsymbol{x}+\boldsymbol{c}_i\delta_t, t+\delta_t) - \boldsymbol{f}(\boldsymbol{x}, t) = -\boldsymbol{M}^{-1}\boldsymbol{S}(\boldsymbol{m}-\boldsymbol{m}^{eq}) \tag{2.63}$$

Construction of the transformation matrices is dependent on the type of lattice being used, the process for constructing this for a two dimensional lattice is detailed in Bouzidi, d'Humières, Lallemand & Luo (2001). Following on this work d'Humières (2002) shows how this is achieved for three dimensional lattices. Compared to the BGK method the addition of the moment space transformation step naturally adds to the computational requirements, but since $\boldsymbol{M}$ is an orthogonal matrix it does not have a heavy impact as proven by d'Humières (2002).

In a more recent attempt to compromise the computational efficiency of the BGK scheme and the accuracy and stability of the MRT scheme, Ginzburg (2005) proposed a two relaxation time (TRT) model. The central premise of the model lies in the fact that most lattices are constructed such that the discrete velocities each have an opposite one, therefore, the velocity distribution functions can be decomposed into a symmetric and anti-symmetric component. The TRT-LBE, therefore takes the form

$$f_i(\boldsymbol{x}+\boldsymbol{c}_i\delta_t, t+\delta_t) - f_i(\boldsymbol{x}, t) = -\lambda_s(f_i^+ - f_i^{(eq)+}) - \lambda_a(f_i^- - f_i^{(eq)-}) \tag{2.64}$$

where λ_s and λ_a are the symmetric and antisymmetric relaxation factors and the +,- notation is similarly used to make the same distinction in the distribution functions. The computational benefits of the TRT were investigated by Karlin et al. (2011).

2.6.3 Regularised Lattice Boltzmann (RLB)

The regularised method as proposed by Latt & Chopard (2006) argues that the instabilities of the BGK method lie in the fact that certain symmetries of the flow are not preserved prior to the collision step. Their solution was based on the fact that the non-equilibrium components of the distribution is approximated using only the first order expansion term in the Chapman-Enskog procedure, as detailed in section 2.5. When comparing the approximated solution using the Chapman-Enskog expansion to a numerically calculated one the approximation lacked symmetry properties due to the exclusion of the higher order contributions. In their solution they proposed incorporating the non-equilibrium component of the momentum flux tensor, $\Pi^{neq}_{\alpha\beta}$, such that,

$$f_i^1 = \frac{t_i}{2c_s^4} Q_{i\alpha\beta}\Pi^{neq}_{\alpha\beta}. \tag{2.65}$$

Therefore, the general expression for the distribution function would be as so,

$$f_i^{reg} = f_i^{eq}(\rho, \boldsymbol{u}) + f_i^1. \tag{2.66}$$

Since the calculation of the momentum flux is a standard procedure anyway when solving the majority of fluid flow problems. And given that the procedure is a local one, the addition of this extra step has a small impact on the overall computation of the simulation.

2.6.4 Summary of Collision Operators

In this section the different methods to model the collision operation of the LBE have been discussed. In summary these are:

$$\begin{aligned}
\Omega_{BGK} &= -\frac{1}{\tau}\left[\boldsymbol{f} - \boldsymbol{f}^{eq}\right] \\
\Omega_{MRT} &= -\boldsymbol{M}^{-1}\boldsymbol{S}\left[\boldsymbol{m} - \boldsymbol{m}^{eq}\right] \\
\Omega_{TRT} &= -\left[\lambda_s(\boldsymbol{f}^+ - \boldsymbol{f}(eq)^+) + \lambda_a(\boldsymbol{f}^- - \boldsymbol{f}(eq)^-)\right]
\end{aligned}$$

2.7 LBM Computation

The LBM starts in the same way as the LGA in that the domain needs to be divided into a series of lattices. At the nodes of these lattices the distribution functions for the particles are allocated, and as the simulation is run these are allowed to stream to neighbouring nodes through a fixed number of directions

Table 2.1: Common Lattice Boltzmann Method Lattice models

Lattice Type	Discrete Velocity Vector, $\boldsymbol{c}_i$	Weight factor, w_i	Sound speed, c_s^2
D2Q9	$(0,0)$	$4/9$	$1/3$
	$(\pm1,0)$, $(0,\pm1)$	$1/9$	
	$(\pm1,\pm1)$	$1/36$	
D3Q19	$(0,0,0)$	$1/3$	$1/3$
	$(\pm1,0,0)$, $(0,\pm1,0)$, $(0,0,\pm1)$	$1/18$	
	$(\pm1,\pm1,0)$, $(\pm1,0,\pm1)$, $(0,\pm1,\pm1)$	$1/36$	

dependent on the lattice type chosen. A key requirement of the lattices being that in order to maintain isotropy the set of velocities in the lattice must be symmetrical.

By convention lattices are named following D_nQ_b where n is the number of dimensions and b is the number of discrete lattice velocities. As mentioned in subsection 2.4.3 each of the discrete velocities is weighted such that the model maintains Galilean invariance and isotropy. In Table 2.1 the associated weights for the most common lattice types are shown as derived by Qian et al. (1992) (see also Qian & Humières (1990)). Additionally, some examples of the lattice arrangements can be seen in Figure 2.5 and in more detail in Appendix C.

All lattice models are based on the same principle wherein, the particles stream to neighbouring nodes from a common central node. In fluid flow applications, the most commonly used lattices are the D2Q9 and D3Q19 for two and three dimensional problems respectively. (Mohamad 2011, p. 19-22)

The main advantage of using LBM over CFD is the relative simplicity of the equations, remember when any of the dynamics models are applied the LBE becomes a simple linear PDE, shown below in its discrete form,

$$f_i(\boldsymbol{x} + \boldsymbol{c}_i\delta_t, t + \delta_t) - f_i(\boldsymbol{x}, t) = \Omega_i \tag{2.67}$$

The LBM intends to solve the LBE (Eq 2.67) for every lattice in the domain, this usually involves the following steps:

- Setup and mesh
- Initialisation
- Streaming

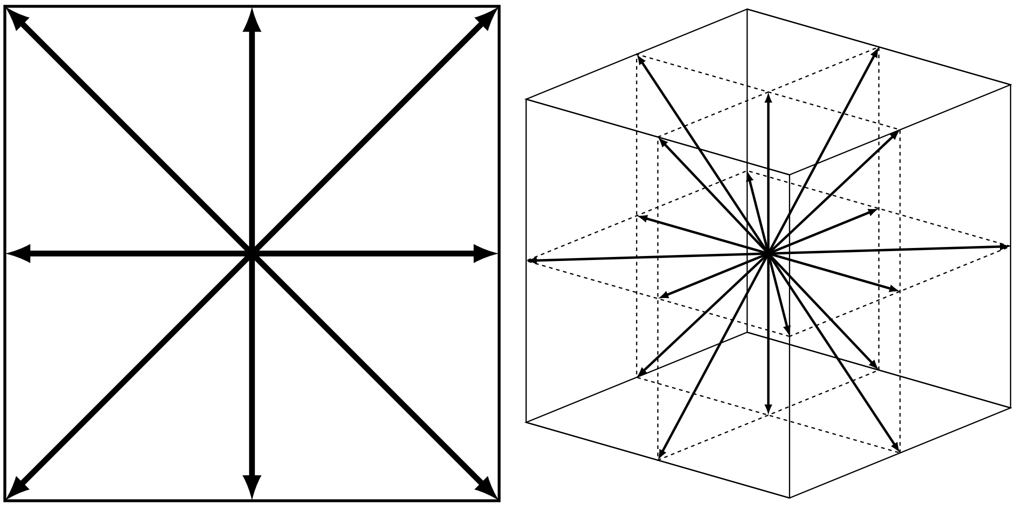

(a) D2Q9

(b) D3Q19

Figure 2.5: Examples of common lattice arrangements used in LBM for fluid flow simulations

- Collision
- Boundaries

2.7.1 Setup and mesh

This process is similar to other CFD methods, wherein the geometry and outer domain is defined. Once the geometry is defined a mesh must be applied to the domain, which will define the position of each node in the current domain. The simplest choice consists of a regular lattice with a fixed grid spacing, δ_x and the timestep used is denoted as δ_t. The reason for using a fixed grid is due to the evolution of LBM from LGA which used this type to avoid having to interpolate between the nodes. However, as the complexity of the fluid being simulated is increased and non-rectilinear boundaries are used it necessary to consider more advanced meshing methods.

2.7.1.1 Non Uniform Meshes

Local refinement of meshes is a key criterion in maximising computational efficiency of a fluid simulation. The use of a single fixed spacing between nodes in a mesh can become prohibitively expensive when simulating cases with large domains, as this results in unnecessary resources being spent in solving parts of the domain with either simplistic flow characteristics or sections where the researcher is not interested. Additionally if there are sections of the boundaries or obstacles in the flow which would not be aligned with the nodes of the mesh, then again a local refinement of the grid to match the boundaries appropriately would increase the mesh density in the entire domain.

The method of local grid refinement, hereby referred to as the multi-grid approach, was first introduced by Filippova & Hänel (1998), see Figure 2.6, can be looked as having different layers of the domain. The base layer, i.e. the coarsest, occupies the full domain and areas of where the flow is expected to have a large gradient will be locally refined using a finer resolution. The method allows for multi level refinement and also non-consistent refinement levels can also be implemented. The first obstacle in implementing this process is how to maintain dynamical similarity between two refinement layers. In LBM computations are performed in lattice space, necessitating a conversion from the physical space. This conversion is achieved from the characteristics of the grid. In a fixed grid arrangement we can define the following,

$$\delta_x = \frac{L}{N} \tag{2.68}$$

$$\delta_t = \frac{u_{phy}}{u_{lbm}}\delta_x \tag{2.69}$$

where L is the characteristic length, N is the number of gridpoints on the length L, u_{phy} is the velocity in physical space and u_{lbm} is the velocity in lattice space. To maintain dynamic similarity the Reynolds number in both lattice and physical space must match such that,

$$\underbrace{\frac{u_{lbm}(L/\delta_x)}{\nu_{lbm}}}_{Re_{lbm}} = \underbrace{\frac{u_{phy}L}{\nu_{phy}}}_{Re_{phy}}$$

therefore, the viscosity in lattice units is,

$$\nu_{lbm} = \nu_{phy}\frac{\delta_t}{\delta_x^2}. \tag{2.70}$$

Given that the Chapman-Enskog expansion demonstrated a relationship between the relaxation parameter and the viscosity see Eq 2.56, then changing the grid resolution in any way will result in a different Reynolds number for the refined areas. Therefore, it is necessary to rescale the relaxation factor in the finer mesh

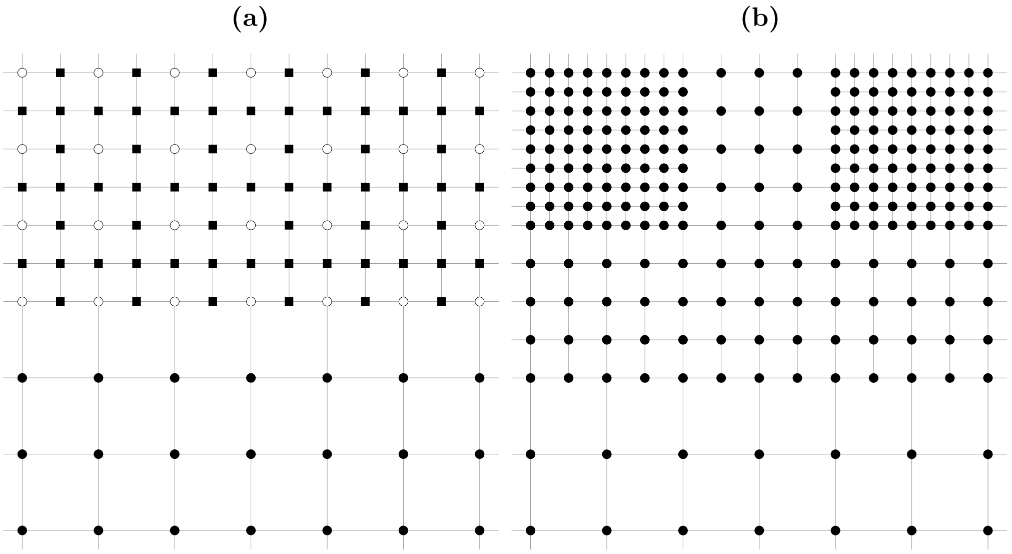

Figure 2.6: Advanced meshing options for LBM. (a) Multigrid (b) Multiblock. In the case of the Multigrid case the solid circular nodes represent the coarse mesh region, the open circular nodes are the common nodes between the fine and coarse layers, and the solid square nodes are the mesh nodes.

based on the coarse mesh as so,

$$\tau^f = \frac{1}{2} + n\left(\tau^c - \frac{1}{2}\right) \tag{2.71}$$

where the subscripts f and c represent the fine and coarse mesh quantities respectively, and the refinement factor $n = \delta_x^c/\delta_x^f$. Similarly the timestep in the refined grid must also be rescaled using the refinement factor, $\delta_t^f = \delta_t^c/n$. Under this new method first the coarse mesh streaming and collisions are computed for the time $t + \delta_t^c$ and then the distribution functions for the fine mesh boundaries are interpolated from the coarse mesh and then the streaming and collisions are computed for the fine mesh for $t, t + \delta_t^f, \cdots, t + (n-1)\delta_t^f$.

This method increases the complexity of the solver and the domain, but it can drastically reduce the total number of nodes and as direct result reduce the hardware requirement needed to solve the problem. An alternative to Fillipova's multi-grid approach is the proposed method of Yu et al. (2002), see Figure 2.6, wherein instead of having a coarse layer and fine layer with information exchanging at the common nodes the mesh is split into independent blocks with their own resolutions and information is only exchanged between the blocks at the interfaces.

More recently progress has been made in designing algorithms for adaptive meshes, this involves placing a number of "sensors" and if the critical value is exceeded then the area surrounding the sensor is locally refined using a hierarchical data structure, known as quad-tree or oct-tree in two and three dimensions (Crouse et al. 2003, Tölke et al. 2006). In addition to the multi-grid/block methods described here other methods with non-uniform grids have been developed for LBM,

- Interpolation methods
- Finite difference methods
- Finite volume methods
- Finite element methods
- Taylor series expansion and least squares methods

However, these lie beyond the scope of this investigation, and the reader is directed to the following literature for further information: He et al. (1996), Cao et al. (1997), Nannelli & Succi (1992), Lee & Lin (2001), Shu et al. (2001).

2.7.2 Initialisation

Initial conditions are intrinsic to any fluid flow simulation. Therefore, it is necessary at the very beginning of the simulation to define the distribution functions at all nodes in the lattice. Since general macroscopic quantities such as initial velocity and density are given as parameters a simple way to initialise the nodes is given by,

$$f_i(t_0) = f_i^{eq}(\rho_0, \boldsymbol{u}_0) \tag{2.72}$$

In the case that density is not given, the initial pressure must first be calculated from the the Poisson equation and then the density may be computed.

2.7.3 Streaming

Streaming is simply allowing the velocity distribution functions to move across lattice linkages to neighbouring nodes, a graphical representation can be seen in Figure 2.7. This step is by far the least intensive as it merely requires changing

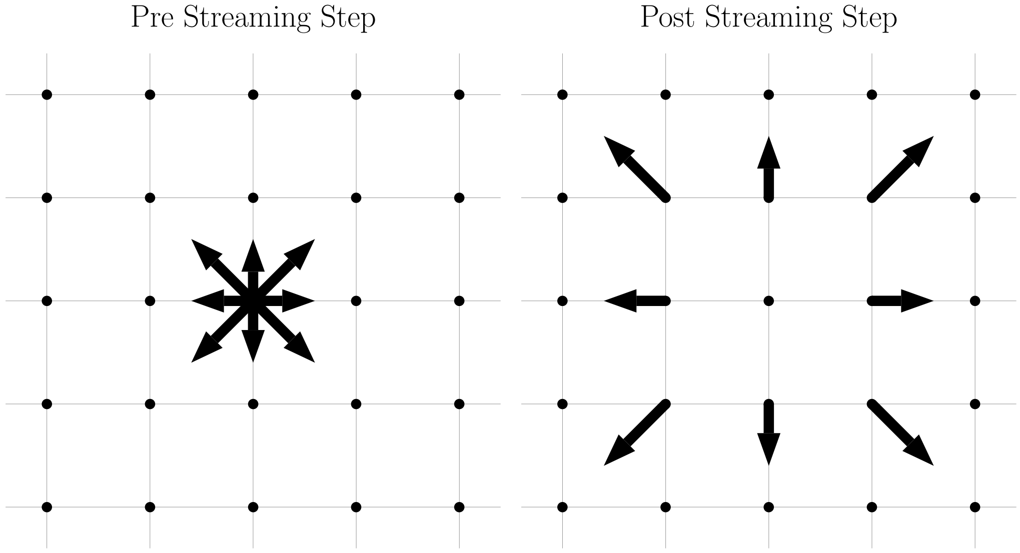

Figure 2.7: Illustration of the streaming process of a lattice node for the D2Q9 case

the indexes of the distribution functions to those of node at which it is moving to,

$$f_i'(\boldsymbol{x}+\boldsymbol{c}_i,t)=f_i(\boldsymbol{x},t) \tag{2.73}$$

2.7.4 Collision

The collision is the computational step in the algorithm, it entails the computation of the equilibrium distribution functions and the subsequent relaxing of the distribution function in line with the model to arrive at the post collision distribution function. The process is model dependent as each lattice type has a different equilibrium distribution function and depending on the dynamics model chosen it may be necessary to pre-compute certain parameters or conduct space transformations.

For example taking the BGK method,

- Based on the streamed distribution functions the macroscopic variables are computed via the relations shown in Eq 2.41

- The computed macroscopic variables are used to construct the equilibrium distribution function as per the lattice structure chosen.

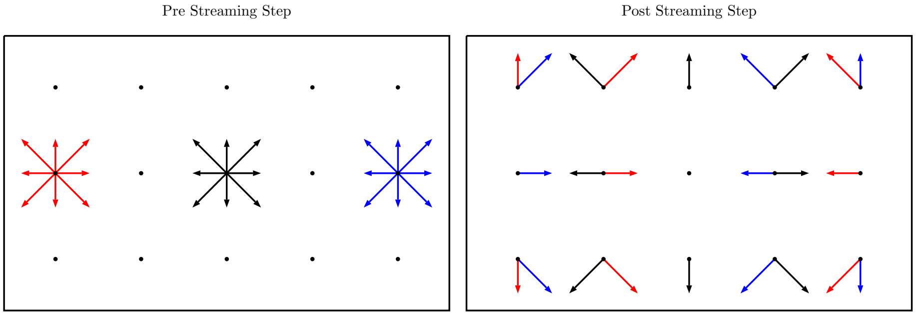

Figure 2.8: Illustration of the periodic boundary condition on a D2Q9 lattice.

- The streamed distributions are relaxed towards their equilibrium to yield the post collision distribution function $f_i(\boldsymbol{x} + \boldsymbol{c}_i\delta_t, t + \delta_t)$

In the case of the MRT scheme the process is similar but it computed in the moment space as detailed in subsection 2.6.2

2.7.5 Boundaries

In order to conform to a real system boundary conditions are applied where necessary. The most common boundary conditions will be explored here.

The simplest boundary to implement is the periodic boundary, see Figure 2.8. In this case, the distribution functions leaving the domain are streamed back to the opposite side. This situation is useful when simulating large or infinite domains, however, simply allowing distributions to stream is only physical when there is no pressure gradient in that direction, i.e. in the case of fluid moving over an infinitely wide plate. In the case of requiring periodicity in the same direction of the flow a correction term based on the density, pressure gradient and the sound speed is necessary as demonstrated by Zhang & Kwok (2006).

When dealing with a flat solid boundary the bounce-back method is the most widely used. Its premise is quite simple, it assumes that when a particle encounters a boundary its velocity is reversed. In doing so, the momentum of all particles hitting a boundary is always reversed such that the macroscopic velocity at the boundary is zero. Hence, the bounce back method effectively implements a no-slip boundary condition, which is necessary at all fixed wall boundaries. The two main ways to implement this are the full-way and half-way schemes. In the full-way bounce back, as shown in Figure 2.9, all the distribution functions that leave the fluid are reverted and streamed back to the prior node. It should be

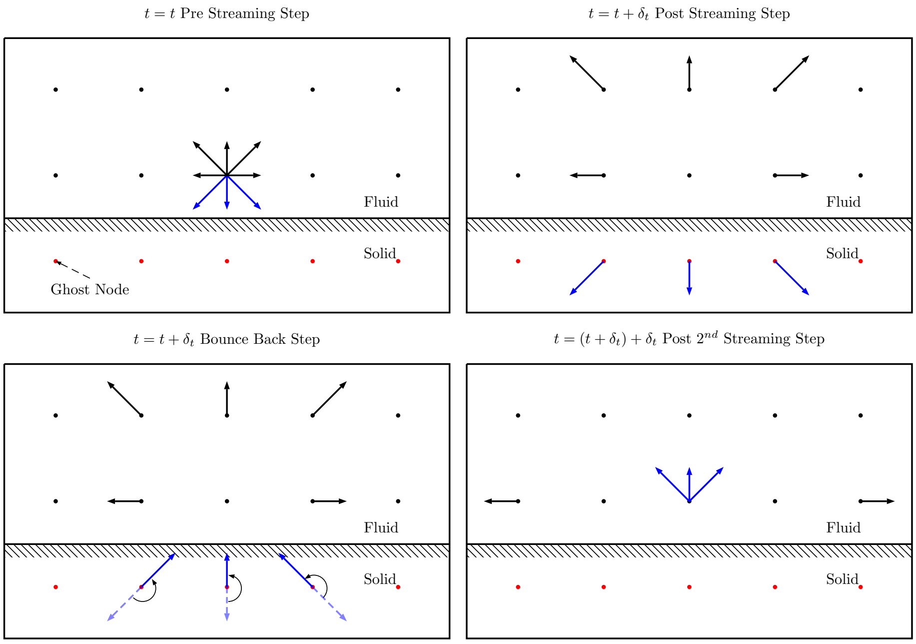

Figure 2.9: Illustration of the full-way bounce-back boundary condition on a D2Q9 lattice, for a no-slip wall located at the bottom of the simulation domain.

noted that since the distribution functions are physically leaving the domain then the scheme requires the presence of "ghost" nodes to temporarily store the values of exiting distribution functions but no collisions are computed on these nodes, since they are a part of the solid boundary.

The half-way bounce back is a more accurate scheme, since it allows the boundary nodes to remain wet, i.e. they are still part of the simulation domain. In this case the distributions leaving the domain are reflected, and then due to the node being inside the domain the collision step is calculated, see Figure 2.10

An additional scheme called the specular reflection method which can be used with either the full or half way bounce back schemes, see Figure 2.11 and Figure 2.12. This method reflects the distribution functions with respect to the wall normal direction effectively cancelling out the wall normal momentum but preserving the tangential momentum to impose a free-slip boundary condition.

These boundary methods focus on the local behaviour at the boundary only, since no relations between the macroscopic variables and the distribution functions are defined this can lead to some errors. As such the works of Noble et al. (1995), Inamuro et al. (1995), Zou & He (1997) would be of interest to minimise such errors.

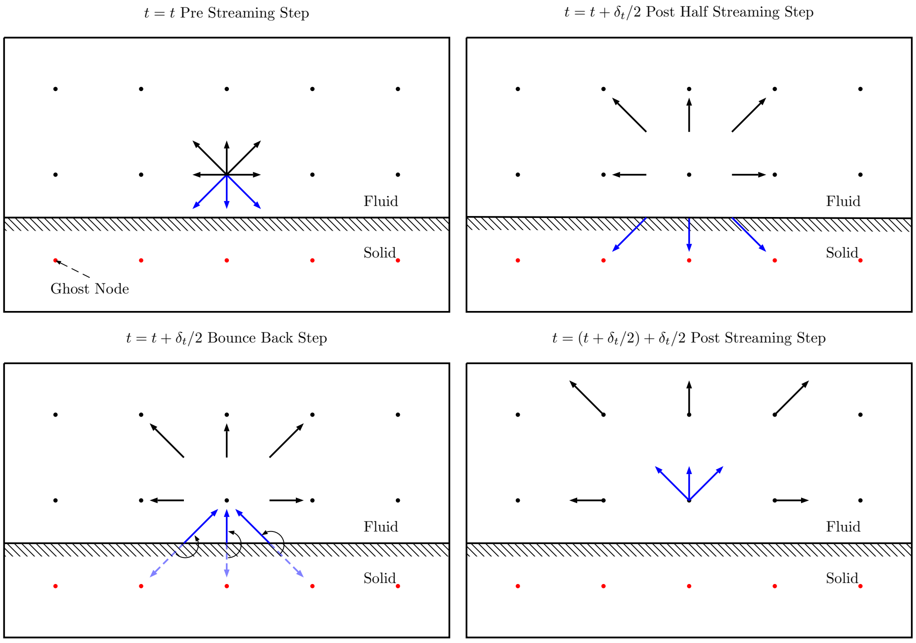

Figure 2.10: Illustration of the half-way bounce-back boundary condition on a D2Q9 lattice, for a no-slip wall located at the bottom of the simulation domain.

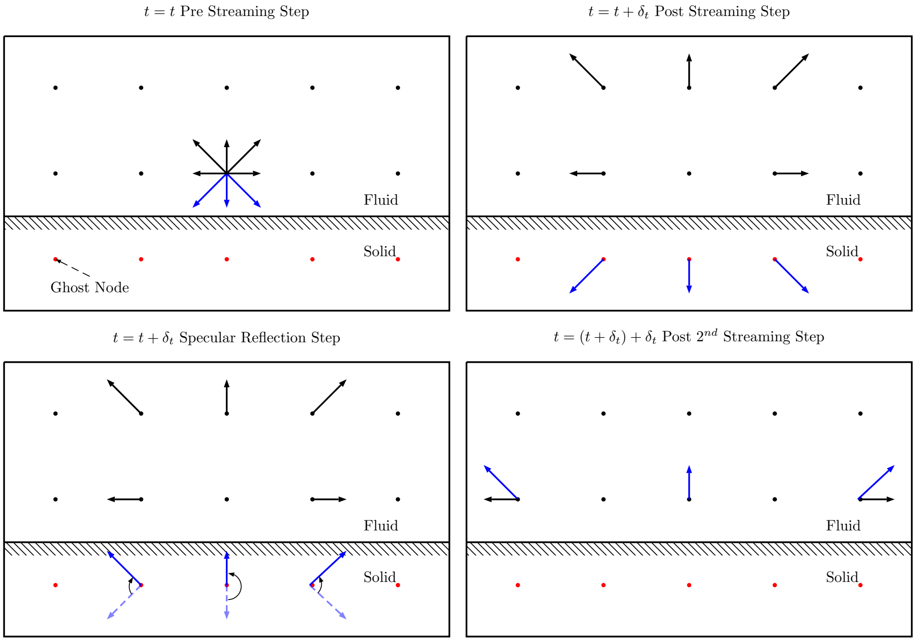

Figure 2.11: Illustration of the full-way bounce-back boundary condition on a D2Q9 lattice, for a free-slip surface located at the bottom of the simulation domain.

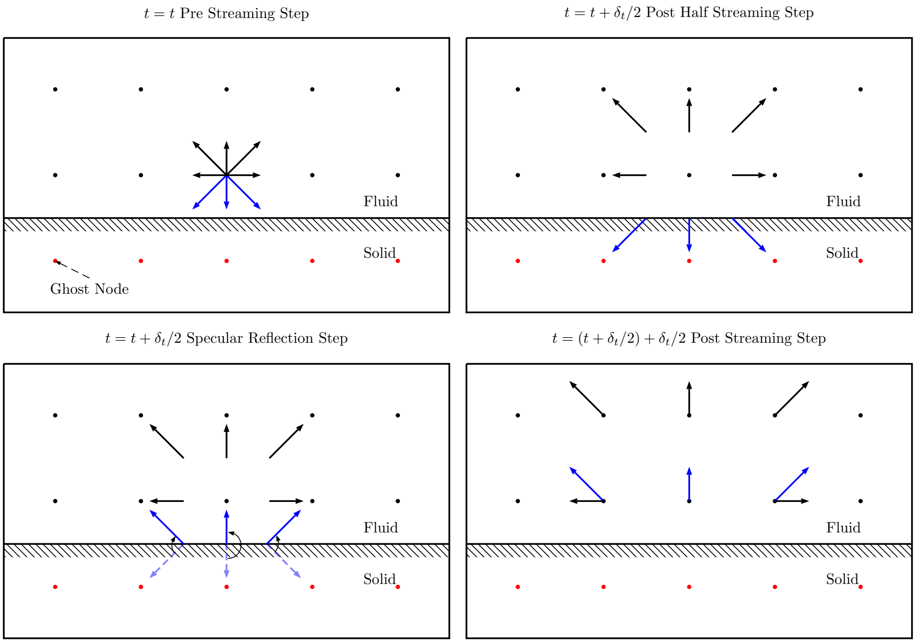

Figure 2.12: Illustration of the half-way specular boundary condition on a D2Q9 lattice, for a free-slip surface located at the bottom of the simulation domain.

All the methods discussed here are only valid for flat boundaries for the case of a curved boundary such as a sphere a number of interpolation and extrapolation schemes also based on the bounce back methods have been successfully implemented. However, for the purpose of this investigation only rigid and flat boundaries are used, therefore, the reader is directed to the extensive literature such as Bouzidi, Firdaouss & Lallemand (2001) and Guo et al. (2002) for further details.

2.8 Turbulence modelling - Large Eddy Simulation (LES)

Computing a turbulent flow using a Reynold Averaged Navier Stokes (RANS), see Appendix D, approach yields an averaged solution, and as such the unsteady turbulent motions of a flow are lost. The most popular method to achieve this is to use a two equation model such as the $k - \epsilon$. In the LBM the approach to solve this model is to introduce another two distribution functions for k and ϵ which are resolved in the collision step of the algorithm. (Teixeira 1998, Succi et al. 1995)

A very similar approach can be taken to apply the two-equation model $k-\omega$ to the LBM algorithm. In this model ω is the specific rate of dissipation of the turbulence kinetic energy into internal thermal energy. (Shu et al. 2006)

On the other hand, using a Direct Numerical Simulation (DNS) approach to model all the scales of the flow, a very high resolution is required and as such the computational cost of using DNS $\propto Re^3$, this results in the majority of the resources being spent on resolving small dissipation scales. Due to the large Reynolds numbers involved in any engineering flow, and the current computing resources available, using DNS techniques is wildly impractical.

The introduction of LES in Smagorinsky (1963) allowed for more accurate solutions to be achieved without a large computational demand. The LES approach sits in between RANS and DNS, in this scenario large scale motions are resolved explicitly whilst small scales are modelled. The effectiveness of this technique is based upon that small scale motions are universal and can be represented by simple models, whereas large scale motions, which are affected by the flow geometry, contain the majority of the flow's energy and anisotropy are resolved exactly. Hence, LES avoids the large computational cost associated with DNS, and it also proves to be superior than RANS approaches for flows with large scale unsteadiness i.e. vortex shedding and flow separation in bluff body cases. A graphical representation of the differences between the different approaches can be seen in Figure 2.13. A simplification of the LES method is that it acts as a low pass filter so the high frequency components (small scales) are removed from the computation.

From a computational demand point of view, since the small scales of the flow are not resolved the domain can be discretised with a coarser mesh, which results in a reduction of the number of degrees of freedom in the problem.

In practice LES simulations use the simple model introduced by Smagorinsky (1963) this involves the consideration of a filter function G to separate the scales and then using a simple eddy-viscosity approach the Navier-Stokes equations can be closed. The simplicity of this method has allowed it to remain a popular choice for use in LES simulations involving isotropic turbulence. (Fernandino et al. 2009)

The Smagorinsky model postulates that the total viscosity can be decomposed to the physical and turbulent viscosity, where the turbulent viscosity represents

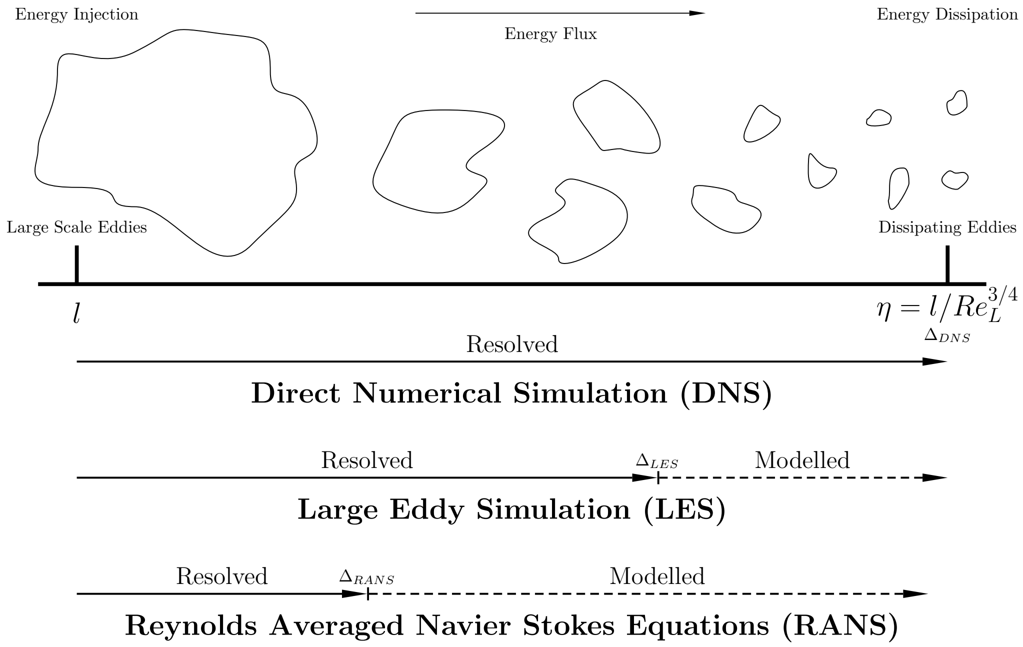

Figure 2.13: Differences between the different turbulence models

the small scales that are being modelled.

$$\nu_{total} = \nu + \nu_t \tag{2.74}$$

Thus, the turbulent eddy viscosity, ν_t is expressed as,

$$\nu_t = C_s \Delta^2 |\overline{S}| \tag{2.75}$$

where C_s is the Smagorinsky constant, which depends on the geometry of the system, but usually takes the values between 0.1-0.2. The Δ is the filter width, in LBM this is taken as the lattice spacing, and $|\overline{S}|$ is calculated from the local strain stress tensor, $\overline{S}_{\alpha\beta}$ as $|\overline{S}| = \sqrt{2\overline{S}_{\alpha\beta}\overline{S}_{\alpha\beta}}$ The local stress tensor being defined as,

$$\overline{S}_{\alpha\beta} = \frac{1}{2}\left(\frac{\partial u_\alpha}{\partial x_\beta} + \frac{\partial u_\beta}{\partial x_\alpha}\right) \tag{2.76}$$

In LBM the local stress tensor can be computed from the non-equilibrium stress tensor defined as,

$$\overline{\Pi}_{\alpha\beta} = \sum_{i=1}^{q} \boldsymbol{c_{i\alpha} c_{i\beta}} \left(f_i - f_i^{eq}\right) \tag{2.77}$$

The turbulence viscosity can, therefore, be shown as (Hou et al. 1994, Delbosc et al. 2014)

$$\nu_t = \frac{1}{6}\left(\sqrt{\nu^2 + 18C_s^2\Delta^2\sqrt{\overline{\Pi}_{\alpha\beta}\overline{\Pi}_{\alpha\beta}}} - \nu\right) \tag{2.78}$$

The above method has been shown to work in the LBM framework, and although they provide acceptable results shown by Delbosc et al. (2014), Sagaut (2010) argues that the since the original Smagorinsky model was derived directly from the Navier-Stokes equations the same non-linearities do not apply to LBM. As such, building from the work of Stoltz and Adamas they were able to present a different approach to improve the performance of LBM-LES algorithms. (Stolz & Adams 1999, Stolz et al. 2001)

Although no simulations have been presented in this report to validate subgrid LES models in an LBM framework. There are multiple cases in the literature proving its validity as a research tool. Fernandino et al. (2009), Hou et al. (1994), Sagaut (2010), Koda & Lien (2015). Hence, the author is confident of the applicability of this method to the proposed investigation.

Chapter 3

Results

The purpose of this chapter will be to primarily expose the simulation setup used, and explain to the reader the methodology used during the investigation. Finally the results of the investigation will be presented for each case and an analysis including observations will be presented in chapter 4

3.1 Simulation Domain and Boundary conditions

As the purpose of this investigation was to determine the validity of LBM as a suitable alternative to other CFD methods at high Reynolds numbers, the numerical domain was chosen to simulate a prior experimental set-up of which validation data was readily available. The experiment, conducted at the University of Sheffield by Prof. Wernher Brevis, placed a single obstacle in a water flume and measured the wake characteristics using an acoustic doppler velocimeter (ADV). The experimental condition was set such that, given the obstacle with diameter D, the Reynolds Number, Re_D, was 28350. Although the experimental data being used as a comparative source in this investigation remains unpublished the reader is directed to the following experimental investigation conducted in the same flume Higham & Brevis (2018).

In order to fully understand whether the LBM is a viable numerical method, it is crucial to first simplify the problem to its basic components. The final objective, is to conduct a simulation of a flow moving over a fractal canopy, this scenario can be seen as the superposition of different processes, which can be identified as follows,

- Quasi 2D flow past a single or porous obstacle.

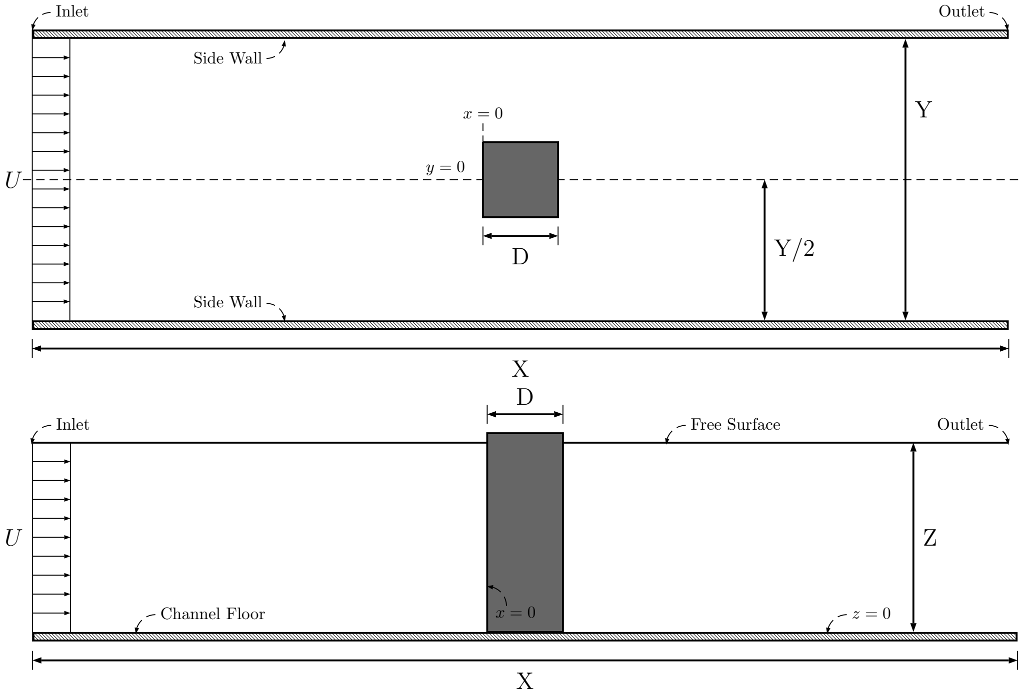

Figure 3.1: Schematic of the flume and geometry of the numerical domain

- Quasi 2D flow past a confined obstacle
- Fully 3D flow past a obstacle.

For reasons that will be detailed further in chapter 5, only results pertaining to the first point will be presented in this thesis. For this scenario three obstacles were simulated; a basic square cylinder and two porous obstacles, one with a regular arrangement and a second using a fractal geometry, refer to Figure 3.2 for the obstacle geometries. Both porous obstacles were designed so that their volume fraction, i.e. porosity, was the same. For all three cases the obstacle was placed at the centre of the domain, such that the upstream and downstream portion of the domain was equal, and the side walls were also at an equal distance from the obstacle. Whilst there is no experimental data available for the case of the square cylinder to perform a quantitative analysis, there exists sufficient evidence in the published literature to conduct a qualitative analysis. For all cases presented here the LBM software used was Palabos, developed at the University of Geneva by J. Latt and B. Chopard (Latt 2009). For all three obstacle types simulations, we run over a range of Reynolds numbers varying from laminar flow to turbulent flow; in all cases a three dimensional domain was constructed

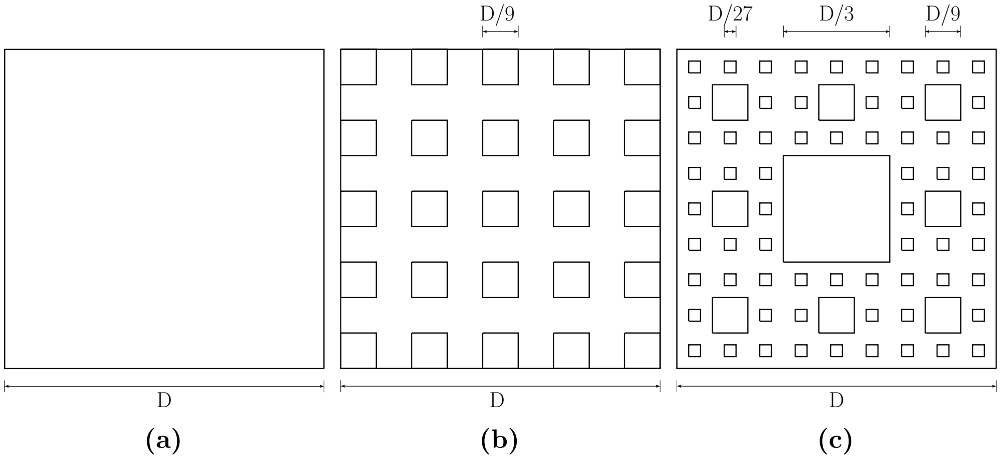

Figure 3.2: Top view of the obstacles being used for this investigation and their geometries. (a) Solid Square, (b) Porous Regular, (c) Porous Fractal (Sierpinski)

using D3Q19 lattices. Table 3.1 details the simulation parameters common to all three obstacles. Additionally, for each Reynolds number a mesh sensitivity analysis was conducted using the same mesh densities for all seven cases. Due to differing inlet velocities for each case, variation in the timestep and subsequently the relaxation time for each mesh is to be expected, as an example Table 3.2 shows the corresponding parameters for case VII. This being a water channel, the domain boundary conditions remained the same irrespective of the obstacle and flowrate simulated. Hence, the bottom and side walls were set to a no-slip condition whilst the top boundary was set to free-slip. A uniform inlet was set at the left side of the domain and an outlet at the right. Refer to Figure 3.1 for a schematic of the numerical domain. Due to the explicit nature of the LBM it is necessary to allow the flow to develop to the stage where it is fully developed. Therefore for all three cases the time at which data recording starts corresponds to when the flow has cycled ten times over the entire domain. Additionally for all flowrate cases, Smagorinsky subgrid modelling was selected using a Smagorinsky constant $C_s = 0.2$.

3.2 Mean Velocity and TKE

In this section the mean velocity, turbulent kinetic energy (TKE) and the convergence of the simulations will be discussed.

Table 3.1: LBM setup parameters common to all three obstacles.

Case	I	II	III	IV	V	VI	VII
Reynolds Number, Re_D	100	500	2470	12352	24705	37057	49410
Obstacle Diameter, D (m)	0.135	0.135	0.135	0.135	0.135	0.135	0.135
Channel Length, X (m)	1.635	1.635	3.135	3.135	3.135	3.135	3.135
Channel Width, Y (m)	0.486	0.486	0.486	0.486	0.486	0.486	0.486
Flow Height, Z (m)	0.326	0.326	0.326	0.326	0.326	0.326	0.326
Physical Inlet Velocity, U_∞ (ms^{-1}) 10^{-3}	0.741	3.70	18.3	91.5	183	275	366
LBM Inlet Velocity, U_{LBM}	0.100	0.100	0.040	0.050	0.100	0.100	0.100
Physical Viscosity, ν (m^2s^{-1}) 10^{-6}	1.00	1.00	1.00	1.00	1.00	1.00	1.00
Acquisition Frequency, ζ_s (Hz)	1.00	1.00	100	100	100	100	100
Acquisition Time, T_N (s)	5000	5000	50.0	50.0	50.0	50.0	50.0
Acquisition Start Time, T_0 (s)	22073	4415	1714	343	172	115	86

Table 3.2: LBM Mesh sensitivity parameters, for $Re_D = 49410$. For all other Reynolds numbers the same mesh densities were used, however, the remaining parameters will differ due to differing LBM inlet velocity.

Mesh Density, NPM $(Nodes/m)$	226	244	275	300	318	349	374	399	417
Node Spacing, δ_x (m) 10^{-3}	4.418	4.091	3.636	3.336	3.145	2.864	2.673	2.509	2.397
Timestep interval, δ_t (s) 10^{-4}	12.07	11.18	9.935	9.116	8.594	7.824	7.303	6.855	6.550
LBM Viscosity, ν_{LBM} 10^{-5}	6.184	6.679	7.514	8.189	8.686	9.541	10.22	10.89	11.40
BGK Relaxation, τ_{BGK} 10^{-3}	500.19	500.20	500.23	500.25	500.26	500.29	500.31	500.33	500.34

3.2.1 Solid Square Obstacle

Of the three obstacles tested the solid case is the simplest, therefore, it is the obvious choice to start with. First of all, it is necessary to identify the suitability of dynamics models previously discussed. At this stage, in order to validate the results, it is unnecessary to consider the entire domain for analysis as this would result in significantly large data files. Therefore, it was decided to consider the following planes in the domain,

- Z-Normal plane at 40% of the flow depth from the channel floor.
- Y-Normal plane at 50% of the channel width.
- X-Normal plane at 25%, 50% and 75% of the channel length.

Furthermore, in order to prevent the formation of a large gradient at the inlet when starting the simulation, the inlet velocity is gradually increased over a time period equivalent to 20000 timesteps.

3.2.1.1 Dynamics Models - BGK

The first model tested was the BGK as it is the simplest. For the slowest of all the flows, case I, Figure 3.3 demonstrates the convergence of the average kinetic energy in the whole domain, and as it can be seen for all mesh cases the data was sampled at a sufficiently converged state. Furthermore, the mean velocity maps shown in Figure 3.4 are as expected. The recirculation zone behind the obstacle is easily identifiable spanning approximately 2 diameters downstream with the flow surrounding the obstacle being accelerated around it.

Upon closer inspection at the centreline velocity profiles as shown in Figure 3.5, there are still some issues. First of all the near wake region appears to be fully converged and the magnitude of the recirculation region does seem in line with what is expected from the literature. Secondly the flow recovery after the wake cannot be fully determined as the length of the channel chosen for this case is too short so it is not inconceivable that the outlet may be having an effect on the flow. Finally the flow appears to accelerate in the inlet portion of the domain, since there are no other obstacles in the channel this behaviour is unexpected.

All remaining cases resulted in diverged solutions.

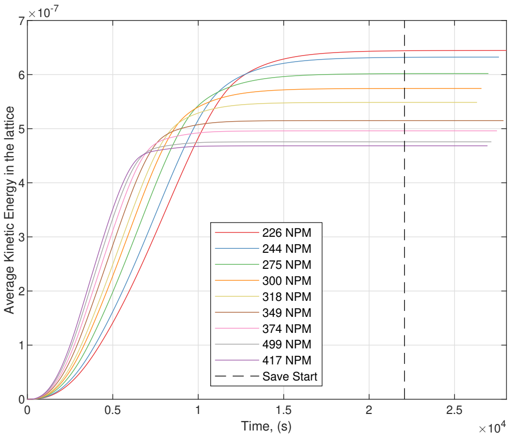

Figure 3.3: Average kinetic energy in the lattice over time, with BGK dynamics. Solid square obstacle at $Re_D = 100$.

3.2.1.2 Dynamics Models - RLB

The second model tested was the regularised method of Latt & Chopard (2006). As explained previously, this method maintains the single relaxation time of the BGK, but redefines the eqilibrium distribution function to account for symmetries lost in the Chapman-Enskog expansion.

This method, whilst still using a single relaxation factor like the BGK, proved to be stable enough that the high Reynolds number cases produced a converged result.

3.2.1.2.1 Laminar Cases A stark difference in the laminar cases from the BGK is that case II did produce a converged result. This immediately demonstrates that the regularized procedure can be an alternative to the BGK method. The centreline streamwise profiles shown in Figure 3.6, for case I, once again show a very well converged near wake region as in the BGK profiles. However, the RLB does nothing to affect the upstream and far wake region of the flow, although the variation between mesh densities is slightly smaller for the RLB case.

On the other hand, for case II, the upstream region appears markedly decelerated than case I. However, the near wake and far wake regions appear to be considerably affected. What stands out the most here is the loss of symmetry in the recirculation zone. The far wake region appears to recover at a different rate than the near wake region, a behaviour not observed in case I. Although the BGK case did diverge, the relative closeness of two cases in terms of Reynolds

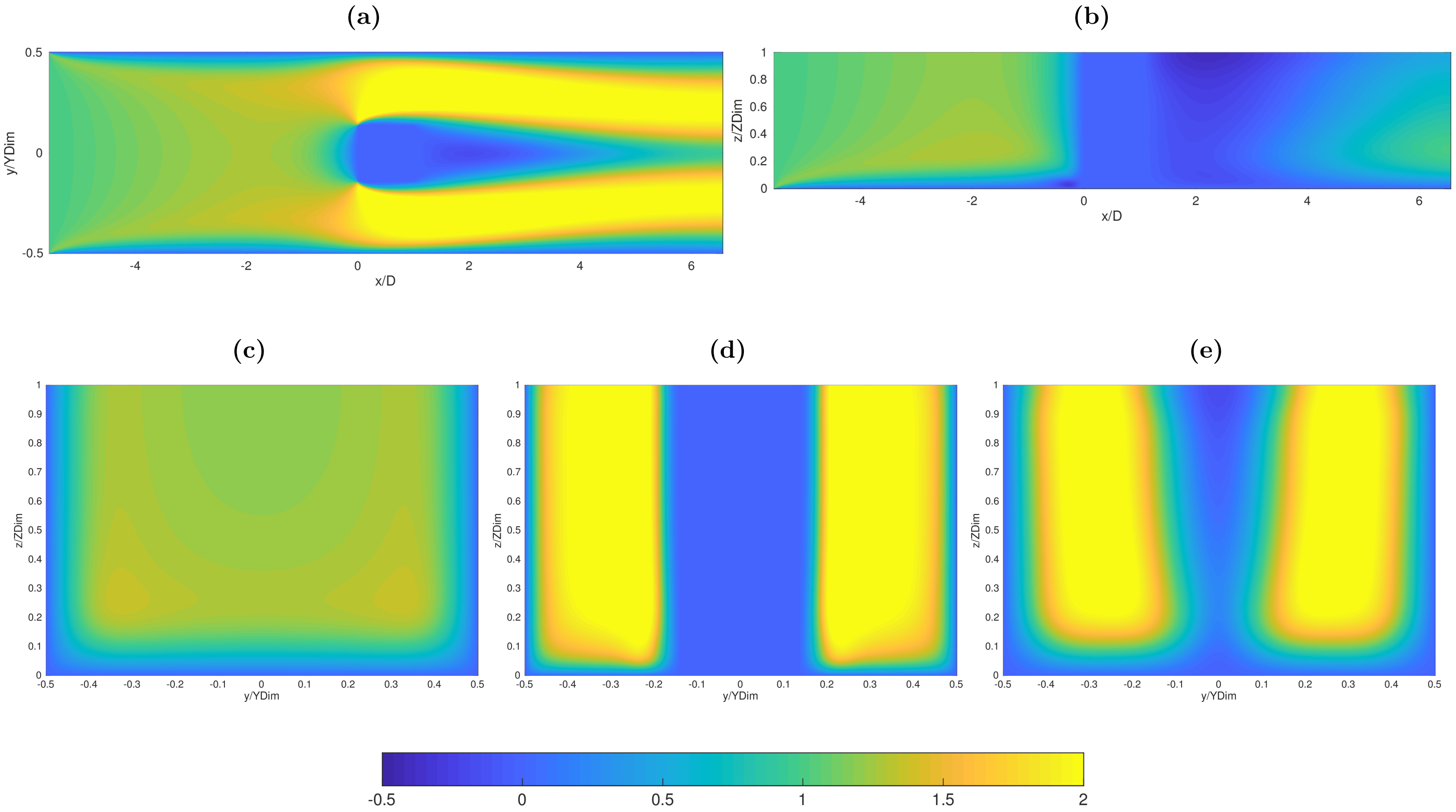

Figure 3.4: Normalised mean streamwise velocity maps, $\overline{u}/U_{\infty}$, with BGK dynamics. Solid square obstacle at $Re_D = 100$ (Case I). (a) shows the Z-normal plane at 40% flow depth from the channel floor. (b) shows the Y-normal plane at 50% of the channel width. (c), (d) and (e) show the X-normal planes at 25%, 50% and 75% of the channel length respectively.

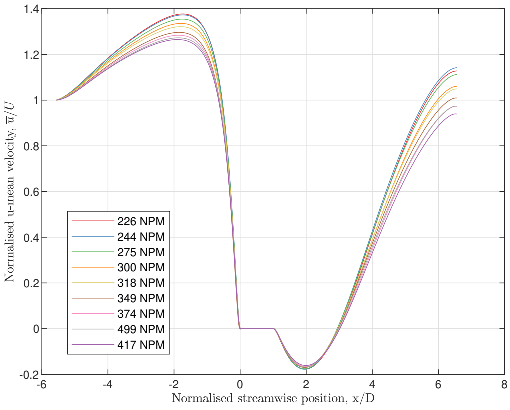

Figure 3.5: Normalised mean streamwise velocity profile along the centreline of the Z-normal plane, with BGK dynamics. Solid square obstacle at $Re_D = 100$ (Case I).

numbers, means that it to be expected that the two cases should have results which are close to one another.

3.2.1.2.2 Turbulent Cases Again where the RLB shows superiority over the BGK method is in the ability for converged results at higher Reynolds numbers, since all turbulent flow cases had a converged result. By first taking a look at the kinetic energy convergence for cases III-VII, Figure 3.7, it is immediately clear that the energy of the system is not smooth and constant at all times like the laminar cases, however, fluctuations remain relatively constant and small over time for all cases. A noticeable difference is that for case III irrespective of mesh density the average kinetic energy fluctuates around the same value, whilst for the remaining cases consistently there is about ∼15% difference between the coarsest and finest meshes.

Turning to the mean profile data for each case, Figure 3.8. Firstly, the upstream domain shows that the flow is accelerated less with increasing Reynolds numbers. This indicates a lessening influence at the centreline by the wall boundary layers, as already by the densest meshes of case IV the upstream velocity is no longer accelerated

Secondly, in the near wake region it can be observed that the recirculation bubble for cases III and IV is smaller than for the remaining cases. Furthermore, cases III and IV do not show a converged result whilst the remaining cases show a stronger convergence in this region. A noticeable difference to the BGK cases is the magnitude of the recirculation zone, whilst the BGK cases consistently

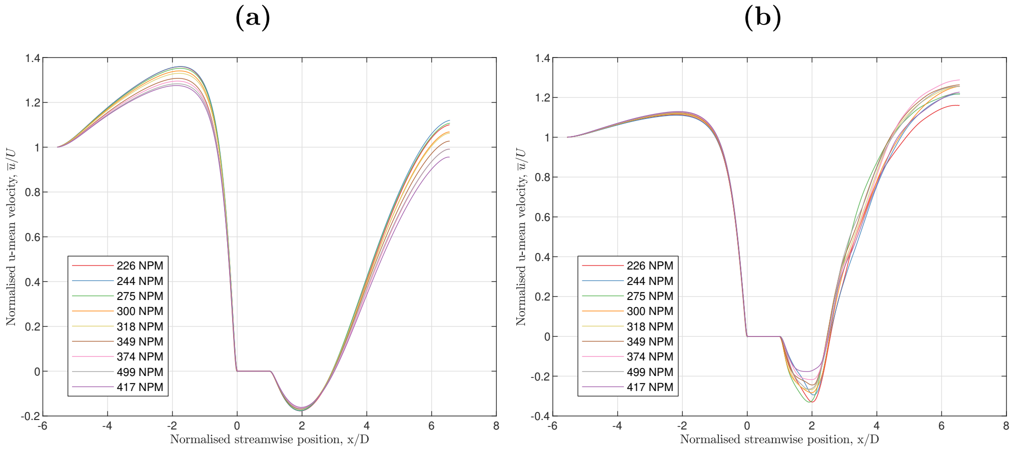

Figure 3.6: Normalised mean streamwise velocity profile along the centreline of the Z-normal plane, with RLB dynamics. Solid square obstacle at (a) $Re_D = 100$ (Case I) (b) $Re_D = 500$ (Case II).

predicted a minimum normalised streamwise velocity of -0.2. Cases III and IV, due to not having a converged result, show a minimum velocity between -0.25 and -0.5 for case III and -0.2 and -0.4 for case IV. The remaining cases are more consistent indicating a recirculation velocity of about -0.35. Additionally, it should be noted that in each case, regardless of the mesh density, the location of the minimum velocity is always the same.

Thirdly, observations in the far wake region of the profiles make clear the weaknesses of the RLB method. Case III has a completely unphysical downstream acceleration, beyond the initial inlet velocity and even stranger is the fact that there appears to be no clear path to convergence via mesh density. Previous cases, including Case I with BGK, all showed a clear convergence of the results in all three identified regions of the flow. Case IV, does have some acceleration, but this phenomenon is only observed at the coarser meshes. However, whist case III showed no indication of achieving a converged result, case IV is more promising, but only for the coarse meshes, 226 NPM - 349 NPM, the subsequent mesh densities break with the convergence established by the prior meshes and in the instance of 374 NPM the unphysical acceleration can be once again observed. Interestingly, cases V and VI show a divergence at higher mesh resolutions from an already converged low resolution result. Finally in case VII, is can be seen that there is no acceleration at any mesh density and also the result appears to be converged even at the lower resolutions.

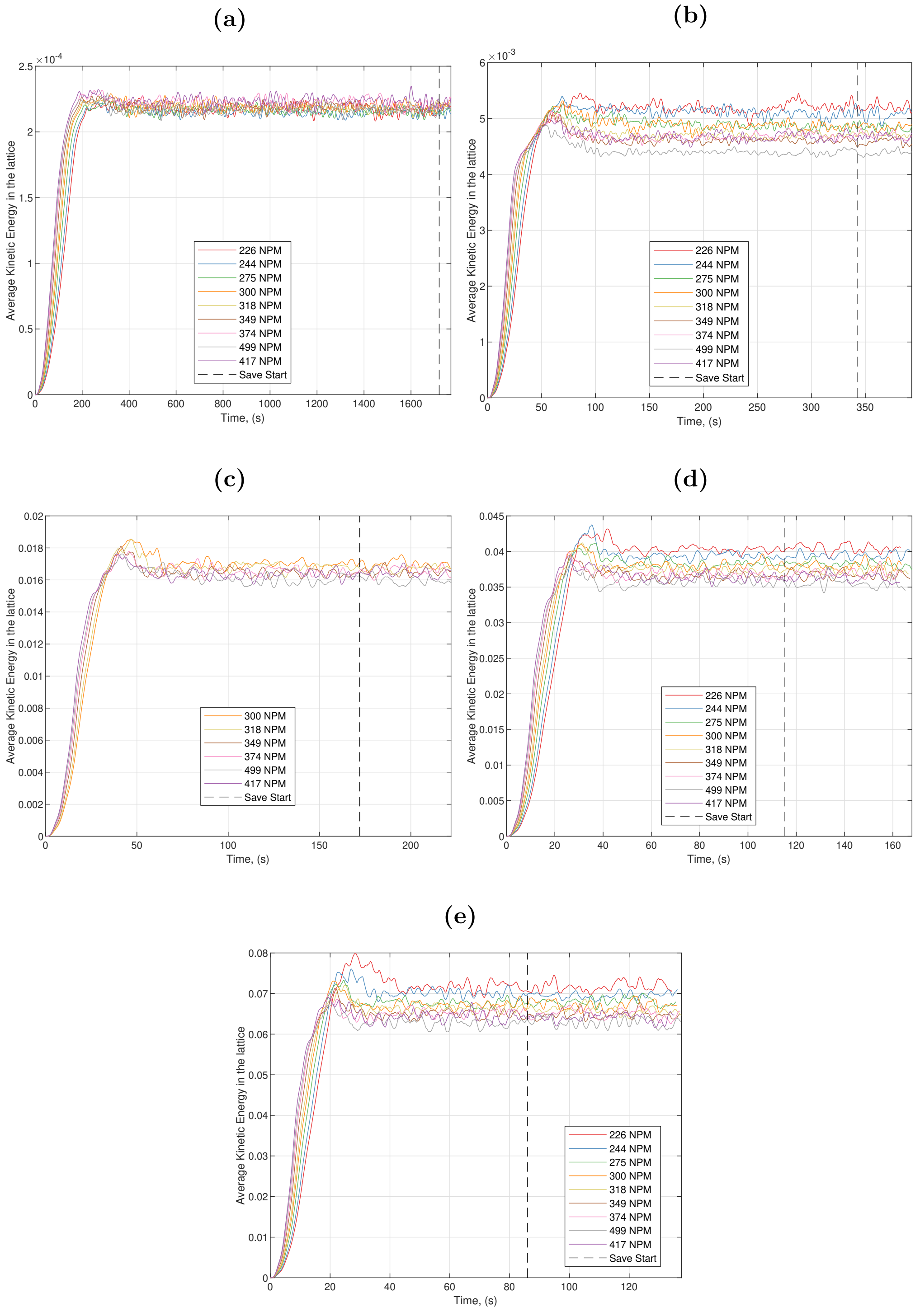

Figure 3.7: Average kinetic energy in the lattice over time for turbulent flow past solid square cylinder, with RLB dynamics. (a) $Re_D = 2470$ (Case III) (b) $Re_D = 12352$ (Case IV) (c) $Re_D = 24705$ (Case V) (d) $Re_D = 37057$ (Case VI) (e) $Re_D = 49410$ (Case VII)

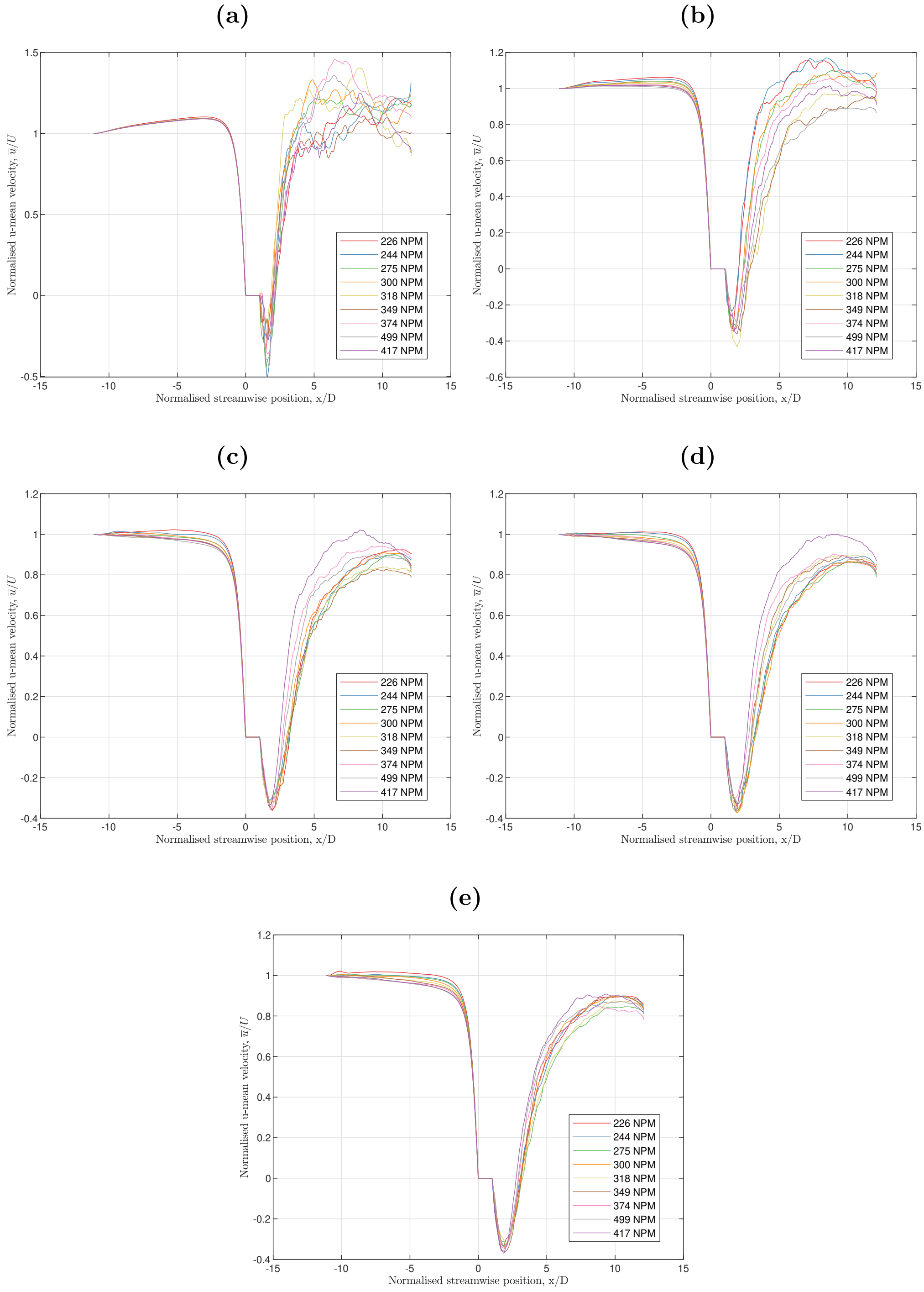

Figure 3.8: Normalised mean streamwise velocity profiles along the centreline of the Z-normal plane, with RLB dynamics. Square cylinder obstacle at (a) $Re_D = 2470$ (Case III) (b) $Re_D = 12352$ (Case IV) (c) $Re_D = 24705$ (Case V) (d) $Re_D = 37057$ (Case VI) (e) $Re_D = 49410$ (Case VII)

Comparing the profiles of turbulent kinetic energy (TKE), Figure 3.9. For case III, contrary to the results of Figure 3.8a, the profiles show what would seem as converged result. However, the large fluctuations of TKE along the profile are unrealistic in time averaged data. In the subsequent cases, the profiles all appear much smoother with the higher Reynolds cases again appearing to be more converged than the others.

Figure 3.10 presents the velocity profiles upstream of the obstacle at locations corresponding to: 0.0X (inlet), 0.1X, 0.2X, 0.3X and 0.4X of the channel length, the obstacle centre being positioned at 0.5X in all cases. For case III the entire velocity profile is accelerated in the upstream region concurrent with the results of Figure 3.8a, furthermore the profile is not logarithmic as would be expected from a channel flow, instead there seems to be a sustained acceleration in the flow around 0.1Z, whilst the magnitude of this jet dampens along the channel it is not sufficient to completely correct this behaviour. Similarly, case IV also experiences this jet phenomenon in the same region of the domain, and once again the anomaly is still present at 0.4X. The rest of the profile appears unaffected by this jet, although, from 0.2X onwards a secondary shear layer, increasing over time, can be seen forming at the surface of the flow. Since the top of the channel is a free stream surface with no solid surfaces this phenomenon is also completely unphysical. The remaining cases all show similar evolutions of the flow there is still the jet at the bottom of the channel but this is quickly damped out and a fully logarithmic profile consistent with what is expected from the theory is observed by 0.3X - 0.4X.

The profiles shown in Figure 3.11, show the evolution of the flow after the obstacle at locations 0.6X, 0.7X, 0.8X, 0.9X and 1.0X (outlet). Once again there is a clear distinction in the evolution for cases III and IV compared to the rest. Cases V, VI and VII by 0.9X a turbulent logarithmic profile can be observed, however, for cases III and IV due to the unphysical downstream acceleration observed in Figure 3.8a and Figure 3.8b, more so for case III than case IV, the flow recovers to what appears to be a shear flow.

3.2.1.2.3 Outlet zone types A key feature observed in Figure 3.8, in the far wake region of the velocity profiles, the flow will reach a maxima and then slowly decelerate as it approaches the outlet. This effect should not be observed as in physical scenario the velocity after an obstacle should recover to a certain value and then remain constant at that value. One explanation for this phenomenon

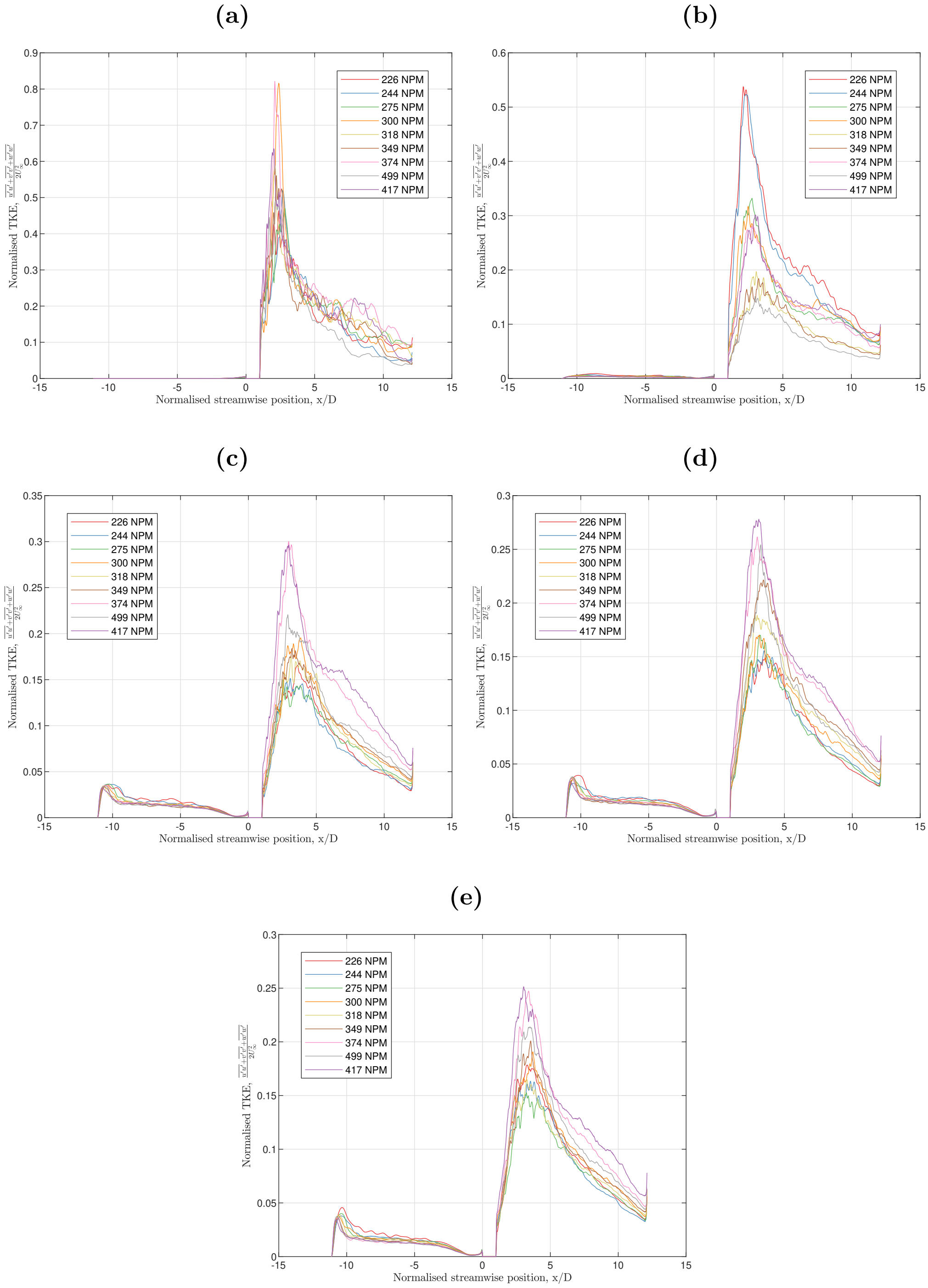

Figure 3.9: Normalised turbulent kinetic energy profiles along the centreline of the Z-normal plane, with RLB dynamics. Solid square obstacle at (a) $Re_D = 2470$ (Case III) (b) $Re_D = 12352$ (Case IV) (c) $Re_D = 24705$ (Case V) (d) $Re_D = 37057$ (Case VI) (e) $Re_D = 49410$ (Case VII)

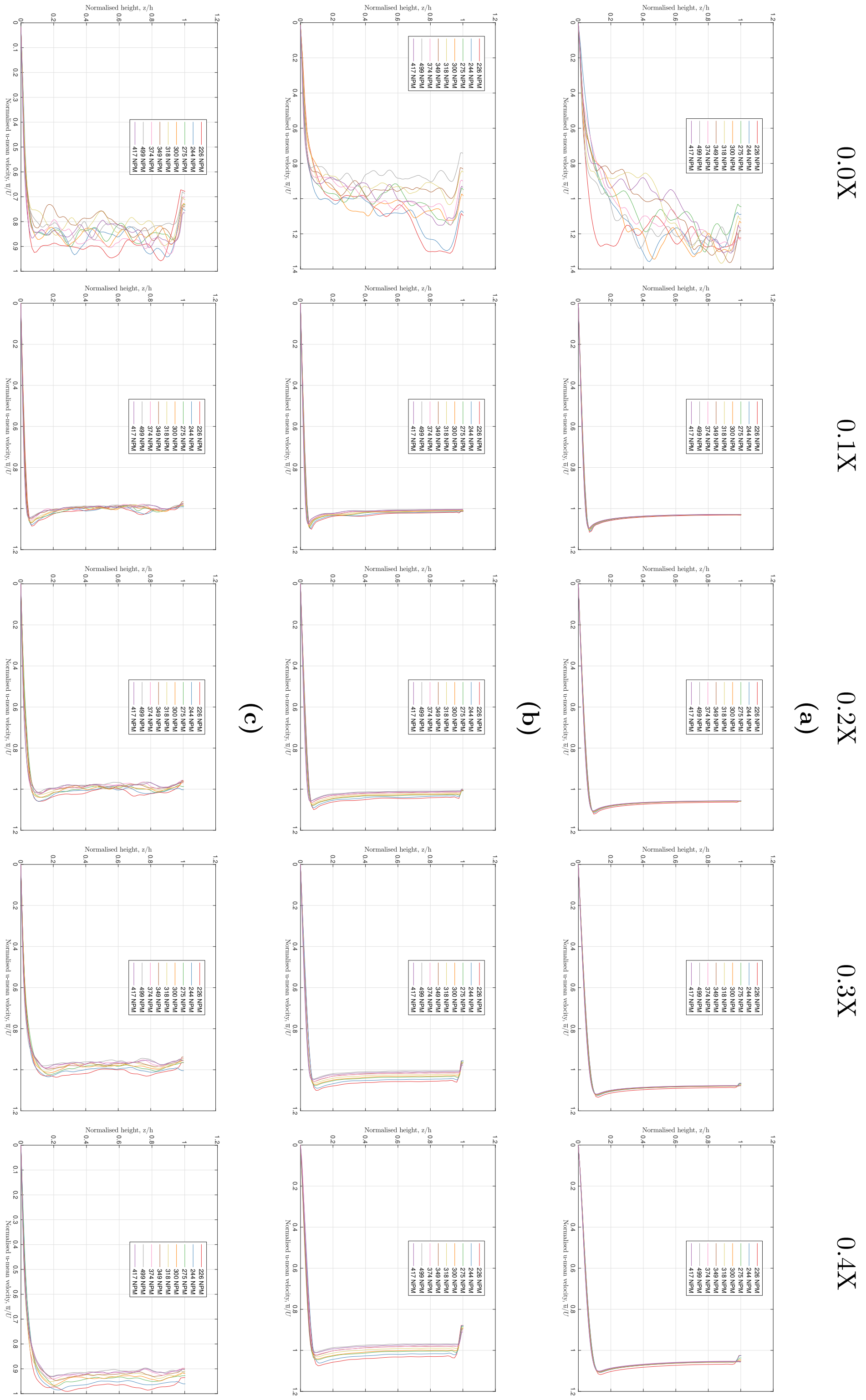
0.0X
0.1X
0.2X
0.3X
0.4X
(a)
(b)
(c)
Normalised height, z/h
Normalised u-mean velocity, ū/U
226 NPM
244 NPM
275 NPM
300 NPM
318 NPM
349 NPM
374 NPM
499 NPM
417 NPM

0.0X 0.1X 0.2X 0.3X 0.4X

(d)

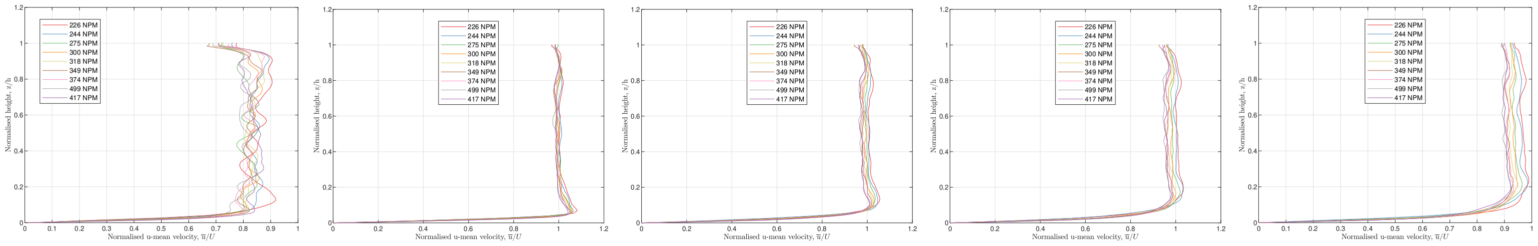

(e)

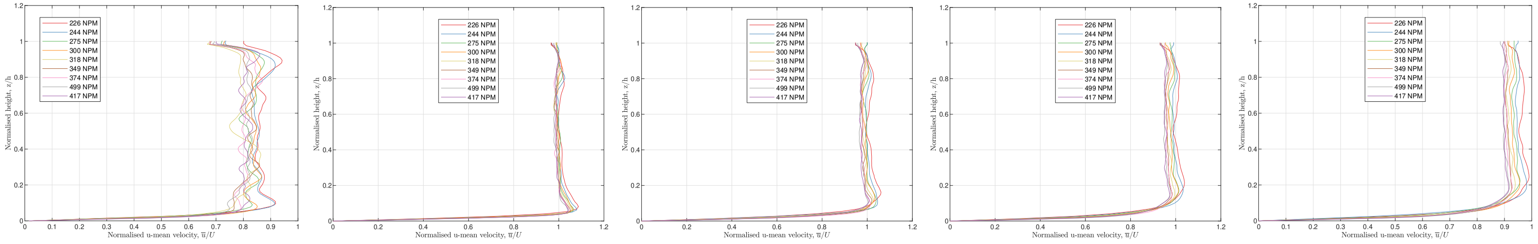

Figure 3.10: Normalised mean streamwise velocity profiles at varying positions in the channel (0%, 10%, 20%, 30%, 40% channel length) of the Y-normal plane, with RLB dynamics. Solid square obstacle at (a) $Re_D = 2470$ (Case III) (b) $Re_D = 12352$ (Case IV) (c) $Re_D = 24705$ (Case V) (d) $Re_D = 37057$ (Case VI) (e) $Re_D = 49410$ (Case VII)

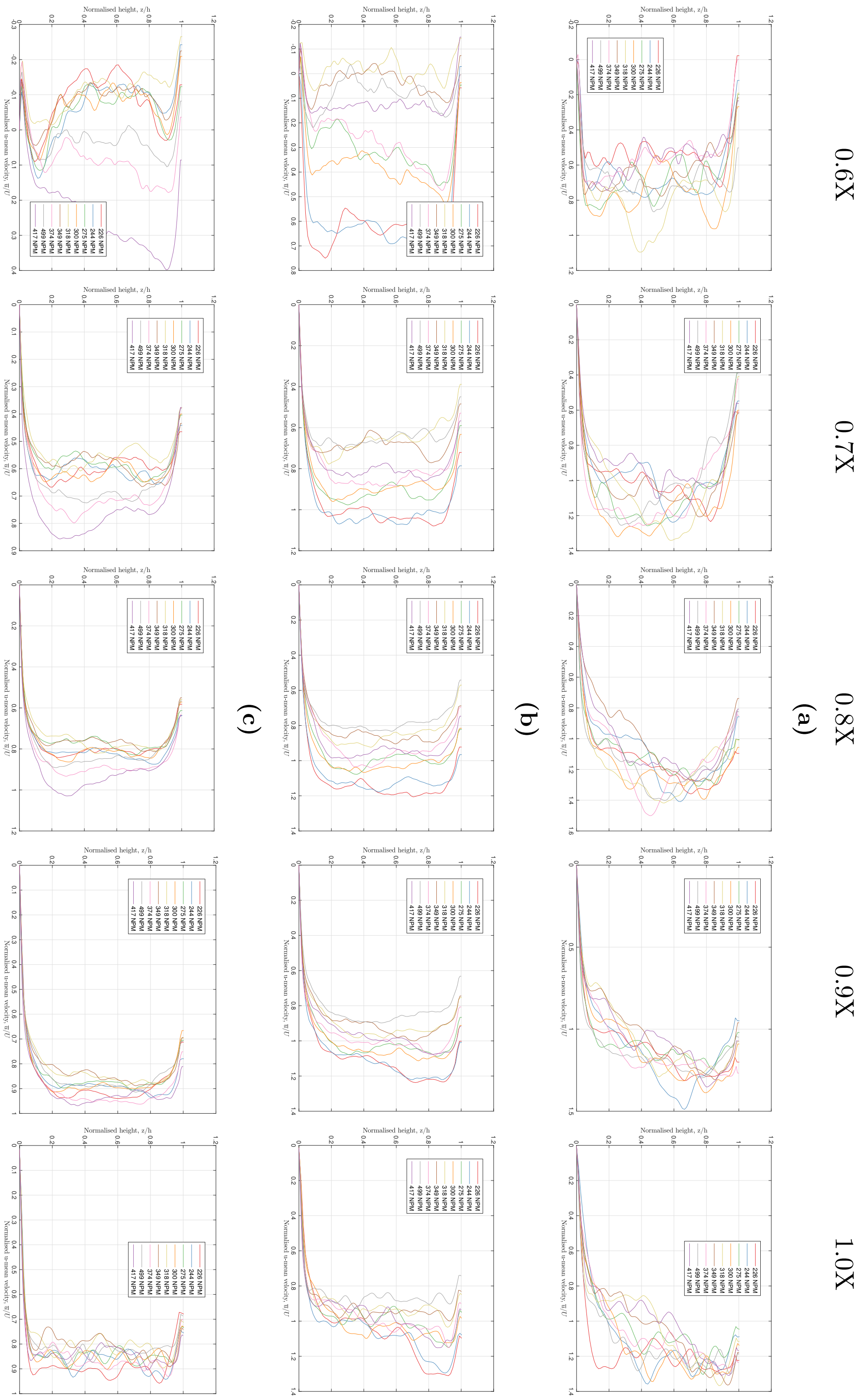
0.6X
0.7X
0.8X
0.9X
1.0X
(a)
(b)
(c)
Normalised height, z/h
Normalised u-mean velocity, ū/U
226 NPM
244 NPM
275 NPM
300 NPM
318 NPM
349 NPM
374 NPM
499 NPM
417 NPM

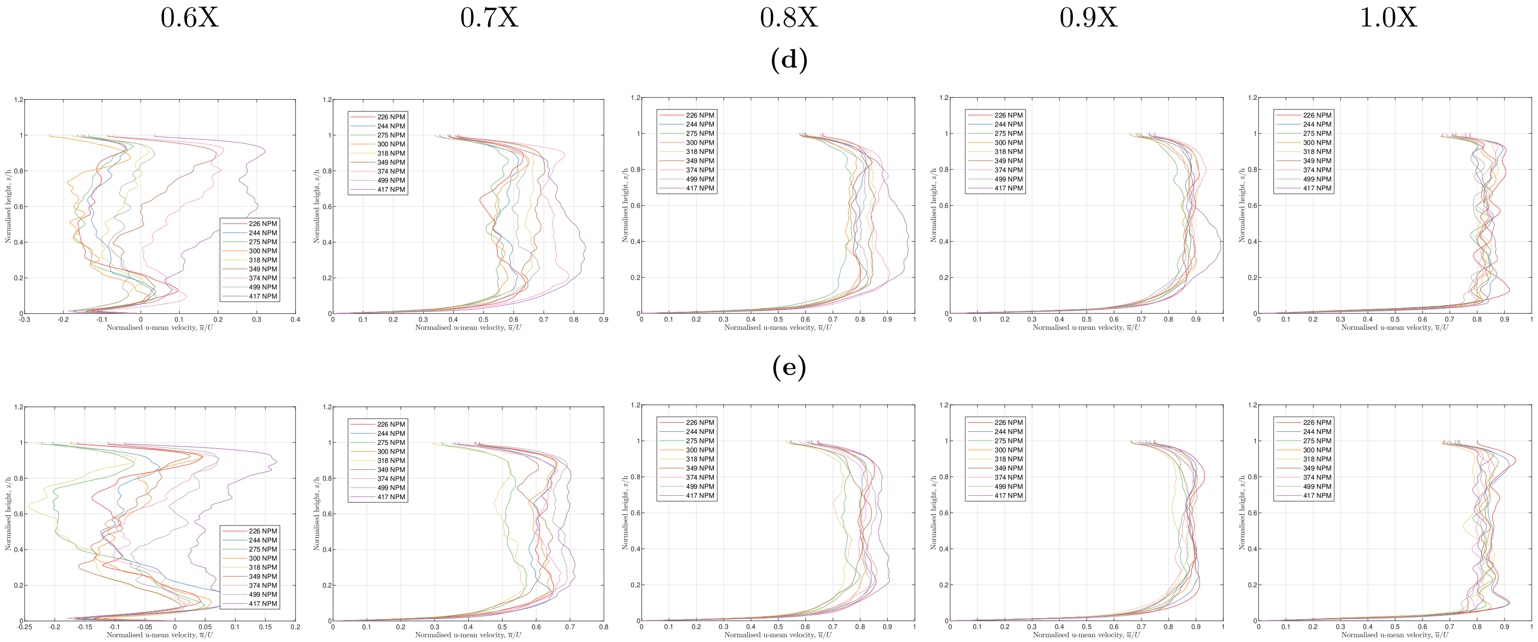

Figure 3.11: Normalised mean streamwise velocity profiles at varying positions in the channel (60%, 70%, 80%, 90%, 100% channel length) of the Y-normal plane, with RLB dynamics. Solid square obstacle at (a) $Re_D = 2470$ (Case III) (b) $Re_D = 12352$ (Case IV) (c) $Re_D = 24705$ (Case V) (d) $Re_D = 37057$ (Case VI) (e) $Re_D = 49410$ (Case VII)

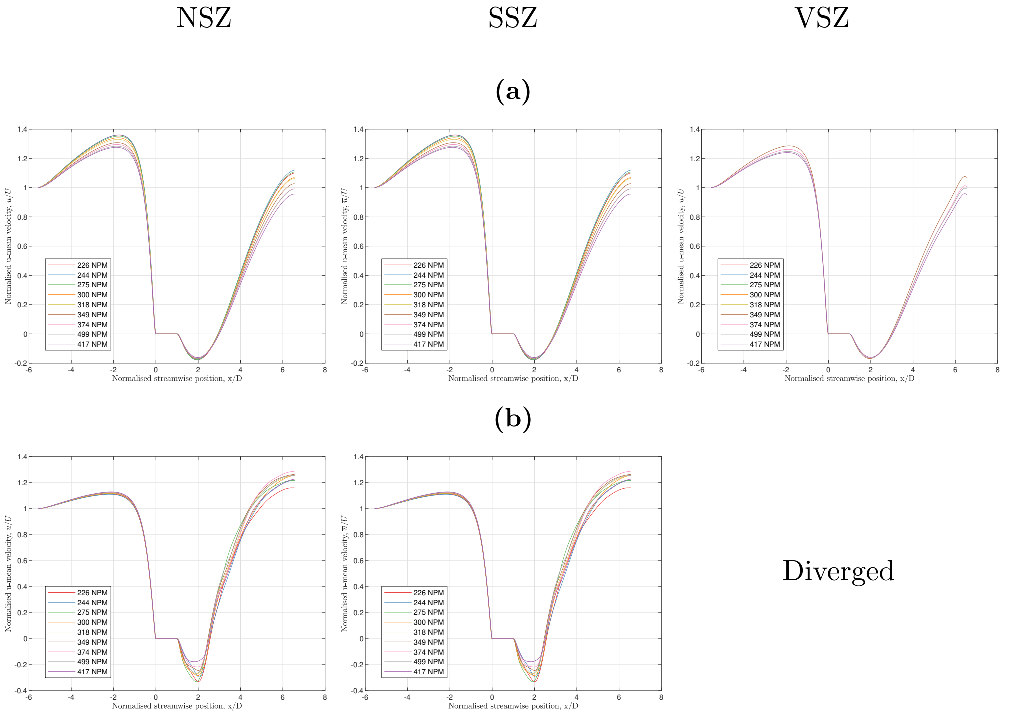

Figure 3.12: Normalised mean streamwise velocity profiles comparing three different outlet sponge zone types (None - NSZ, Smagorinsky - SSZ and Viscous - VSZ) along the centreline of the Z-normal plane, with RLB dynamics. Solid square obstacle at (a) $Re_D = 100$ (Case I) (b) $Re_D = 500$ (Case II)

is that the cause is a numerical error, due to the fact that infinitely long domain cannot be simulated, and an outlet has to be defined. If not positioned sufficiently far away it is possible to have the flow reflect at the boundary and affect the incoming flow after it. As a means of ensuring that the outlet was not causing additional reflections in the flow, a sponge zone (a localised area of higher viscosity, that would allow the flow to slow down much faster prior to reaching the outlet) of length D was placed in front of the outlet. Furthermore, two different sponge zones were tested, a Smagorinsky based one wherein the Smagorinsky constant in the sponge zone was increased to 0.6 and a simpler viscosity based sponge zone.

For the two laminar cases, Figure 3.12 only case I was able to produce a result for the viscous based sponge zone but only for the four finest meshes. Additionally, only a very slight change can be observed in the outlet region of the profile where the recovery rate has slightly slowed down. In the cases where a Smagorinski sponge zone was implemented, there is no change with respect to not having a sponge zone.

Similarly for the turbulent cases, the streamwise profiles are shown in Figure 3.13. Cases IV to VII show that the viscous type sponge zone results in a diverged solution, and direct comparison between the runs without a sponge zone and a Smagorinsky type one show near identical profiles for each case at all resolutions as well. Hence, it is clear that the unphysical phenomena must be arising from the underlying dynamics model chosen. Therefore, the MRT method needs to be explored as well.

3.2.1.3 Dynamics Models - MRT

Finally the last dynamic model tested was the multiple relaxation time. Since, the choice of outlet sponge zone was determined to have no net positive effect on the simulation outcome, to keep the cases as simple as possible the MRT model was tested without a sponge zone only. Similarly to the RLB this method was effective in the high Reynolds number region.

3.2.1.3.1 Laminar cases The two laminar cases, presented in Figure 3.14, both show that near the side walls the flow separates forming quite large bubbles forcing the accelerated flow into the central region of the transversal plane. This effect is more dominant in case I, hence the shape of the wake appears to be more triangular compared to the elliptical shape of case II. The downstream cross-stream velocity maps, Figure 3.15, show the formation of two recirculation zones side by side aft of the obstacle, with case I showing more clearly defined structures and symmetrical structures about the centreline.

A significant difference can be made between the two cases by looking at the average kinetic energy, Figure 3.16, whilst case I demonstrates a smooth constant average kinetic energy in the domain that does not change, case II fluctuates over a constant value. However, case II shows that the mesh resolution has very little effect on the average kinetic energy, whilst case I demonstrates the opposite.

Additionally, with respect to the RLB method, the MRT offers no change in the streamwise profiles, Figure 3.17.

3.2.1.3.2 Turbulent cases For the turbulent cases, first consider the mean velocity maps, Figure 3.18. It can be seen that as the velocity of the flow is increased so does the wake length, but only between cases IV and V. Furthermore, both cases III and IV show that the accelerated portion of the flow is quickly

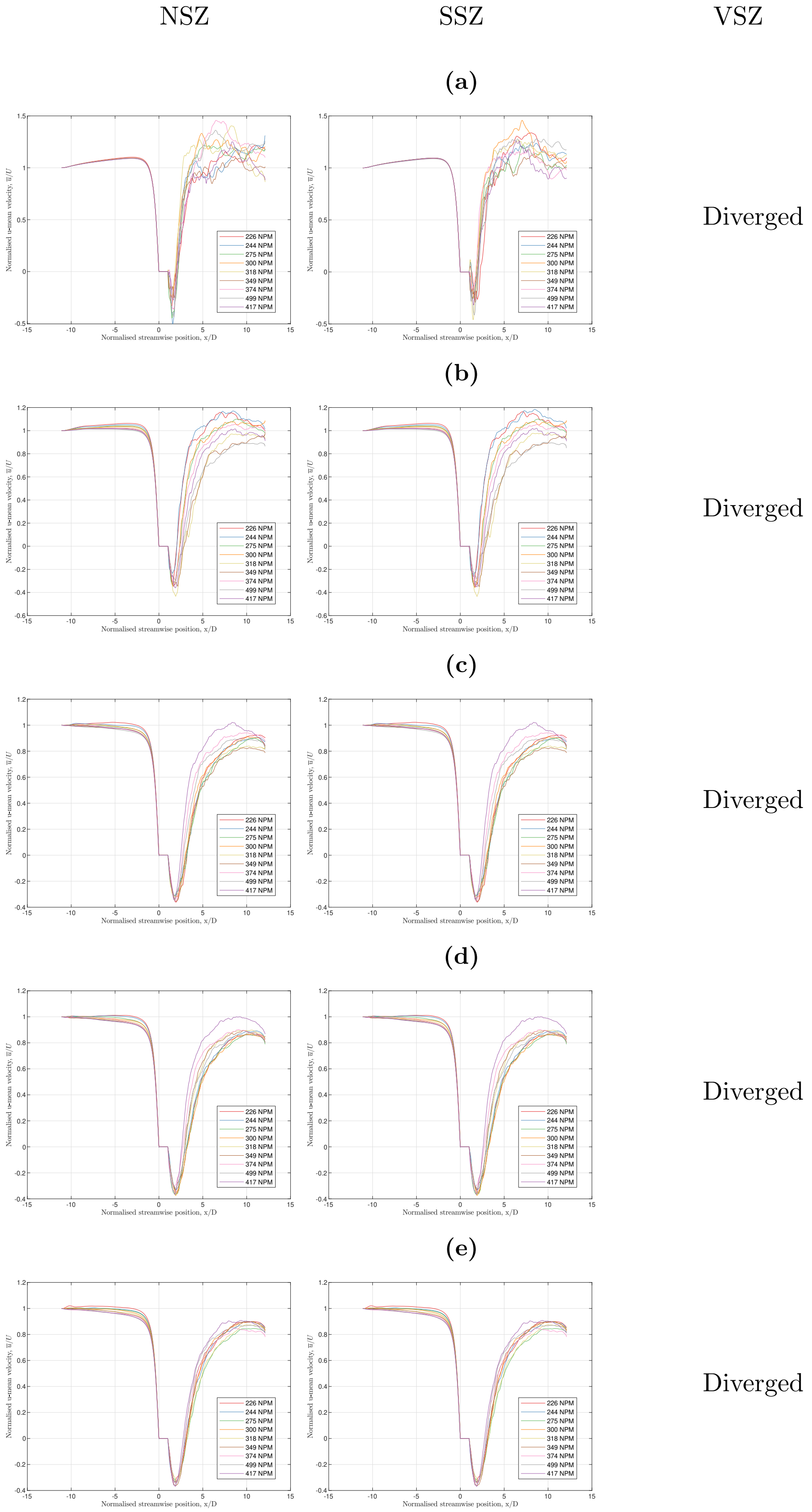

Figure 3.13: Normalised mean streamwise velocity profiles comparing three different outlet sponge zone types (None - NSZ, Smagorinsky - SSZ and Viscous - VSZ) along the centreline of the Z-normal plane, with RLB dynamics. Solid square obstacle at (a) $Re_D = 2470$ (Case III) (b) $Re_D = 12352$ (Case IV) (c) $Re_D = 24705$ (Case V) (d) $Re_D = 37057$ (Case VI) (e) $Re_D = 49410$ (Case VII)

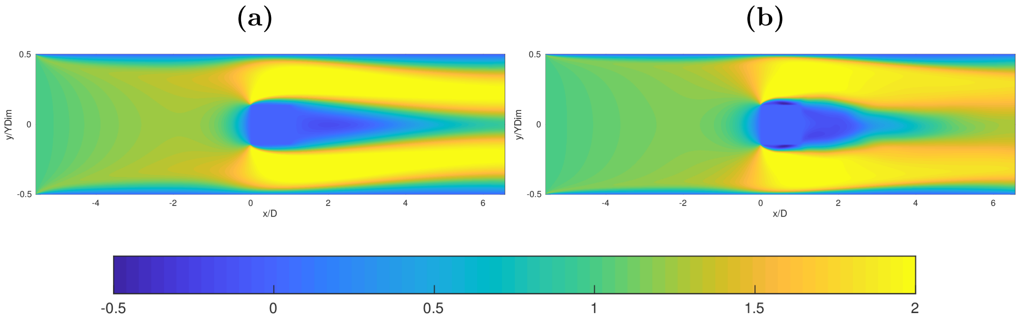

Figure 3.14: Normalised mean streamwise velocity maps, $\overline{u}/U_\infty$, of the Z-normal plane at 40% flow depth from the channel floor with MRT dynamics and a resolution of 417 NPM. Solid square obstacle at (a) $Re_D = 100$ (Case I) (b) $Re_D = 500$ (Case II)

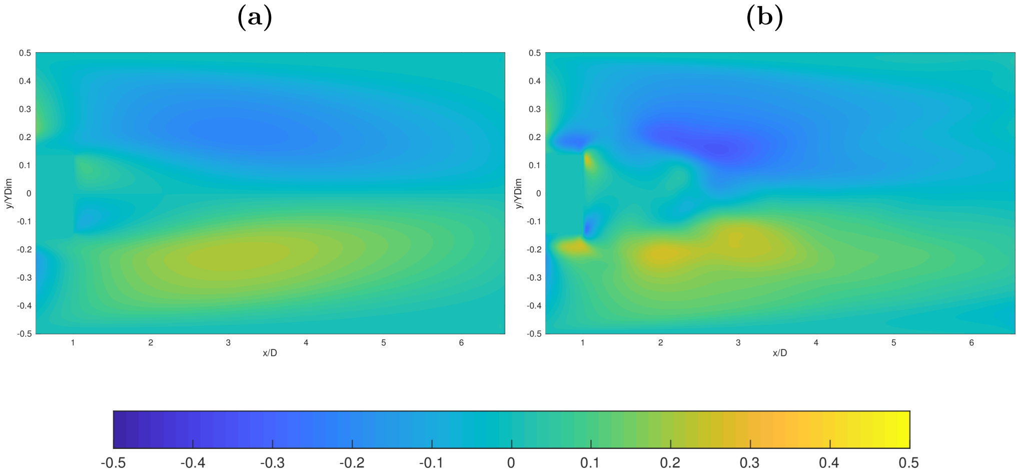

Figure 3.15: Normalised downstream mean cross-stream velocity maps, $\overline{v}/U_\infty$, of the Z-normal plane at 40% flow depth from the channel floor with MRT dynamics and a resolution of 417 NPM. Solid square obstacle at (a) $Re_D = 100$ (Case I) (b) $Re_D = 500$ (Case II)

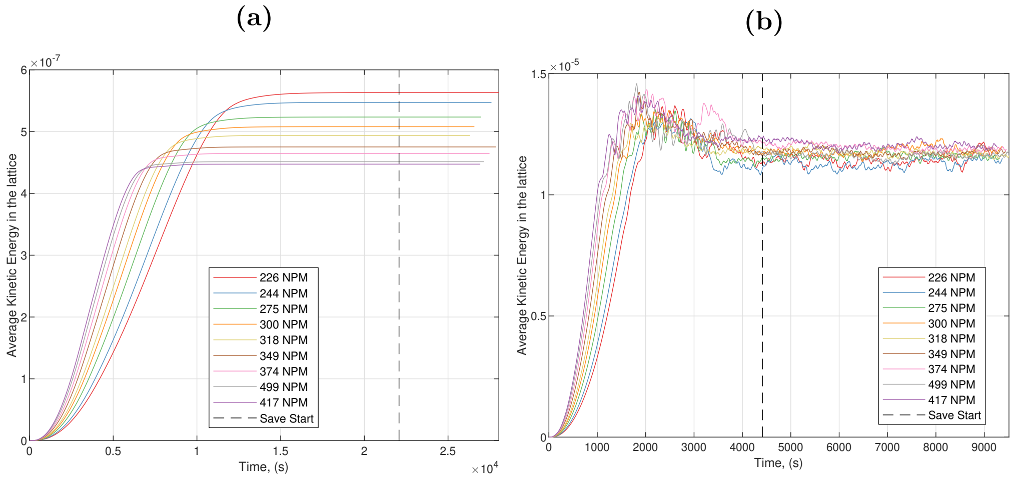

Figure 3.16: Average kinetic energy in the lattice over time for turbulent flow past solid square obstacle, with MRT dynamics. (a) $Re_D = 100$ (Case I) (b) $Re_D = 500$ (Case II)

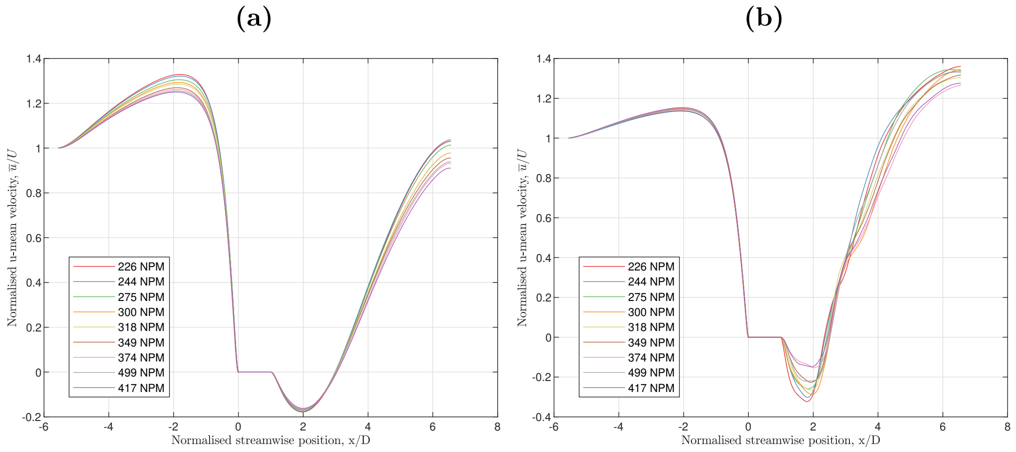

Figure 3.17: Normalised mean streamwise velocity profiles along the centreline of the Z-normal plane, with MRT dynamics. Solid square obstacle at (a) $Re_D = 100$ (Case I) (b) $Re_D = 500$ (Case II)

drawn into the centre of the channel forming a number of pockets of low velocity surrounded by areas of high velocity flow. By comparison the remaining cases do not develop this phenomenon instead the high velocity flow remains as two jets, one on either side of the obstacle, that dissipate over the channel length.

Turning to the cross-stream maps, Figure 3.19, all cases show the two recirculation zones previously. However, cases III-IV show far more cross-stream activity in the flow closer to the outlet, case III clearly shows a third recirculation zone, which when compared to the corresponding streamwise map indicates that the flow is being draw towards the centreline. The far wake structures of case IV suggest the contrary where the flow is being pushed towards the side walls.

The kinetic energy convergence and the velocity profiles are shown in Figure 3.20 and Figure 3.21 respectively. From the kinetic energy convergence there appears to be a subdivision between cases III-IV and V-VII, both cases III and IV have little to no variation between the meshes whilst the remaining cases do demonstrate a noticeable variation between the meshes.

By observing the velocity profiles, this separation becomes clear as cases III and IV are those which present the most unphysical flow. It should be noted that all turbulent cases demonstrate an unphysical upstream region. Although, as the Reynolds number and mesh density are increased, this anomaly seems to correct itself. However, at the finest mesh of case VII the upstream region still remains unphysical but only slightly. When observing the near wake region case III shows a very erratic flow, across the meshes there does not seem to be a clear convergence and the magnitude of the recirculation velocity along with case IV is the largest compared to the remaining cases. Furthermore, as in the RLB results, the shortest recirculation bubble is observed in case III. Case IV does show some improvement, and the near wake region appears to be quite converged, although the size of the recirculation bubble grows and contracts as the mesh density increases. The remaining cases all show little to no variation of the wake size at all resolutions, however the magnitude does vary, but by the finest resolution a sufficiently converged result can be observed.

In the far wake region cases III and IV both show unphysical results, with case III showing the most erratic behaviour akin to the RLB results. The remaining cases all maintain physicality of the flow and also show little variation between resolutions.

The TKE profiles, shown in Figure 3.22, for case III further reinforce the erratic description of the flow observed in the velocity profiles. Case IV stands

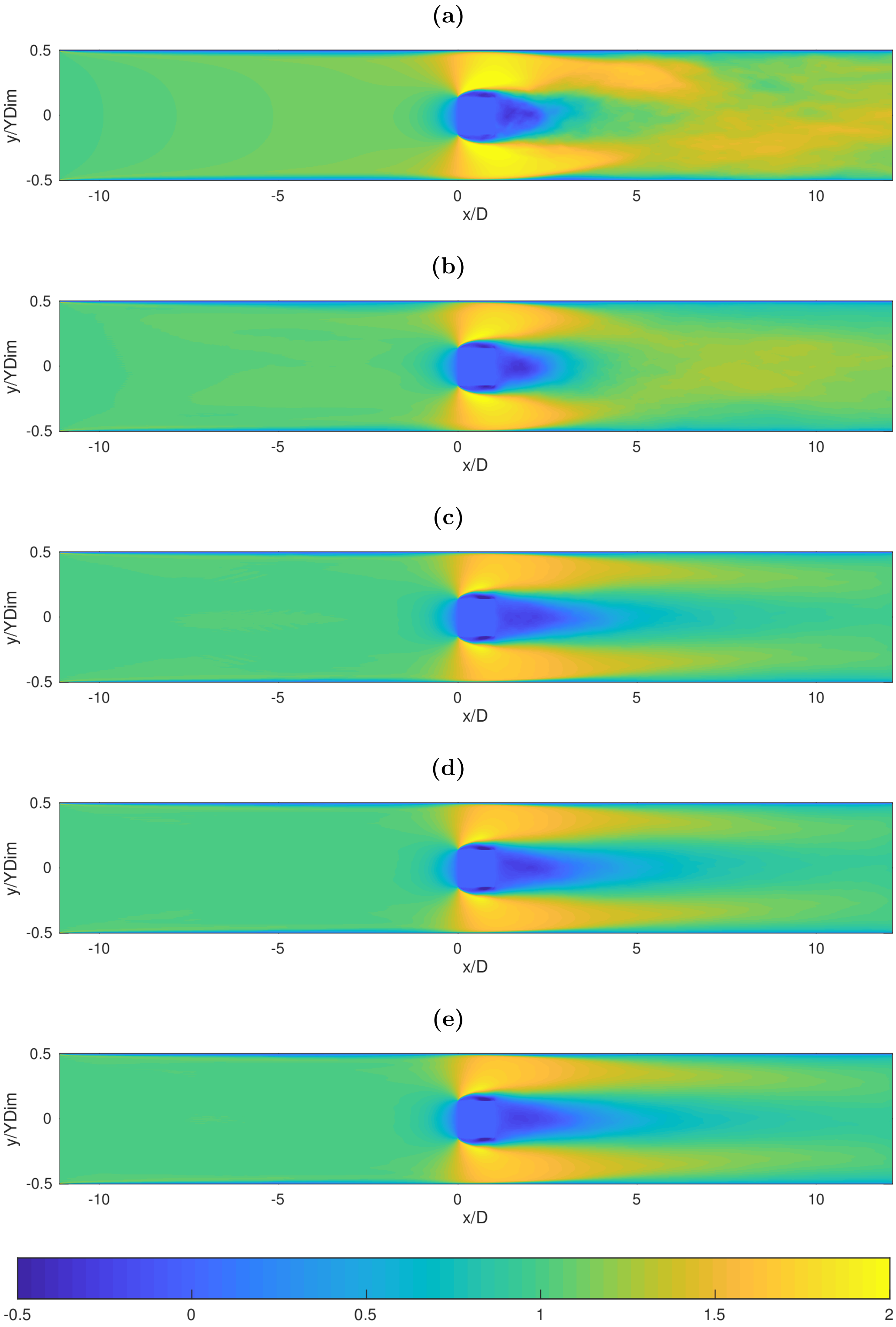

Figure 3.18: Normalised mean streamwise velocity maps, $\overline{u}/U_\infty$, of the Z-normal plane at 40% flow depth from the channel floor with MRT dynamics and a resolution of 417 NPM. Solid square obstacle at (a) $Re_D = 2470$ (Case III) (b) $Re_D = 12352$ (Case IV) (c) $Re_D = 24705$ (Case V) (d) $Re_D = 37057$ (Case VI) (e) $Re_D = 49410$ (Case VII)

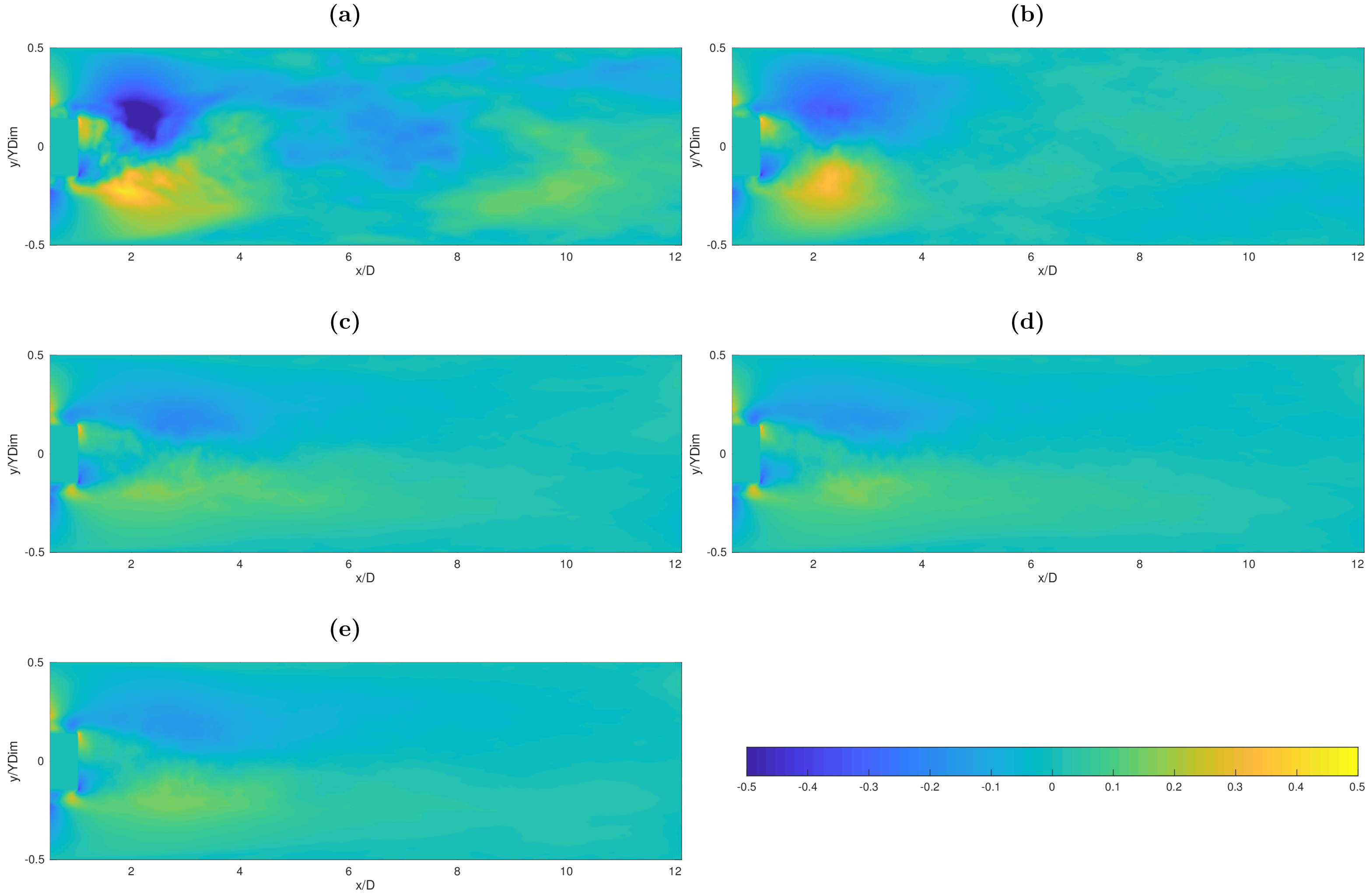

Figure 3.19: Normalised mean cross-stream velocity maps, $\overline{v}/U_\infty$, of the Z-normal plane at 40% flow depth from the channel floor with MRT dynamics and a resolution of 417 NPM. Solid square obstacle at (a) $Re_D = 2470$ (Case III) (b) $Re_D = 12352$ (Case IV) (c) $Re_D = 24705$ (Case V) (d) $Re_D = 37057$ (Case VI) (e) $Re_D = 49410$ (Case VII)

out from the other cases in that the variation across the different resolutions is the greatest of all the cases, most significantly in the peak TKE. Compared to all other turbulent cases the peak TKE for case IV has the greatest change, the outlier appears to be the 499 NPM mesh, the simulations with 300 - 374 NPM do show somewhat of a convergence with the finest mesh, however the 499 NPM mesh shows a dramatic reduction in TKE over the entire profile. Cases V-VII show much less variation between resolutions but significant fluctuations can be observed in the profiles of case V with these fluctuations becoming smoother as the flow velocity is increased. Contrary to the observations in the RLB cases the upstream region of the flow appears to be only slightly uniformly accelerated.

Looking at the upstream vertical velocity profiles along the channel, shown in Figure 3.23, there is a significant difference between the inlet profiles for all cases and the other locations, whilst cases III and IV seem to develop a shear velocity profile with case III being more pronounced the remaining cases do show a well defined logarithmic turbulent profile as predicted in the theory. Additionally as in the RLB cases, significant fluctuations can be observed with low resolution cases experiencing a lower frequency and higher magnitude oscillation compared to the finer meshes. Immediately after the inlet, at 0.1X, all velocity profiles for all cases appear similar, the channel floor jet observed in the RLB results is clearly present again and the profile appears to have reverted to a near uniform profile. Furthermore, cases III and IV also have developed a top shear layer which becomes increasingly pronounced over the channel length. In cases V-VII the top shear layer also develops but at a later stage, and it again grows as the flow advances in the channel. Comparing the evolution of the profiles for cases V-VII after the inlet, it can be observed that as the flow develops across the channel the variations between the resolutions grow, however, a clear convergence can be observed in every case.

Figure 3.24 shows the downstream vertical profiles. As with the streamwise profiles a distinction can be made between cases III-IV and V-VII, the wake profiles, at 0.6X, for cases III and IV appear remarkably shear-like, this contrasts cases V-VII where by the finest resolution the flow is relatively uniformly decelerated across the entire height of the channel, but in case III an overall negative shear can be observed across each resolution, only the finest mesh breaks the pattern with a positive shear, additionally case IV resolutions show a positive shear. Moreover, the slowest two cases also appear to develop near parabolic profiles around 0.7-0.8X with case VI being more prominent. Further evolution

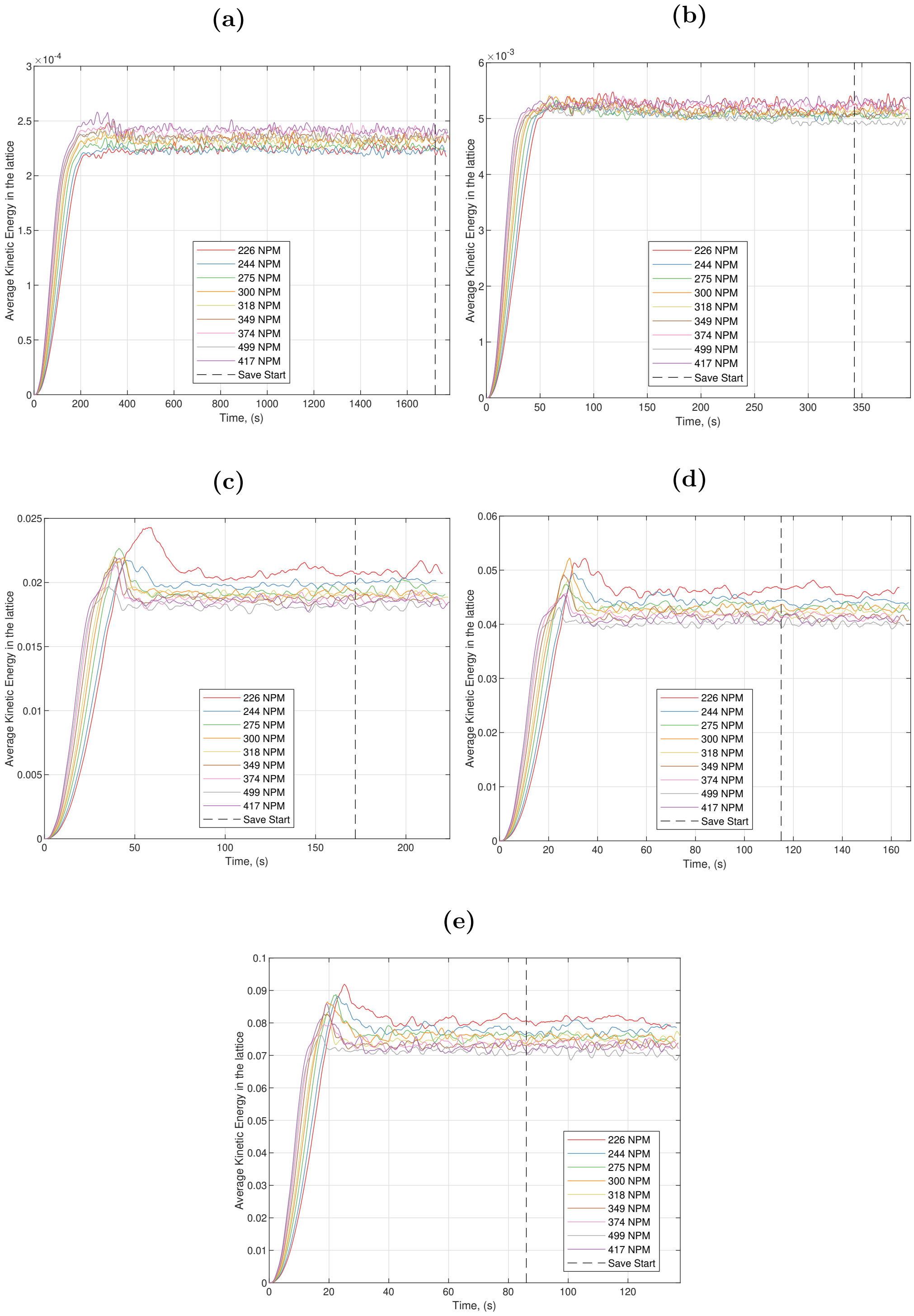

Figure 3.20: Average kinetic energy in the lattice over time for turbulent flow past solid square obstacle, with MRT dynamics. (a) $Re_D = 2470$ (Case III) (b) $Re_D = 12352$ (Case IV) (c) $Re_D = 24705$ (Case V) (d) $Re_D = 37057$ (Case VI) (e) $Re_D = 49410$ (Case VII)

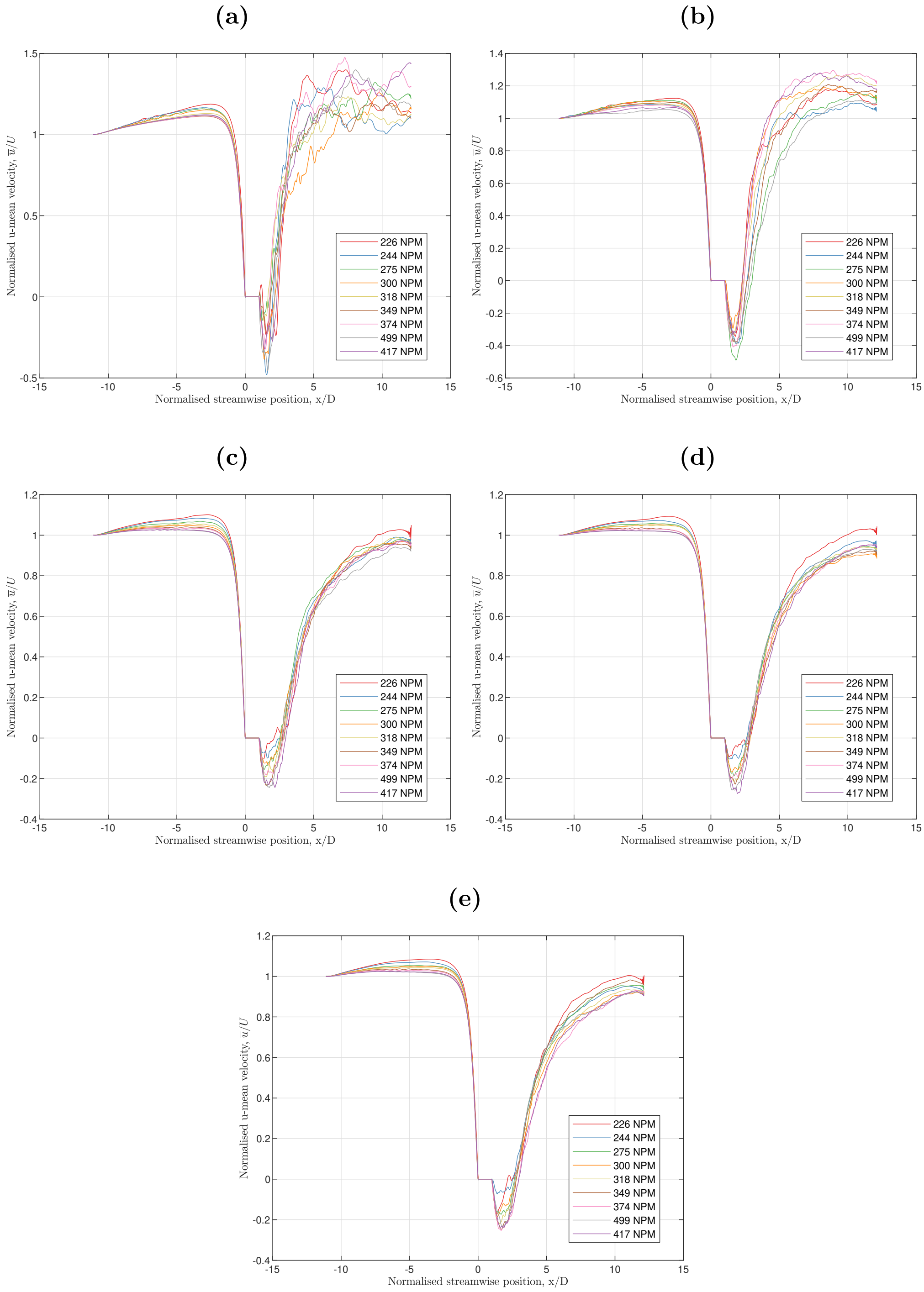

Figure 3.21: Normalised mean streamwise velocity profiles along the centreline of the Z-normal plane, with MRT dynamics. Solid square obstacle at (a) $Re_D = 2470$ (Case III) (b) $Re_D = 12352$ (Case IV) (c) $Re_D = 24705$ (Case V) (d) $Re_D = 37057$ (Case VI) (e) $Re_D = 49410$ (Case VII)

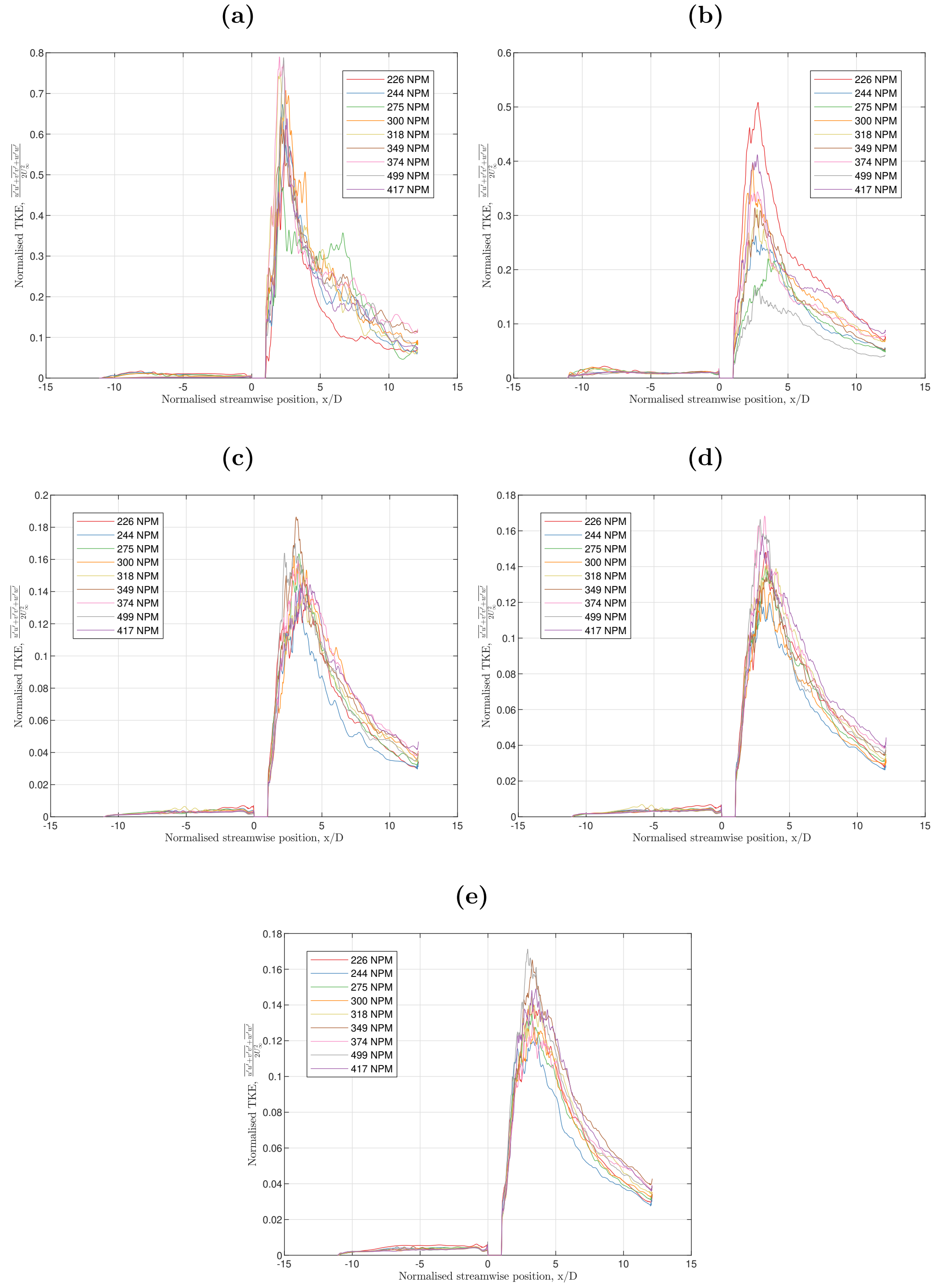

Figure 3.22: Normalised turbulent kinetic energy profiles along the centreline of the Z-normal plane, with MRT dynamics. Solid square obstacle at (a) $Re_D = 2470$ (Case III) (b) $Re_D = 12352$ (Case IV) (c) $Re_D = 24705$ (Case V) (d) $Re_D = 37057$ (Case VI) (e) $Re_D = 49410$ (Case VII)

along the channel, the flow experiences a deceleration close to the bottom of the channel forcing the flow into a shear flow profile. The remaining cases, shortly after the wake, recover to a logarithmic profile and maintain this characteristic until the outlet.

As will be explained in further detail in chapter 4 the MRT model has proven to be reliable choice than the RLB and BGK options. Hence, the remaining obstacles will be studied only using the MRT model and without a sponge zone. Furthermore, cases I and II will also be omitted as 1) No suitable validation data could be acquired from the literature and 2) the focus of this thesis lies on the turbulent regime.

3.2.2 Porous Regular Obstacle

The first of the two porous obstacles explored was the regular obstacle. As it can be seen in the mean velocity maps, Figure 3.25, since the obstacle is essentially a grid of square cylinders there is a direct path for the fluid to take through the rows of the obstacle, hence, behind each row of obstacles a wake can be seen, with the middle three rows forming a smaller wake compared to the two edge rows. Furthermore, it can be clearly seen that although the individual obstacles are apart they do have a group effect on the flow as the general area behind the obstacle is noticeably decelerated. Compared to cases IV-VII case III has a significantly larger wake size especially behind the far rows of the obstacle.

In the cross-stream velocity maps, Figure 3.26, it can be seen that the column of obstacles closest to the outlet each form a small recirculation zone after it, subsequently the group effect dominates the flow and two larger recirculation zones are formed. For this obstacle it is only case III that demonstrates continued cross-stream activity in the far wake region.

Following on to the streamwise profiles, shown in Figure 3.27 and Figure 3.28. Although the experimental data is of a case ran at an $Re_D = 28350$, since the turbulent cases except for case III are all of the same order of magnitude it is a reasonable assumption that all cases should be relatively similar.

Observations in the upstream region of the flow show identical behaviour as in the solid case, this is natural as there has been no change in this area of the domain.

The near wake region for all cases shows a convergence toward the experimental data, however, an exact match is not achieved in any. A trend can be


0.0X
0.1X
0.2X
0.3X
0.4X
(a)
(b)
(c)
226 NPM
244 NPM
275 NPM
300 NPM
318 NPM
349 NPM
374 NPM
499 NPM
417 NPM
Normalised height, z/h
Normalised u-mean velocity, ū/U

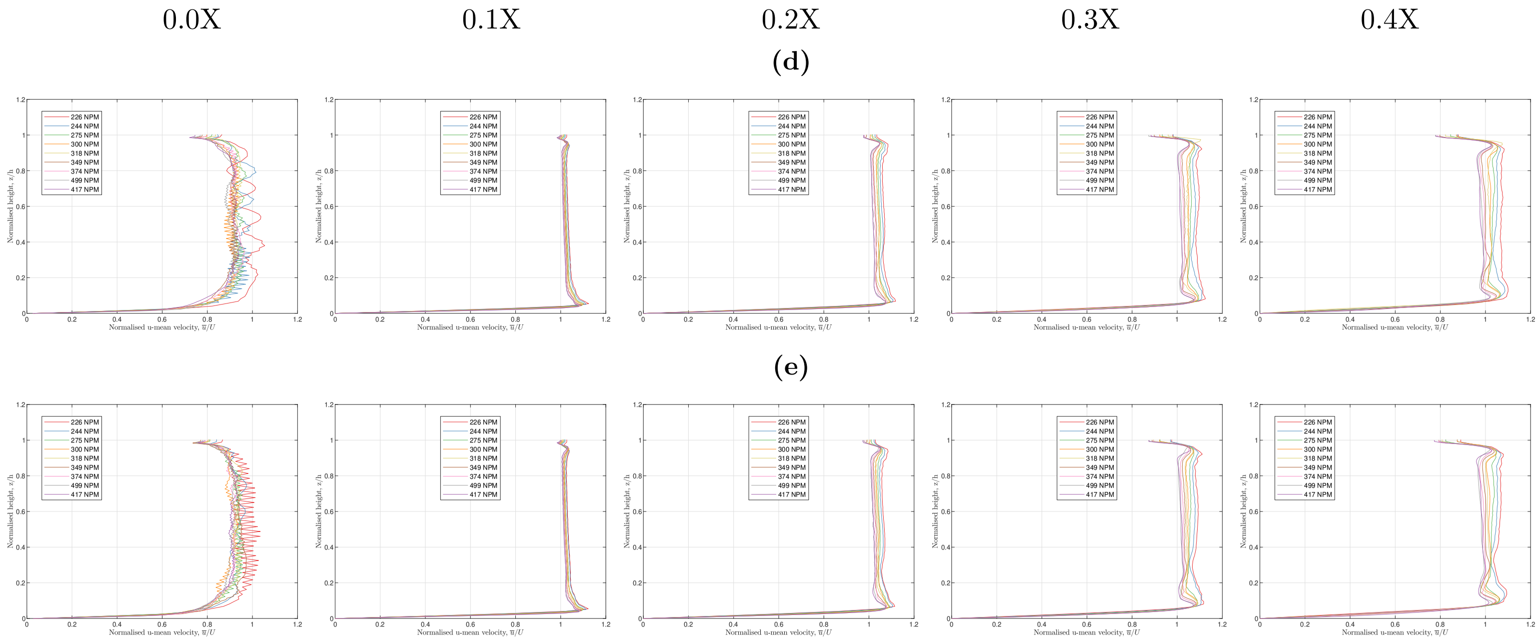

Figure 3.23: Normalised mean streamwise velocity profiles at varying positions in the channel (0%, 10%, 20%, 30%, 40% channel length) of the Y-normal plane, with MRT dynamics. Solid square obstacle at (a) $Re_D = 2470$ (Case III) (b) $Re_D = 12352$ (Case IV) (c) $Re_D = 24705$ (Case V) (d) $Re_D = 37057$ (Case VI) (e) $Re_D = 49410$ (Case VII)

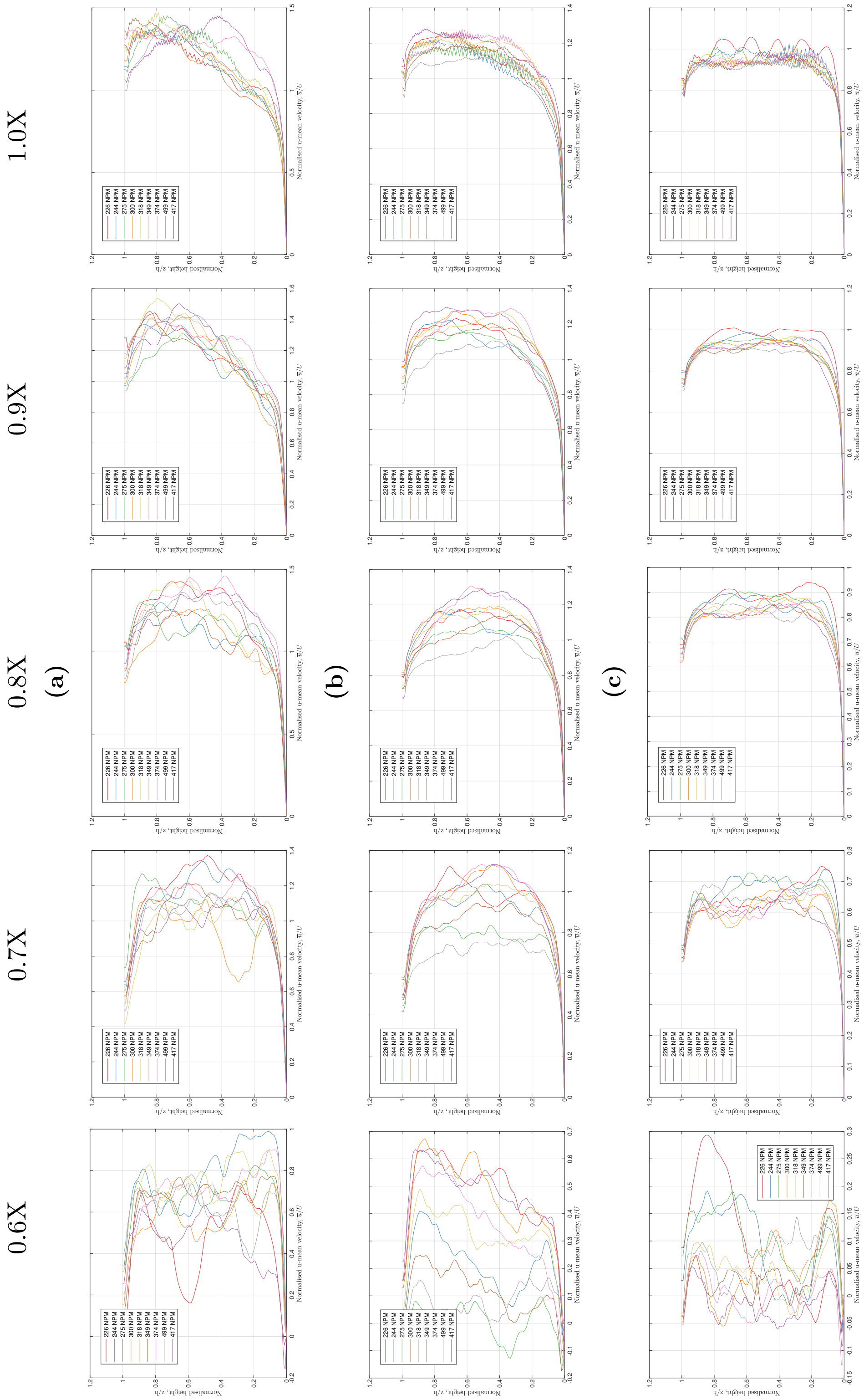
1.0X
0.9X
0.8X
0.7X
0.6X
(a)
(b)
(c)
226 NPM
244 NPM
275 NPM
300 NPM
318 NPM
349 NPM
374 NPM
499 NPM
417 NPM
Normalised height, z/h
Normalised u-mean velocity, ū/U

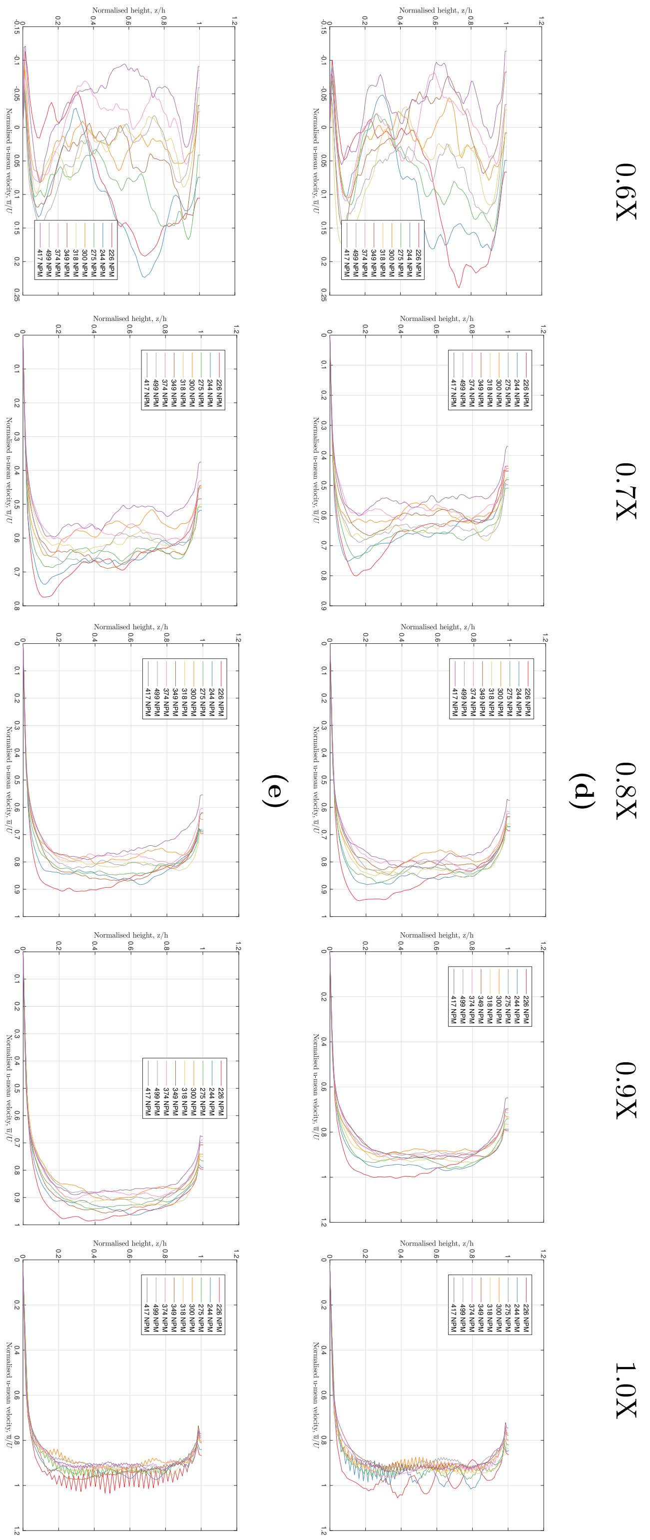

Figure 3.24: Normalised mean streamwise velocity profiles at varying positions in the channel (60%, 70%, 80%, 90%, 100% channel length) of the Y-normal plane, with MRT dynamics. Solid square obstacle at (a) $Re_D = 2470$ (Case III) (b) $Re_D = 12352$ (Case IV) (c) $Re_D = 24705$ (Case V) (d) $Re_D = 37057$ (Case VI) (e) $Re_D = 49410$ (Case VII)

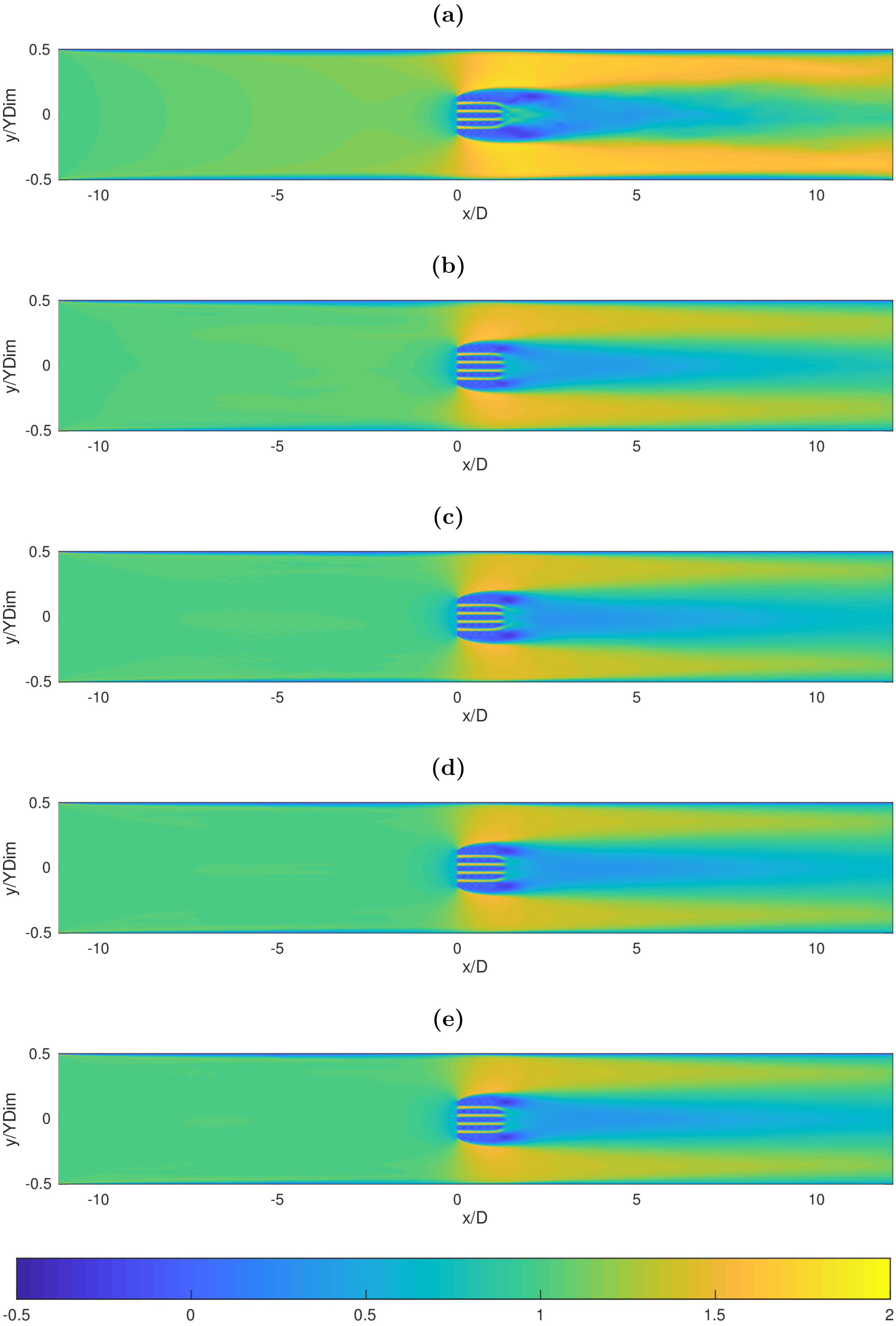

Figure 3.25: Normalised mean streamwise velocity maps, $\overline{u}/U_\infty$, of the Z-normal plane at 40% flow depth from the channel floor with MRT dynamics and a resolution of 417 NPM. Porous regular obstacle at (a) $Re_D = 2470$ (Case III) (b) $Re_D = 12352$ (Case IV) (c) $Re_D = 24705$ (Case V) (d) $Re_D = 37057$ (Case VI) (e) $Re_D = 49410$ (Case VII)

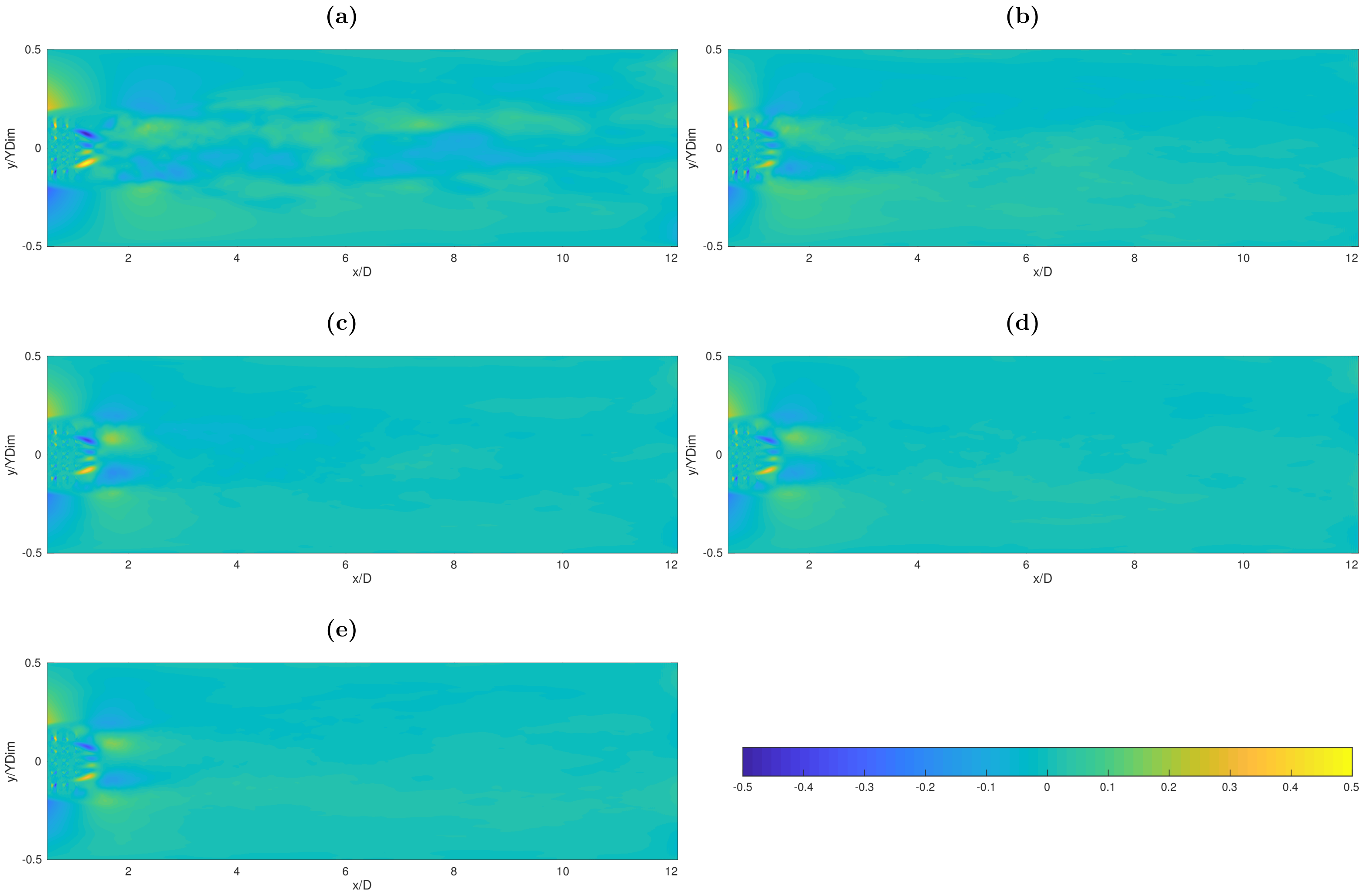

Figure 3.26: Normalised mean cross-stream velocity maps, $\overline{v}/U_\infty$, of the Z-normal plane at 40% flow depth from the channel floor with MRT dynamics and a resolution of 417 NPM. Porous regular obstacle at (a) $Re_D = 2470$ (Case III) (b) $Re_D = 12352$ (Case IV) (c) $Re_D = 24705$ (Case V) (d) $Re_D = 37057$ (Case VI) (e) $Re_D = 49410$ (Case VII)

observed that as the Reynolds number is increased the velocity profiles become smoother irrespective of the resolution in both the near and far wake regions.

Similar observations can be made from the TKE profiles, in all cases the low resolutions severely overestimate the actual value as measured experimentally but quickly converge towards the experimental data at the higher resolutions. Additionally since the TKE peak is so narrow the experimental profile does not capture it properly, however, looking at the individual measurement points, again both case IV and V are the ones that most accurately match the experimental data. Furthermore, cases IV and V both seem to diverge from the experimental data at approximately the same location. Moreover, whilst in the mean velocity profiles its the far wake region that mostly aligns with the experimental, for all cases the TKE profile correctly matches the near wake as measured.

Figure 3.29 shows the downstream vertical profiles, as the inlet region has not changed it is necessary to analyse this area of the domain. A key difference for the regular obstacle is that for cases IV-VII the flow does not appear to have recovered to a fully turbulent velocity profile. at 0.9X and 1.0X it is clearly shown that the bulk centre flow is still decelerated

3.2.3 Porous Fractal Obstacle

A clear characteristic of the flow for the fractal obstacle is that the recirculation does not happen immediately behind the obstacle. In fact the recirculation zone is delayed till about 4D for case III and 2.5D for cases IV-VII as shown in Figure 3.30.

The cross-stream maps show similar observations already described, however, for the fractal obstacle, Figure 3.31, all cases demonstrate a degree of cross-stream flow activity, with the magnitude decreasing with higher flow velocities. Furthermore, the cross-stream flow in the far wake region acts to push the flow towards the side walls.

The mean streamwise profiles, as shown in Figure 3.32, continue the established trend wherein the results become smoother as the Reynolds number is increased. Additionally, for this obstacle the results also fail to locate the recirculation point accurately, whilst for the other obstacles irrespective of resolution the location of the recirculation was well defined, for the fractal obstacle as the resolution is increased the minima of the profile also changes without a clear convergence at higher resolutions. However, as shown in the experimental data and

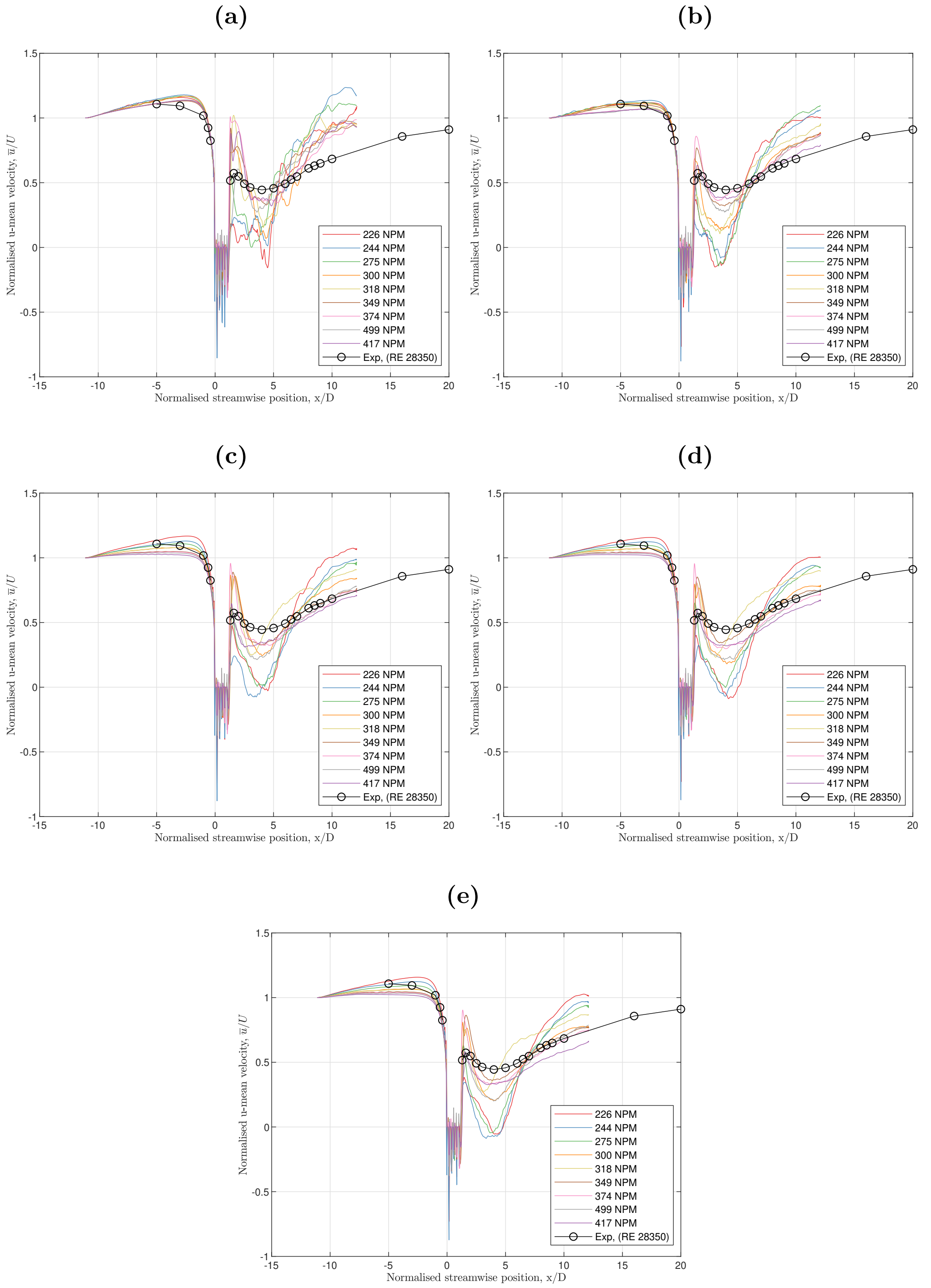

Figure 3.27: Normalised mean streamwise velocity profiles along the centreline of the Z-normal plane, with MRT dynamics. Porous regular obstacle at (a) $Re_D = 2470$ (Case III) (b) $Re_D = 12352$ (Case IV) (c) $Re_D = 24705$ (Case V) (d) $Re_D = 37057$ (Case VI) (e) $Re_D = 49410$ (Case VII)

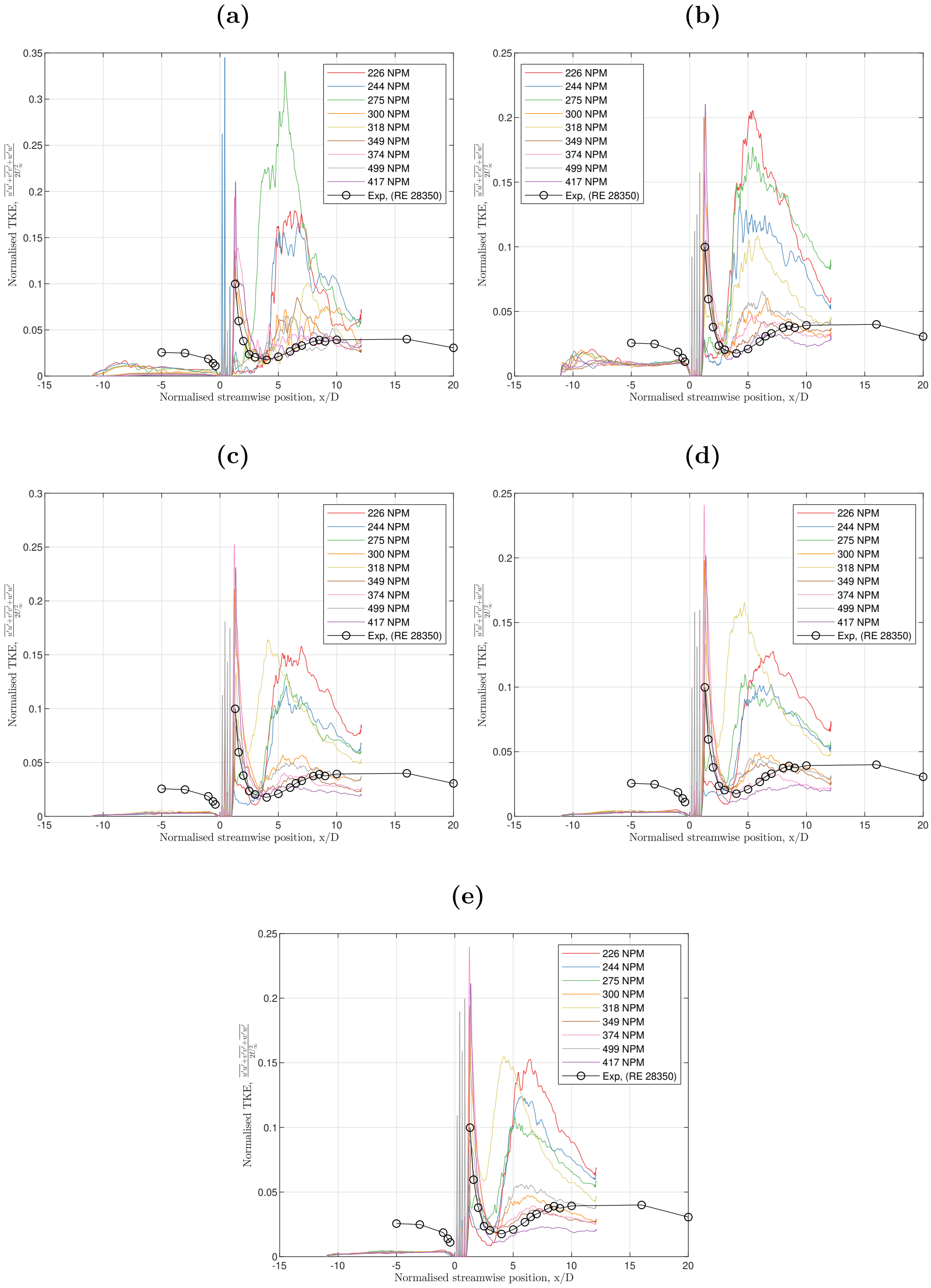

Figure 3.28: Normalised turbulent kinetic energy profiles along the centreline of the Z-normal plane, with MRT dynamics. Porous regular obstacle at (a) $Re_D = 2470$ (Case III) (b) $Re_D = 12352$ (Case IV) (c) $Re_D = 24705$ (Case V) (d) $Re_D = 37057$ (Case VI) (e) $Re_D = 49410$ (Case VII)

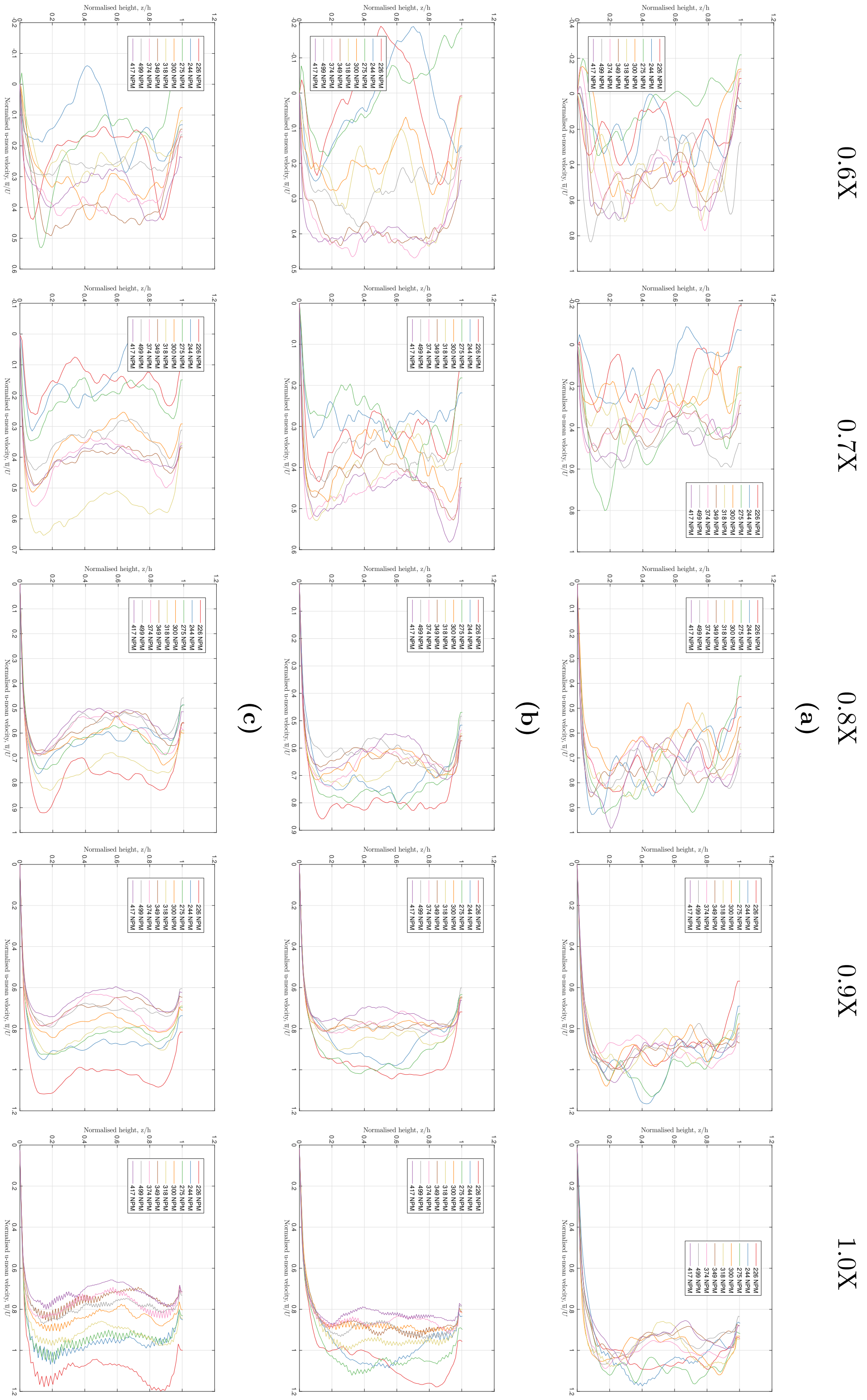
0.6X
0.7X
0.8X
0.9X
1.0X
(a)
(b)
(c)
Normalised height, z/h
Normalised u-mean velocity, $\overline{u}/U$
226 NPM
244 NPM
275 NPM
300 NPM
318 NPM
349 NPM
374 NPM
499 NPM
417 NPM

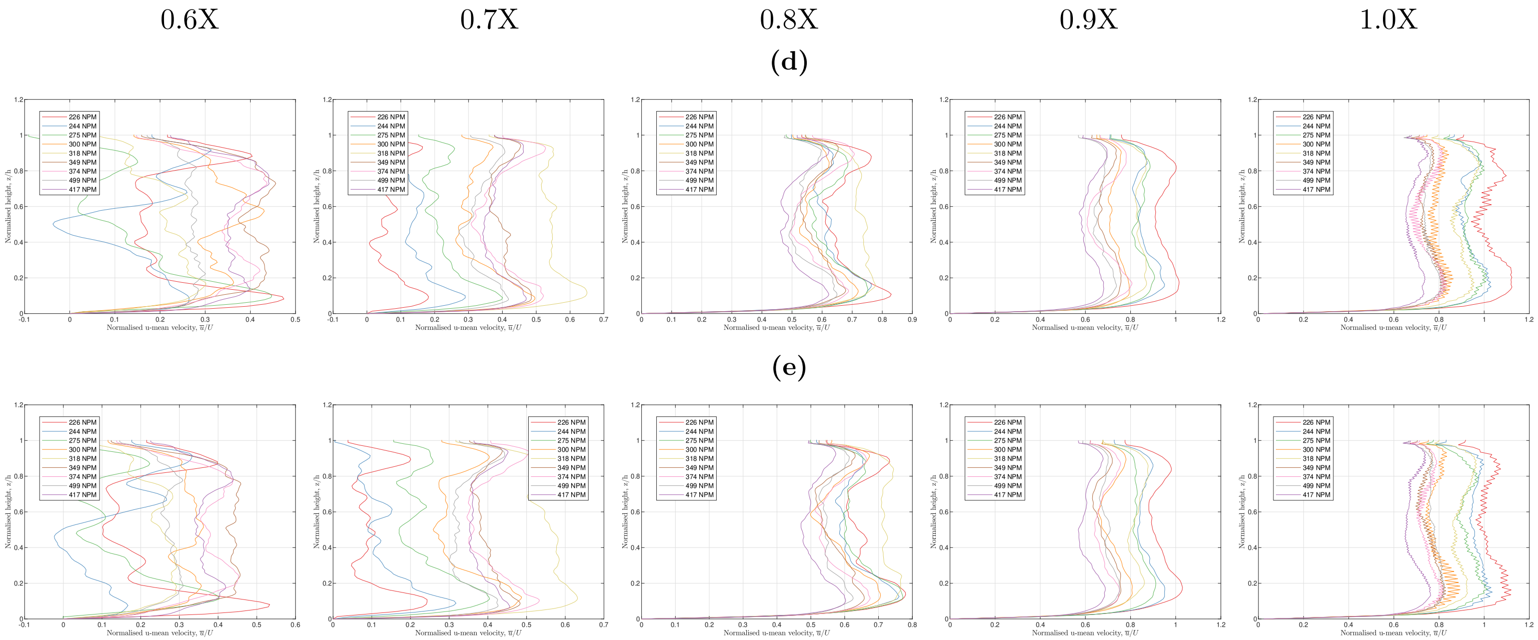

Figure 3.29: Normalised mean streamwise velocity profiles at varying positions in the channel (60%, 70%, 80%, 90%, 100% channel length) of the Y-normal plane, with MRT dynamics. Porous regular obstacle at (a) $Re_D = 2470$ (Case III) (b) $Re_D = 12352$ (Case IV) (c) $Re_D = 24705$ (Case V) (d) $Re_D = 37057$ (Case VI) (e) $Re_D = 49410$ (Case VII)

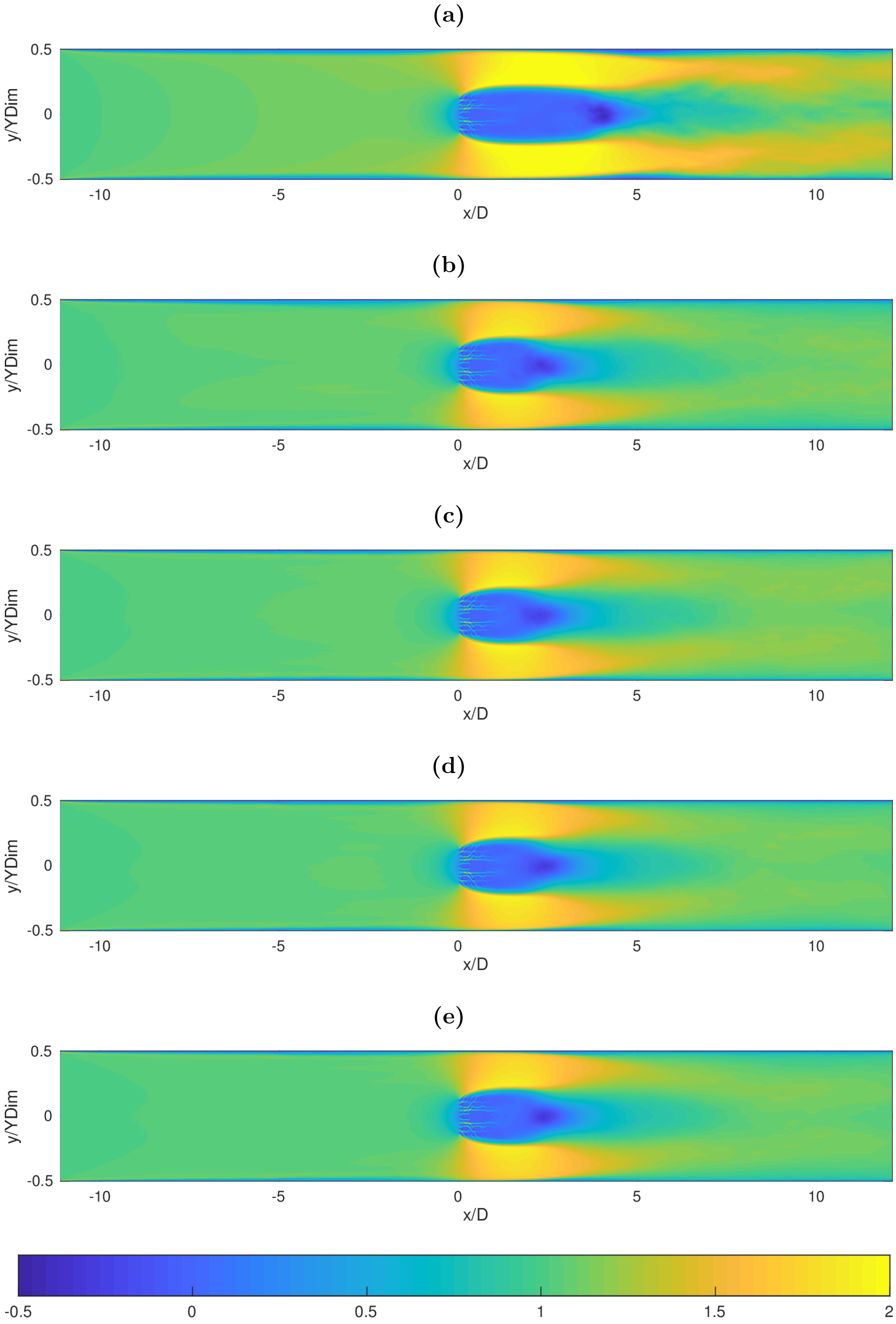

Figure 3.30: Normalised mean streamwise velocity maps, $\overline{u}/U_\infty$, of the Z-normal plane at 40% flow depth from the channel floor with MRT dynamics and a resolution of 417 NPM. Porous fractal obstacle at (a) $Re_D = 2470$ (Case III) (b) $Re_D = 12352$ (Case IV) (c) $Re_D = 24705$ (Case V) (d) $Re_D = 37057$ (Case VI) (e) $Re_D = 49410$ (Case VII)

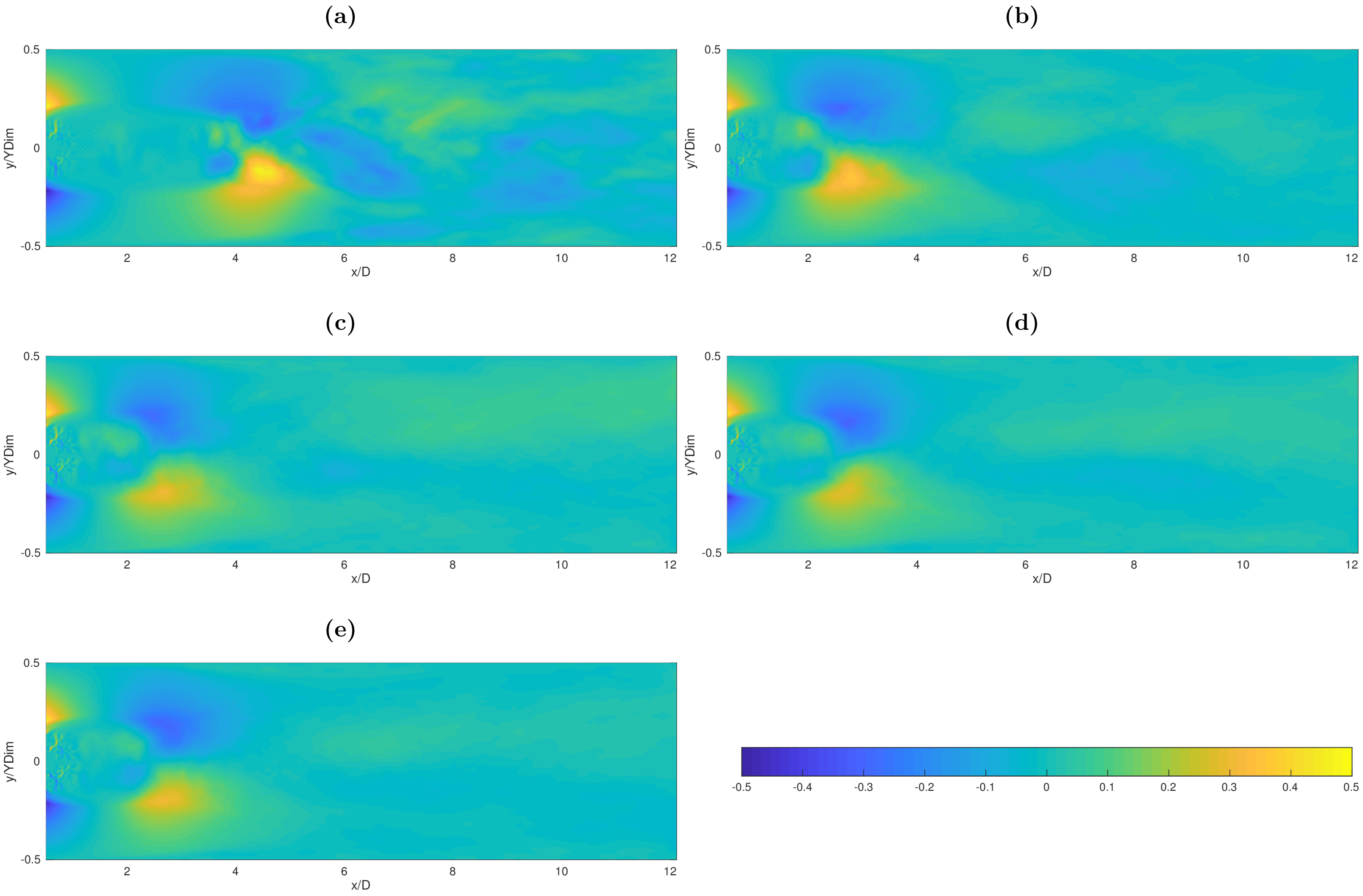

Figure 3.31: Normalised mean cross-stream velocity maps, $\overline{v}/U_{\infty}$, of the Z-normal plane at 40% flow depth from the channel floor with MRT dynamics and a resolution of 417 NPM. Porous fractal obstacle at (a) $Re_D = 2470$ (Case III) (b) $Re_D = 12352$ (Case IV) (c) $Re_D = 24705$ (Case V) (d) $Re_D = 37057$ (Case VI) (e) $Re_D = 49410$ (Case VII)

the mean velocity maps the flow immediately after the obstacle is slightly accelerated before decelerating into the recirculation zone. This behaviour is captured momentarily in cases V-VII at 374 NPM but subsequent meshes fail to capture this. Overall, the general trend and shape of the experimental profile is replicated by the numerical results, but the differences between individual resolution cases are cause for further analysis.

The TKE profiles of Figure 3.33 show significant agreement between the experimental and numerical results in the far wake region. Again, due to undersampling of the near wake region the experimental profile fails to accurately identify the peak TKE.

For the vertical profiles, Figure 3.34, downstream of the obstacles all cases fail to recover to a fully developed turbulent profile instead remaining as a shear profile.

3.3 Mass Flowrate

An inviolable law in physical systems is that of mass conservation. This principle can be checked by calculating the mass flowrate of the three X normal planes, at 25%, 50% and 75% of the channel length. The results presented are of cases corresponding to 417 NPM resolution, MRT dynamics and no sponge zone.

3.3.1 Solid Square Obstacle

Figure 3.35 shows the mass flowrates for the tree velocity components as a time signal for each plane. What immediately becomes clear is that the mass flowrate is not constant instead it fluctuates over time, of which both the frequency and amplitude of the oscillations increase as the Reynolds number is increased. Both the transverse and vertical components show a near zero average mass flowrate over the recorded period, this meaning that the entire flow is being driven in the streamwise direction. For case III it is clear that as the flow travels down the channel, the streamwise mass flowrate increases. Case IV also stands out in that the streamwise mass flowrate appears to be constant at all three locations indicating that the obstacle has little to no effect on the streamwise flow. The remaining cases, V-VII, show a more appropriate evolution wherein after the obstacle the flow has decelerated in the streamwise direction and there is increased activity in the transverse and vertical directions.

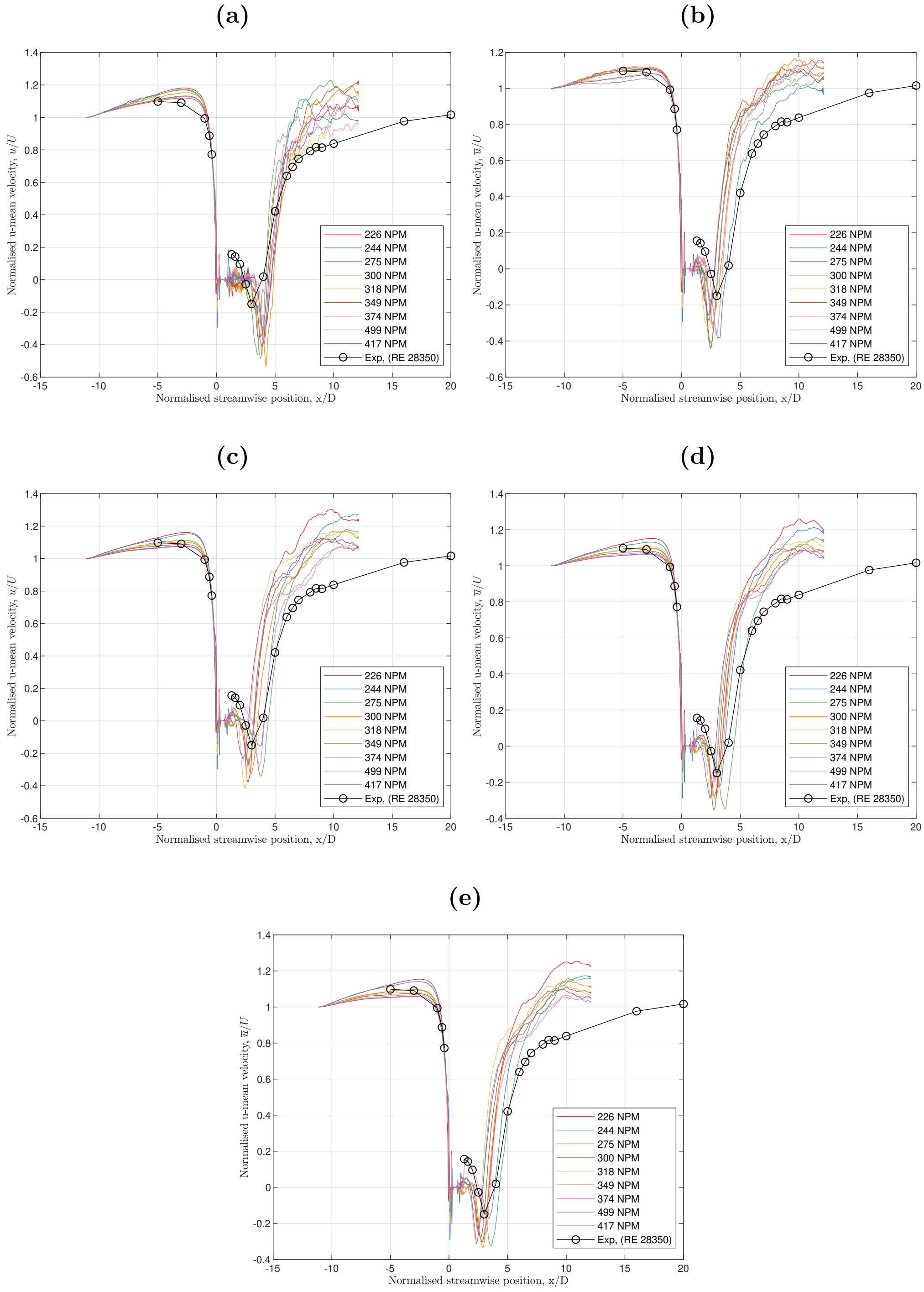
(a) **(b)** **(c)** **(d)** **(e)**

Figure 3.32: Normalised mean streamwise velocity profiles along the centreline of the Z-normal plane, with MRT dynamics. Porous fractal obstacle at (a) $Re_D = 2470$ (Case III) (b) $Re_D = 12352$ (Case IV) (c) $Re_D = 24705$ (Case V) (d) $Re_D = 37057$ (Case VI) (e) $Re_D = 49410$ (Case VII)

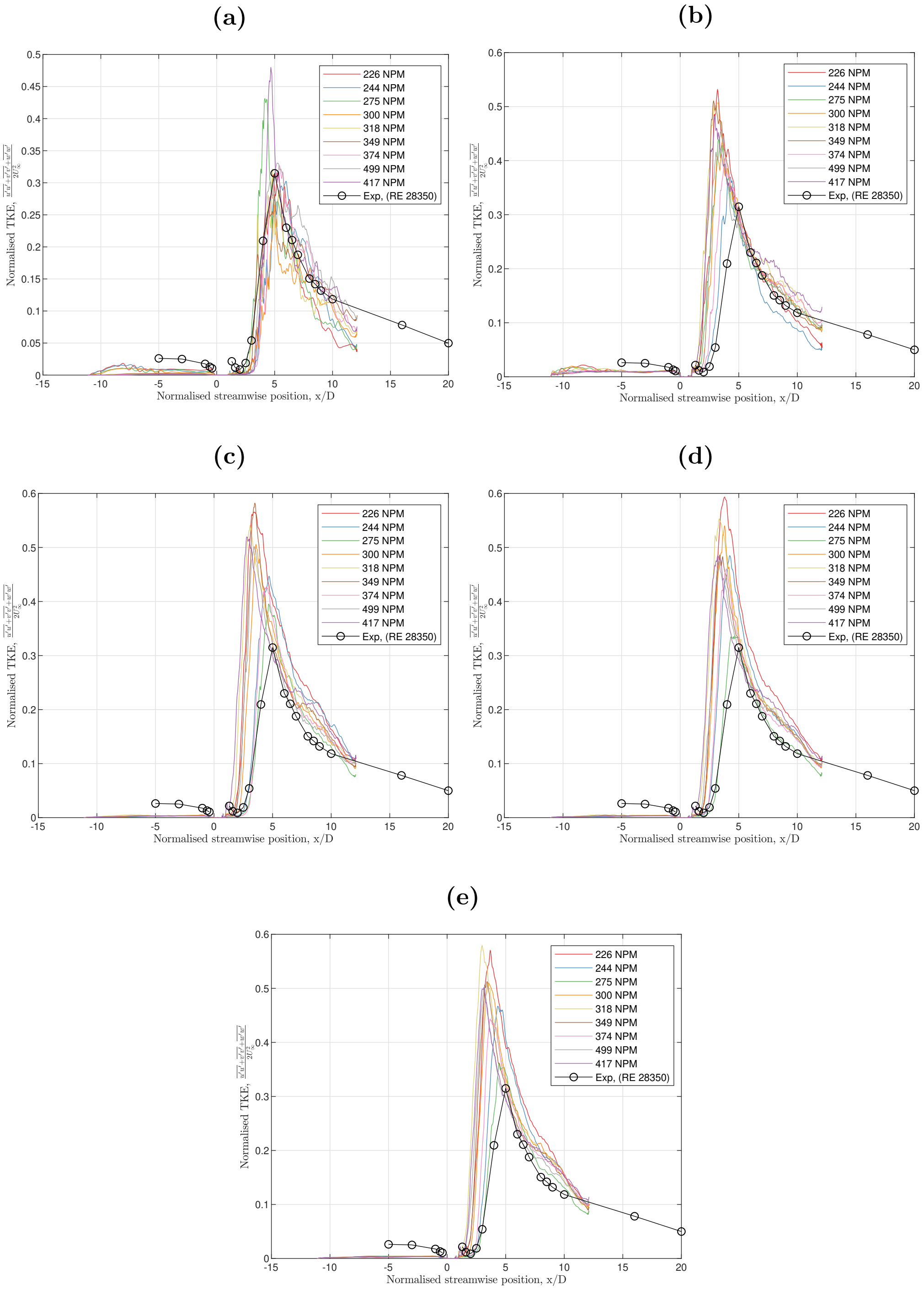

Figure 3.33: Normalised turbulent kinetic energy profiles along the centreline of the Z-normal plane, with MRT dynamics. Porous fractal obstacle at (a) $Re_D = 2470$ (Case III) (b) $Re_D = 12352$ (Case IV) (c) $Re_D = 24705$ (Case V) (d) $Re_D = 37057$ (Case VI) (e) $Re_D = 49410$ (Case VII)

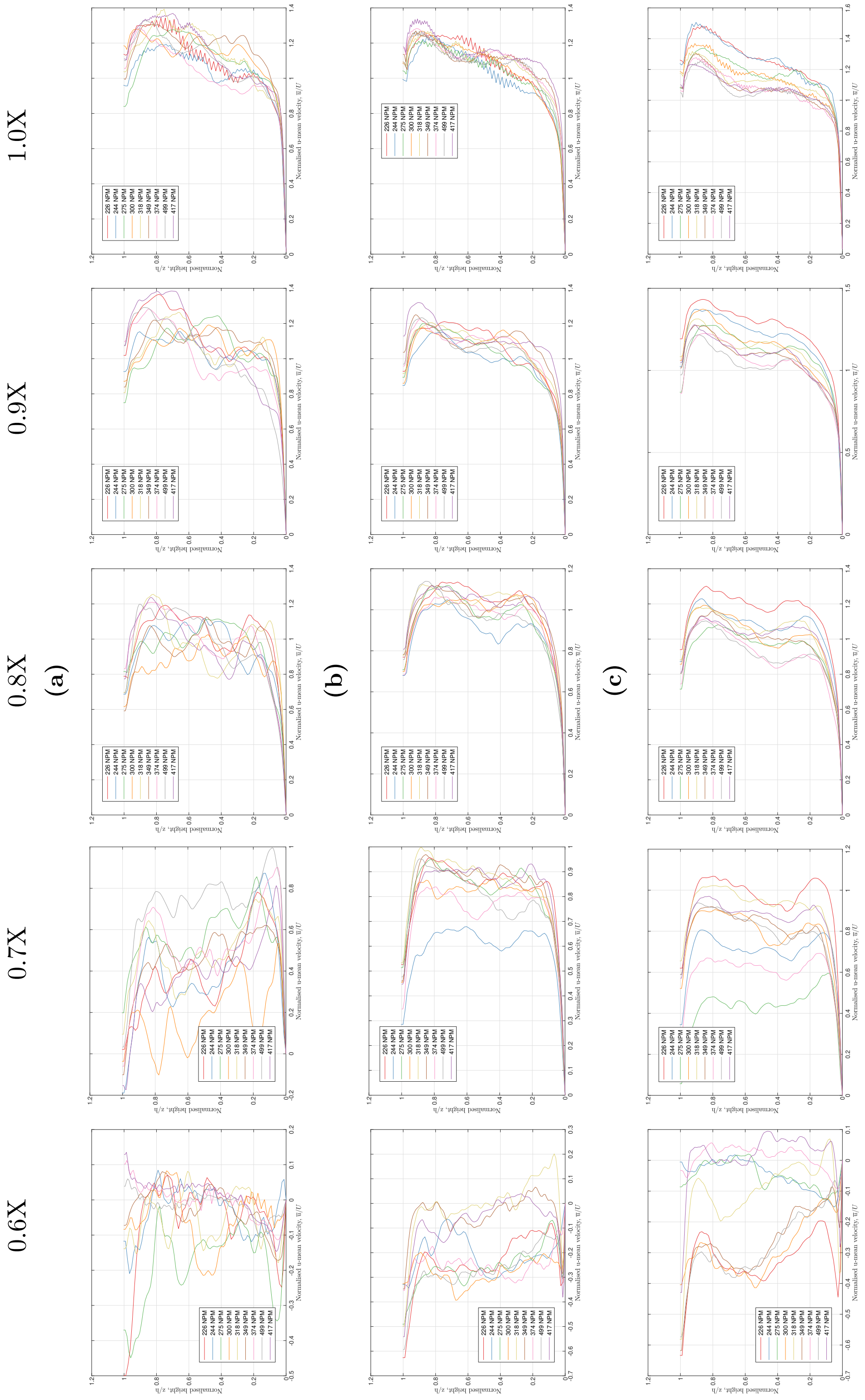
1.0X
0.9X
0.8X
0.7X
0.6X
(a)
(b)
(c)
226 NPM
244 NPM
275 NPM
300 NPM
318 NPM
349 NPM
374 NPM
499 NPM
417 NPM
Normalised height, z/h
Normalised u-mean velocity, ū/U

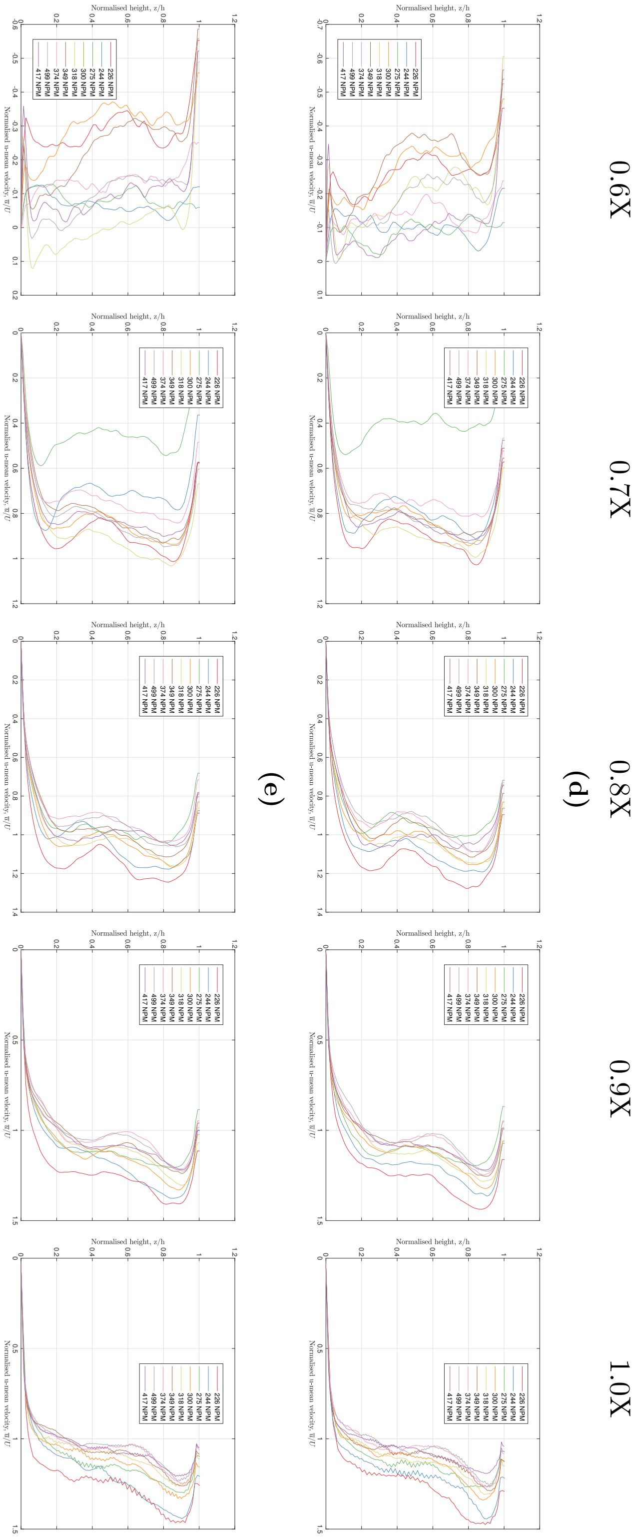

Figure 3.34: Normalised mean streamwise velocity profiles at varying positions in the channel (60%, 70%, 80%, 90%, 100% channel length) of the Y-normal plane, with MRT dynamics. Porous fractal obstacle at (a) $Re_D = 2470$ (Case III) (b) $Re_D = 12352$ (Case IV) (c) $Re_D = 24705$ (Case V) (d) $Re_D = 37057$ (Case VI) (e) $Re_D = 49410$ (Case VII)

Table 3.3: Mean and signal frequencies (f, Hz) for mass flowrate (MFR, kg/s) of solid square obstacle.

Re_D		U		V		W	
		MFR	f	MFR	f	MFR	f
2470	0.25X	3.00	0.05	0.00	0.04	0.01	0.54
	0.50X	3.11	0.05	-0.01	0.04	-0.02	0.02
	0.75X	3.21	0.02	-0.13	0.04	0.02	0.06
12352	0.25X	14.54	0.20	-0.01	0.15	0.03	0.22
	0.50X	14.66	0.02	0.02	0.15	-0.11	0.02
	0.75X	14.65	0.02	0.03	0.15	0.17	0.28
24705	0.25X	28.33	0.16	0.00	1.04	0.01	1.73
	0.50X	28.42	0.16	0.03	1.04	-0.09	0.26
	0.75X	27.26	0.02	-0.03	0.31	0.09	0.56
37057	0.25X	42.30	0.21	0.00	1.43	0.02	2.76
	0.50X	42.20	0.06	0.06	1.43	-0.10	0.34
	0.75X	40.30	0.06	-0.01	0.45	0.11	0.34
49410	0.25X	56.32	0.28	0.00	1.95	0.03	0.18
	0.50X	56.11	0.28	0.08	1.95	-0.14	0.34
	0.75X	53.54	0.28	-0.04	0.71	0.18	1.12

Mean flowrates and signal frequencies can be seen in Table 3.3

3.3.2 Porous Regular Obstacle

With the regular obstacle, Figure 3.36, the same signal frequency and amplitude trend is observed. However, in the vertical direction there is a noticeable loss of energy at 0.5X, whilst the prior and latter locations both show an average near zero the 0.5X location has a sustained negative average mass flowrate vertically. In the transverse direction prior to and at the obstacle there is effectively no transversal motion only after the obstacle is the fluid moving in this direction. Along the streamwise direction the same observations as for the square obstacles can be made for cases II and IV. However, cases V-VII, at 0.50X the flowrate has slowed down noticeably from the 0.25X and then it further decelerates by the time it arrives at 0.75X.

Mean flowrates and signal frequencies can be seen in Table 3.4

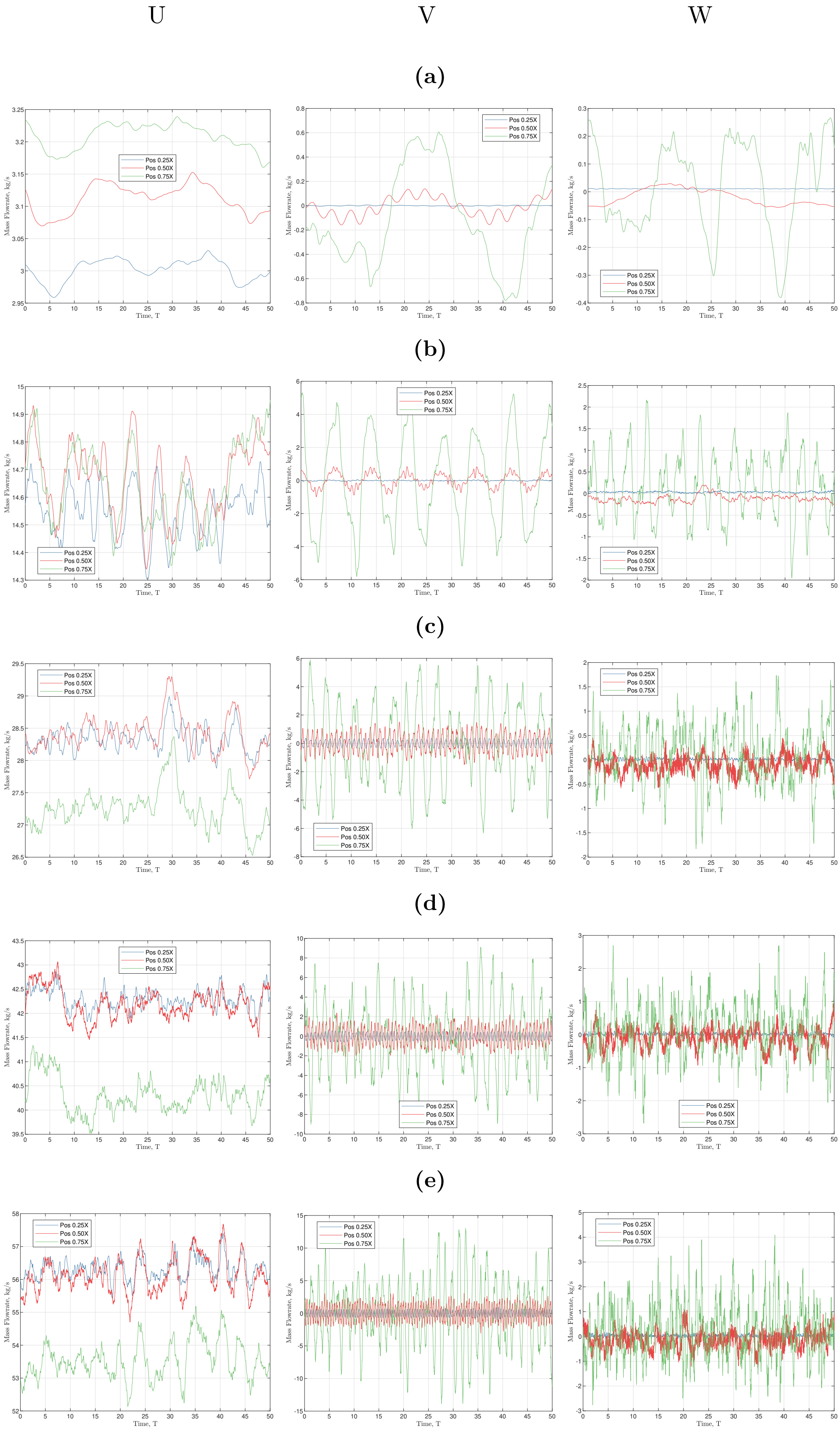

Figure 3.35: Mass flowrate evolution at different locations (0.25X, 0.50X and 0.75X) in the channel for the three velocity components (U - streamwise, V - transversal, W - vertical), with MRT dynamics. Solid square obstacle at (a) $Re_D = 2470$ (Case III) (b) $Re_D = 12352$ (Case IV) (c) $Re_D = 24705$ (Case V) (d) $Re_D = 37057$ (Case VI) (e) $Re_D = 49410$ (Case VII)

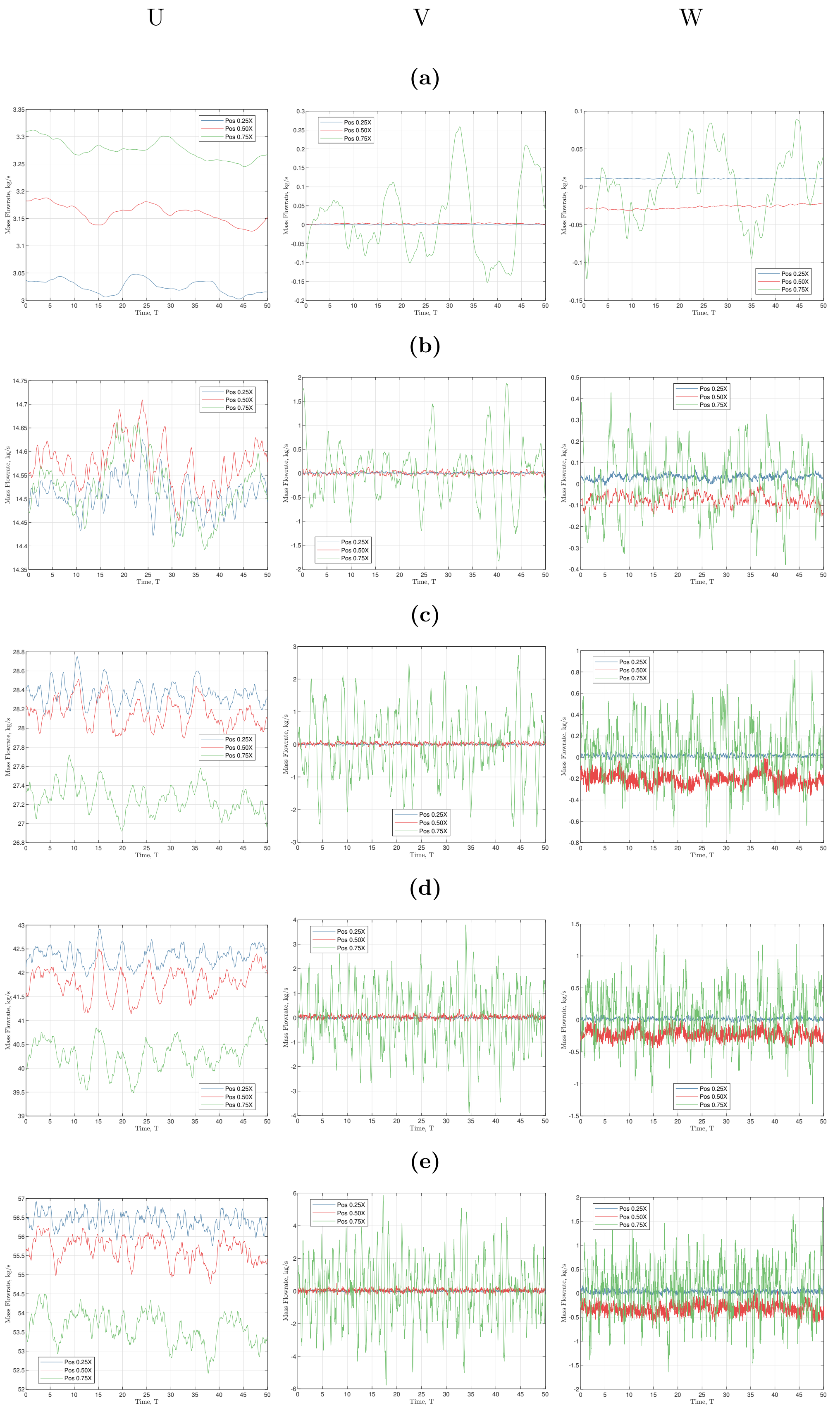

Figure 3.36: Mass flowrate evolution at different locations (0.25X, 0.50X and 0.75X) in the channel for the three velocity components (U - streamwise, V - transversal, W - vertical), with MRT dynamics. Porous regular obstacle at (a) $Re_D = 2470$ (Case III) (b) $Re_D = 12352$ (Case IV) (c) $Re_D = 24705$ (Case V) (d) $Re_D = 37057$ (Case VI) (e) $Re_D = 49410$ (Case VII)

Table 3.4: Mean and signal frequencies (f, Hz) for mass flowrate (MFR, kg/s) of porous regular obstacle.

Re_D		U		V		W	
		MFR	f	MFR	f	MFR	f
2470	0.25X	3.03	0.06	0.00	0.34	0.01	0.43
	0.50X	3.16	0.04	0.00	0.34	-0.03	0.01
	0.75X	3.28	0.04	0.01	0.07	0.00	0.04
12352	0.25X	14.51	0.04	0.01	0.06	0.03	0.04
	0.50X	14.58	0.04	0.00	0.15	-0.07	0.06
	0.75X	14.52	0.04	0.02	0.27	0.01	0.15
24705	0.25X	28.36	0.33	0.00	1.14	0.02	1.73
	0.50X	28.15	0.15	0.02	0.40	-0.21	0.04
	0.75X	27.27	0.13	-0.01	0.45	0.05	0.57
37057	0.25X	42.34	0.18	0.00	1.55	0.02	2.43
	0.50X	41.81	0.18	0.03	0.31	-0.22	0.11
	0.75X	40.29	0.18	0.02	0.45	0.06	0.26
49410	0.25X	56.42	0.12	0.00	2.08	0.04	0.18
	0.50X	55.67	0.12	0.04	0.35	-0.32	0.02
	0.75X	53.62	0.01	0.00	0.71	0.07	0.56

3.3.3 Porous Fractal Obstacle

For the cases ran with a fractal obstacle, both the transverse and vertical directions show similar behaviour described for the regular obstacle. The distinct change in the established pattern occurs in the streamwise direction. In this direction, for cases IV-VII, both the 0.50X and 0.75X locations show an increased mass flowrate, though as the Reynolds number is increased the difference is lessened.

Mean flowrates and signal frequencies can be seen in Table 3.5

3.4 Strouhal Number

In addition to the temporal analysis, exposed in the previous section, a frequency analysis was conducted. This consisted in identifying the dominant frequency via a Fourier analysis of each velocity signal at every node in the domain, then the Strouhal number can be computed using the equation,

$$St = \frac{\zeta D}{U_\infty}$$

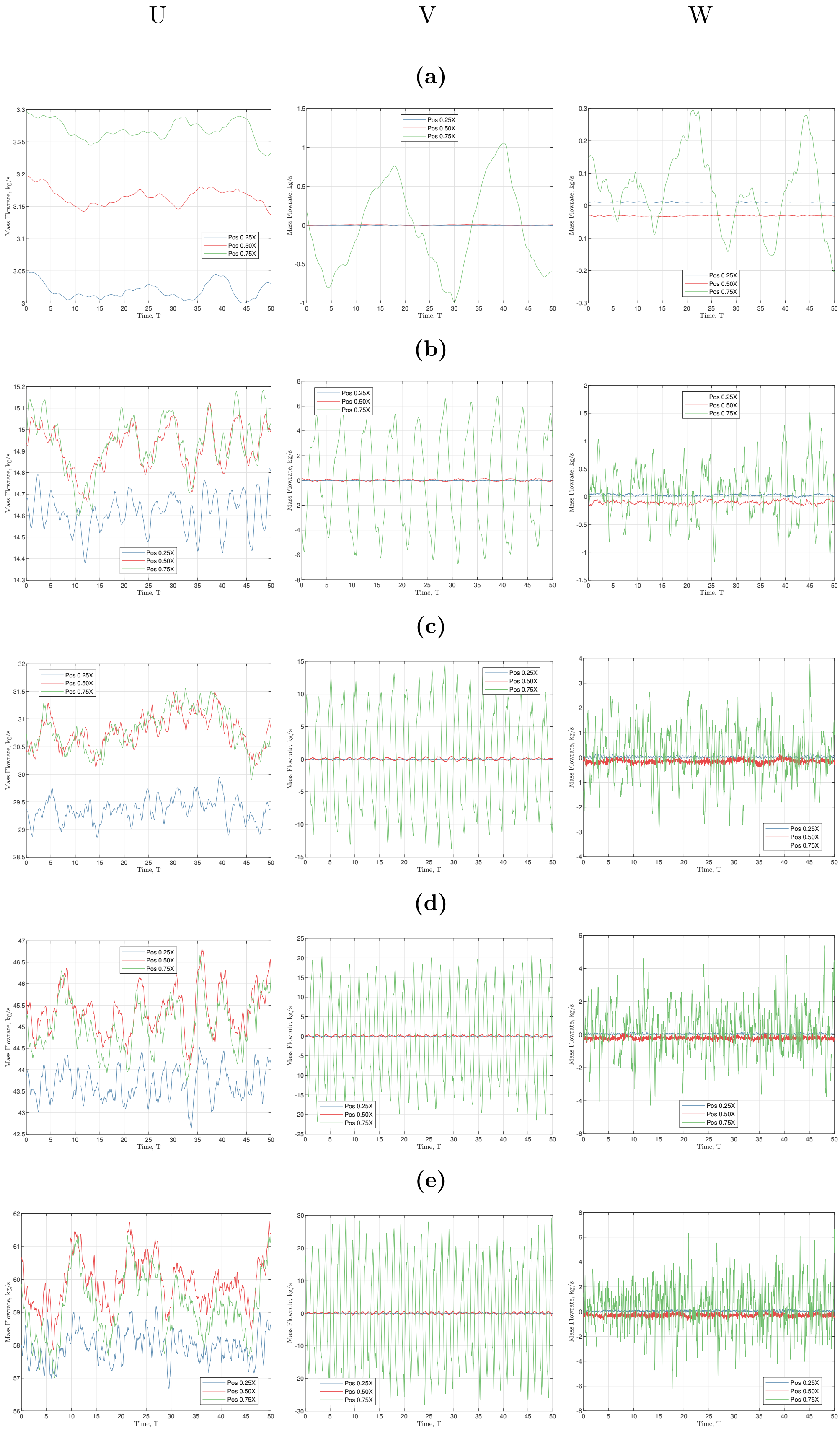

Figure 3.37: Mass flowrate evolution at different locations (0.25X, 0.50X and 0.75X) in the channel for the three velocity components (U - streamwise, V - transversal, W - vertical), with MRT dynamics. Porous fractal obstacle at (a) $Re_D = 2470$ (Case III) (b) $Re_D = 12352$ (Case IV) (c) $Re_D = 24705$ (Case V) (d) $Re_D = 37057$ (Case VI) (e) $Re_D = 49410$ (Case VII)

Table 3.5: Mean and signal frequencies (f, Hz) for mass flowrate (MFR, kg/s) of porous fractal obstacle.

Re_D		U		V		W	
		MFR	f	MFR	f	MFR	f
2470	0.25X	3.02	0.09	0.00	0.32	0.01	0.44
	0.50X	3.17	0.05	0.00	0.05	-0.03	0.05
	0.75X	3.27	0.02	-0.06	0.05	0.05	0.09
12352	0.25X	14.61	0.38	0.00	0.29	0.03	0.04
	0.50X	14.92	0.05	0.02	0.20	-0.10	0.09
	0.75X	14.94	0.05	0.05	0.20	0.10	0.38
24705	0.25X	29.36	0.02	0.00	1.25	0.03	1.77
	0.50X	30.78	0.02	0.03	0.39	-0.15	0.12
	0.75X	30.80	0.02	-0.05	0.39	0.18	0.78
37057	0.25X	43.68	0.22	0.00	1.56	0.04	2.66
	0.50X	45.36	0.17	0.06	0.54	-0.20	0.18
	0.75X	45.03	0.07	0.03	0.54	0.25	1.09
49410	0.25X	57.96	0.07	0.00	2.33	0.05	3.21
	0.50X	59.90	0.07	0.07	0.72	-0.28	0.11
	0.75X	59.19	0.07	0.02	0.72	0.32	1.44

Strouhal number values will be presented only for the finest mesh scenario using MRT dynamics and no sponge zone.

3.4.1 Solid Square Obstacle

See Figure 3.38 and Figure 3.39.

3.4.2 Porous Regular Obstacle

See Figure 3.40 and Figure 3.41.

3.4.3 Porous Fractal Obstacle

See Figure 3.42 and Figure 3.43.

3.5 Outlet Sensitivity

As demonstrated, by the lack of recovery to a fully developed profile in the regular and fractal cases it calls into question whether the choice to use a 1.5m

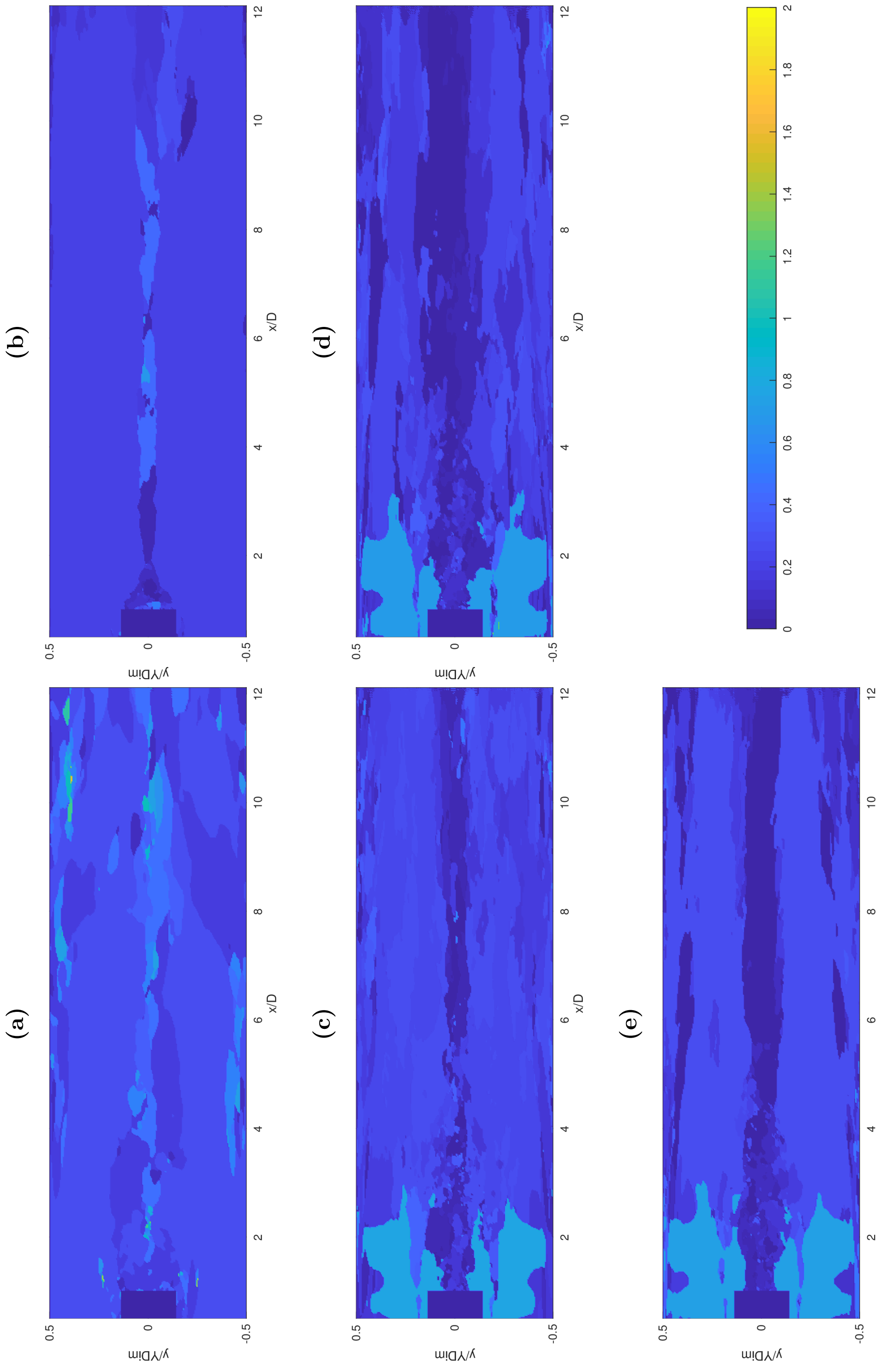

Figure 3.38: Strouhal number, St, maps of the Z-normal plane at 40% flow depth from the channel floor with MRT dynamics and a resolution of 417 NPM. Solid square obstacle at (a) $Re_D = 2470$ (Case III) (b) $Re_D = 12352$ (Case IV) (c) $Re_D = 24705$ (Case V) (d) $Re_D = 37057$ (Case VI) (e) $Re_D = 49410$ (Case VII) . Domain cropped to show only downstream area.

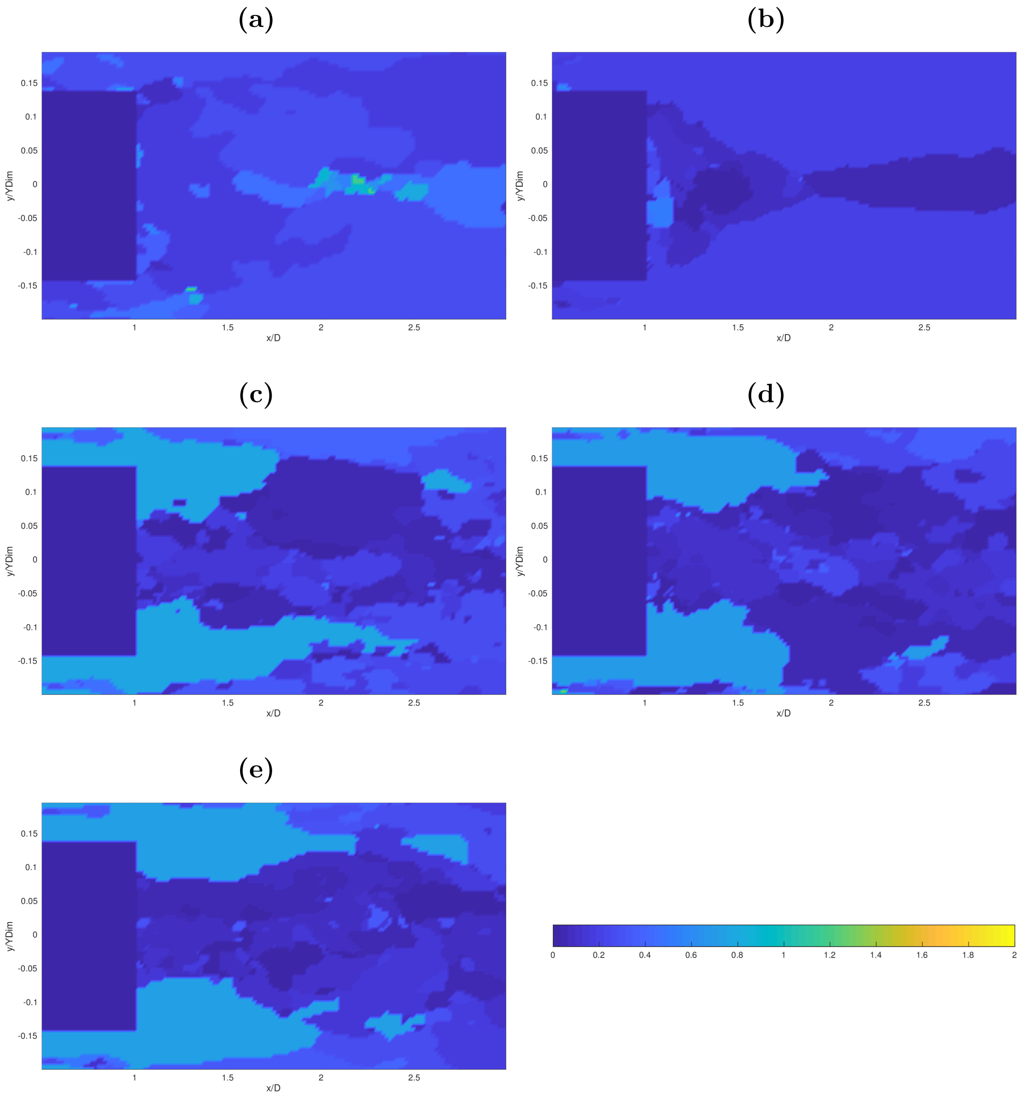

Figure 3.39: Strouhal number, St, maps of the Z-normal plane at 40% flow depth from the channel floor with MRT dynamics and a resolution of 417 NPM. Solid square obstacle at (a) $Re_D = 2470$ (Case III) (b) $Re_D = 12352$ (Case IV) (c) $Re_D = 24705$ (Case V) (d) $Re_D = 37057$ (Case VI) (e) $Re_D = 49410$ (Case VII) . Domain cropped to show area immediately downstream of the obstacle

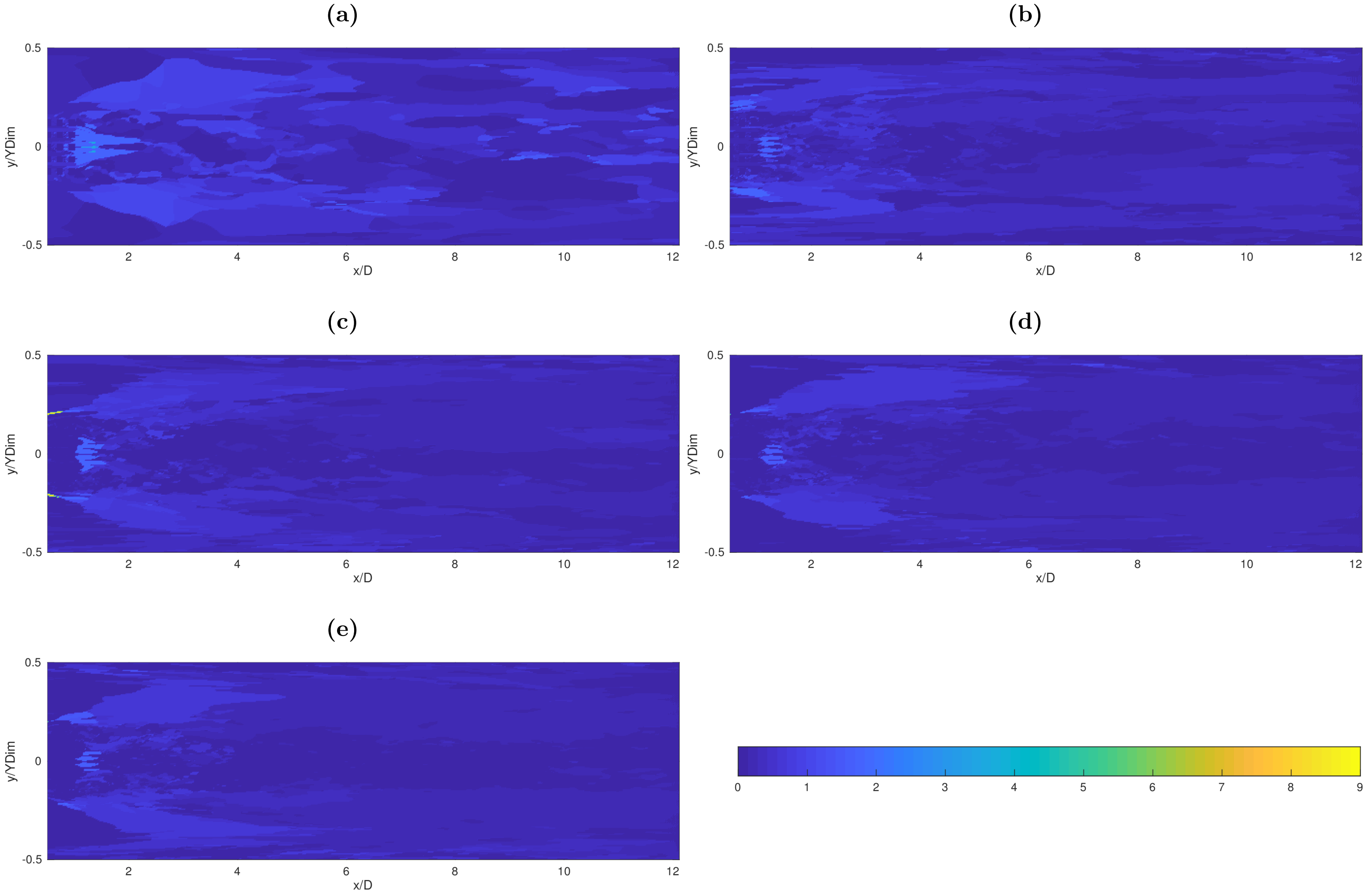

Figure 3.40: Strouhal number, St, maps of the Z-normal plane at 40% flow depth from the channel floor with MRT dynamics and a resolution of 417 NPM. Porous regular obstacle at (a) $Re_D = 2470$ (Case III) (b) $Re_D = 12352$ (Case IV) (c) $Re_D = 24705$ (Case V) (d) $Re_D = 37057$ (Case VI) (e) $Re_D = 49410$ (Case VII) . Domain cropped to show only downstream area.

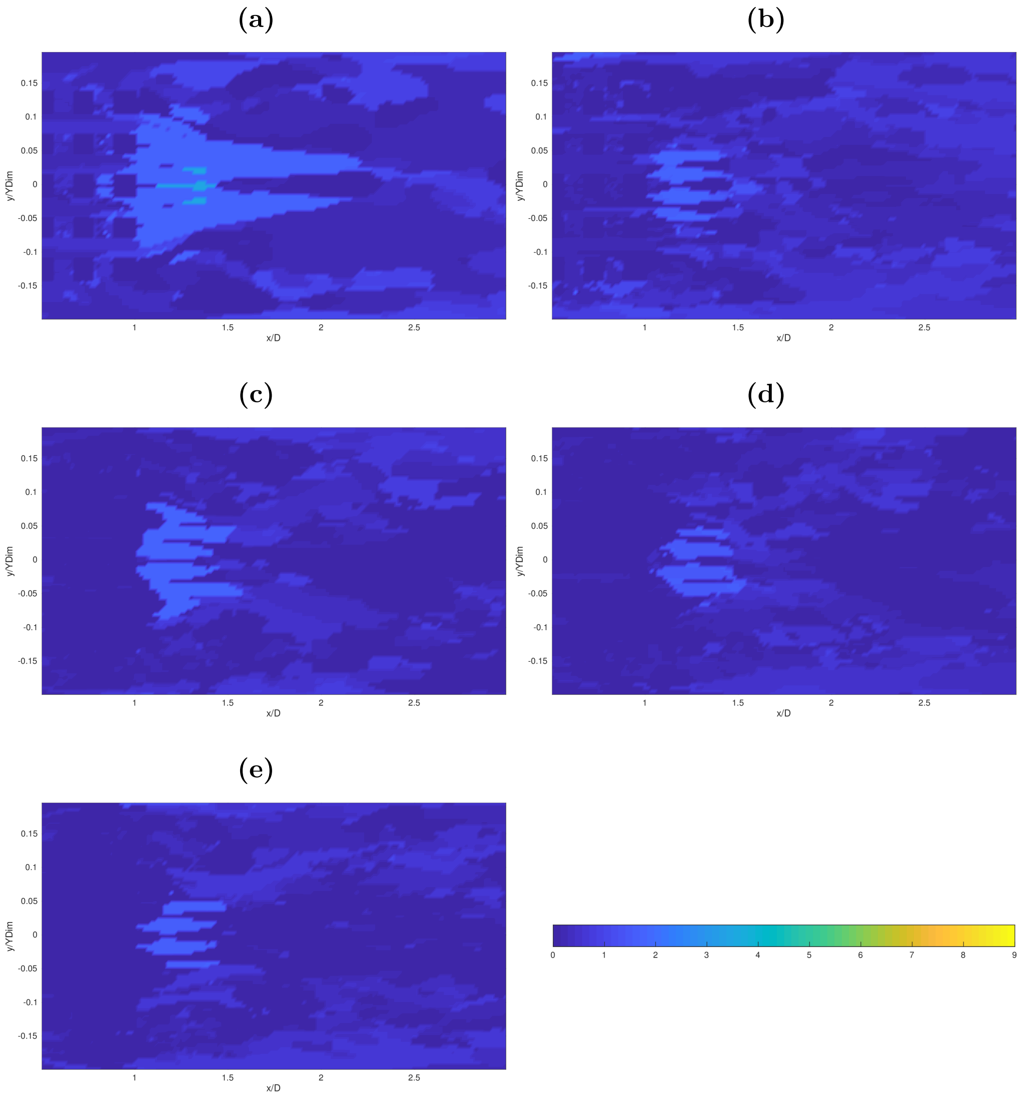

Figure 3.41: Strouhal number, St, maps of the Z-normal plane at 40% flow depth from the channel floor with MRT dynamics and a resolution of 417 NPM. Porous regular obstacle at (a) $Re_D = 2470$ (Case III) (b) $Re_D = 12352$ (Case IV) (c) $Re_D = 24705$ (Case V) (d) $Re_D = 37057$ (Case VI) (e) $Re_D = 49410$ (Case VII) . Domain cropped to show area immediately downstream of the obstacle

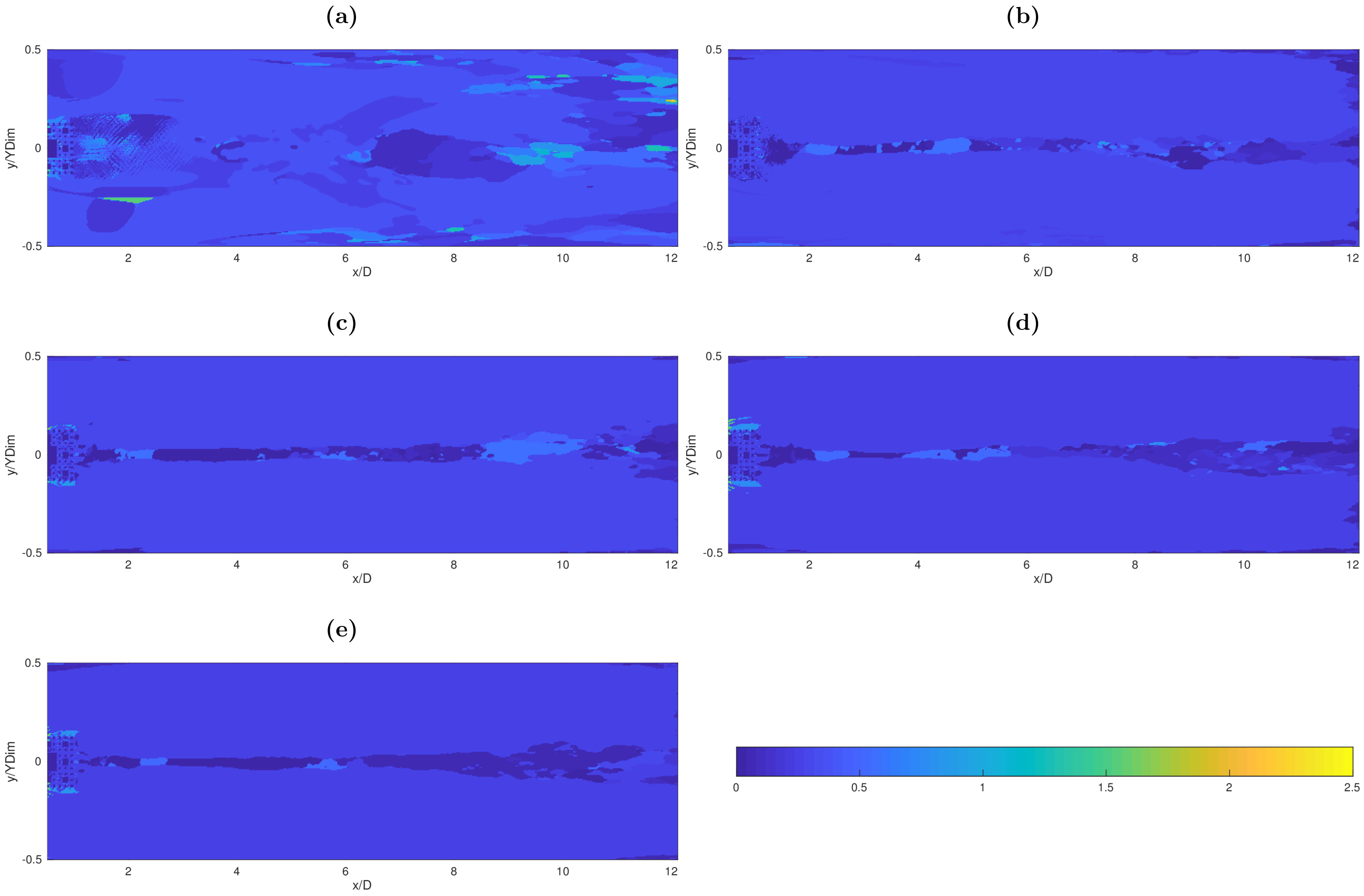

Figure 3.42: Strouhal number, St, maps of the Z-normal plane at 40% flow depth from the channel floor with MRT dynamics and a resolution of 417 NPM. Porous fractal obstacle at (a) $Re_D = 2470$ (Case III) (b) $Re_D = 12352$ (Case IV) (c) $Re_D = 24705$ (Case V) (d) $Re_D = 37057$ (Case VI) (e) $Re_D = 49410$ (Case VII) . Domain cropped to show only downstream area.

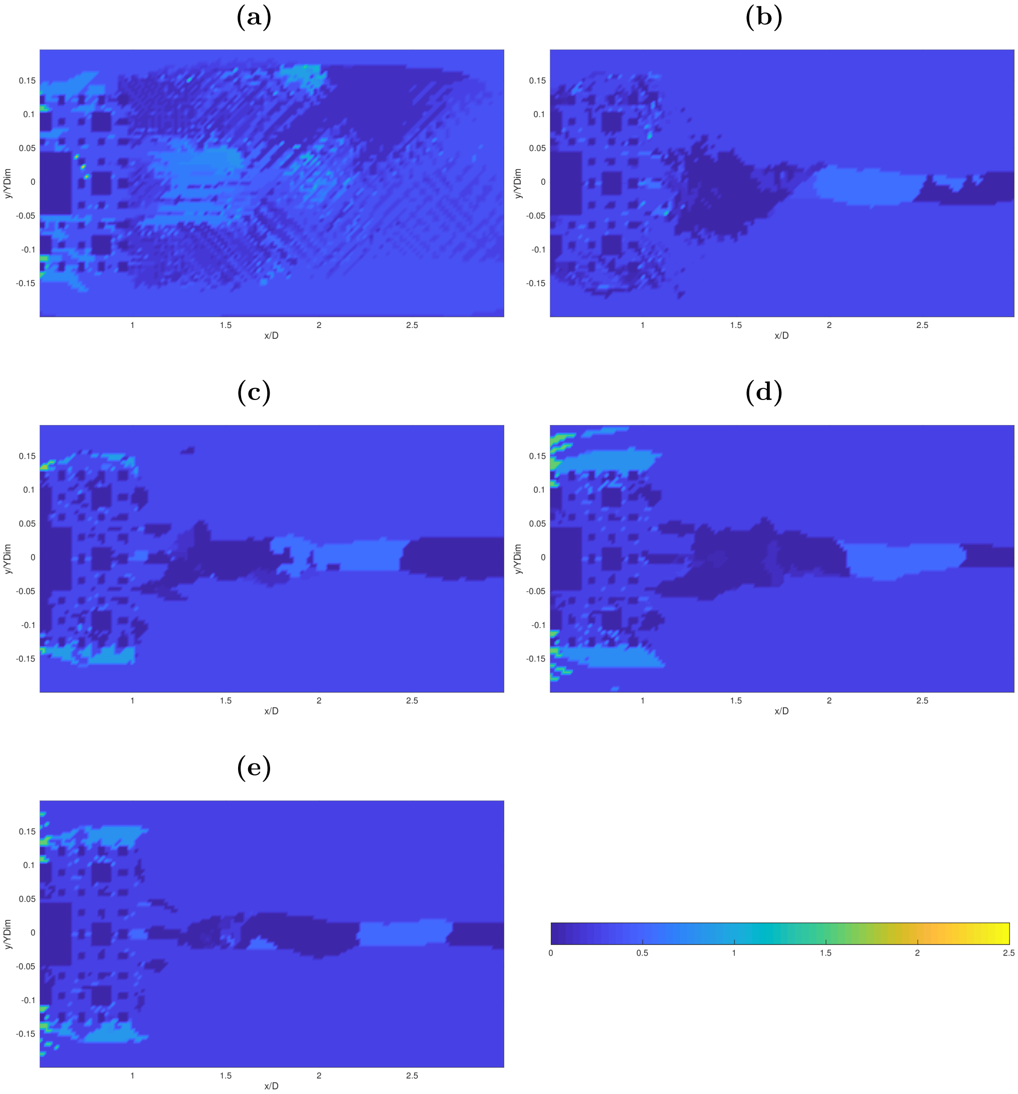

Figure 3.43: Strouhal number, St, maps of the Z-normal plane at 40% flow depth from the channel floor with MRT dynamics and a resolution of 417 NPM. Porous fractal obstacle at (a) $Re_D = 2470$ (Case III) (b) $Re_D = 12352$ (Case IV) (c) $Re_D = 24705$ (Case V) (d) $Re_D = 37057$ (Case VI) (e) $Re_D = 49410$ (Case VII) . Domain cropped to show area immediately downstream of the obstacle

Table 3.6: Domain sizes tested in addition to 1.5m.

Outlet length (m)	1.0	1.1	1.2	1.3	1.4
Obstacle Diameter, D (m)	0.135	0.135	0.135	0.135	0.135
Channel Length, X (m)	2.635	2.735	2.835	2.935	3.035
Channel Width, Y (m)	0.486	0.486	0.486	0.486	0.486
Flow Height, Z (m)	0.326	0.326	0.326	0.326	0.326

Outlet length (m)	1.6	1.7	1.8	1.9	2.0
Obstacle Diameter, D (m)	0.135	0.135	0.135	0.135	0.135
Channel Length, X (m)	3.235	3.335	3.435	3.535	3.635
Channel Width, Y (m)	0.486	0.486	0.486	0.486	0.486
Flow Height, Z (m)	0.326	0.326	0.326	0.326	0.326

downstream channel is sufficient. The initial choice was made in order to balance the available resources because of the uniform mesh required by Palabos, a small increase in the domain size can exponentially increase the total number of nodes, thus requiring more resources to complete. Although an optimum domain length should have been identified prior to running the mesh sensitivity cases, no indication has been made towards a correlation between the mesh density and the domain size. As such an outlet sensitivity analysis was conducted for all the turbulent cases using the coarsest mesh, 226 NPM, and MRT dynamics for all three obstacle types. A list of the additional outlet domain sizes and the relevant simulation parameters are given in Table 3.6.

3.5.1 Solid Square Obstacle

In the solid obstacle case, first observe the mean profiles as shown in Figure 3.44. It is quite clear that changing the outlet length has very little to no effect on the overall numerical result. The only exception being the two shortest domains in cases V-VII, wherein both the near and far wake region are severely affected. Nonetheless, 1.2m outlet length shows sufficient agreement in the mean profiles to be considered a minimum outlet length.

Continuing the streamwise profile observations for the TKE, Figure 3.45, the profiles show once again suitable agreement along the entire profile with outlet lengths greater than 1.2m in all cases.

Given that the size of the outlet domain is variable that changes, to correctly view the evolution of the vertical profile it is best to consider fixed normalised streamwise locations in the domain based on the obstacle diameter, as shown in Figure 3.46. The vertical profiles, serve to further reinforce the observations made for the streamwise profiles, however, only cases V-VII recover to a logarithmic profile, whilst the two slower cases maintain a shear profile.

3.5.2 Porous Regular Obstacle

For the porous regular obstacle a significant effect can be observed in the higher Reynolds cases (cases V-VII), Figure 3.47. Although the near wake region remains unaffected, except in the shortest domain sizes, the far wake region of the profile shows better agreement with outlet lengths of at least 1.8m. Once again the TKE profiles agree with this assessment, Figure 3.48.

With regards to the vertical profiles, Figure 3.49, a clear distinction can once gain be made between cases III-IV and cases V-VII, the slower cases again show a tendency to recover towards a slight shear profile. The faster cases do eventually recover to a logarithmic profile with the longest domain showing the most agreement and the 1.8m and 1.9m cases still showing a slight acceleration near the free surface.

3.5.3 Porous Fractal Obstacle

For the fractal cases both the mean velocity, Figure 3.50, and the TKE, Figure 3.51, again follow the established trend explained previously and similar to the regular case an acceptable minimum outlet length is deemed as 1.8m.

The vertical profiles, Figure 3.52, show that for all cases the flow fails to properly recover at any of the tested domain lengths rather it maintains a constant shear profile.

3.6 Full Domain results

Finally, taking all the results presented into account a singular full domain dataset was produced for each obstacle corresponding to case VII with a resolution of 417 NPM and an outlet length of 1.8m. Flow visualisations are shown in Figure 3.53, Figure 3.54 and Figure 3.55 for all three obstacles.

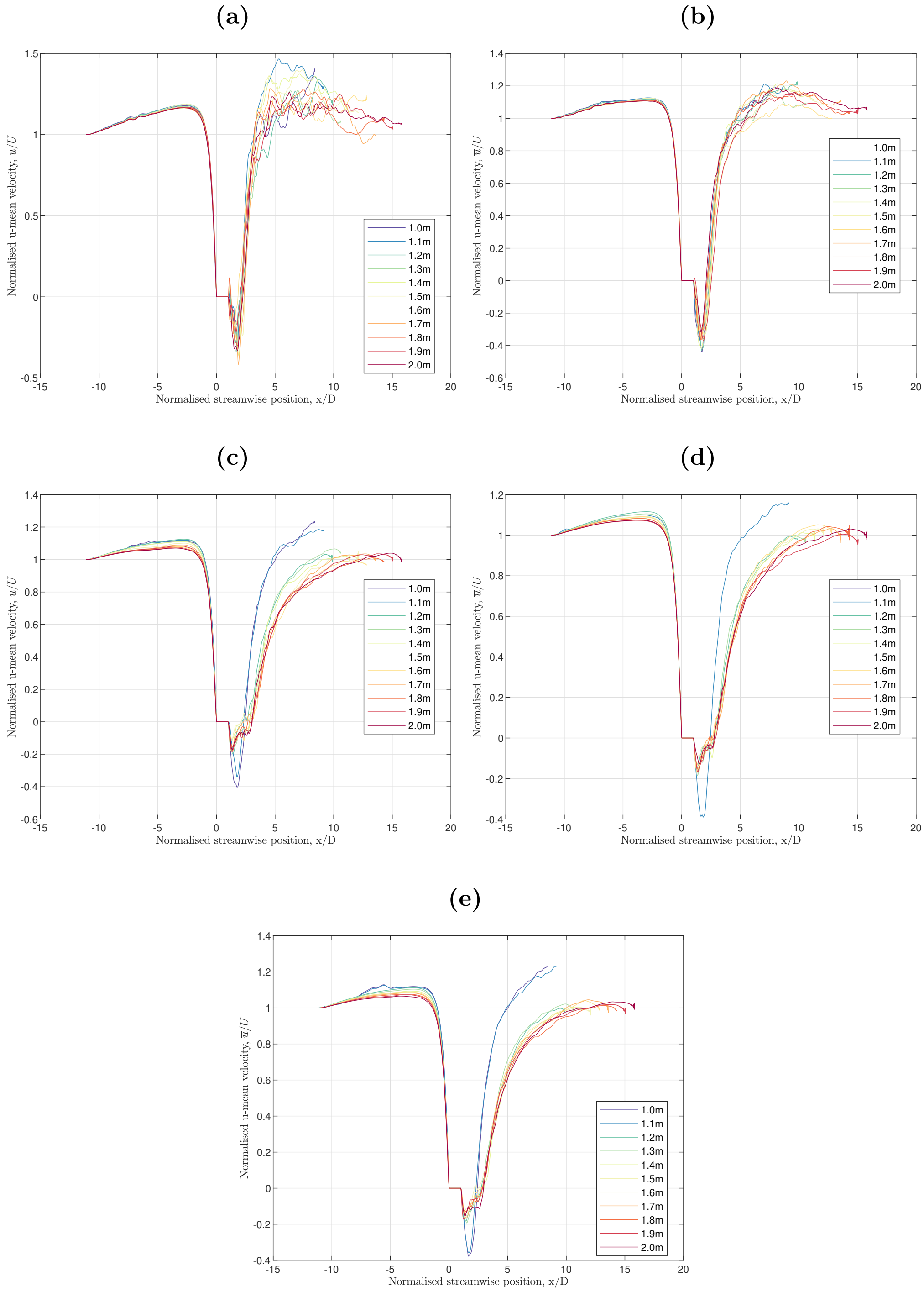

Figure 3.44: Normalised mean streamwise velocity profiles along the centreline of the Z-normal plane for domains with varying outlet lengths, with MRT dynamics. Solid square obstacle at (a) $Re_D = 2470$ (Case III) (b) $Re_D = 12352$ (Case IV) (c) $Re_D = 24705$ (Case V) (d) $Re_D = 37057$ (Case VI) (e) $Re_D = 49410$ (Case VII)

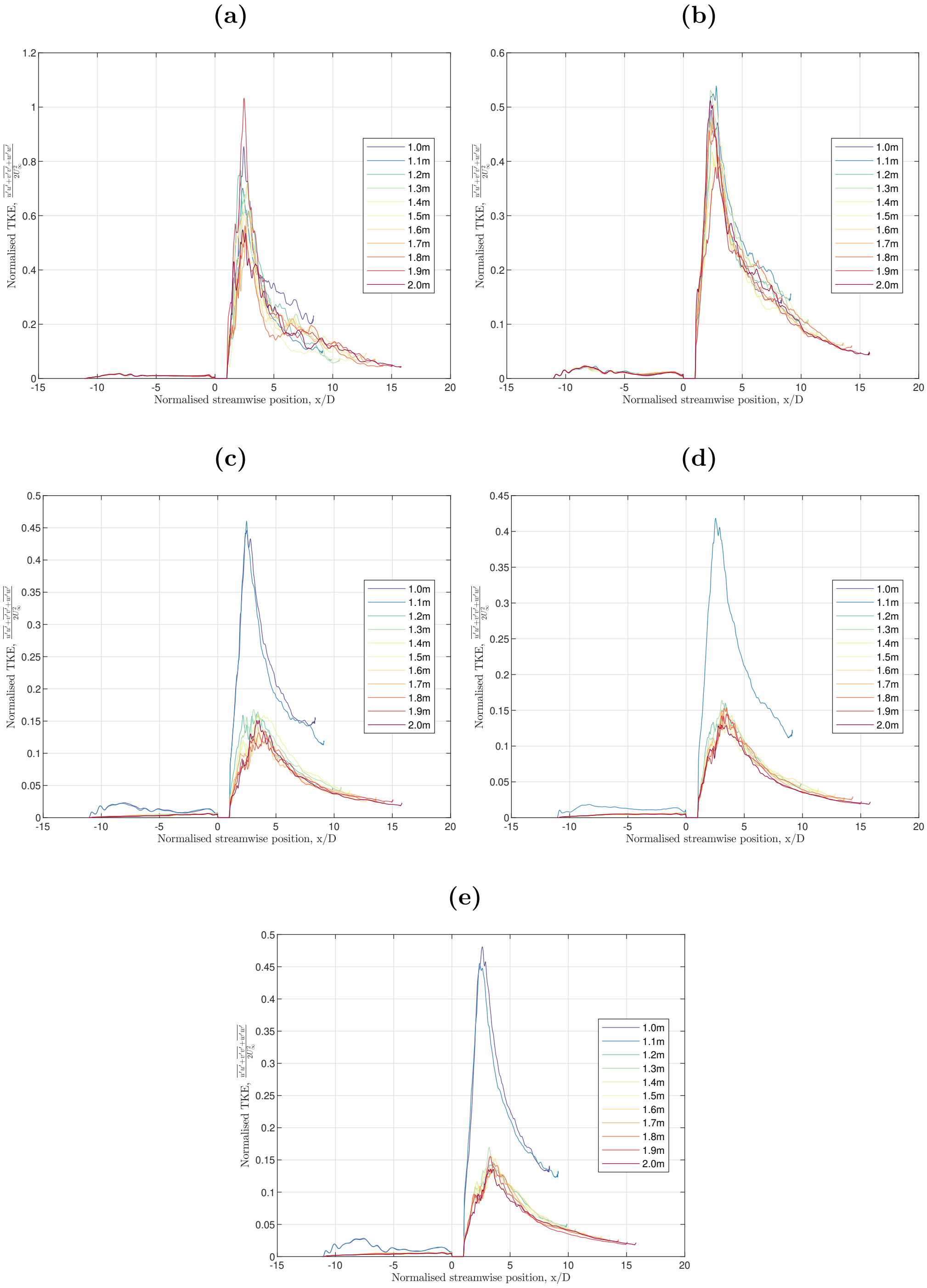

Figure 3.45: Normalised turbulent kinetic energy profiles along the centreline of the Z-normal plane for domains with varying outlet lengths, with MRT dynamics. Solid square obstacle at (a) $Re_D = 2470$ (Case III) (b) $Re_D = 12352$ (Case IV) (c) $Re_D = 24705$ (Case V) (d) $Re_D = 37057$ (Case VI) (e) $Re_D = 49410$ (Case VII)

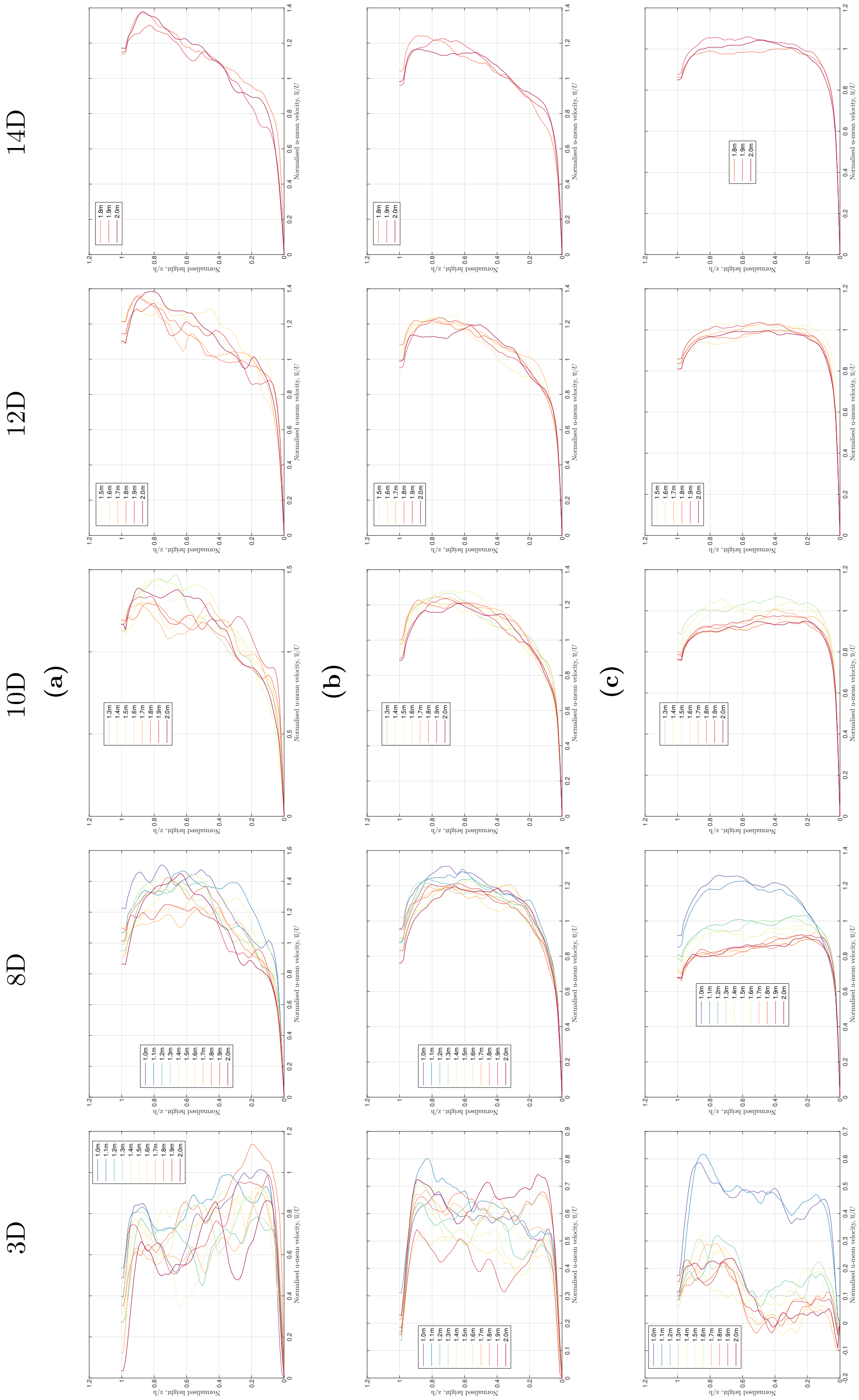
14D
12D
10D
8D
3D
(a)
(b)
(c)
Normalised height, z/h
Normalised u-mean velocity, ū/U
1.0m
1.1m
1.2m
1.3m
1.4m
1.5m
1.6m
1.7m
1.8m
1.9m
2.0m

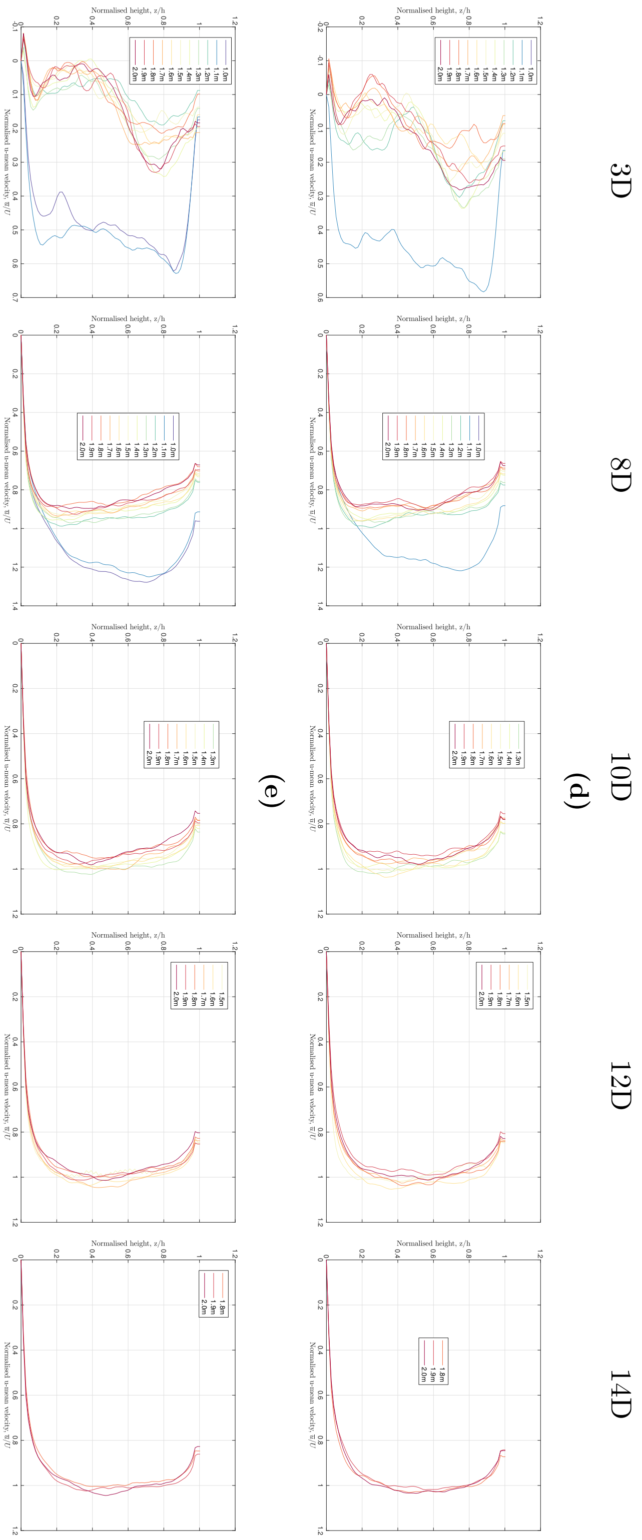

Figure 3.46: Normalised mean streamwise velocity profiles at varying positions in the channel (3D, 8D, 10D, 12D, 14D after the obstacle) of the Y-normal plane, with MRT dynamics. Solid square obstacle at (a) $Re_D = 2470$ (Case III) (b) $Re_D = 12352$ (Case IV) (c) $Re_D = 24705$ (Case V) (d) $Re_D = 37057$ (Case VI) (e) $Re_D = 49410$ (Case VII)

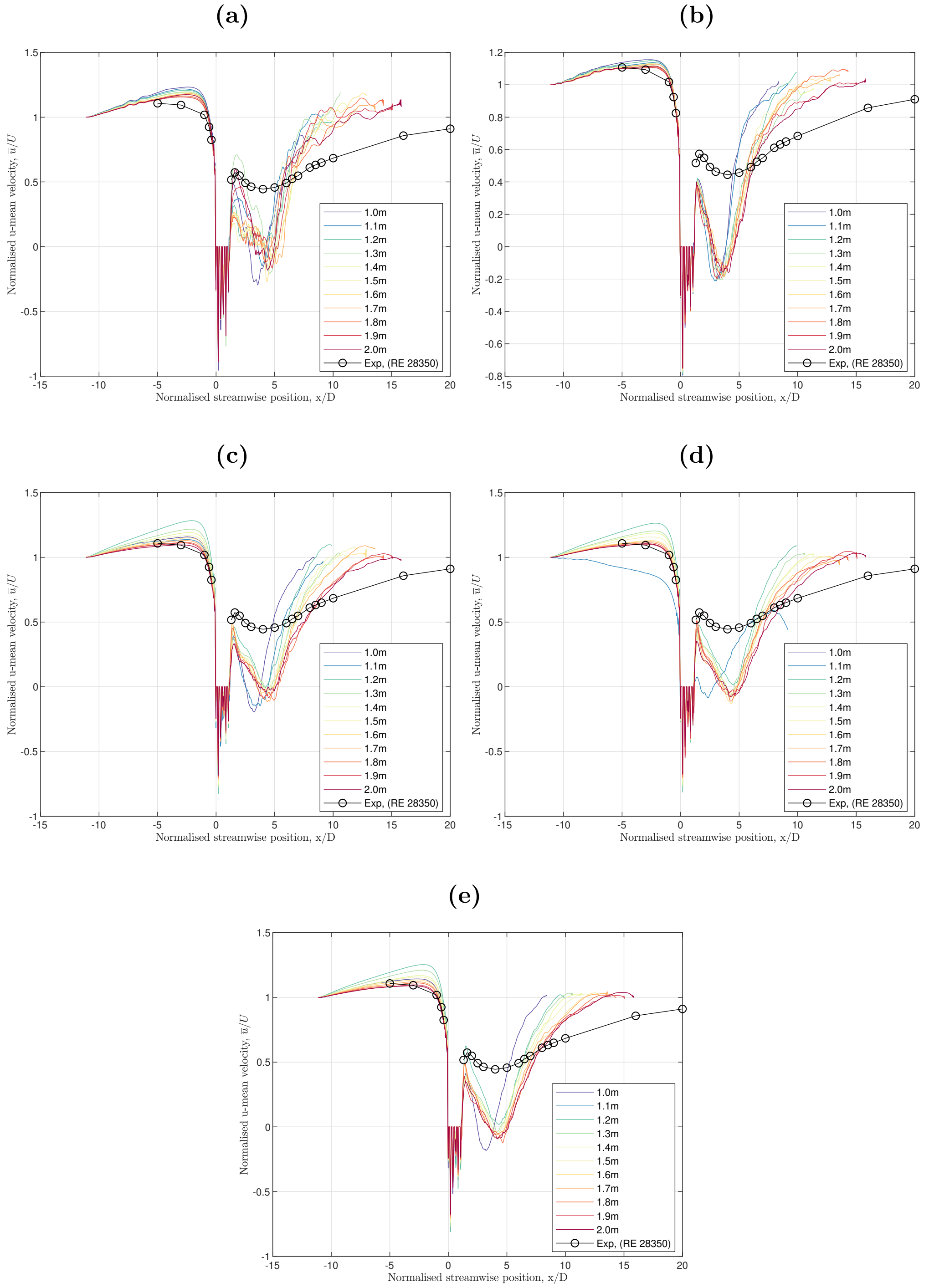

Figure 3.47: Normalised mean streamwise velocity profiles along the centreline of the Z-normal plane for domains with varying outlet lengths, with MRT dynamics. Porous regular obstacle at (a) $Re_D = 2470$ (Case III) (b) $Re_D = 12352$ (Case IV) (c) $Re_D = 24705$ (Case V) (d) $Re_D = 37057$ (Case VI) (e) $Re_D = 49410$ (Case VII)

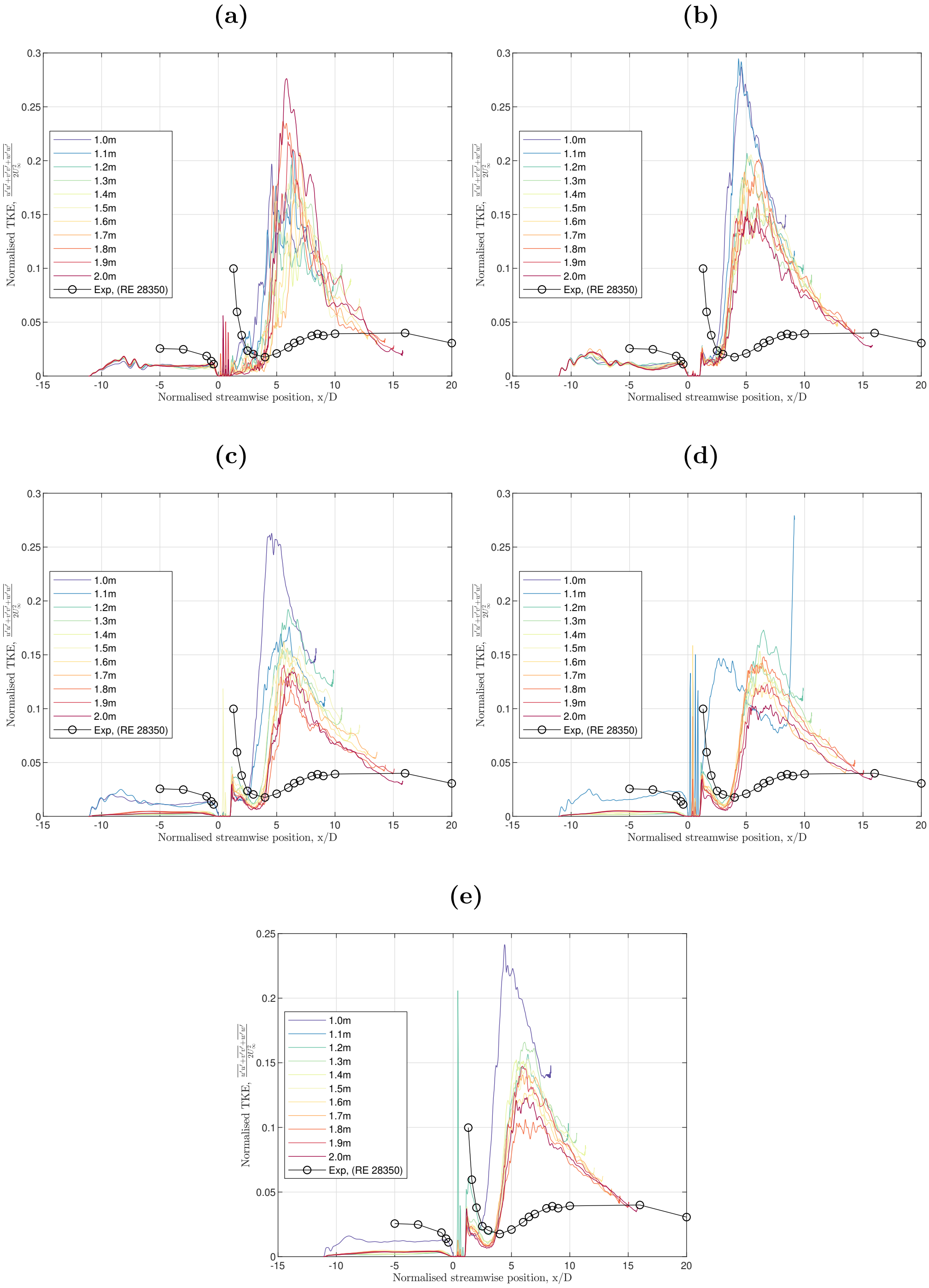

Figure 3.48: Normalised turbulent kinetic energy profiles along the centreline of the Z-normal plane for domains with varying outlet lengths, with MRT dynamics. Porous regular obstacle at (a) $Re_D = 2470$ (Case III) (b) $Re_D = 12352$ (Case IV) (c) $Re_D = 24705$ (Case V) (d) $Re_D = 37057$ (Case VI) (e) $Re_D = 49410$ (Case VII)

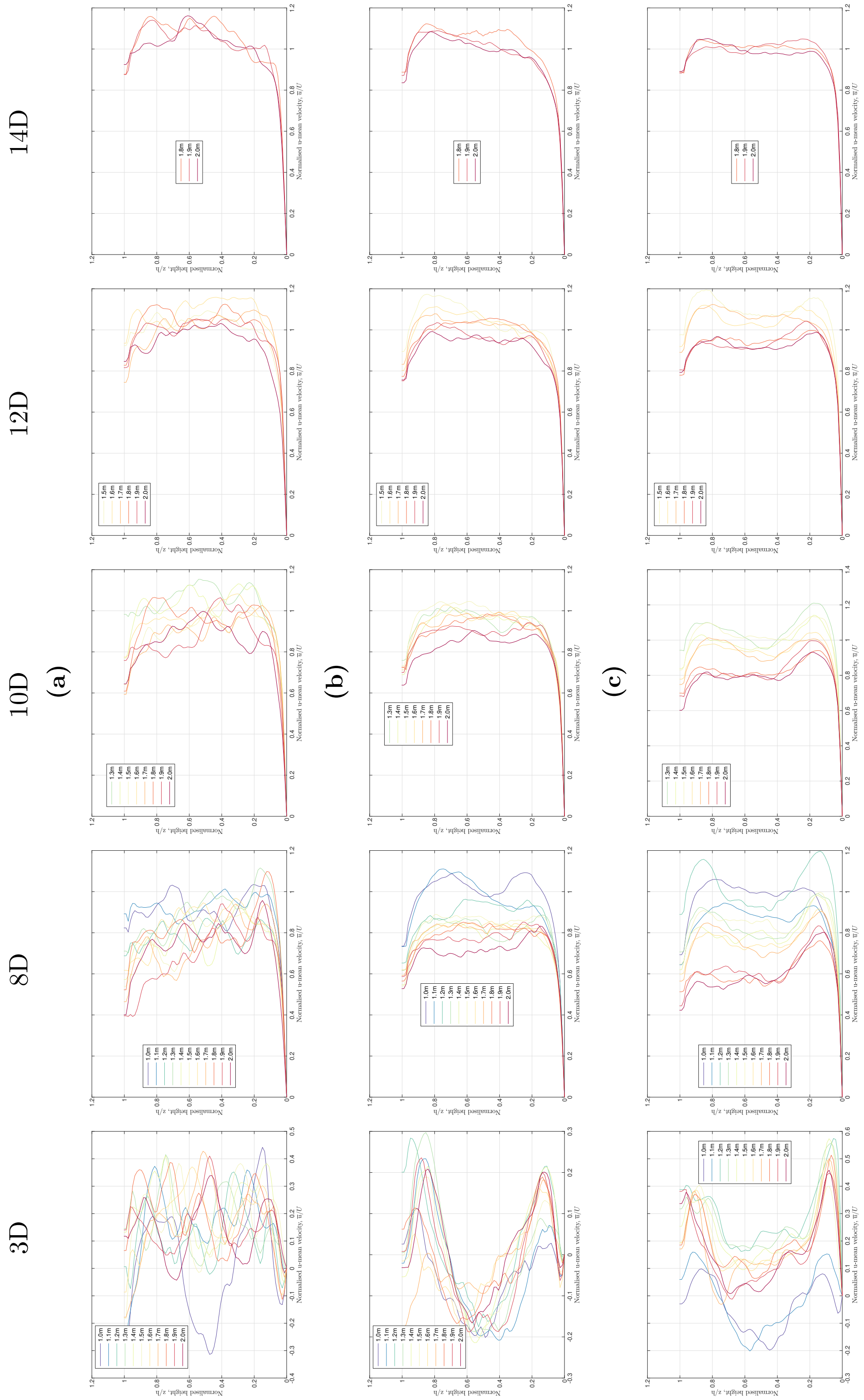
14D
12D
10D
8D
3D
(a)
(b)
(c)
Normalised height, z/h
Normalised u-mean velocity, ū/U
1.0m
1.1m
1.2m
1.3m
1.4m
1.5m
1.6m
1.7m
1.8m
1.9m
2.0m

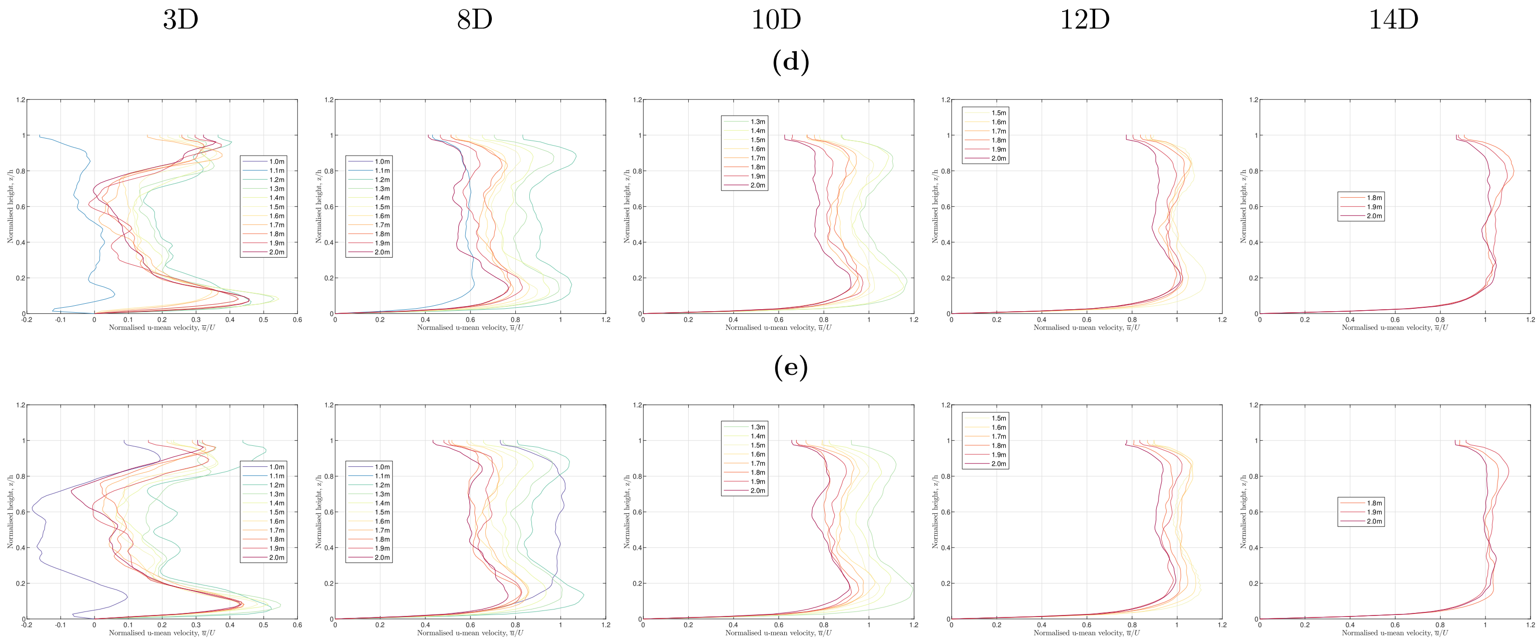

Figure 3.49: Normalised mean streamwise velocity profiles at varying positions in the channel (3D, 8D, 10D, 12D, 14D after the obstacle) of the Y-normal plane, with MRT dynamics. Porous regular obstacle at (a) $Re_D = 2470$ (Case III) (b) $Re_D = 12352$ (Case IV) (c) $Re_D = 24705$ (Case V) (d) $Re_D = 37057$ (Case VI) (e) $Re_D = 49410$ (Case VII)

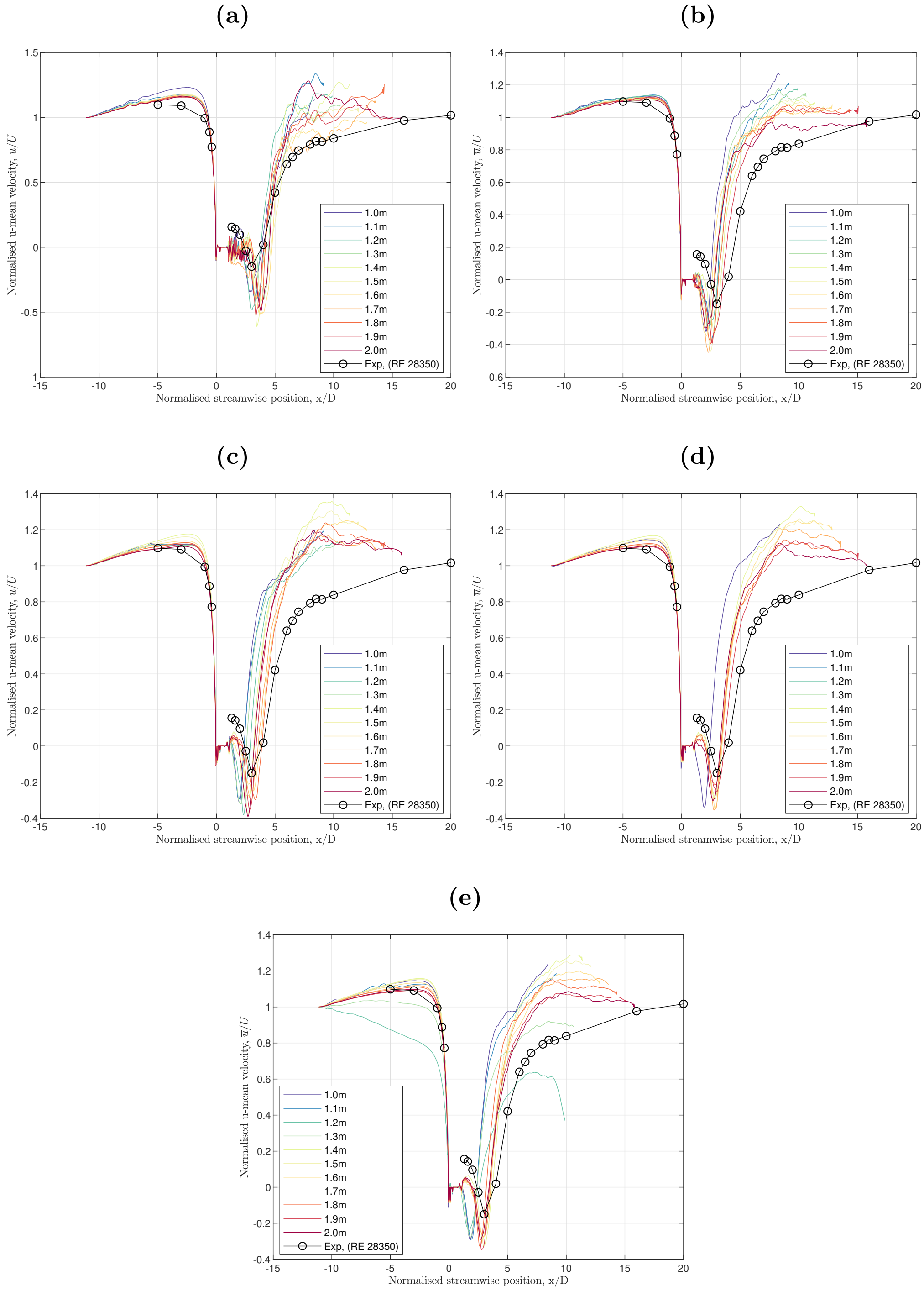

Figure 3.50: Normalised mean streamwise velocity profiles along the centreline of the Z-normal plane for domains with varying outlet lengths, with MRT dynamics. Porous fractal obstacle at (a) $Re_D = 2470$ (Case III) (b) $Re_D = 12352$ (Case IV) (c) $Re_D = 24705$ (Case V) (d) $Re_D = 37057$ (Case VI) (e) $Re_D = 49410$ (Case VII)

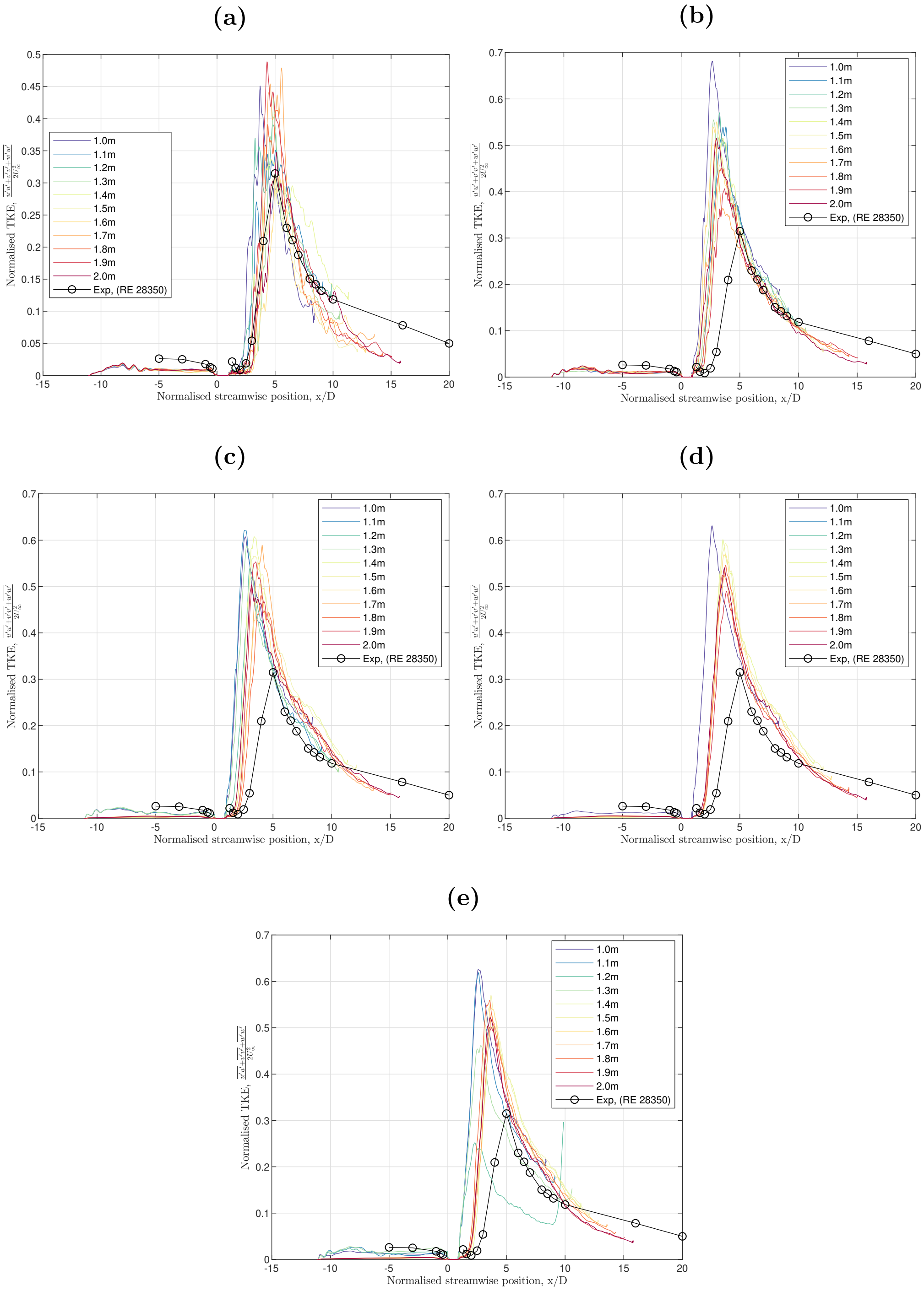

Figure 3.51: Normalised turbulent kinetic energy profiles along the centreline of the Z-normal plane for domains with varying outlet lengths, with MRT dynamics. Porous fractal obstacle at (a) $Re_D = 2470$ (Case III) (b) $Re_D = 12352$ (Case IV) (c) $Re_D = 24705$ (Case V) (d) $Re_D = 37057$ (Case VI) (e) $Re_D = 49410$ (Case VII)

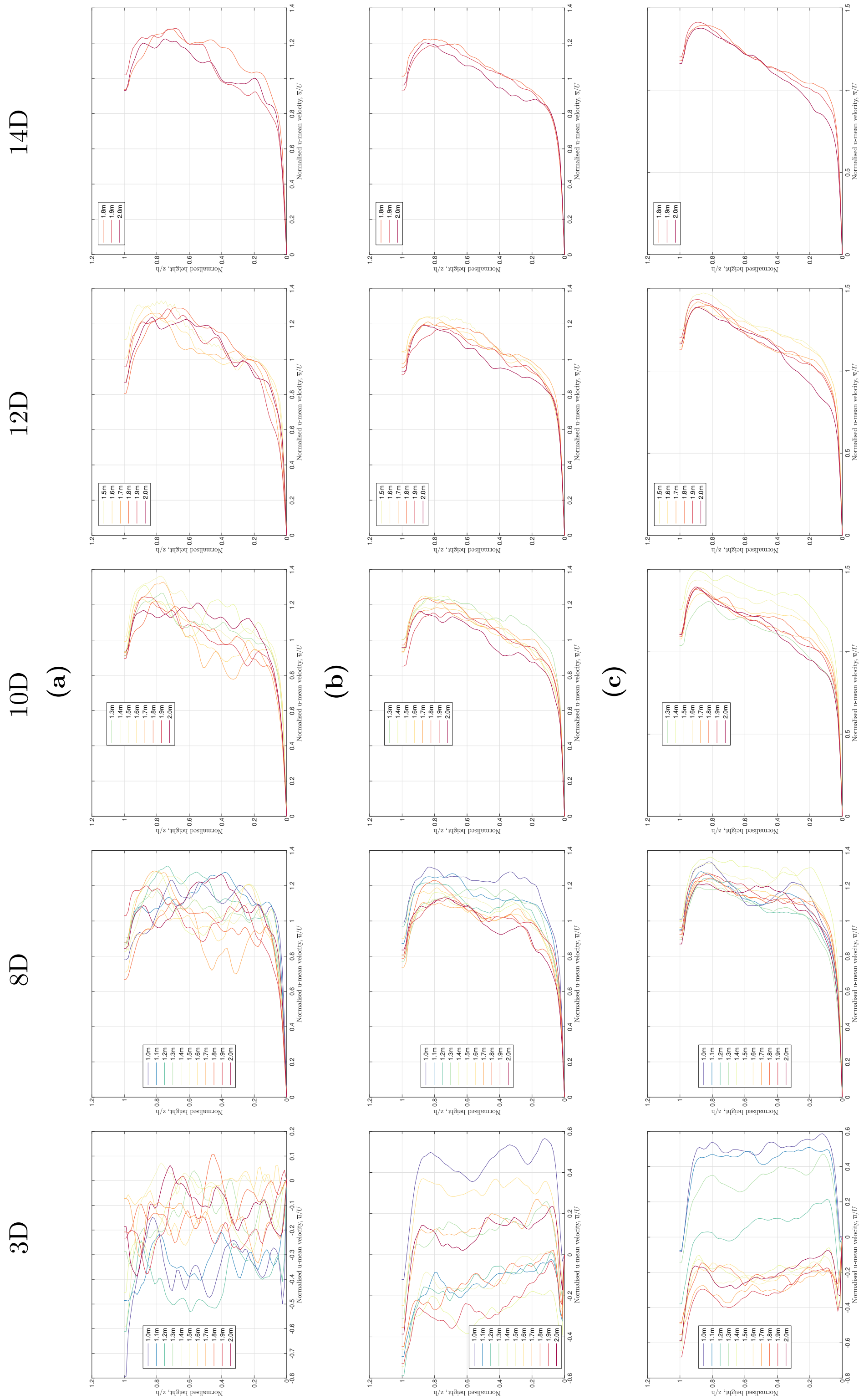
3D
8D
10D
12D
14D
(a)
(b)
(c)
Normalised height, z/h
Normalised u-mean velocity, ū/U
1.0m
1.1m
1.2m
1.3m
1.4m
1.5m
1.6m
1.7m
1.8m
1.9m
2.0m

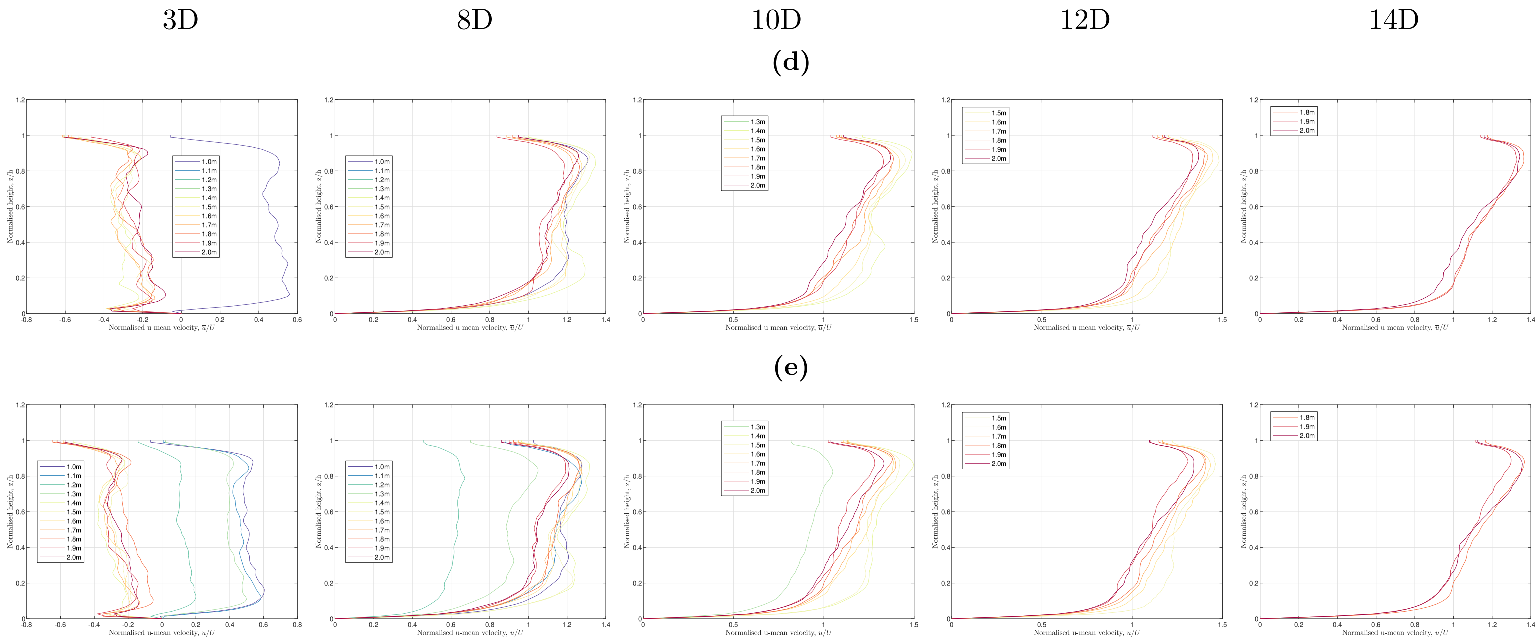

Figure 3.52: Normalised mean streamwise velocity profiles at varying positions in the channel (3D, 8D, 10D, 12D, 14D after the obstacle) of the Y-normal plane, with MRT dynamics. Porous fractal obstacle at (a) $Re_D = 2470$ (Case III) (b) $Re_D = 12352$ (Case IV) (c) $Re_D = 24705$ (Case V) (d) $Re_D = 37057$ (Case VI) (e) $Re_D = 49410$ (Case VII)

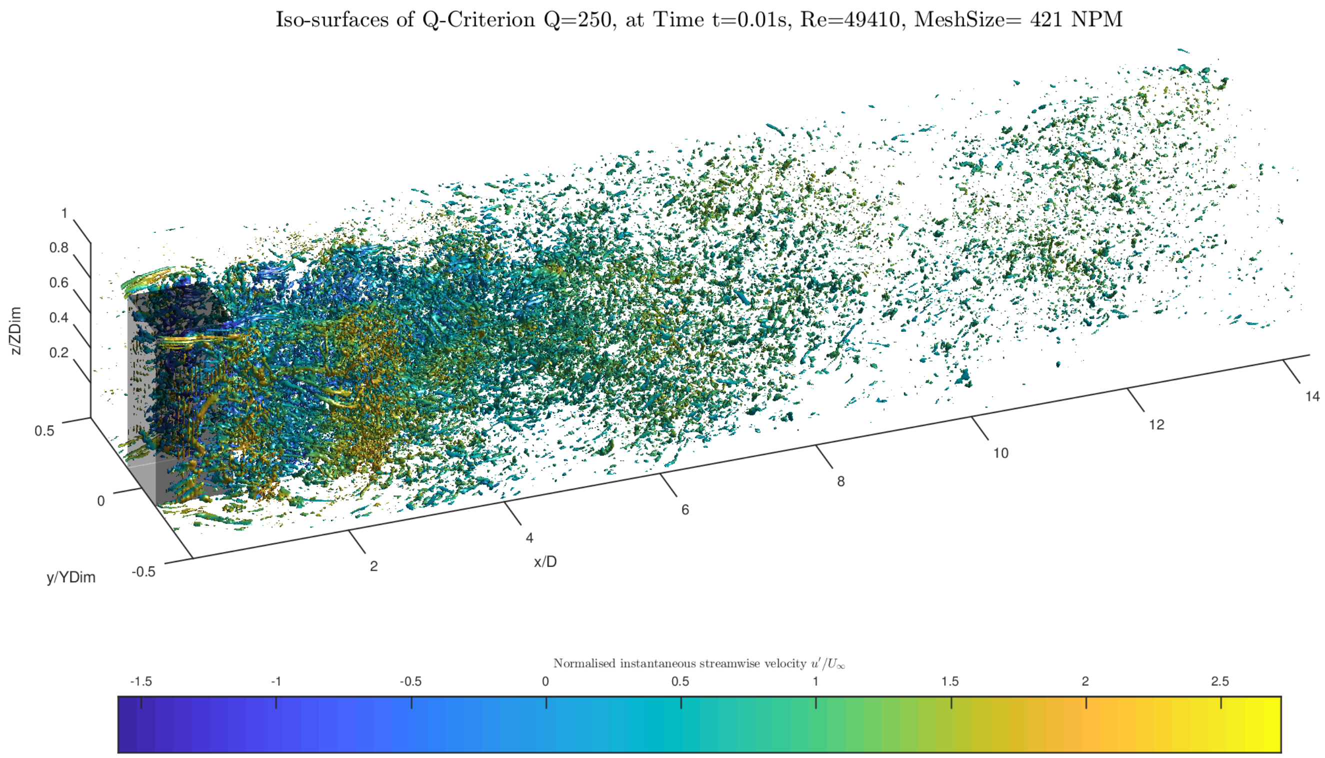

Figure 3.53: Iso-surfaces of the Q-criterion, where Q=250, for the downstream portion of the domain for a solid square obstacle. Surfaces are coloured using the instantaneous streamwise velocity.

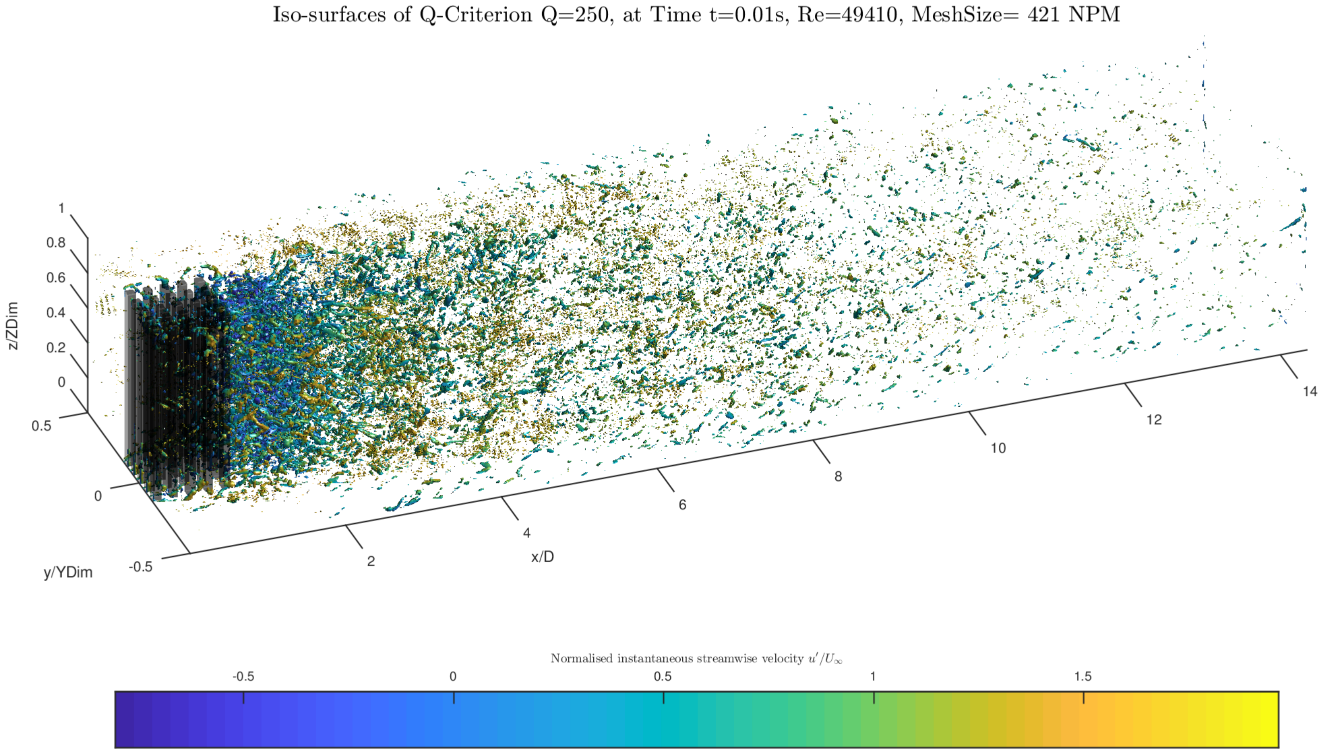

Figure 3.54: Iso-surfaces of the Q-criterion, where Q=250, for the downstream portion of the domain for a porous regular obstacle. Surfaces are coloured using the instantaneous streamwise velocity.

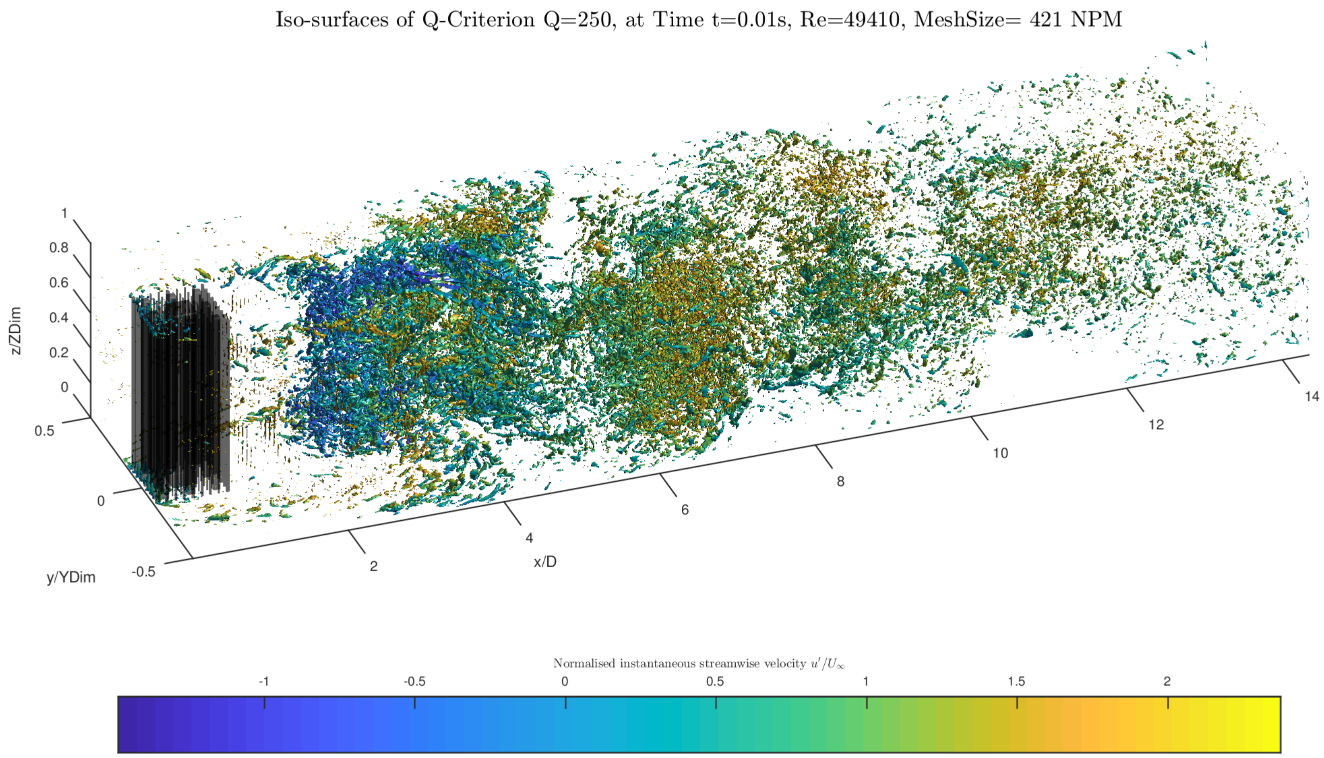

Figure 3.55: Iso-surfaces of the Q-criterion, where Q=250, for the downstream portion of the domain for a porous fractal obstacle. Surfaces are coloured using the instantaneous streamwise velocity.

Chapter 4

Discussions and Analysis

In this chapter an analysis of the results presented in the previous chapter will discussed.

First of all, the stability of the LBM is directly influenced by the relaxation factor. The Chapman-Enskog expansion from chapter 2, demonstrates that there exists a relationship between viscosity and the relaxation factor, Eq 2.56. Which also tells us that the closer the relaxation factor reaches to 0.5 the more likely the simulation is to diverge. This is particularly important for SRT cases as the relaxation factor will solely depend on the chosen setup parameters. Since computations in LBM are conducted in lattice space there is no requirement for the simulated fluid to be physically accurate only the Reynolds numbers have to match to maintain dynamic similarity, this allows the user to alter the lattice properties to achieve a stable solution. Starting from Eq 2.56 and substituting the conversion factors for δ_t and the value of c_s^2 for a D3Q19 lattice (see Table 2.1) the following expression is obtained,

$$\tau = 3\frac{u_{lbm}}{u_{phy}}\frac{1}{\delta_x}\nu_{phy} + 0.5 \tag{4.1}$$

which means that the relaxation factor is directly proportional to the ratio of the LBM velocity and the physical velocity and also inversely proportional to the lattice spacing. Therefore, in order to get a converging simulation there are two actions that can be taken.

- **Decrease node spacing,** δ_x. Due to the uniform grid requirement of Palabos, this has the consequence of exponentially increasing the domain size, thus increasing the resources required.

- **Increase the lattice speed,** u_{lbm}. This results in an increased timestep, thus losing high frequency components of the flow, which are of interest in turbulent flows. Furthermore, lattice speed can only be increased to a certain point as the Mach number in LBM must be kept artificially low to avoid compressibility effects.

4.1 Choice of Dynamics Model

In choosing the dynamic model for the simulation the weakness of the BGK method was presented for high Reynolds number cases, as the BGK method failed to produce a converged result for flows faster than case I. On the other hand both the RLB and MRT schemes proved to be effective at higher Reynolds numbers with both methods being able to achieve a stable solution for all cases.

Since no experimental data was available for validation purposes for the square obstacle a qualitative analysis using representative results found in the literature will be conducted. In the cases involving the BGK model the results of Breuer et al. (2000), wherein a square cylinder was modelled using both LBM and Finite Volume Method (FVM) for a range of Reynolds numbers with the maximum being 300. Since the BGK method only produced results for the $Re_D = 100$ case the results of Breuer are an acceptable starting point. The difference between the results of this investigation and those of Breuer are that the present investigation was entirely conducted using a three dimensional lattice whilst that of Breuer was two dimensional. The centreline velocity profiles of Breuer and the present investigation at $Re_D = 100$ are presented in Figure 4.1.

Immediately it can be determined that the present results for the BGK method do agree with established results in the near wake region.

Furthermore the recovery rate for the far wake region also appears to be in agreement, however, since the present results lack any information beyond 7D, the oscillatory behaviour of the flow observed in Breuer's work is not present in the current domain. Additionally, the present results show that the recovery period in the far wake is smooth, but the results of Breuer indicate that there is a small deceleration around 4D after the obstacle.

The results of the inlet region show the largest disparity, whilst the present results show a significant acceleration as the flow approaches the obstacle, the literature contradicts this behaviour. Considering that there are no further obstacles in this region of the flow this behaviour is entirely unphysical. One could

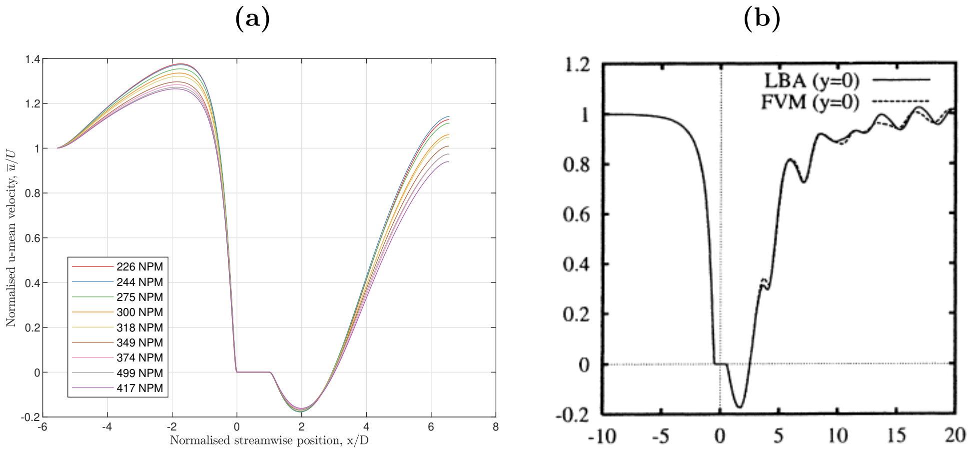

Figure 4.1: Mean centreline velocity profiles for flow past solid square cylinder at $Re_D = 100$ (Case I). (a) Present Investigation (b) Results of Breuer et al. (2000)

attribute this effect to the normalisation procedure, i.e. since the normalisation velocity is that of a uniform profile there could be a disparity, at that height, between the uniform profile velocity and the actual logarithmic velocity profile. However, the results presented are those of corresponding to 0.4Z which is the point at which a uniform and logarithmic velocity profile intersect, meaning that any flow acceleration should be minimal at best. Since, this behaviour must be a numerical artefact, as further demonstrated by the fact that higher resolutions show a tendency to decrease the acceleration, it follows that the mesh resolution chosen is in fact not fine enough. However, a comparison of the resolutions used by Breuer indicate that the finest mesh case simulated in fact used a smaller lattice spacing than that of Breuer. Therefore, this leads to the only conclusion that the disparity between the results must lie with the domain length chosen. Since the results of Breuer are two dimensional, a longer domain has a much less computational burden than that of a three dimensional case.

For the RLB and MRT only the turbulent cases (III-VII) are being considered, since this is the focus of the investigation. Therefore, the results of Bosch & Rodi (1998), Figure 4.4, will be used as a comparative measure, wherein both numerical and experimental results were presented at $Re_D = 22000$. Figure 4.2 shows the centreline profiles of the MRT and RLB results of the present study.

The first point to be made, is that for both the RLB and MRT methods, the method appears to be more stable with increasing Reynolds numbers, which is counter intuitive as an increase in Reynolds number would mean a more chaotic flow, therefore, more numerically unstable.

Now, comparing the near wake region of the flow, it becomes clear that the RLB method severely overestimates the magnitude of the recirculation zone, but the wake length does appear to agree with the established measurements. In the far wake region there does appear to be some agreement in the data, but when approaching the outlet the uncharacterised deceleration of the flow is observed. As posited in the previous chapter, it was thought that this could be an artefact of the domain size and an attempt to reduce this effect via the use of sponge zones prior to the outlet was investigated. As further demonstrated, in Figure 3.13 the inclusion of a sponge zone in the domain did not positively affect the results and in the case of the viscous type caused a stable solution to diverge. The reason for the viscous type sponge zone causing a divergence could be due to an incompatibility of having one area of the lattice use Smagorinski and another use purely viscous subgrid model. Therefore, it was determined that the deceleration effect at the outlet of the RLB cases must have been a product of the dynamic model implemented.

On the other hand, the MRT method does show agreement in both the near and far wake region in the higher flow cases with the experimental results presented by Bosch.

Comparisons made of the TKE profiles can also be made. Figure 4.3 shows that both methods, with the exception of case III and case IV (in MRT only), lie in between the bounds of the results presented by Bosch, with the RLB method showing more agreement with the experimental data and the MRT scheme agreeing with the numerical results.

Given that the RLB severely overestimated the near wake region of the flow, the MRT is the only option to consider for high Reynolds number flows.

4.2 Porous Obstacles

For the porous obstacles only the MRT scheme was used without sponge zones, as it was demonstrated in the previous section this combination yielded the most satisfactory results. The mean velocity profiles, Figure 4.6, show that in the case of the regular obstacle at a resolution of 417 NPM, compared to the experimental results the LBM approximations lie below the experimental results including those of case V which is the closest match the experimental conditions. Overall, case IV is the case that best matches the experimental data, this is interesting

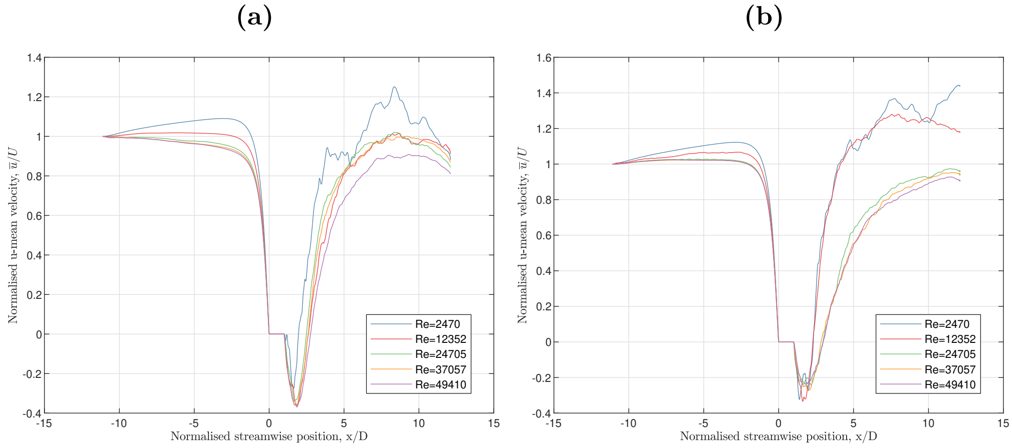

Figure 4.2: Mean centreline velocity profiles for flow past solid square cylinder in the turbulent regime. (a) RLB Model (b) MRT Model. $Re_D = 2470$ (Case III), $Re_D = 12352$ (Case IV), $Re_D = 24705$ (Case V), $Re_D = 37057$ (Case VI), $Re_D = 49410$ (Case VII).

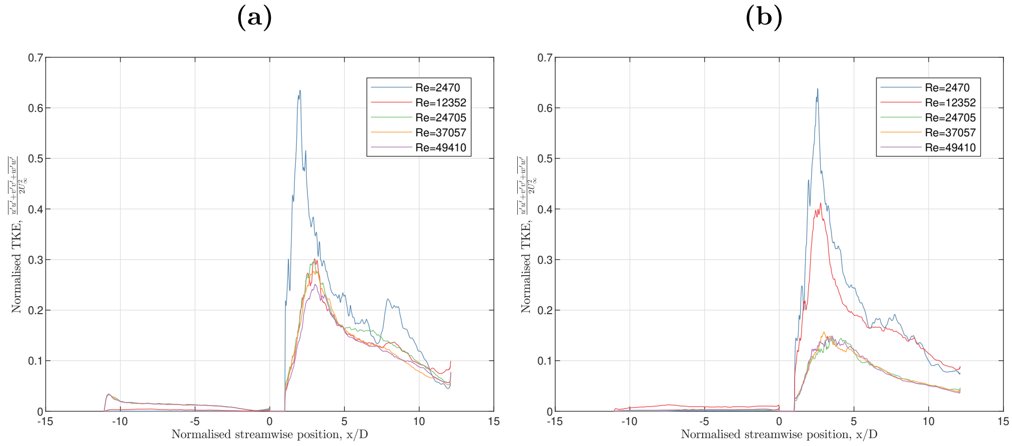

Figure 4.3: Mean centreline TKE profiles for flow past solid square cylinder in the turbulent regime. (a) RLB Model (b) MRT Model. $Re_D = 2470$ (Case III), $Re_D = 12352$ (Case IV), $Re_D = 24705$ (Case V), $Re_D = 37057$ (Case VI), $Re_D = 49410$ (Case VII).

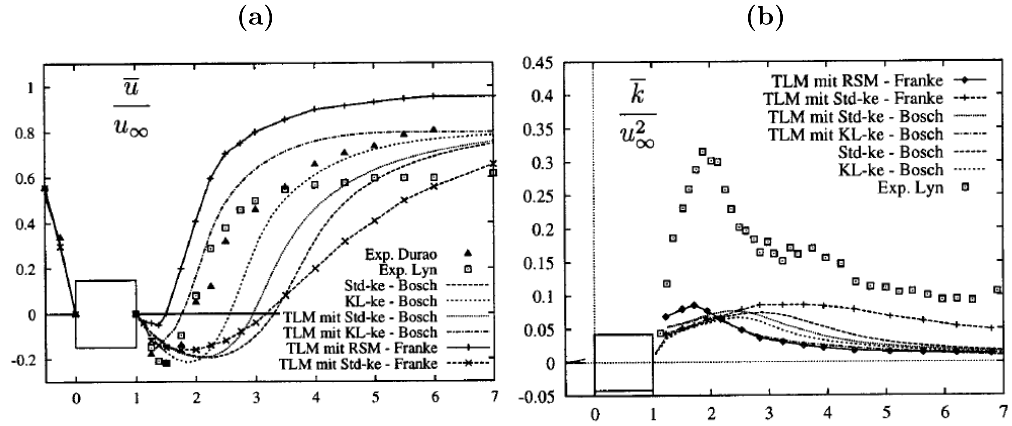

Figure 4.4: Experimental and numerical results presented by Bosch & Rodi (1998). (a) Mean streamwise velocity profile (b) Mean TKE profile

as it is case V which most closely matches the experimental conditions, case IV being less than half of the experimental Reynolds number.

In the case of the fractal obstacle, comparisons using the highest resolution, 417 NPM, is not appropriate. Consistently from the mesh sensitivity analysis exposed in chapter 3 the resolution that most adequately matches the experimental results (especially in the near wake region) is that of 374 NPM. The mesh of the fractal obstacle at the highest resolution, Figure 4.5, shows that although the lattice spacing is smaller than the smallest iteration of the fractal geometry, not all instances of the third iteration obstacles have the same size for the 417 NM resolution, however, the 374 NPM resolution is a more faithful representation of the fractal geometry as the majority of the individual obstacles maintain the square cross-section. This fact is quite substantial as it indicates that the flow is heavily influenced by the geometry of the fractal, which would lead to the speculation that the same obstacle but with the sub-obstacles arranged in a different manner would yield an entirely different near wake.

Returning back to the streamwise profiles of Figure 4.6, the acceleration immediately after the obstacle is well captured by the LBM for cases V-VII, however, cases III-IV do demonstrate this effect to a lesser extent. Given that cases III-IV represent flow speeds slower than the experimental data it could be that this behaviour is specific to the higher flowrate cases. Subsequently, there is a disagreement between the LBM cases for the location of the profile minima, with cases IV, VI, VII predicting a location closer to the obstacle than cases III, V. Although this location predicted by the first group appears to agree with the ex-

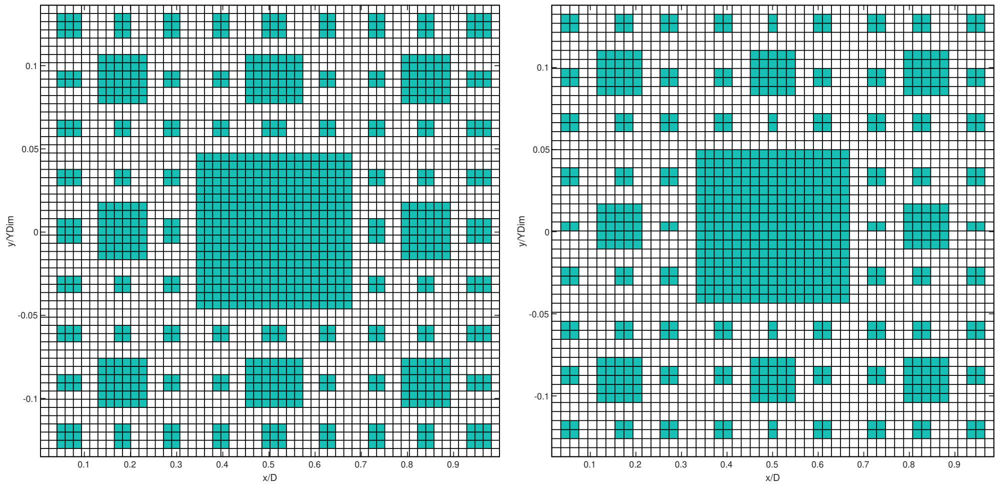

(a)

(b)

Figure 4.5: Meshing of the fractal obstacle. Each square represents a node in the lattice, with the filled squares representing the obstacle. (a) 417 NPM (b) 374 NPM

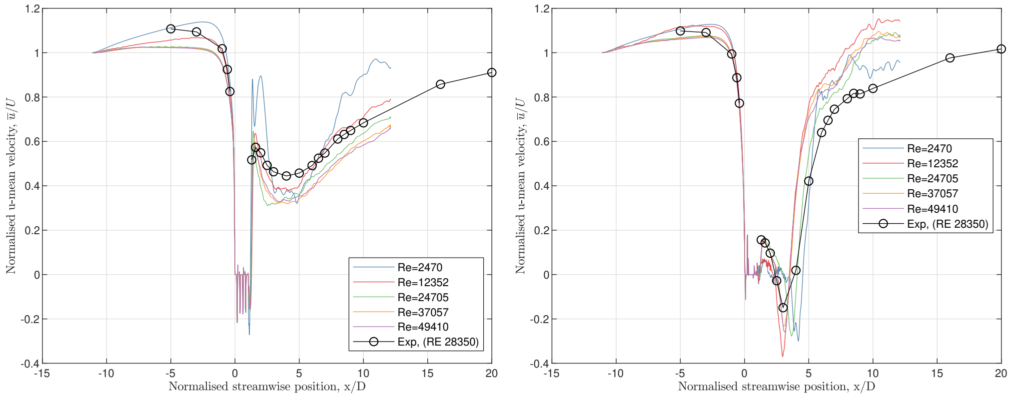

(a)

(b)

Figure 4.6: Mean centreline velocity profiles for flow past porous obstacle in the turbulent regime. (a) Regular (b) Fractal. $Re_D = 2470$ (Case III), $Re_D = 12352$ (Case IV), $Re_D = 24705$ (Case V), $Re_D = 37057$ (Case VI), $Re_D = 49410$ (Case VII).

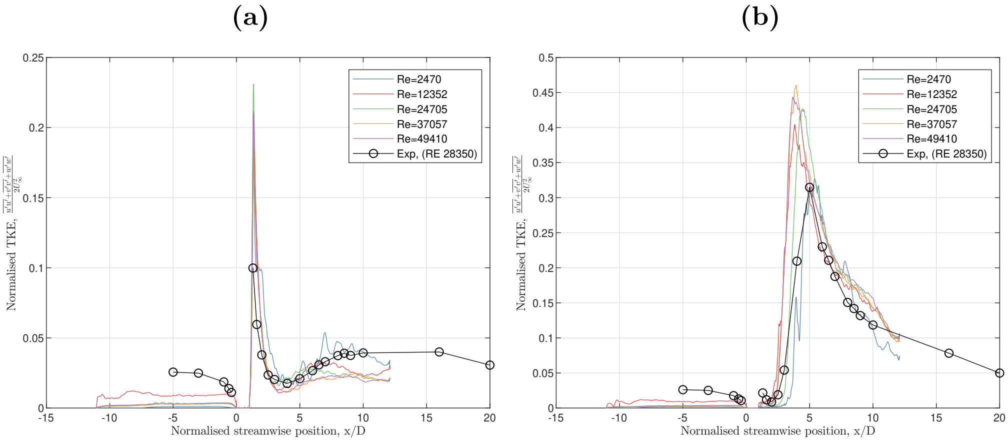

Figure 4.7: Mean centreline TKE profiles for flow past porous obstacle in the turbulent regime. (a) Regular (b) Fractal. $Re_D = 2470$ (Case III), $Re_D = 12352$ (Case IV), $Re_D = 24705$ (Case V), $Re_D = 37057$ (Case VI), $Re_D = 49410$ (Case VII).

perimental data it may not be correct. Given the undersampling of the velocity profile in this region, if one were to interpolate the experimental data using the minima of the profile predicted by the LBM, the location of the minima would agree more with cases III and V. In the far wake region the LBM results all show significant disagreement with the experimental results, with cases IV-VII showing an unphysical flow acceleration close to the outlet. Given that the result is still clearly dependent on the mesh resolution, the results of the fractal obstacle cannot be declared conclusive and finer mesh studies are required. To a certain extent the divergence from the experimental data is also expected, because it is where the subgrid model would struggle the most to match the complex vortex shredding interaction occurring there. The simple Smagorinski closure used is only valid for homogeneous isotropic turbulence cascade and clearly breaks down in this region.

Looking at the TKE profiles, Figure 4.7, in the case of the regular obstacle there is significant agreement between the LBM results and the experimental data. Since the experimental data was collected via an ADV, which is an intrusive method data near or close to the obstacle is very difficult to collect, and since the peak occurs immediately aft of the obstacle its natural for the experimental data in this region to be underestimated.

For the fractal obstacle, the TKE profiles, show a decent agreement with experimental data, more so in the far wake than in the near wake. Case III appears to fully agree with the experimental data, however, given the fact that all other results point to case III being more transitional flow than fully developed turbulent flow, it is more likely that the peak TKE was not correctly captured in the experimental data due to under sampling along the profile.

4.3 Transversal Profiles

The evolution of the wake can be further observed in the transverse direction. Both the streamwise, Figure 4.8, and cross-stream, Figure 4.9, velocity profiles in this direction help to characterise the shape of the wake for each obstacle. At 1D length after the obstacle we can observe three distinct wake shapes for each obstacle. Given that the regular obstacle allows the flow to pass un impeded on alternate rows, the retardation of the velocity is significantly less than the other obstacles with the central gaps acting as a small nozzle. Furthermore, the effects of the obstacle can clearly be seen long into the far wake than the solid and fractal obstacles. For the fractal case although it can be seen that by 6D the wake is approximately the same as the solid square obstacle for cases IV-VII considering it took the square obstacle 5D to reach to this point from a recirculating wake it took the fractal obstacle 3D. Furthermore, in the far wake, for the fractal the flow is less affected by the obstacle compared to solid case with increasing Reynolds numbers.

The cross-stream near wake can be characterised quite simply as a clockwise rotating structure for the solid obstacle and quite interestingly for the porous obstacles there are two side by side clockwise structures. In the case of the regular obstacle these structures are short lived and by 6D the flow is behaving as if the obstacle were a solid one. However, in the fractal case these structures persist for longer until 6D and slowly by 9D they merge into a single anticlockwise structure near the centreline and then separate out forcing the flow towards the walls at 12D. On the other hand, as the flowrate is increased, and the flow continues downstream for the regular and solid case, the flow maintains a centreline attractive behaviour preserving the singular clockwise structure. Given that the cross-stream velocity is a direct result of placing the obstacle in the flow, looking at the profiles at 12D it can certainly be said that the porous obstacles have a much longer effect than the solid obstacle.

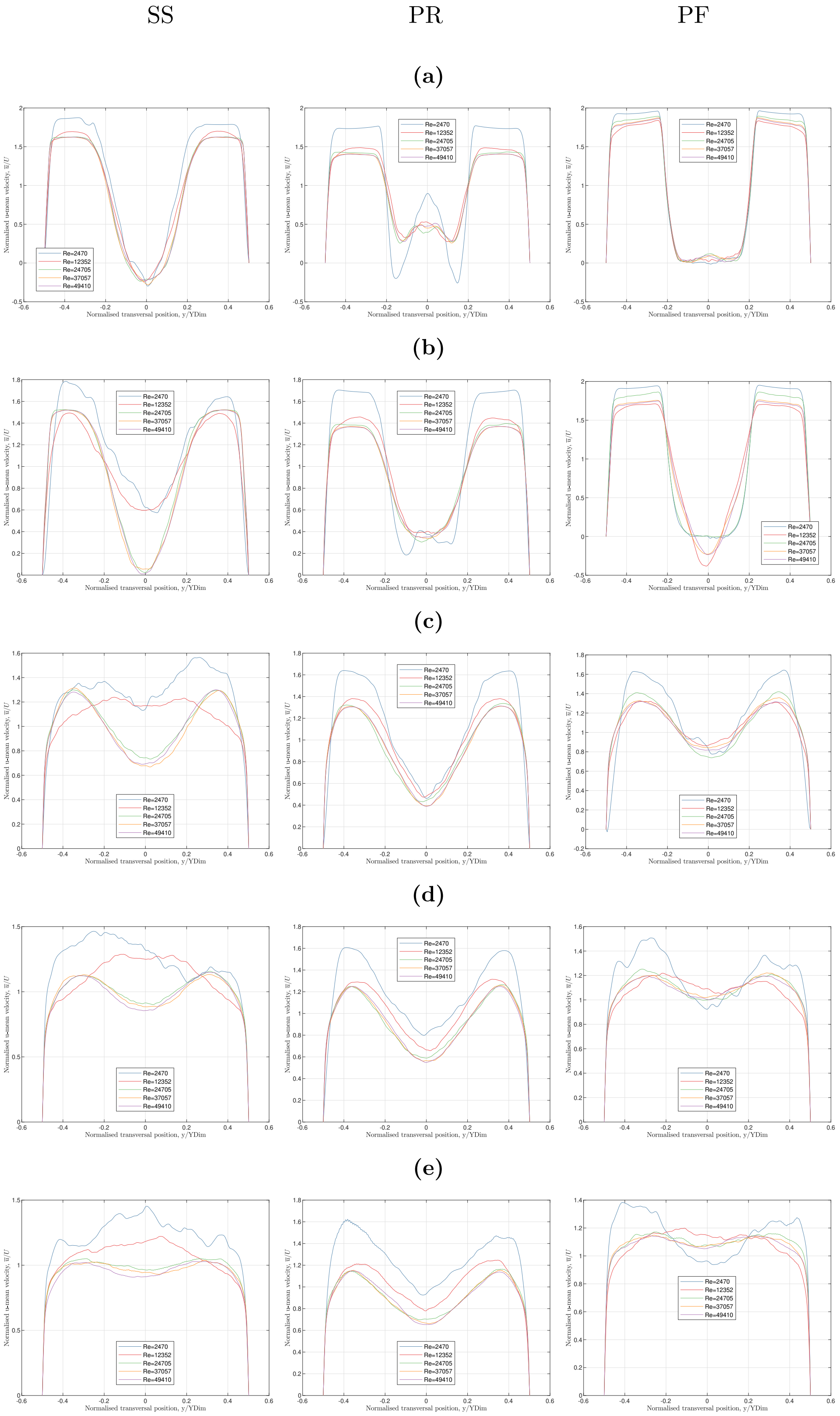

Figure 4.8: Transverse streamwise velocity profiles at different locations in the channel for the three obstacles (SS - Solid Square, PR - Porous Regular, PF - Porous Fractal), with MRT dynamics. (a) 2D (b) 3D (c) 6D (d) 9D (e) 12D. $Re_D = 2470$ (Case III), $Re_D = 12352$ (Case IV), $Re_D = 24705$ (Case V), $Re_D = 37057$ (Case VI), $Re_D = 49410$ (Case VII).

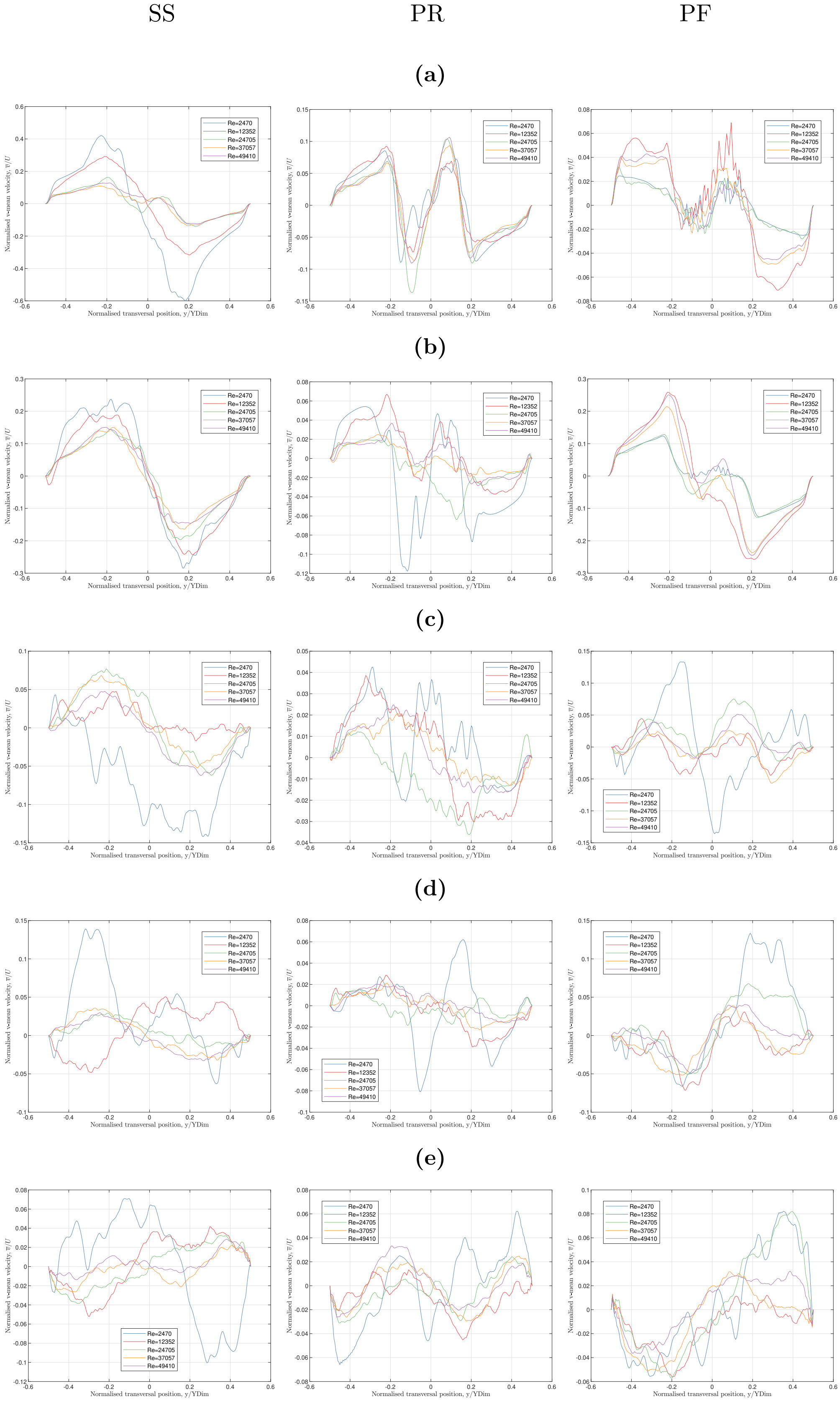

Figure 4.9: Transverse cross-stream velocity profiles at different locations in the channel for the three obstacles (SS - Solid Square, PR - Porous Regular, PF - Porous Fractal), with MRT dynamics. (a) 2D (b) 3D (c) 6D (d) 9D (e) 12D. $Re_D = 2470$ (Case III), $Re_D = 12352$ (Case IV), $Re_D = 24705$ (Case V), $Re_D = 37057$ (Case VI), $Re_D = 49410$ (Case VII).

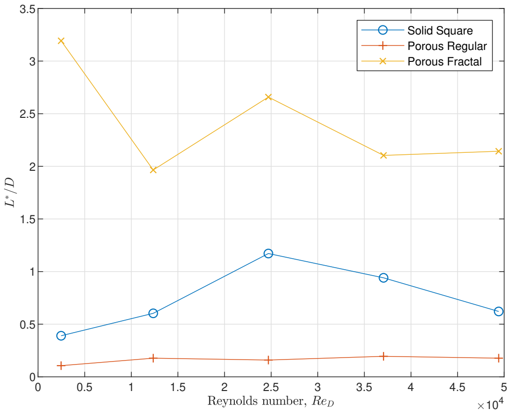

Figure 4.10: Length to minimum streamwise velocity, L^*, from the base of the obstacle in the streamwise direction for all three obstacles

4.4 Wake Length

Given that the regular obstacle does not form a wake, wake lengths can only truly be compared between the fractal and solid obstacle. Additionally, due to the fractal delaying the formation of the recirculation zone two definitions could be adopted, one being the length from the base of the obstacle to the point where the streamwise velocity remains positive or the maximum length where the streamwise velocity is negative. Therefore, to adequately compare the three different obstacles a parameter common to all three is defined as follows: L^* is the length from the base of the obstacle to the minimum mean streamwise velocity. Figure 4.10, shows the variation in this length for all the tested obstacles and Reynolds numbers.

Overall, the flow is least impeded by the regular obstacle, given that along the centreline there are no sub-obstacles this is natural and expected. However, the fractal obstacle having one third the porosity of the solid obstacle has a greater impeding effect on the flow. In the fully developed turbulent cases (VI-VII) both the solid and fractal cases show a similar pattern, the maximum length to the minima occurs at $Re_D = 24705$. In the case of the solid obstacle it then steadily decreases with increasing flowrate, whilst for the fractal obstacle L* remains constant after $Re_D = 37057$. This further demonstrates the earlier conclusion that although the near wake region is increased by the use of a fractal obstacle the recovery is much faster with increasing Reynolds numbres.

4.5 Mass Flowrate

Based on the mass flowrate results presented, we can see that flow is entirely dominated by the streamwise velocity, which is expected as the flow is entering and exiting the domain in that direction. Although the mean flowrates in the remaining two directions is near zero, it is quite clear that some momentum is exchanged between the streamwise flow with the transverse and vertical flow, just that the exchange is made equally in either direction of the dimension after the obstacle. This is to be expected as vortex shedding from cylinders follows an alternating pattern, namely the von Karman street.

Additionally, in the streamwise direction for all three obstacles we can isolate case III as anomalous because the flowrate accelerates as it goes downstream this is unphysical as it is expected that the momentum gained in the transverse and vertical directions would be drawn from the streamwise direction. When calculating mass flow a constant density was assumed, this is because the Mach number was sufficiently low that compressibility should not have been an issue. However, it seems that for case III there may have been some compressibility effects appearing.

The fractal obstacle also stands out because the higher flowrate cases also show this acceleration in the downstream section of the channel contrary to what is observed for the other two obstacles which follow a more predictable behaviour. Considering that the fractal obstacle profiles showed the most disparity with established results, this is further indication that more analysis is required for the fractal obstacle cases. However, it should be pointed out that comparisons of mass flowrates between the obstacles are all done for the 417 NPM case, as this was the only resolution for which X-Normal plane data was recorded. As pointed out earlier, since 417 NPM is not a true representation of the geometry, mass flowrate comparisons for the fractal case should be done with the 374 NPM case, or other resolutions that maintain the most representative geometry of the fractal obstacle.

4.6 Strouhal Numbers

For the Strouhal numbers for the square obstacle, we can once again look at the published results of Bosch & Rodi (1998) for expected values, in which the Strouhal number is expected to range between 0.125-0.145. The Strouhal number maps presented in the previous chapter agree with this in the area where the near wake ends.

Since there is no global wake region for the regular obstacle as the is little to impede the flow from going straight through, there is no clearly defined near wake. However, in the immediate area after the obstacle there is a region which has a relatively higher frequency compared to the surrounding region. This Strouhal number is roughly nine times the expected value. Considering that the regular obstacle comprises square cylinders which are nine times smaller than the solid obstacle it yields that this group of obstacles is not behaving as a group instead the vortex shedding is being dominated by the individual cylinders.

In the case of the fractal obstacle since there is a defined wake region, by looking at the edge of the near wake we again see similar scaling effect instead this time the vortex shedding is being dominated by the largest cylinder in the obstacle.

4.7 Outlet Sensitivity

From the results presented in the previous chapter, in the case of the square obstacle it was determined that the length of the downstream section has a minimal effect on the outcome, with data being reasonably converged as early as 1.2m. However, it becomes more important with the two porous cases as the minimum downstream section was determined to be 1.8m. Nevertheless, this length has a greater effect on the far wake region of the flow, with the near wake being left unaffected, except for the fractal obstacle. In this scenario, the near wake does seem affected by the downstream length, however, as the flow velocity is increased the effect becomes smaller.

Chapter 5

Conclusions, Issues and Future Work

5.1 Conclusions

In conclusion, a parametric study has been conducted to investigate whether LBM is a suitable option to simulate high Reynolds number flows in a channel with Smagorinsky subgrid modelling. Flows ranging from Reynolds numbers of 100 to 49410 were tested using three different dynamics models, BGK, RLB and MRT, for three different obstacle types: Solid Square (SS), Porous Regular (PR) and Porous Fractal (PF) in a 3D domain.

Based on the results, the BGK method is suitable for the simplest of flows and requires a sufficiently long outlet domain, therefore, confining the simulation to only 2D cases. The RLB, whilst more stable than the BGK it overestimates the near wake region of the flow. The MRT method, in the turbulent regime, does yield results that agree with the established literature in the case of square cylinder. In cases involving a porous regular obstacle the MRT-LBM is capable of predicting very well the centreline streamwise velocity and TKE proflies, when comparing to ADV experimental results. Similarly, in the cases of a porous fractal obstacle the near wake characteristics are predicted well, but the far wake region of the streamwise velocity profiles differ to the experimental results. Additionally, a tendency towards a universal behaviour is observed across all three obstacles, with the porous obstacles achieving this universal behaviour faster than the solid obstacle. For the solid square case this is achieved for $Re_D > 24000$.

In the case of the fractal obstacle it is paramount to check that the smallest fractal scale is properly meshed. The local capture of the smallest geometry is more important than its fine meshing.

Additional tests also concluded that whilst the downstream portion of the domain has an effect on the results, these are confined to the far wake regions of the flow and the near wake region converges with acceptably short domains. Attempts to minimise the effects of the outlet region via the use of sponge zones showed no change in the case of Smagorinsky based sponge zones and divergence in the case of viscous based sponge zones.

As expected the wake observed after the obstacle depends greatly on the internal structure of the porous object. The oscillation observed for the solid square is annihilated in the case of the porous regular obstacle but only pushed downstream in the case of the porous fractal obstacle. Strouhal numbers in the near wake region, again for the solid square case, agree with the established literature. For the porous regular, the vortex shedding scales with the size of the individual cylinders and in the porous fractal case its the largest iteration that dominates.

Considering the computational benefits (highly parallelisable linear equations), LBM does prove itself to be a significant contender to established CFD methods for investigations involving high Reynolds number flows.

5.2 Issues

As is the case with any investigative project the time constraints limit the amount of work that can possibly be conducted, and this was no difference in this project. Therefore, in the following sections a clear plan of what remains to be done for this project will be given. In addition, the issues that were faced by the lead investigator during this project will also be laid out.

One of the main issues faced in this investigation was the need to balance computational resources due to the uniform grid requirement imposed by Palabos. It should be noted that although Palabos does have advanced meshing capabilities, these are only available in two dimensions at the time of investigation.

Initially, a version of LBM developed at the University of Leeds by Delbosc et al. (2014) that is GPU accelerated was going to be used. However, this proved to be more difficult to implement than originally thought. The results from this software were quite unrealistic, which included,

- Slow evolution of the vertical profile
- Unphysical downstream acceleration
- Overestimation of the near wake region for the simplest solid square cylinder
- Results were sensitive to inlet domain lengths rather than outlet domain lengths.

5.3 Future Work

The results presented in this investigation are an exhaustive exploration of LBM simulations for a quasi two dimensional flow past an obstacle, however this is still not complete. Results for a fractal porous obstacle indicate that a mesh independent result still has not been achieved. Therefore, before continuation of the investigation finer mesh studies of the fractal obstacle need to be conducted.

As stated in the first part of this thesis the eventual goal of the investigation is to use LBM to simulate the flow past a fractal bed as a simplified model of a city. Prior to simulating a fully three dimensional case using a fractal bed it would be necessary to investigate a confined obstacle but also changing the arrangement of individual obstacles so as to keep the same porosity but have different lacunarity and sucolarity.

Finally implement a periodic boundary condition with a forcing term to simulate a fractal canopy. One major benefit of simulating this case is the lack of inlet and outlet regions therefore extremely high resolutions should be easily achievable, which should allow investigations of on effects that the smaller scales beyond the 3^{rd} iteration have on the flow.

Appendix A

Fractals

A.1 Fractal Dimension

The Oxford dictionary defines a fractal as "a curve or geometrical figure, each part of which has the same statistical character as the whole." It is this self-repeating pattern that distinguishes a fractal from a regular mathematical object, and thus they may not be defined using the typical topological dimensions. A dimension is defined as the number of coordinates necessary to specify a point within the object. In the case of a mathematical object, when the topological dimension is a positive integer, the number of coordinates necessary to define it is known as the Euclidean dimension, as shown in Table A.1. For example, on a curve, a single coordinate is required, i.e. X-coordinate, therefore it is said to have a Euclidean dimension of one.

A critical feature that all objects defined by Euclidean dimensions must have is that they are everywhere differentiable except in a set with dimension zero, meaning that a derivative of the function exists at every point in the domain with the exception of edges or similar. This property is violated by fractals, for example the Von Koch curve, Figure A.2, can continue to infinity without

Table A.1: Euclidean Dimension

Object	Eucledian Dimension	SI Units
Point	0	
Line/Curve	1	m
Surface	2	m^2
Volume	3	m^3

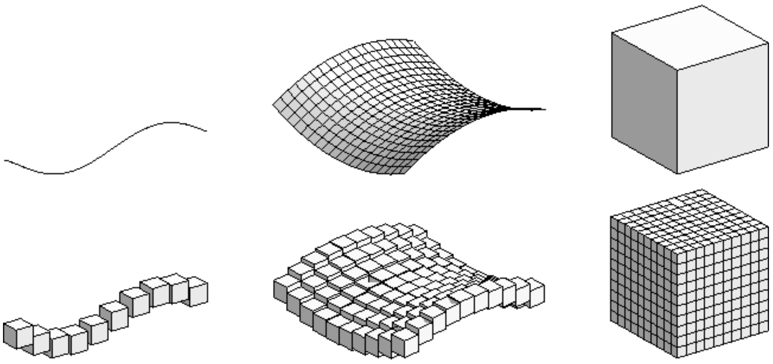

Figure A.1: Visual representation of the box counting method. Covering a curve, a surface, and a solid with cubes of edge length 'r'.

ever being a smooth object. Therefore, a different dimension must be applied to define them; the Hausdorff dimension is used instead. An advantage of using this definition is that it may be used for any object. Whilst the Euclidean dimension can only define the dimension as integers, the Hausdorff method uses a rational number. A principal feature of a fractal is that it must have a similar geometry in ever decreasing scales. It is this repetition of the same geometry that forms the basis of the Hausdorff dimension.

An easy way to explain this is to use the box-counting method as shown in Figure A.1. In order to cover the curve of unit length with boxes of length r, the number of boxes needed, N, is 1/r. Similarly to cover the surface of unit area with boxes of length r the number required is $1/r^2$ and for an object of unit volume $1/r^3$ boxes will be needed. It should be noted that the exponent r matches the Euclidean dimension of the object that needs to be defined; therefore, the Hausdorff dimension, D, is expressed as in (A.1).

$$N(r) \sim r^{-D}$$

Taking the limit as r $\rightarrow$ 0 the constant A is defined as:

$$A = \lim_{r \to 0} \frac{N(r)}{r^{-D}}$$
$$ln(A) = \lim_{r \to 0} (lnN(r) + Dln(r))$$

$$D = \lim_{r \to 0} \frac{ln(A) - ln(N(r))}{ln(r)}$$

$$D = -\frac{ln(N(r))}{ln(r)} \tag{A.1}$$

Note that the constant term $ln(A)$ disappears, this remains as a constant and as r tends to 0 the denominator becomes infinite. The following shows an example of how the Hausdorff dimension is calculated for the Von Koch curve, shown in Figure A.2.

$$N(r) = 4^n N_o \textbf{ and } r = 3^{-n} r_0$$

$$\begin{aligned} D_F &= -\frac{lnN}{lnr} \\ &= -\frac{nln4}{-nln3} \\ &= \frac{ln4}{ln3} \\ &\therefore \\ D_F &= 1.26 \end{aligned}$$

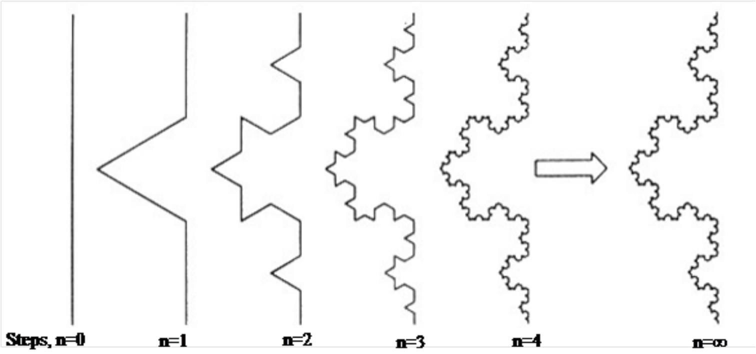

Figure A.2: Von Koch curve fractal geometry

Based on the dimension calculated, it can be seen that the Von Koch curve is neither a surface nor a line, instead something in between.

A.2 Self similarity

In addition to the conditions being nowhere differentiable and having a fractal dimension, i.e. Hausdorff dimension. Falconer (2003) proposed that a fractal must also have the following:

- **Fine structure:** A fractal is repeated over an infinity of scales.
- **Local and global irregularities:** A fractal cannot be described using traditional Euclidean geometric language.
- **Simple definition:** A fractal is generally composed of the same pattern repeated recursively; therefore, the fractal can be defined as function of the repeating pattern.
- **Self-similarity:** This can occur in a number of ways:
  - Exact self-similarity: The shape is identical on all scales (i.e Von Koch curve, Figure A.2)
  - Quasi self-similarity: Approximations of the pattern, or a copy of the entire fractal, appears on different scales. (i.e Mandelbrot set) The specific area shown in the Mandelbrot fractal is known as the elephant valley because spiral shapes appearing resemble elephants, but in fact they are a repetition of the whole macro geometry.

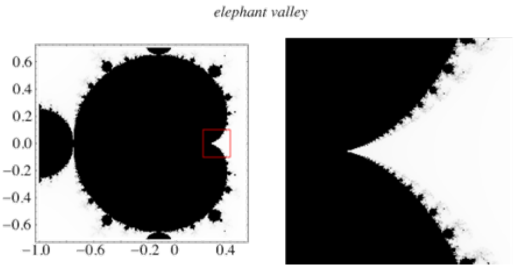

Figure A.3: Mandlebrot fractal

  - Statistical self-similarity: Patterns are repeated stochastically, such that statistical measures are preserved. (i.e. The coastline of Great Britain) This is a well documented example for a statistical fractal, because the measuring object (orange line) appears to repeat itself in a random fashion, also changing the dimension of the measuring

Figure A.4: Approximating the perimeter of the UK using a fractal

object increases the length of the coastline. If this process were to be continued as the measurement length decreases the total length of the coastline would seem to increase. This was first documented by Mandelbrot and is known as the coastline paradox.

- Qualitative self-similarity: Like in a time series Repeating patterns in a time series like the stock market, or cardiac response signals can be considered as fractal objects. It is in fact these repeating patterns that allow us to extract useful information from the signal and not attribute it to random noise.

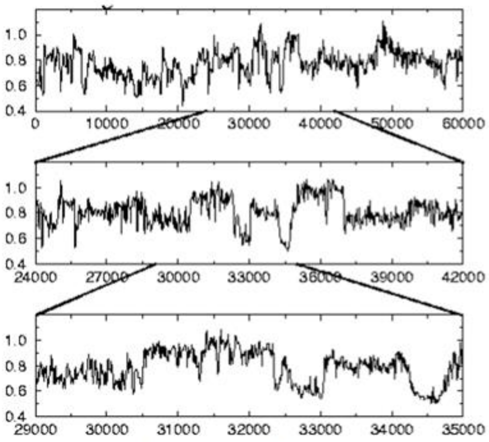

Figure A.5: A time series

- Multi-fractal Scaling: A fractal that displays two or more of the expressed self-similarity forms above.

Since nature does not produce exact and perfect, geometries, all fractal shapes that occur in nature tend to be statistically self-similar, whilst mathematical fractals tend to follow either exact or quasi self-similarity conditions

Appendix B

Derivation of the distribution functions

B.1 Boltzmann Distribution

A simplified proof for the derivation of the Boltzmann distribution is given here.

Consider a small system of particles, A, in a large thermal reservoir, B at a fixed temperature T. Hence. the total energy of the system can be defined as

$$E_{tot} = E_A + E_B \tag{B.1}$$

When the system is at equilibrium every microstate of the combined system has energy, E_{tot}, so there is an equal chance of observing any microstate. To find the number of microstates in system B for a given energy state of system A, E_A we start with the Boltzmann entropy formula

$$S(E_B) = klog(\Omega(E_B)) \tag{B.2}$$

Thus the number of microstates is

$$\Omega(E_B) = e^{\frac{S(E_B)}{k}} \tag{B.3}$$

This can be rewritten as

$$\Omega(E_{tot} - E_A) = e^{\frac{S(E_{tot}-E_A)}{k}} \tag{B.4}$$

This shows that the number of microstates of B is dependent on the microstate of A. Therefore, it can be stated that the probability of A being in state E_A, $f(E_A)$ is

$$f(E_A) \propto f_0 e^{\frac{S(E_{tot}-E_A)}{k}} \tag{B.5}$$

where f_0 is the value of $f(E_A)$ when $E_A = 0$. Since $E_A \ll E_{tot}$, then the entropy of the system B can be expanded to;

$$S_B(E_{tot} - E_A) \approx S_B(E_{tot}) - E_A \frac{dS_B}{dE_B} \tag{B.6}$$

The term $\frac{dS_B}{dE_B}$ is just the inverse of the temperature as per the Gibbs entropy formula. Introducing this term into the above formula for $f(E_A)$ and normalising the probability yields the Boltzmann distribution:

$$f(E) = Ae^{\frac{-E}{kT}} \tag{B.7}$$

B.2 Maxwell Distribution

The Maxwell distribution can easily be arrived from the Boltzmann distribution. Since the Maxwell distribution considers the velocity distribution of the particles, considering a one-dimensional kinetic energy the Boltzmann distribution can be rewritten as

$$f(\xi_x) = Ae^{\frac{-m{\xi_x}^2}{2kT}} \tag{B.8}$$

In order to find A, the above function is normalised,

$$\int_{-\infty}^{\infty} f(\xi_x) d(\xi_x) = 1 \tag{B.9}$$

It is also known that the above definite integral takes the form

$$\int_{-\infty}^{\infty} e^{-ax^2} dx = \sqrt{\frac{\pi}{a}} \tag{B.10}$$

Therefore, the constant A can be evaluated to be

$$A = \sqrt{\frac{m}{2\pi kT}} \tag{B.11}$$

So that the probability $f(\xi_x)$ becomes,

$$f(\xi_x) = \sqrt{\frac{m}{2\pi kT}} e^{\frac{-m\xi_x^2}{2kT}} \tag{B.12}$$

Now, if all Cartesian directions are considered,and assuming that the motions in all three directions are independent, i.e. the probability of finding a particle with x component velocity is not dependent on the probability of finding the particle's y component velocity. The probability is now the product of each velocity component independently, which gives the three dimensional energy distribution

$$\begin{aligned} f(\xi_x, \xi_y, \xi_z) &= f(\xi_x).f(\xi_y).f(\xi_z) && \text{(B.13)} \\ &= \left(\frac{m}{2\pi kT}\right)^{3/2} e^{\frac{-m(\xi_x^2+\xi_y^2+\xi_z^2)}{2kT}} && \text{(B.14)} \\ &= \left(\frac{m}{2\pi kT}\right)^{3/2} e^{\frac{-m\xi^2}{2kT}} && \text{(B.15)} \end{aligned}$$

The above equation only considers one particle in the system, in order to get the Maxwell distribution all the particles in the system must be considered. This can be easily achieved by visualising the distribution of the particles in a velocity space, therefore, all the particles with the same speed will fall on the surface of a sphere where the area is $4\pi c^2$. Finally multiplying this to the three-dimensional energy distribution yields the Maxwell distribution.

$$f(\xi) = 4\pi\xi^2 \left(\frac{m}{2\pi kT}\right)^{3/2} e^{\frac{-m\xi^2}{2kT}} \tag{B.16}$$

Appendix C

LBM Lattice Types

In here the various lattice types available for use in LBM schemes will be presented. The lattices follow, by convention, the naming standard: D_nQ_b where n is the dimension of the lattice and b is the numer of discrete velocities.

The key factor in the design of each lattice is the weight associated with discrete velocity, as they are necessary for the computation of the equilibrium distribution functions as demonstrated earlier in chapter 2

$$f_i^{eq} = \Phi \mathrm{w}_i \left[A + B\boldsymbol{c}_i \cdot \boldsymbol{u} + C(\boldsymbol{c}_i \cdot \boldsymbol{u})^2 + Du^2\right] \tag{C.1}$$

Two general rules are usually adopted in each lattice. The central velocity is always labelled as $\boldsymbol{c}_0$, and in order to maintain isotropy in the model the total number of discrete velocities must be odd.

In the following sections a detailed description of the most common lattice types for one, two and three dimensions will be given. For clarity and ease vectors of the with the equal weight will be coloured the same.

C.1 D1Q3 - $c_s = 1/3$

$\boldsymbol{c}_0 = (0,0)$ $\quad w_0 = 4/6$
$\boldsymbol{c}_1 = (1,0)$ $\quad w_1 = 1/6$
$\boldsymbol{c}_2 = (-1,0)$ $\quad w_2 = 1/6$

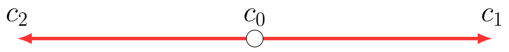

C.2 D1Q5 - $c_s = 1$

$$\begin{aligned}
\boldsymbol{c}_0 &= (0,0) & w_0 &= 6/12\\
\boldsymbol{c}_1 &= (1,0) & w_1 &= 2/12\\
\boldsymbol{c}_2 &= (-1,0) & w_2 &= 2/12\\
\boldsymbol{c}_3 &= (2,0) & w_3 &= 1/12\\
\boldsymbol{c}_4 &= (-2,0) & w_4 &= 1/12
\end{aligned}$$

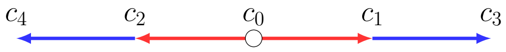

C.3 D2Q7 - $c_s = 1/4$

$$\begin{aligned}
\boldsymbol{c}_0 &= (0,0) & w_0 &= 6/12\\
\boldsymbol{c}_1 &= (1,0) & w_1 &= 2/12\\
\boldsymbol{c}_2 &= (-1,0) & w_2 &= 2/12\\
\boldsymbol{c}_3 &= (-1/2, \sqrt{3}/2) & w_3 &= 1/12\\
\boldsymbol{c}_4 &= (1/2, -\sqrt{3}/2) & w_4 &= 1/12\\
\boldsymbol{c}_5 &= (1/2, \sqrt{3}/2) & w_5 &= 1/12\\
\boldsymbol{c}_6 &= (-1/2, -\sqrt{3}/2) & w_6 &= 1/12
\end{aligned}$$

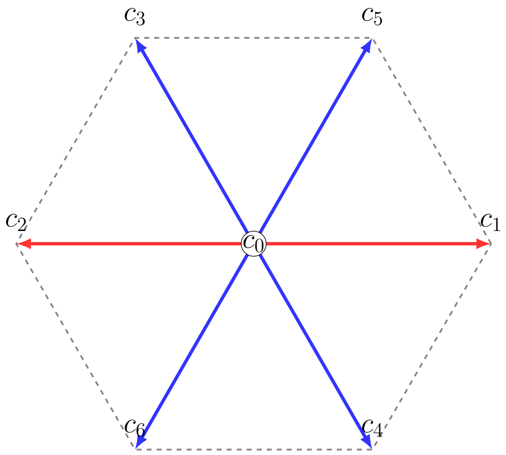

C.4 D2Q9 - $c_s = 1/3$

$$\begin{aligned}
\boldsymbol{c}_0 &= (0,0) & w_0 &= 4/9\\
\boldsymbol{c}_1 &= (1,0) & w_1 &= 1/9\\
\boldsymbol{c}_2 &= (-1,0) & w_2 &= 1/9\\
\boldsymbol{c}_3 &= (0,1) & w_3 &= 1/9\\
\boldsymbol{c}_4 &= (0,-1) & w_4 &= 1/9\\
\boldsymbol{c}_5 &= (1,1) & w_5 &= 1/36\\
\boldsymbol{c}_6 &= (-1,-1) & w_6 &= 1/36\\
\boldsymbol{c}_7 &= (-1,1) & w_7 &= 1/36\\
\boldsymbol{c}_8 &= (1,-1) & w_8 &= 1/36
\end{aligned}$$

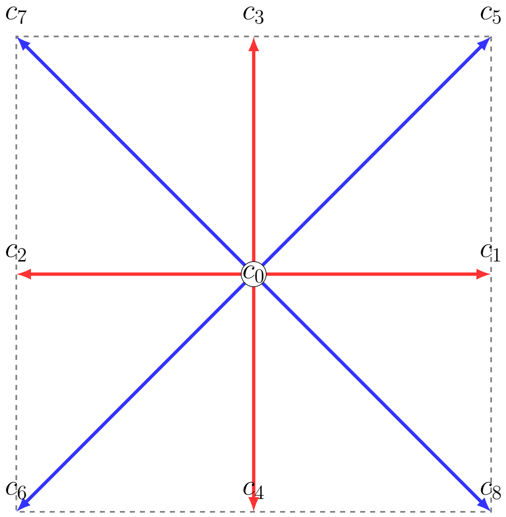

C.5 D3Q15 - $c_s = 1/3$

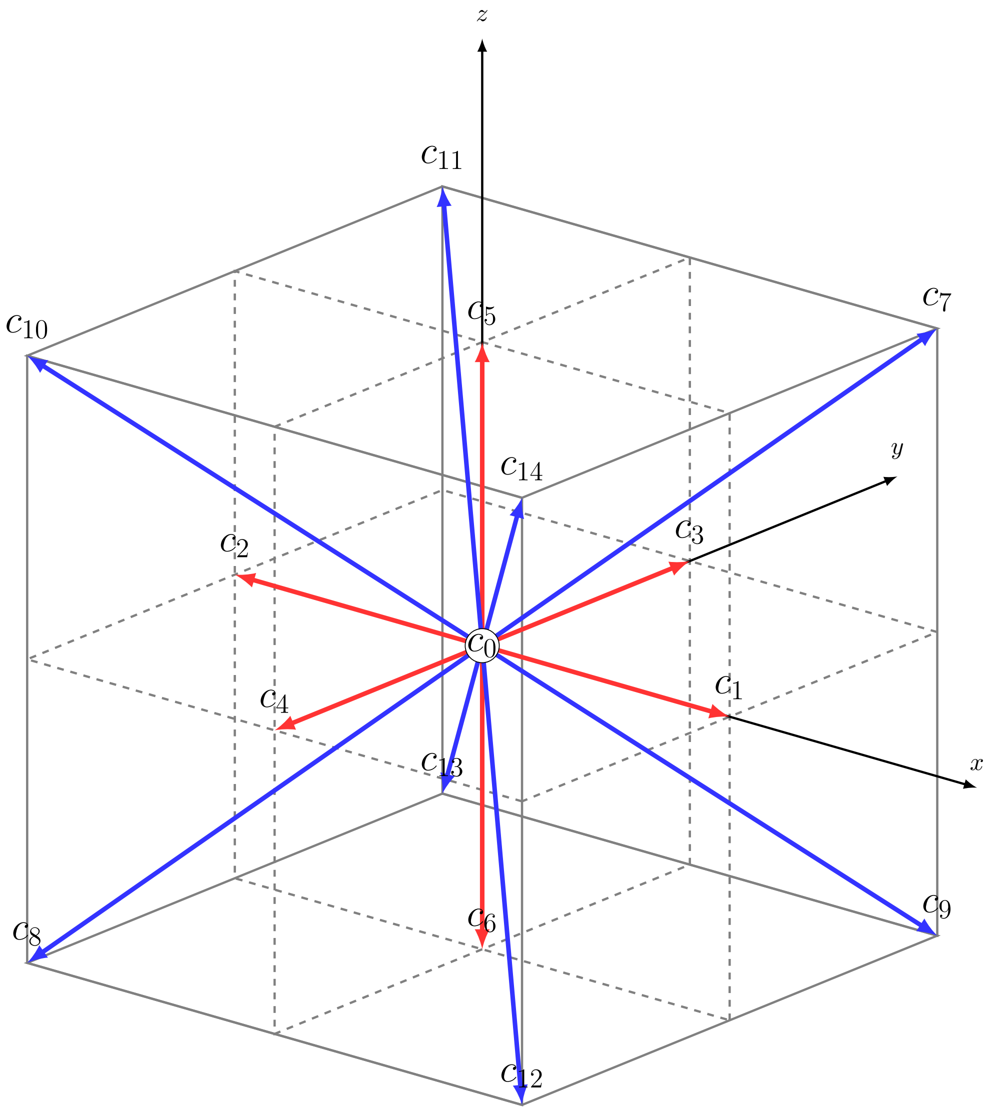

	$\boldsymbol{c}_0 = (0,0,0)$	$w_0 = 2/9$	
$\boldsymbol{c}_1 = (1,0,0)$	$w_1 = 1/9$	$\boldsymbol{c}_8 = (-1,-1,-1)$	$w_8 = 1/72$
$\boldsymbol{c}_2 = (-1,0,0)$	$w_2 = 1/9$	$\boldsymbol{c}_9 = (1,1,-1)$	$w_9 = 1/72$
$\boldsymbol{c}_3 = (0,1,0)$	$w_3 = 1/9$	$\boldsymbol{c}_{10} = (-1,-1,1)$	$w_{10} = 1/72$
$\boldsymbol{c}_4 = (0,-1,0)$	$w_4 = 1/9$	$\boldsymbol{c}_{11} = (-1,1,1)$	$w_{11} = 1/72$
$\boldsymbol{c}_5 = (0,0,1)$	$w_5 = 1/9$	$\boldsymbol{c}_{12} = (1,-1,-1)$	$w_{12} = 1/72$
$\boldsymbol{c}_6 = (0,0,-1)$	$w_6 = 1/9$	$\boldsymbol{c}_{13} = (-1,1,-1)$	$w_{13} = 1/72$
$\boldsymbol{c}_7 = (1,1,1)$	$w_7 = 1/72$	$\boldsymbol{c}_{14} = (1,-1,1)$	$w_{14} = 1/72$

C.6 D3Q19 - $c_s = 1/3$

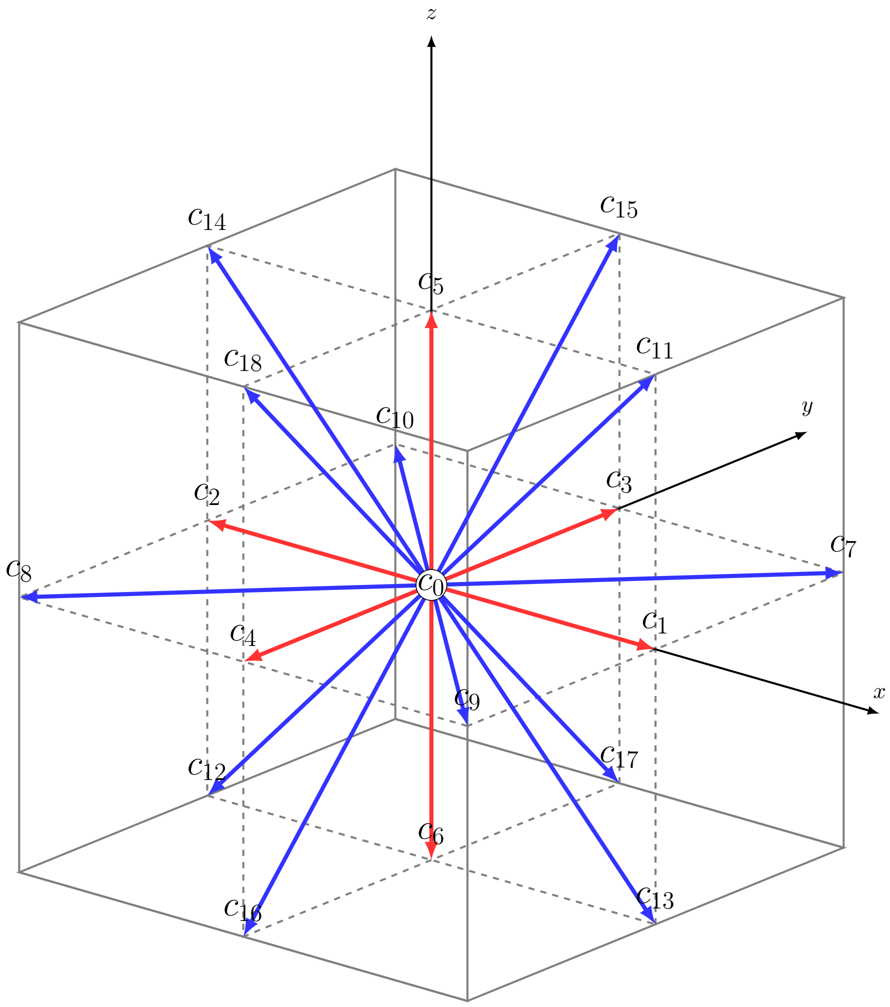

	$\boldsymbol{c}_0 = (0,0,0)$	$w_0 = 1/3$	
$\boldsymbol{c}_1 = (1,0,0)$	$w_1 = 1/18$	$\boldsymbol{c}_{10} = (-1,1,0)$	$w_{10} = 1/36$
$\boldsymbol{c}_2 = (-1,0,0)$	$w_2 = 1/18$	$\boldsymbol{c}_{11} = (1,0,1)$	$w_{11} = 1/36$
$\boldsymbol{c}_3 = (0,1,0)$	$w_3 = 1/18$	$\boldsymbol{c}_{12} = (-1,0,-1)$	$w_{12} = 1/36$
$\boldsymbol{c}_4 = (0,-1,0)$	$w_4 = 1/18$	$\boldsymbol{c}_{13} = (1,0,-1)$	$w_{13} = 1/36$
$\boldsymbol{c}_5 = (0,0,1)$	$w_5 = 1/18$	$\boldsymbol{c}_{14} = (-1,0,1)$	$w_{14} = 1/36$
$\boldsymbol{c}_6 = (0,0,-1)$	$w_6 = 1/18$	$\boldsymbol{c}_{15} = (0,1,1)$	$w_{15} = 1/36$
$\boldsymbol{c}_7 = (1,1,0)$	$w_7 = 1/36$	$\boldsymbol{c}_{16} = (0,-1,-1)$	$w_{16} = 1/36$
$\boldsymbol{c}_8 = (-1,-1,0)$	$w_8 = 1/36$	$\boldsymbol{c}_{17} = (0,1,-1)$	$w_{17} = 1/36$
$\boldsymbol{c}_9 = (1,-1,0)$	$w_9 = 1/36$	$\boldsymbol{c}_{18} = (0,-1,1)$	$w_{18} = 1/36$

Appendix D

Turbulence Modelling: RANS

Following his original work, Reynolds (1894) introduced the notion of a decomposition for the flow variables into mean and fluctuating components,

$$u = \overline{u} + u', \tag{D.1}$$

where u represents the instantaneous velocity as a sum of the mean, $\overline{u}$ and the fluctuating component, u'. This decomposition can be then introduced into the Navier-Stokes equation ((2.5)) to give the Reynolds Averaged Navier Stokes (RANS)

$$\frac{\partial \boldsymbol{u}}{\partial t} + (\overline{\boldsymbol{u}} \cdot \nabla)\overline{\boldsymbol{u}} = -\frac{1}{\rho}\frac{\partial \overline{p}}{\partial \boldsymbol{x}} + \nu \frac{\partial^2 \overline{\boldsymbol{u}}}{\partial \boldsymbol{x}^2} - \frac{\partial}{\partial \boldsymbol{x}}(\overline{u_i' u_j'}) \tag{D.2}$$

where $\overline{u_i' u_j'}$ are known as the Reynolds stresses and represent the changes in the fluid's momentum caused by the fluctuating component of the flow.

What (D.2) shows, is that by time averaging the Navier-Stokes equations a new term, Reynolds stresses, has been introduced. This is what is referred to as the closure problem in turbulence, since there are no new equations for the variables introduced in the RANS equations, a modelling approach has to be adopted in order to close the system. In order to solve these equations using numerical methods a model for the Reynolds stresses has to be introduced.

Most turbulence models for the RANS equations are based upon the Boussinesq hypothesis of 1877 (Boussinesq 1877, Schmitt 2007). In these methods the Reynolds stresses are approximated as:

$$-\rho\overline{u_i' u_j'} = \mu_t\left(\frac{\partial \overline{u}_i}{\partial x_j} + \frac{\partial \overline{u}_j}{\partial x_i}\right) - \frac{2}{3}\delta_{ij}\left(\rho k + \mu_t \frac{\partial \overline{u}_k}{\partial x_k}\right) \tag{D.3}$$

where μ_t and k are the turbulent viscosity and kinetic energy respectively.

D.0.1 Two Equation Models

The most commonly used model is the Standard $k - \epsilon$ of Launder & Spalding (1974), which improved upon the previous mixing length model of Prandtl (1925) by introducing two additional transport equations for turbulent kinetic energy, k, and the turbulent dissipation, ϵ. In this model the eddy viscosity is given by

$$\mu_t = C_\mu \frac{k^2}{\epsilon} \tag{D.4}$$

where the turbulence constant $C_\mu = 0.09$, is an accepted value obtained empirically (Launder & Spalding 1974).

D.0.2 One Equation Model

A one equation model was introduced in Spalart & Allmaras (1992). In this case the transported variable is $\overline{\nu}$ which is a modified eddy viscosity (It is identical to the kinematic viscosity except in the near-wall region). Thus the turbulent viscosity is

$$\mu_t = \rho \overline{\nu} f_{v1} \tag{D.5}$$

where f_{v1} is a damping function dependent on $\overline{\nu}/\nu$. It should be noted that since this model does not calculate k the Reynolds stresses can only be approximated as per the Boussinesq equation (D.3). This model can be applied to the LBM by taking the total viscosity to be the sum of the molecular viscosity and the turbulent viscosity. (Chen 2012, Shu et al. 2006)

Bibliography

Anderson, J. D. & Wendt, J. (1995), *Computational fluid dynamics*, Vol. 206, Springer.

Bai, K., Meneveau, C. & Katz, J. (2012), 'Near-wake turbulent flow structure and mixing length downstream of a fractal tree', *Boundary-layer meteorology* **143**(2), 285–308.

Batchelor, G. K. (2000), *An introduction to fluid dynamics*, Cambridge university press.

Bhatnagar, P. L., Gross, E. P. & Krook, M. (1954), 'A model for collision processes in gases. i. small amplitude processes in charged and neutral one-component systems', *Physical review* **94**(3), 511.

Boltzmann, L. (1872), 'Weitere studien über das wärmegleichgewicht unter gasmolekülen', *K. Acad. Wiss.(Wein) Sitzb., II Abt* **66**.

Bosch, G. & Rodi, W. (1998), 'Simulation of vortex shedding past a square cylinder with different turbulence models', *International journal for numerical methods in fluids* **28**(4), 601–616.

Boussinesq, J. (1877), *Essai sur la théorie des eaux courantes*, Imprimerie nationale.

Bouzidi, M., d'Humières, D., Lallemand, P. & Luo, L.-S. (2001), 'Lattice boltzmann equation on a two-dimensional rectangular grid', *Journal of Computational Physics* **172**(2), 704–717.

Bouzidi, M., Firdaouss, M. & Lallemand, P. (2001), 'Momentum transfer of a boltzmann-lattice fluid with boundaries', *Physics of fluids* **13**(11), 3452–3459.

Breuer, M., Bernsdorf, J., Zeiser, T. & Durst, F. (2000), 'Accurate computations of the laminar flow past a square cylinder based on two different methods: lattice-boltzmann and finite-volume', *International journal of heat and fluid flow* **21**(2), 186–196.

Cao, N., Chen, S., Jin, S. & Martinez, D. (1997), 'Physical symmetry and lattice symmetry in the lattice boltzmann method', *Physical Review E* **55**(1), R21.

Cercignani, C. (1988), The boltzmann equation, *in* 'The Boltzmann Equation and Its Applications', Springer, pp. 40–103.

Chen, S., Chen, H., Martnez, D. & Matthaeus, W. (1991), 'Lattice boltzmann model for simulation of magnetohydrodynamics', *Phys. Rev. Lett.* **67**, 3776–3779.

Chen, X.-P. (2012), 'Applications of lattice boltzmann method to turbulent flow around two-dimensional airfoil', *Engineering Applications of Computational Fluid Mechanics* **6**(4), 572–580.

Crouse, B., Rank, E., Krafczyk, M. & Tölke, J. (2003), 'A lb-based approach for adaptive flow simulations', *International Journal of Modern Physics B* **17**(01n02), 109–112.

Delbosc, N., Summers, J. L., Khan, A., Kapur, N. & Noakes, C. J. (2014), 'Optimized implementation of the lattice boltzmann method on a graphics processing unit towards real-time fluid simulation', *Computers & Mathematics with Applications* **67**(2), 462–475.

d'Humières, D. (1992), 'Generalized lattice-boltzmann equations', *Rarefied gas dynamics* pp. 450–458.

d'Humières, D. (2002), 'Multiple–relaxation–time lattice boltzmann models in three dimensions', *Philosophical Transactions of the Royal Society of London A: Mathematical, Physical and Engineering Sciences* **360**(1792), 437–451.

d'Humières, D., Lallemand, P. & Frisch, U. (1986), 'Lattice gas models for 3d hydrodynamics', *EPL (Europhysics Letters)* **2**(4), 291.

European Environment Agency (2016), *Urban sprawl in Europe*, number 11, European Environment Agency.

Falconer, K. (2003), ‘Fractal geometry’.

Fernandino, M., Beronov, K. & Ytrehus, T. (2009), ‘Large eddy simulation of turbulent open duct flow using a lattice boltzmann approach’, *Mathematics and Computers in Simulation* **79**(5), 1520–1526.

Feynman, R. P., Leighton, R. B. & Sands, M. (2013), *The Feynman Lectures on Physics, Desktop Edition Volume I*, Vol. 1, Basic books.

Filippova, O. & Hänel, D. (1998), ‘Grid refinement for lattice-bgk models’, *Journal of Computational physics* **147**(1), 219–228.

Frisch, U., d’Humières, D., Hasslacher, B., Lallemand, P., Pomeau, Y. & Rivet, J. (1987), ‘Lattice gas hydrodynamics in two and three dimensions’, *Complex Systems* **1**, 649–707.

Frisch, U., Hasslacher, B. & Pomeau, Y. (1986), ‘Lattice-gas automata for the navier-stokes equation’, *Physical review letters* **56**(14), 1505.

George, W. K. (1989), ‘The self-preservation of turbulent flows and its relation to initial conditions and coherent structures’, *Advances in turbulence* **3973**.

Ginzburg, I. (2005), ‘Equilibrium-type and link-type lattice boltzmann models for generic advection and anisotropic-dispersion equation’, *Advances in Water Resources* **28**(11), 1171 – 1195.

Grad, H. (1949), ‘On the kinetic theory of rarefied gases’, *Communications on Pure and Applied Mathematics* **2**(4), 331–407.

Guo, Z., Zheng, C. & Shi, B. (2002), ‘An extrapolation method for boundary conditions in lattice boltzmann method’, *Physics of Fluids* **14**(6), 2007–2010.

Hardy, J., Pomeau, Y. & De Pazzis, O. (1973*a*), ‘Time evolution of a two-dimensional classical lattice system’, *Physical Review Letters* **31**(5), 276.

Hardy, J., Pomeau, Y. & De Pazzis, O. (1973*b*), ‘Time evolution of a two-dimensional model system. i. invariant states and time correlation functions’, *Journal of Mathematical Physics* **14**(12), 1746–1759.

He, X., Luo, L.-S. & Dembo, M. (1996), ‘Some progress in lattice boltzmann method. part i. nonuniform mesh grids’, *Journal of computational Physics* **129**(2), 357–363.

Higham, J. & Brevis, W. (2018), ‘Modification of the modal characteristics of a square cylinder wake obstructed by a multi-scale array of obstacles’, *Experimental Thermal and Fluid Science* **90**, 212–219.

Higuera, F. J. & Jiménez, J. (1989), ‘Boltzmann approach to lattice gas simulations’, *EPL (Europhysics Letters)* **9**(7), 663.

Hou, S., Sterling, J., Chen, S. & Doolen, G. (1994), ‘A lattice boltzmann subgrid model for high reynolds number flows’, *arXiv preprint comp-gas/9401004* .

Inamuro, T., Yoshino, M. & Ogino, F. (1995), ‘A non-slip boundary condition for lattice boltzmann simulations’, *Physics of Fluids* **7**(12), 2928–2930.

Karlin, I., Asinari, P. & Succi, S. (2011), ‘Matrix lattice boltzmann reloaded’, *Philosophical Transactions: Mathematical, Physical and Engineering Sciences* **369**(1944), 2202–2210.

Karman, T. v. (1911), ‘Ueber den mechanismus des widerstandes, den ein bewegter körper in einer flüssigkeit erfährt’, *Nachrichten von der Gesellschaft der Wissenschaften zu Göttingen, Mathematisch-Physikalische Klasse* **1911**, 509–517.

Koda, Y. & Lien, F.-S. (2015), ‘The lattice boltzmann method implemented on the gpu to simulate the turbulent flow over a square cylinder confined in a channel’, *Flow, Turbulence and Combustion* **94**(3), 495–512.

Koelman, J. (1991), ‘A simple lattice boltzmann scheme for navier-stokes fluid flow’, *EPL (Europhysics Letters)* **15**(6), 603.

Laizet, S. & Vassilicos, J. (2012), ‘Fractal space-scale unfolding mechanism for energy-efficient turbulent mixing’, *Physical Review E* **86**(4), 046302.

Lallemand, P. & Luo, L.-S. (2000), ‘Theory of the lattice boltzmann method: Dispersion, dissipation, isotropy, galilean invariance, and stability’, *Phys. Rev. E* **61**, 6546–6562.

Latt, J. (2009), ‘Palabos, parallel lattice boltzmann solver’.

Latt, J. & Chopard, B. (2006), ‘Lattice boltzmann method with regularized precollision distribution functions’, *Mathematics and Computers in Simulation* **72**(2-6), 165–168.

Launder, B. E. & Spalding, D. (1974), 'The numerical computation of turbulent flows', *Computer methods in applied mechanics and engineering* **3**(2), 269–289.

Lee, T. & Lin, C.-L. (2001), 'A characteristic galerkin method for discrete boltzmann equation', *Journal of Computational Physics* **171**(1), 336–356.

Liouville, J. (1838), 'Note on the theory of the variation of arbitrary constants', *J. Math. Pure. Appl.* **3**, 342–349.

Lu, S. & Willmarth, W. (1973), 'Measurements of the structure of the reynolds stress in a turbulent boundary layer', *Journal of Fluid Mechanics* **60**(03), 481–511.

Mandelbrot, B. B. (1983), 'The fractal geometry of nature/revised and enlarged edition', *New York, WH Freeman and Co., 1983, 495 p.* **1**.

Maxwell, J. C. (1860), 'V. illustrations of the dynamical theory of gases.—part i. on the motions and collisions of perfectly elastic spheres', *The London, Edinburgh, and Dublin Philosophical Magazine and Journal of Science* **19**(124), 19–32.

Mazellier, N. & Vassilicos, J. (2010), 'Turbulence without richardson–kolmogorov cascade', *Physics of Fluids (1994-present)* **22**(7), 075101.

McNamara, G. R. & Zanetti, G. (1988), 'Use of the boltzmann equation to simulate lattice-gas automata', *Phys. Rev. Lett.* **61**, 2332–2335.

Mohamad, A. A. (2011), *Lattice Boltzmann method: fundamentals and engineering applications with computer codes*, Springer Science & Business Media.

Mouhot, C. & Strain, R. M. (2007), 'Spectral gap and coercivity estimates for linearized boltzmann collision operators without angular cutoff', *Journal de mathématiques pures et appliquées* **87**(5), 515–535.

Nannelli, F. & Succi, S. (1992), 'The lattice boltzmann equation on irregular lattices', *Journal of Statistical Physics* **68**(3-4), 401–407.

Nepf, H. (1999), 'Drag, turbulence, and diffusion in flow through emergent vegetation', *Water resources research* **35**(2), 479–489.

Nicolle, A. & Eames, I. (2011), 'Numerical study of flow through and around a circular array of cylinders', *Journal of Fluid Mechanics* **679**, 1–31.

Noble, D. R., Chen, S., Georgiadis, J. G. & Buckius, R. O. (1995), 'A consistent hydrodynamic boundary condition for the lattice boltzmann method', *Physics of Fluids* **7**(1), 203–209.

Pope, S. (2000), *Turbulent Flows*, Cambridge University Press.

Prandtl, L. (1925), 'Bericht über untersuchungen zur ausgebildeten turbulenz', *Z. Angew. Math. Mech* **5**(2), 136–139.

Qian, Y., d'Humières, D. & Lallemand, P. (1992), 'Lattice bgk models for navier-stokes equation', *EPL (Europhysics Letters)* **17**(6), 479.

Qian, Y. H. & Humières, D. d. (1990), Gaz sur reseaux et theorie cinetique sur reseaux appliquee a l'equation de navier-stokes, PhD thesis. Thèse de doctorat dirigée par Lallemand, Pierre Mécanique et physique statistique Paris 6 1990.

Rapaport, D. C. & Rapaport, D. C. R. (2004), *The art of molecular dynamics simulation*, Cambridge university press.

Raupach, M. & Shaw, R. (1982), 'Averaging procedures for flow within vegetation canopies', *Boundary-Layer Meteorology* **22**(1), 79–90.

Reynolds, O. (1883), 'An experimental investigation of the circumstances which determine whether the motion of water shall be direct or sinuous, and of the law of resistance in parallel channels.', *Proceedings of the royal society of London* **35**(224-226), 84–99.

Reynolds, O. (1894), 'On the dynamical theory of incompressible viscous fluids and the determination of the criterion.', *Proceedings of the Royal Society of London* **56**(336-339), 40–45.

Sagaut, P. (2010), 'Toward advanced subgrid models for lattice-boltzmann-based large-eddy simulation: theoretical formulations', *Computers & Mathematics with Applications* **59**(7), 2194–2199.

Sangtani Lakhwani, N. M., Nicolleau, F. C. G. A. & Brevis, W. (2018), 'Lattice boltzman method simulation of high reynolds number flows pass porous obstacles', *International Journal of Applied Mechanics* **00**(submitted), 00.

Schmitt, F. G. (2007), 'About boussinesq's turbulent viscosity hypothesis: historical remarks and a direct evaluation of its validity', *Comptes Rendus Mécanique* **335**(9), 617–627.

Seginer, I., Mulhearn, P., Bradley, E. F. & Finnigan, J. (1976), 'Turbulent flow in a model plant canopy', *Boundary-Layer Meteorology* **10**(4), 423–453.

Seoud, R. & Vassilicos, J. (2007), 'Dissipation and decay of fractal-generated turbulence', *Physics of Fluids (1994-present)* **19**(10), 105108.

Shaw, R. H., Tavangar, J. & Ward, D. P. (1983), 'Structure of the reynolds stress in a canopy layer', *Journal of climate and applied meteorology* **22**(11), 1922–1931.

Shaw, R., Silversides, R. & Thurtell, G. (1974), 'Some observations of turbulence and turbulent transport within and above plant canopies', *Boundary-Layer Meteorology* **5**(4), 429–449.

Shu, C., Chew, Y. & Niu, X. (2001), 'Least-squares-based lattice boltzmann method: a meshless approach for simulation of flows with complex geometry', *Physical Review E* **64**(4), 045701.

Shu, C., Peng, Y., Zhou, C. & Chew, Y. (2006), 'Application of taylor series expansion and least-squares-based lattice boltzmann method to simulate turbulent flows', *Journal of Turbulence* (7), N38.

Smagorinsky, J. (1963), 'General circulation experiments with the primitive equations: I. the basic experiment*', *Monthly weather review* **91**(3), 99–164.

Spalart, P. R. & Allmaras, S. R. (1992), 'A one equation turbulence model for aerodinamic flows.', *AIAA journal* **94**.

Stolz, S. & Adams, N. (1999), 'An approximate deconvolution procedure for large-eddy simulation', *Physics of Fluids (1994-present)* **11**(7), 1699–1701.

Stolz, S., Adams, N. & Kleiser, L. (2001), 'An approximate deconvolution model for large-eddy simulation with application to incompressible wall-bounded flows', *Physics of Fluids (1994-present)* **13**(4), 997–1015.

Stresing, R., Peinke, J., Seoud, R. & Vassilicos, J. (2010), 'Defining a new class of turbulent flows', *Physical review letters* **104**(19), 194501.

Succi, S., Amati, G. & Benzi, R. (1995), 'Challenges in lattice boltzmann computing', *Journal of statistical physics* **81**(1-2), 5–16.

Teixeira, C. M. (1998), 'Incorporating turbulence models into the lattice-boltzmann method', *International Journal of Modern Physics C* **9**(08), 1159–1175.

Tennekes, H. & Lumley, J. L. (1972), *A first course in turbulence*, MIT press.

Tölke, J., Freudiger, S. & Krafczyk, M. (2006), 'An adaptive scheme using hierarchical grids for lattice boltzmann multi-phase flow simulations', *Computers & fluids* **35**(8-9), 820–830.

Versteeg, H. K. & Malalasekera, W. (2007), *An introduction to computational fluid dynamics: the finite volume method*, Pearson Education.

Villani, C. (2002), 'A review of mathematical topics in collisional kinetic theory', *Handbook of mathematical fluid dynamics* **1**, 71–305.

Williamson, C. H. K. (1985), 'Evolution of a single wake behind a pair of bluff bodies', *Journal of Fluid Mechanics* **159**, 1–18.

Williamson, C. H. K. (1996), 'Vortex dynamics in the cylinder wake', *Annual Review of Fluid Mechanics* **28**(1), 477–539.

Wilson, J., Ward, D., Thurtell, G. & Kidd, G. (1982), 'Statistics of atmospheric turbulence within and above a corn canopy', *Boundary-Layer Meteorology* **24**(4), 495–519.

Wolf-Gladrow, D. A. (2004), *Lattice-gas cellular automata and lattice Boltzmann models: an introduction*, Springer.

Wolfram, S. (1986), 'Cellular automaton fluids 1: Basic theory', *Journal of statistical physics* **45**(3-4), 471–526.

Wygnanski, I., Champagne, F. & Marasli, B. (1986), 'On the large-scale structures in two-dimensional, small-deficit, turbulent wakes', *Journal of Fluid Mechanics* **168**, 31–71.

Yu, D., Mei, R. & Shyy, W. (2002), 'A multi-block lattice boltzmann method for viscous fluid flows', *International journal for numerical methods in fluids* **39**(2), 99–120.

Yue, W., Parlange, M. B., Meneveau, C., Zhu, W., van Hout, R. & Katz, J. (2007*a*), 'A comparative quadrant analysis of turbulence in a plant canopy', *Water resources research* **43**(5).

Yue, W., Parlange, M. B., Meneveau, C., Zhu, W., van Hout, R. & Katz, J. (2007*b*), 'Large-eddy simulation of plant canopy flows using plant-scale representation', *Boundary-layer meteorology* **124**(2), 183–203.

Zdravkovich, M. (1987), 'The effects of interference between circular cylinders in cross flow', *Journal of fluids and structures* **1**(2), 239–261.

Zhang, J. & Kwok, D. Y. (2006), 'Pressure boundary condition of the lattice boltzmann method for fully developed periodic flows', *Physical review E* **73**(4), 047702.

Zou, Q. & He, X. (1997), 'On pressure and velocity boundary conditions for the lattice boltzmann bgk model', *Physics of fluids* **9**(6), 1591–1598.